Platinum Based Electrocatalysts for Proton Exchange Membrane Fuel Cells

By

Dongguo Li

B.S., University of Science and Technology of China, 2008

M.A., Brown University, 2012

A Dissertation Submitted in Partial Fulfillment of the
Requirements for the Degree of Doctor of Philosophy
in the Department of Chemistry at Brown University

Providence, Rhode Island

April 2014

This dissertation by Dongguo Li is accepted in its present form

by the Department of Chemistry as satisfying the

dissertation requirement for the degree of Doctor of Philosophy.

Date _____ _____

Prof. Shouheng Sun, Advisor

Recommended to the Graduate Council by

Date _____ _____

Prof. Wesley Bernskoetter, Reader

Date _____ _____

Prof. Lai-Sheng Wang, Reader

Approved by the Graduate Council

Date _____ _____

Prof. Peter Weber, Dean of the Graduate School

Curriculum Vita

Dongguo Li was born in Mianyang, Sichuan, China on December 30th 1986. From 2004 to 2008, he attended University of Science and Technology of China, where he obtained Bachelor of Science degree from Department of Chemistry in July 2008. He was accepted by Department of Chemistry, Brown University in 2008 toward the degree of Doctor of Philosophy, where he spent his first year as a teaching assistant. He joined Prof. Shouheng Sun's group in early 2009 and worked as a research assistant from then on. At the end 2009, he began his research at Dr. Stamenkovic and Dr. Markovic's group in Argonne National Laboratory due to collaboration between the two groups. He has been focused on studying the catalytic properties of platinum based materials for fuel cell applications.

Acknowledgements

During my first semester in Brown, I was impressed by Prof. Sun's course of nanoscale materials which presented intriguing aspects of nano-science. I was happy to be able to pursue my PhD in his lab. I really appreciate his valuable mentoring not only in daily experiment, but also in how to do research, to learn to have critical thinking about literatures. He also offered a great opportunity for me to carry on my study in Argonne, where I met Dr. Stamenkovic and Dr. Markovic. Their expertise in electrochemistry has supported me to continue my research on fuel cell catalysis, which is also sincerely appreciated. I also would like to thank my committee members, Prof. Wang and Prof. Bernskoetter, for their efforts on helping me through RPD, ORP and thesis.

In the meantime, I enjoyed working in both Brown University and Argonne National Lab, where both groups are full of awesome and easygoing people I feel grateful to. Dr Jaemin Kim, Dr. Hongwang Zhang and Dr. Yi Liu offered great assistance in helping me start hands-on experiment nanoparticle synthesis and characterization. Dr. Chao Wang taught me how to carry out electrochemical experiment. He also taught me how to drive when I first came to Argonne. Dr. Xiaolian Sun, Dr. Shaojun Guo, Dr. Yi Liu, Dr. Sen Zhang and Dr. Vismadeb Mazumder provided me nanoparticles for electrocatalysis. Dr. Yijin Kang, Dr. Dusan Strmcnik, Dr. Dennis van der Vliet, Dr. Dusan Tripkovic, Dr. Arydas Paulikas, Dr. Nemanja Danilovic, Dr. Joshua Snyder, Dr. Masanobu Uchimura and Dr. Ram Subbaraman also helped me with my daily experiment. I also thank all the other group members—Dr. Sheng Peng, Dr. Kai Cheng, Dr. Chenjie Xu, Dr. Youngmin Lee, Dr. Seohyoung Chang, Sally Ho, Dr. Pietro Papa Lopes, Jonghun Lee, Huiyuan Zhu, Dr.

Onder Metin, Aruna Sigdel, Dr. Natalie Huls, Dr. Lise Lacroix, Adriana Mendoza-Garcia, Liheng Wu, Wenlei Zhu. I want to express my gratitude to the collaborators for their valuable help and discussion during my research too, including Dr. Miaofang Chi, Dr. Guofeng Wang, Dr. Kee-Chul Chang, Dr. Karren More.

I always appreciate my parents, grandparents and other family members. Their love and support have always accompanied me throughout my PhD studies. I feel sorry I could not see them often. Especially during the first 2 years, I often heard news about aftershocks after the big earthquake stuck my hometown in 2008. I wish you always healthy and happy.

Abstract of “Platinum Based Electrocatalysts for Proton Exchange Membrane Fuel Cells” by Dongguo Li, Ph. D., Brown University, May 2014.

The rapid advance proton exchange membrane fuel cell technology demand highly efficient platinum based nanoscale electrocatalysts for fuel cell reactions. In this dissertation, monodisperse nanoparticles were successfully synthesized using organic solution phase synthesis methods. Not only the particle size, shape and composition were precisely controlled, but also the electronic properties of the surface atoms were finely tuned to reach the optimal catalytic performance. Moreover, Pt single crystals and sputtered thin films provide a unique insight into the structure-function relationship of the complex nanoparticle surfaces. First, pure Pt nanoparticles were used as a model catalyst to explore the best surface cleaning method for nanoparticle activation. The particle size and shape effects on oxygen reduction reaction (ORR) at fuel cell cathode were studied to optimize particle activity and stability in the ORR condition. Pt alloy nanoparticles and nanowires with Pt skin layer structure were produced with enhanced ORR activity. To minimize the Pt use, core/shell structured Au/PtM (M=Fe, Co, Cu….) nanoparticles were designed and synthesized. These core/shell nanocatalysts demonstrated tunable activities with much enhanced stability. Furthermore, Pt_3Sn nanoparticles were also developed as catalyst at anode to catalyze methanol oxidation reaction (MOR). They exhibited enhanced CO tolerance and were promising next generation anode catalyst for MOR.

Table of Contents

List of Figures and Tables

I. Introduction

1.1 Brief History and Background of Fuel Cells

An article from the Wall Street Journal has caught my eye recently. It says that the hydrogen fuel cell vehicles (FCV) are going to hit the road of California starting from this year (2014),[1] competing with battery electric vehicles (EV) as the gasoline price has soared in the past decade. In addition, FCV has zero emission on the road. However, the article also pointed out that the cost still hinders the commercialization of the FCV.[1]

The earliest model of fuel cells dates back to early 19th century.[2] Over the years, scientists have made marked progress on fuel cell research and development, including first fuel cell vehicle by GM in 1966.[3] However, the high cost made it not viable for mass production under competition from internal combustion engine at that time. Nowadays, as the FCVs receive renewed interest, fuel cell studies also continue to seek higher efficiency and lower cost. Among kinds of fuel cells, the proton exchange membrane fuel cell (PEMFC) using hydrogen as fuel is chosen for automotive applications, which is attributed to its high power density, quick start up at relatively low operating temperature.[3,4] Besides hydrogen, small organic molecules can also serve as the power source such as methanol for direct methanol fuel cell (DMFC). To date, platinum is still the most active catalyst for both cathode and anode reactions of PEMFC.[5] The cost of platinum accounts for a significant portion of the PEMFC.[6] My research is focused on improving the catalytic performance of Pt based catalyst for PEMFC reaction.

1.2 PEMFC Reaction Mechanism

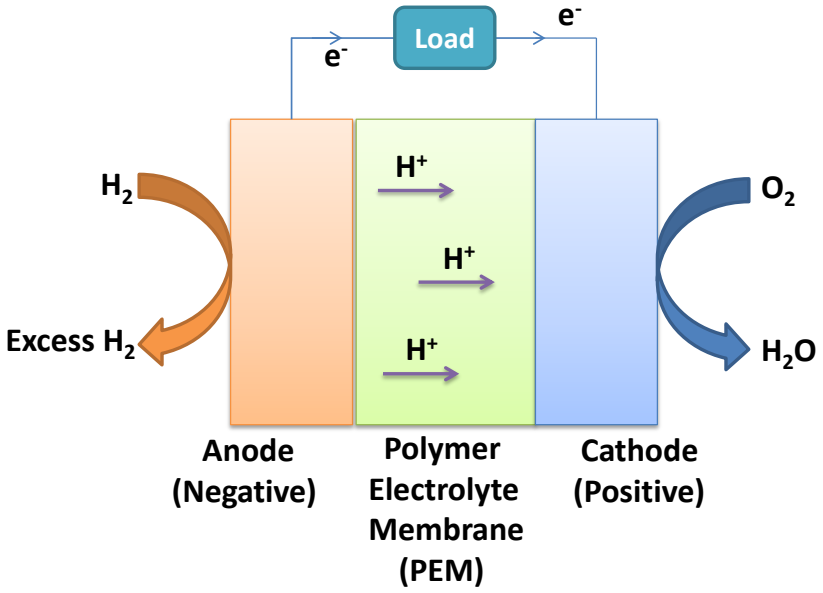

Figure 1-1. Schematic illustration of a proton exchange membrane fuel cell.

A typical PEMFC was shown in Figure 1-1. Hydrogen is oxidized in anode (1). The protons are conducted through the membrane while the electrons pass the external circuit. They both react with oxygen in the cathode to form water (2).

$$H_2 \rightarrow 2H^+ + 2e^- \qquad E^O = 0\,V \qquad (1)$$

$$\frac{1}{2}O_2 + 2H^+ + 2e^- \rightarrow H_2O \qquad E^O = 1.23\,V \qquad (2)$$

Combining (1) and (2), the overall reaction (3) is

$$H_2 + \frac{1}{2}O_2 \rightarrow H_2O \qquad E^O = 1.23\,V \qquad (3)$$

1.3 Challenges to the Fuel Cell Catalysis

While the kinetics of hydrogen oxidation reaction (HOR) in the anode is fast on Pt catalysts, the oxygen reduction reaction (ORR) in the cathode suffers from sluggish kinetics.[5,7] Moreover, the high potential and strongly acidic environment are harsh even to the noble metal platinum.

The higher ORR mass activity is achieved by optimizing the particle size[8,9] and using Pt based alloy (such as PtNi, PtCo and PtFe) with Pt-skin layer structure instead of pure Pt.[10–12] The instability of Pt involving dissolution and re-deposition upon potential cycling has long been observed, resulting in bigger particles and loss of electrochemically active surface area (ECSA).[13–15] The Pt dissolution mechanism includes direct pathway (4) and oxide dissolution (5)-(6).[16] It is worth noting that the smaller particles, despite of higher initial mass activity, are peculiarly prone to Pt dissolution.[17] The leach out of the third row transition metal in Pt alloy poses another threat to catalyst durability. [18,19]

- Direct dissolution

$$Pt \rightarrow Pt^{2+} + 2e^- \qquad E_o = 1.19 + 0.029 \log(Pt^{2+}) \qquad (4)$$

- Oxide formation and dissolution

$$Pt + H_2O \rightarrow PtO + 2H^+ + 2e^- \qquad E_o = 0.98 - 0.59\ pH \qquad (5)$$

$$PtO + 2H^+ \rightarrow Pt^{2+} + H2O \qquad \log(Pt^{2+}) = -7.06 - 2pH \qquad (6)$$

Another problem is that the Pt surface is easily poisoned by carbon monoxide (CO poisoning). CO can be from impurity of feed gas. When small organic molecules (such as methanol and formic acid) are used as fuel, CO may also be generated from partially oxidized fuel. [20] Modified Pt surface with enhanced CO-tolerance can be achieved by adding a foreign metal.

1.4 Outline

At the beginning of my research, I often feel puzzled by the difference of results in literature from different groups regarding the catalytic performance and how to conduct the experiment. I realized that in order to ensure the consistency, the experimental procedure and how we process the raw data need to be set. First, the preconditioning of the electrode such as potential window, the number of cycling and scan rate must be consistent. For example, when doing CO oxidation on Pt surface, I found the polarization curves differ from each scan. Therefore, for the CO oxidation properties on different catalysts, you must specify which scan you are comparing. Second, the data processing and presenting are also important. For example, when presenting ORR activity, one must point out the potential, not just the activity number. I often noticed that for the pure platinum catalyst, the activity number is often recorded at the lower potential (e.g. 0.90 V) while for Pt based alloy the activity number is sometimes reported at a higher potential (e.g. 0.95V). This is because the alloy catalyst is generally more active than pure Pt, at lower potential region, both kinetic and mass transport are affecting the current

density, making the data less accurate although the value is higher from Levich-Koutecky equation.[21,22] With this standard which fits our laboratory's experimental condition best, I can be certain that my own data are comparable with each other, although the test protocol may still be varied in different groups.

Our ultimate goal is to obtain catalyst that is more active, stable and with lower cost (less Pt) and higher CO-tolerance. To approach it, nanoparticles need to be synthesized. The commercial catalyst available is usually made of poor quality NPs with wide size distribution. Our solvo-thermo synthesis approach can achieve monodisperse NPs with better control over the size, shape, structure and composition. As-synthesized NPs are wrapped with surfactant (in our case, i.e. oleylamine and oleic acid), which are important for the monodispersity and prevent particle agglomeration. However, the surfactant also blocks active site for catalysis and therefore must be removed. In the first chapter, different surfactant removal methods were compared to find the best suit for our system. The surface cleanness of the treated catalyst was examined by electrochemical test as well as other analytical technics. The next chapter, size and shape of pure Pt NPs were explored for the best catalytic performance. Based on previous studies, the ORR activity of Pt based catalysts is affected by particle size. However, there are still conflicting reports about the exact particle size rage for the most significant size effect. More importantly, the change of particle size also affected the long term stability under potential cycling. Even pure Pt is not very stable under the ORR potential region (above 0.8 V). Our study showed that although the maximum initial mass activity was observed for the size between 3 and 4 nm, 7 nm NPs are more active after prolonged cycling. Therefore, the 7 nm was favored as a tradeoff between initial mass activity and long term

stability. The effect of particle size distribution on the stability was also explored by manually creating an extreme case of wide size distribution. We found that the instability of smaller particles also affected the bigger ones, resulting in worse overall stability. This may be the reason why the commercial catalyst usually shows poor stability compared with as-synthesized NP catalyst. With the conclusion about size effect, we moved to investigate the particle shape effect. We chose Pt NPs of cubic, cubo-octahedral and octahedral in the size range of 7-9 nm. The well-established single crystal data provided guidance for the shape effect study of NPs. Our results did show some similarities between Pt nanocubes and Pt(100). However, the cyclic voltammograms (CVs) also indicated that, despite uniform shape confirmed by HRTEM, the as-synthesized NPs are full of defects on the surface. In fact, even the single crystal surfaces are not defect-free. Upon cycling to ORR region, both single crystal surfaces and NPs (cubic and octahedral) showed dramatic changes. The NPs of different initial morphologies ended in round shape (cubo-octahedral). The results call for further efforts on stabilizing the particular particle shape in future studies.

The next step, we moved to Pt based alloy in order to pursue higher ORR activity and stability. In Chapter 4, the bimetallic PtNi NPs were synthesized. A unique acid/annealing treatment was developed to produce Pt skin layers on the PtNi sputtered thin film and NP surface. The treated NPs showed further enhancement on ORR activity compared with as-synthesized PtNi NPs. This treatment method can be applied to various kinds of Pt alloy catalysts. The composition alloy catalyst can be also tuned to for better activity. In Chapter 5, Pt based ternary alloy was synthesized as DFT calculation predicted the oxygen-binding energies of the ternary alloy surface may affect the ORR

activity. Our results confirmed that annealed $Pt_3(CoNi)_1$ NPs indeed exhibit higher activity. In the meantime, alloy PtM (M=Fe, Co) nanowires (NWs) of different Pt content were also successfully synthesized and anchored onto carbon support (Chapter 6). The one dimensional alloy structure possesses improved activity and stability compared with pure Pt. The acid/annealing treatment in Chapter 4 was employed to further improve catalytic performance. Of various NWs, 4 nm and above thickness is required for them to survive the treatment instead of breaking apart. Pt-skin layer formation was attributed to the activity enhancement.

NPs with Au core and Pt based alloy shell structure have been proved to show enhanced stability while preserving the activity. The properties of Au/PtM catalysts will be discussed in the following two chapters. In Chapter 7, Au/PtCu NPs were synthesized and studied as a dual catalyst for both cathode (ORR) and anode (MOR) reaction. Again the preconditioning of the catalyst is important as Cu is detrimental for fuel cell operation.[23] Potential cyclings were applied to remove Cu from NP surface prior to other echem tests. The Au/PtCu was more active than pure Pt in ORR and MOR and also showed good stability. In the following chapter, the novel synthesis method of Au/PtCu NPs was extended to a broad system of Au/PtM (M= Fe, Co, Cu, Mn, Ag) NPs with controlled shell thickness and composition. The optimal shell thickness is between 1 and 2 nm in order to reach maximum activity and stability.

In the last chapter, as-synthesized Pt_3Sn NPs were studied for the electro-oxidation of carbon monoxide and methanol. It has been reported that CO oxidation was the key step in the electro-oxidation for some small organic molecule such as methanol.[20] Sn modified Pt surfaces show lower activation energy for CO oxidation. Our as-synthesized Pt_3Sn

exhibited lower on-set potential for CO oxidation and higher current density for MOR compared with pure Pt. The activity and stability was further improved by annealing the catalyst.

1.5 Reference

(1) Pricey Hydrogen Cars to Challenge Electric---Toyota, Others Chase Emissions Credits That Can Offset Gasoline-Powered Vehicles. http://online.wsj.com/news/articles/SB10001424052702303743604579353251333111522*The Wall Street Journal*.

(2) Andújar, J. M.; Segura, F. *Renew. Sustain. Energy Rev.* **2009**, *13*, 2309.

(3) Eberle, U.; Müller, B.; von Helmolt, R. *Energy Environ. Sci.* **2012**, *5*, 8780.

(4) Kirubakaran, A.; Jain, S.; Nema, R. K. *Renew. Sustain. Energy Rev.* **2009**, *13*, 2430.

(5) Holton, O. T.; Stevenson, J. W. *Platin. Met. Rev.* **2013**, *57*, 259.

(6) *Fuel Cell System Cost-2012*.

(7) Gasteiger, H. A.; Marković, N. M. *Science* **2009**, *324*, 48.

(8) Wang, C.; van der Vliet, D.; Chang, K.-C.; You, H.; Strmcnik, D.; Schlueter, J. A.; Markovic, N. M.; Stamenkovic, V. R. *J. Phys. Chem. C* **2009**, *113*, 19365.

(9) Shao, M.; Peles, A.; Shoemaker, K. *Nano Lett.* **2011**, *11*, 3714.

(10) Gasteiger, H. A.; Kocha, S. S.; Sompalli, B.; Wagner, F. T. *Appl. Catal. B Environ.* **2005**, *56*, 9.

(11) Stamenkovic, V. R.; Mun, B. S.; Mayrhofer, K. J. J.; Ross, P. N.; Markovic, N. M. *J. Am. Chem. Soc.* **2006**, *128*, 8813.

(12) Stamenkovic, V. R.; Mun, B. S.; Arenz, M.; Mayrhofer, K. J. J.; Lucas, C. A.; Wang, G.; Ross, P. N.; Markovic, N. M. *Nat. Mater.* **2007**, *6*, 241.

(13) Kinoshita, K.; Lundquist, J. T.; Stonehart, P. *J. Electroanal. Chem. Interfacial Electrochem.* **1973**, *48*, 157.

(14) Ferreira, P. J.; la O', G. J.; Shao-Horn, Y.; Morgan, D.; Makharia, R.; Kocha, S.; Gasteiger, H. A. *J. Electrochem. Soc.* **2005**, *152*, A2256.

(15) Shao-Horn, Y.; Sheng, W. C.; Chen, S.; Ferreira, P. J.; Holby, E. F.; Morgan, D. *Top. Catal.* **2007**, *46*, 285.

(16) Pourbaix, M. Atlas of electrochemical equilibria in aqueous solutions **1974**.

(17) Tang, L.; Han, B.; Persson, K.; Friesen, C.; He, T.; Sieradzki, K.; Ceder, G. *J. Am. Chem. Soc.* **2010**, *132*, 596.

(18) Zhang, S.; Yuan, X.-Z.; Hin, J. N. C.; Wang, H.; Friedrich, K. A.; Schulze, M. *J. Power Sources* **2009**, *194*, 588.

(19) Dubau, L.; Maillard, F.; Chatenet, M.; André, J.; Rossinot, E. *Electrochimica Acta* **2010**, *56*, 776.

(20) Beden, B.; Lamy, C.; de Tacconi, N. R.; Arvia, A. J. *Electrochimica Acta* **1990**, *35*, 691.

(21) Treimer, S.; Tang, A.; Johnson, D. C. *Electroanalysis* **2002**, *14*, 165.

(22) Vidal-Iglesias, F. J.; Solla-Gullón, J.; Montiel, V.; Aldaz, A. *Electrochem. Commun.* **2012**, *15*, 42.

(23) Kinumoto, T.; Inaba, M.; Nakayama, Y.; Ogata, K.; Umebayashi, R.; Tasaka, A.; Iriyama, Y.; Abe, T.; Ogumi, Z. *J. Power Sources* **2006**, *158*, 1222.

II. Surfactant Removal for Colloidal Nanoparticles from Solution Synthesis: The Effect on Catalytic Performance

2.1Introduction

Recently colloidal nanoparticles from aqueous[1–4] or organic[5–7] solution synthesis have attracted increasing interest for the development of advanced catalysts. Through controlled nucleation and growth in a homogeneous solution, this method has been demonstrated to be powerful in controlling nanoparticle (NP) size,[6,8–10] shape,[1,11,12] composition[13–15] and structure,[16–19] which has enabled systematic studies of these parameters in catalysis.[5,10,18–21] However, the NPs obtained by solution synthesis are usually capped by organic surfactants and cannot be directly applied as catalysts. For example, in the organic solution synthesis of Pt and Pt-based alloy NPs, oleylamine and/or oleic acid are usually used to stabilize the NPs and control NP sizes and shapes.[11,18,22,23] While these ligands are indispensible in the NP synthesis, they are detrimental for catalysis as they block the access of reactant molecules to the surface atoms. Therefore, it is critical to establish a proper procedure of surfactant removal and surface cleaning, without inducing particle size and morphology changes, for application of colloidal NPs in catalysis.

Here we report a systematical investigation of the effect of surfactant removal on the electrocatalytic performance of Pt NPs prepared by organic solution synthesis. Various methods were applied to remove the oleylamine surfactant, including thermal annealing, acetic acid washing and UV-Ozone irradiation, and the efficiency of surface cleaning was examined by electrocatalytic studies of the treated catalysts for the oxygen reduction

reaction (ORR). The removal of organic surfactants from NP surface was further confirmed by thermogravimetric analysis (TGA) and infrared adsorption spectroscopy (IRAS) studies.

2.2 Experimental Methods

2.2.1 Nanoparticle Synthesis.

For the synthesis of Pt NPs, 50 mg of platinum acetylacetonate ($Pt(acac)_2$) was dissolved in 10 mL of oleylamine at 100˚C under Ar flow. After 20 minutes, a mixture of 0.2 g of borane tributylamine (Aldrich) and 5 mL of oleylamine was added into the solution. The solution temperature was raised to 120˚C and kept at this temperature for an hour. The solution was then cooled to room temperature and 30 mL of ethanol was added. The product was collected by centrifugation (8,000 rpm, 6 minutes). The obtained precipitation was dispersed in hexane for further experiments.

2.2.2 Catalyst Preparation and Surfactant Removal.

The as-synthesized Pt NPs were washed by ethanol and then dried in vacuum. After that, they were mixed with carbon black (Tanaka, ~900 m^2/g) with a mass ratio of 1:1 in chloroform ($CHCl_3$) by sonication. The solvent was then evaporated at room temperature in air. The obtained powder was denoted as "untreated" catalyst.

The following treatments were applied to the untreated catalyst for surfactant removal: 1) Thermal annealing. The catalyst was heated in a tube furnace for 5 hours at 185˚C in air; 2) Chemical washing. The catalyst was dispersed in pure acetic acid (HAc) with vigorous stirring at 75˚C for 10 hours, and then collected by adding ethanol and centrifugation; 3) UV-Ozone treatment. An aqueous suspension of the untreated catalyst

was deposited onto a glassy carbon electrode. After drying in air, the electrode was placed in a UV-Ozone chamber and subject to UV irradiation for 30 minutes.

2.2.3 Characterizations.

Transmission electron microscopy (TEM) images were collected on a Philips EM 30 (200 kV). Thermogravimetric analysis for the Pt NPs was done with a Pyris 1 TGA/HT Lab System (PerkinElmer). Fourier transformed infrared (FTIR) spectra were collected on a Nicolet Nexus 8700 spectrometer with a MCT detector cooled by liquid nitrogen and *in situ* electrode potential control, following the previous reported procedures.[24]

2.2.4 Electrochemical Studies.

All electrochemical measurements were performed in a three-compartment electrochemical cell in 0.1 M perchloric acid at room temperature. A Ag/AgCl electrode was used as the reference electrode, and a platinum wire as the counter electrode. A mirror-polished glassy carbon disk (6 mm in diameter) was used as the working electrode. The catalyst was dispersed in deionized water by sonication and 30 ~ 40 μL of the suspension was deposited onto the glassy carbon electrode by pipette. The loading of Pt was controlled to be ~20 $\mu g/cm^2_{disk}$. A solution of Nafion (0.1 wt. %, 15 μL) was added on top of the catalyst and the dried in air. Cyclic voltammograms (CVs) was recorded in Ar saturated electrolytes with a scan rate of 50 mV/s. Polarization curves for the ORR were recorded in an oxygen saturated electrolytes at 20 mV/s with an electrode rotation speed of 1600 rpm. All the potentials given were calibrated versus reversible hydrogen electrode (RHE).

2.3 Results and Discussion

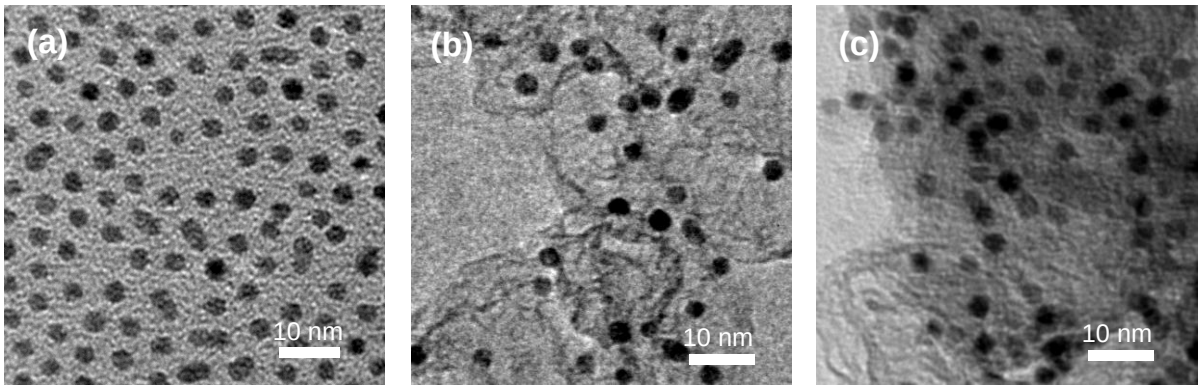

Figure 2-1. TEM images of (a) as-synthesized Pt NPs (b) Pt NPs loaded on carbon black (c) Pt NPs on carbon black after annealing.

Monodisperse Pt NPs were synthesized by reduction of $Pt(acac)_2$ with borane tributylamine in an oleylamine solution (see the Methods). Here oleylamine served as both solvent and surfactant. Figure 1a shows a representative TEM image of the as-synthesized Pt NPs with a particle size of ~3 nm. The synthesized NPs were supported on high-surface-area carbon (Tanaka, ~900 m^2/g) and various treatments were applied to remove the organic surfactants and clean the surface. These include mild-temperature heating (160 ~ 200˚C) in air,[25] chemical washing by acetic acid[26] and UV Ozone irradiation.[27] No significant change in particle size or morphology was found after these treatments, as shown by the TEM images presented in Figure 1, for example, for the 185˚C thermal treatment in air (Figure 2-1b and 1c).

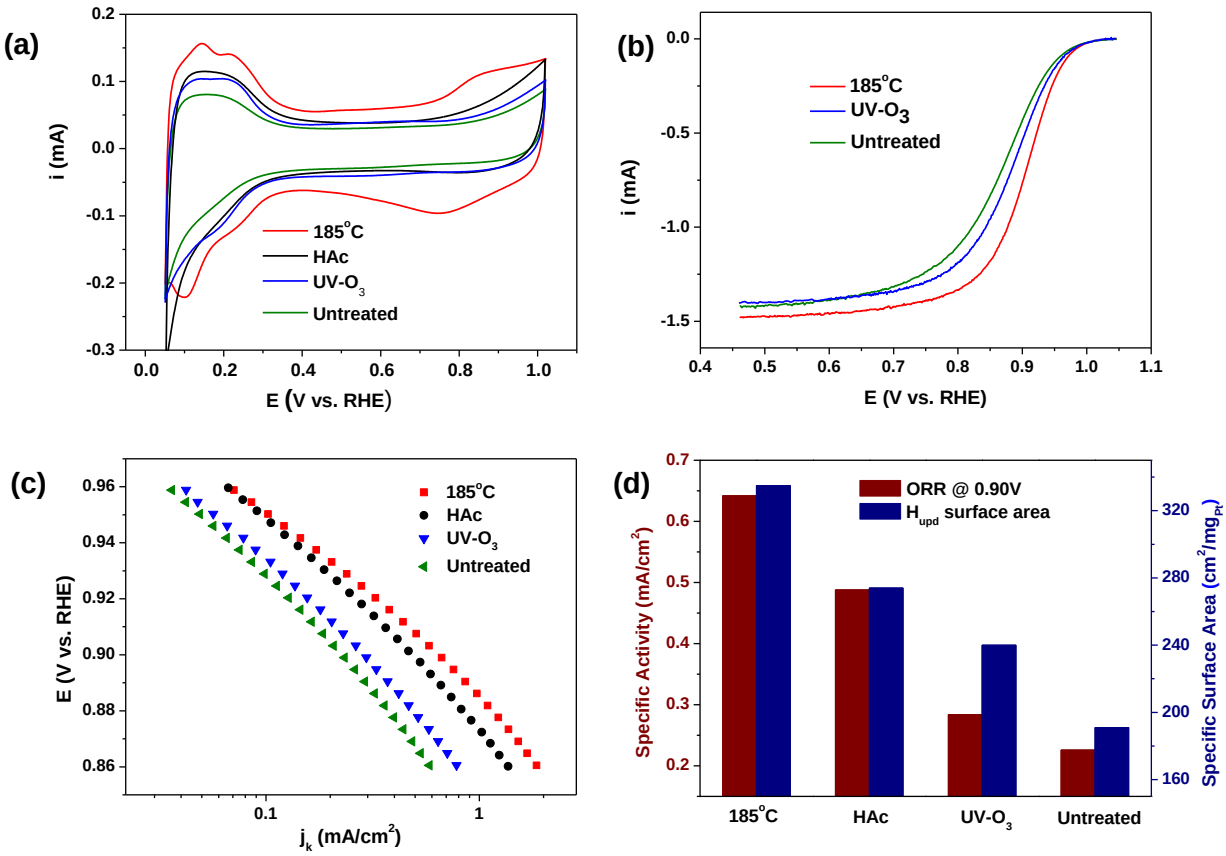

Figure 2-2. (a) Cyclic voltammograms of various Pt/C catalysts. (b) ORR polarization curves of the annealed, the UV-ozone treated and the untreated samples. (c) Tafel plots of Pt/C catalysts at 20 mV/s, 1600 rpm, 20˚C. (d) Specific activity at 0.90 V and specific surface area.

Catalytic performance of the various treated catalysts was examined by the RDE method. Figure 2 summarizes the results of electrochemical studies. CVs show typical Pt like features with under potential deposited hydrogen (H_{upd}) peaks at $E < 0.4$ V (Figure 2a). Among the various treated catalysts, the 185˚C annealed one shows more pronounced H_{upd} peaks than the others. As the catalyst loading was consistently controlled to be ~~20 μg/cm$^2_{disk}$, this difference directly corresponds to the variation in

specific surface area, namely the electrochemically active surface area (ECSA, estimated from the H_{upd} charges by ECSA = $Q_{Hupd}/210\ \mu C/cm^2$) normalized by the mass of Pt in the catalyst. As shown in Figure 2d, the 185˚C annealed catalyst gave a specific surface area of ~330 cm^2/g_{Pt}, versus ~270 cm^2/g_{Pt} for the HAc washed, 240 cm^2/g_{Pt} for the UV-Ozone treated and 190 cm^2/g_{Pt} for the untreated catalyst. Moreover, the electrocatalytic activity was found to be also strongly dependent on the methods of surfactant removal. Both the polarization curves (Figure 2b) and Tafel plots (Figure 2c) show that the 185˚C annealed catalyst has the highest ORR activity, reaching 0.64 mA/cm^2 at 0.9 V, compared to 0.49 mA/cm^2 for the HAc washed, 0.29 mA/cm^2 for the UV-Ozone treated and 0.22 mA/cm^2 for the untreated catalyst. Both the results of specific surface areas and specific activities indicate that the efficiency of surfactant removal follows the trend 185˚C annealing > HAc washing > UV-Ozone (Figure 2-2d). It has to be pointed out that potential cycling can bring additional cleaning for the catalysts. For example, after one hundred potential cycles, the HAc washed Pt/C shows comparable electrocatalytic performance as the thermal annealed one (Figure S1). However, such potential cycling had very limited effect on the UV-Ozone treated and untreated catalysts. In the following discussion, we will focus on the study of surfactant removal by thermal annealing in order to confirm the effectiveness of surfactant removal.

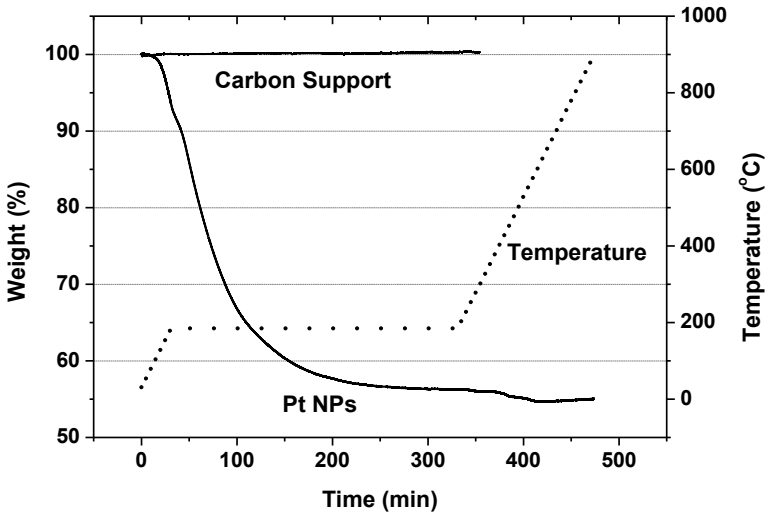

Figure 2-3. TGA of as synthesized Pt NPs and carbon support.

Figure 2-3 shows the weight loss curves for the process of surfactant removal by 185˚C annealing in air for the as-synthesized Pt NPs and carbon support. It was found that a weight loss of up to 44% took place during the isothermal process at 185˚C for the NPs, due to the removal of organic surfactants. Not much organic substances were left after the 185˚C stage, as further increase of the temperature up to 900˚C did not lead to substantial loss in addition (~1%). The total loss in weight, ~45%, corresponds to the weight ratio of surfactants in the NPs. Based on the TGA studies, we can conclude that the thermal annealing at 185˚C in air is efficient for removing the organic surfactants from the Pt NP surface. It is also important to point out that the employed carbon black is stable in the surfactant removal process, as no weight change was observed in TGA for the carbon support at 185˚C.

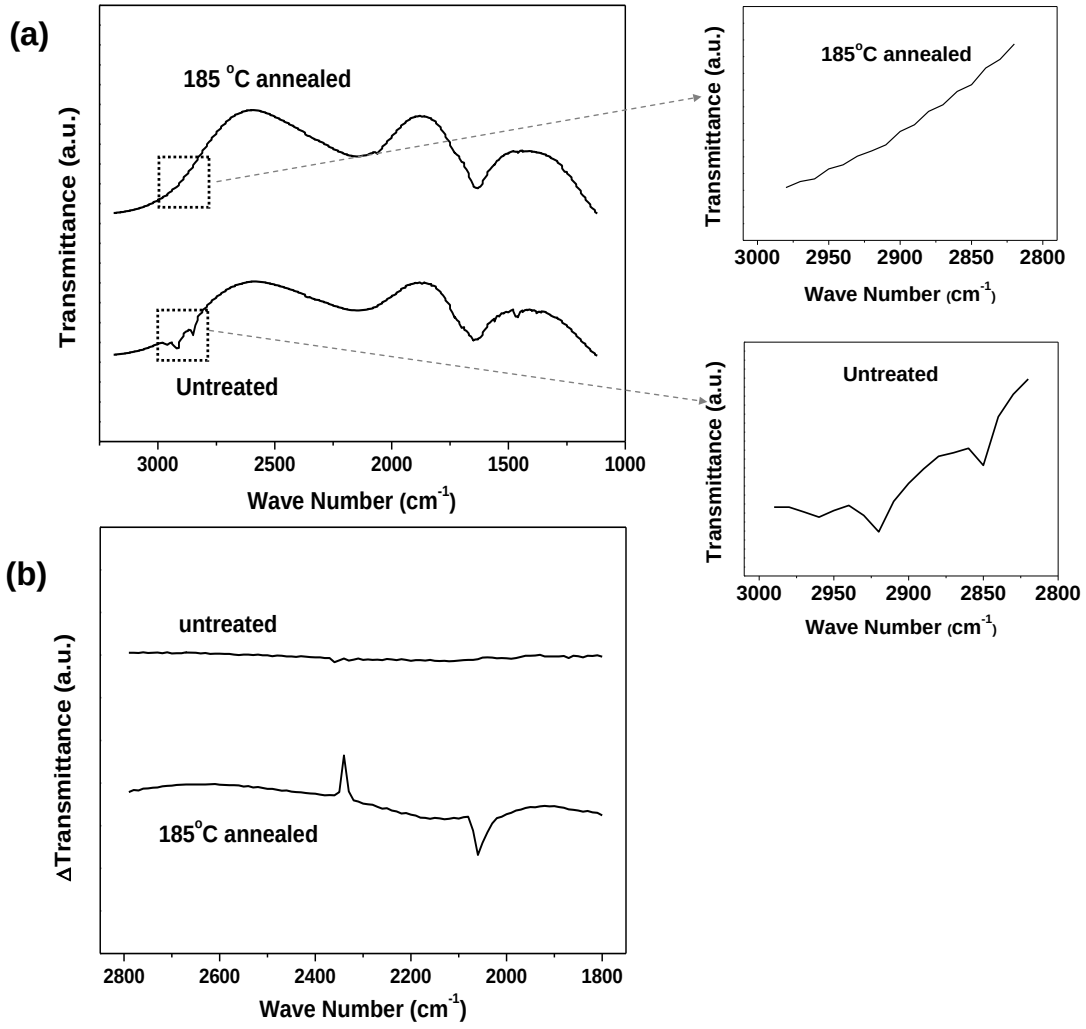

Figure 2-4. (a) FTIR spectra of adsorbed CO on untreated and annealed Pt NPs. The spectra were recorded after CO adsorption at 0.1 V. The insets show region of the spectra that is typical for surfactant molecules. (b) Subtracted IR spectra at 0.9 V and 0.1 V for annealed and untreated samples.

After surfactant removal, surface atoms on the Pt NPs were exposed and became electrochemically active. This was further confirmed by in-situ electrochemical IRAS studies, in which surface conditions of the NPs as well as the CO-Pt interaction[24] was

examined. Figure 2-4a shows the IR spectra of the annealed and untreated NPs collected at 0.1 V in 0.1 M $HClO_4$ electrolyte. The insets of close view highlight the difference between the two spectra in the region from 2800 cm^{-1} to 3000 cm^{-1}. The bands at 2850 cm^{-1} and 2920 cm^{-1} observed in the untreated NPs can be associated to the C-H stretching vibrations in oleylamine molecules.[28] After the thermal annealing, the C-H bands disappeared, suggesting successful removal of surfactants from the particle surface. Figure 2-4b shows the differentiation spectra obtained by subtracting the IR spectra recorded at 0.1 V with the spectra at 0.9 V (see Figure S2-2 for the primary spectra). Considering that the adsorbed CO (CO_{ad}) is oxidized at high potentials (E = 0.9 V) while at low potentials CO is strongly adsorbed on Pt, the differentiation spectra are thus able to exclusively tell the situation of CO adsorption on the particle surface. The untreated NPs do not exhibit any observable feature in the wave number range from 1800 cm^{-1} to 2800 cm^{-1}, due to the blocked CO adsorption on the particle surface. The annealed NPs show a sharp peak at 2060 cm^{-1} which can be assigned to atop-bonded CO on Pt,[29] indicating that the surface atoms were activated by the thermal annealing and became accessible for CO adsorption. The positive peak around 2340 cm^{-1} can be associated with CO_2 which was the product of CO oxidation. Consistent with the observations from electrochemical and TGA studies (Figure 2-2 and 2-3), the IRAS results demonstrate that organic surfactants present on the NP surface, which block H_{upd} and CO adsorption and ORR, can be sufficiently removed by the thermal annealing at a mild temperature in air.

2.4 Conclusion

We have studied the effect of surfactant removal on the electrocatalytic performance of Pt nanoparticles made by organic solution synthesis. Various methods existing in the literature were applied to remove the oleylamine surfactant, and the dependence of electrocatalytic performance for the ORR on the treatment was found to follow the trend: 185˚C annealing in air > HAc washing > UV-Ozone. The effectiveness of surfactant removal and surface cleaning by thermal annealing in air was further confirmed by TGA and IRAS studies. Our work revealed the importance of pretreatment in catalyst preparation and would have great implication for the development of advanced catalysts with colloidal nanoparticles from solution synthesis.

Acknowledgement

This work was conducted at Argonne National Laboratory, a U.S. Department of Energy, Office of Science Laboratory, operated by UChicago Argonne, LLC, under contract no. DE-AC02–06CH11357. This research was sponsored by the U.S. Department of Energy, Office of Energy Efficiency and Renewable Energy, Fuel Cell Technologies Program. Microscopy research was conducted at the Electron Microscopy Center for Materials Research at Argonne.

2.5 References

(1) Ahmadi, T. S.; Wang, Z. L.; Green, T. C.; Henglein, A.; El-Sayed, M. A. *Science* **1996**, *272*, 1924 -1925.

(2) Lee, H.; Habas, S. E.; Kweskin, S.; Butcher, D.; Somorjai, G. A.; Yang, P. *Angew. Chem. Int. Ed.* **2006**, *45*, 7824-7828.

(3) Habas, S. E.; Lee, H.; Radmilovic, V.; Somorjai, G. A.; Yang, P. *Nat Mater* **2007**, *6*, 692-697.

(4) Lim, B.; Jiang, M.; Camargo, P. H. C.; Cho, E. C.; Tao, J.; Lu, X.; Zhu, Y.; Xia, Y. *Science* **2009**, *324*, 1302 -1305.

(5) Wang, C.; Daimon, H.; Lee, Y.; Kim, J.; Sun, S. *J. Am. Chem. Soc.* **2007**, *129*, 6974-6975.

(6) Tsung, C.-K.; Kuhn, J. N.; Huang, W.; Aliaga, C.; Hung, L.-I.; Somorjai, G. A.; Yang, P. *J. Am. Chem. Soc.* **2009**, *131*, 5816-5822.

(7) Zhang, J.; Yang, H.; Fang, J.; Zou, S. *Nano Lett.* **2010**, *10*, 638-644.

(8) Puntes, V. F.; Krishnan, K. M.; Alivisatos, A. P. *Science* **2001**, *291*, 2115 -2117.

(9) Sun, S.; Zeng, H. *J. Am. Chem. Soc.* **2002**, *124*, 8204-8205.

(10) Wang, C.; van der Vliet, D.; Chang, K.-C.; You, H.; Strmcnik, D.; Schlueter, J. A.; Markovic, N. M.; Stamenkovic, V. R. *J. Phys. Chem. C* **2009**, *113*, 19365-19368.

(11) Wang, C.; Hou, Y.; Kim, J.; Sun, S. *Angew. Chem. Int. Ed.* **2007**, *46*, 6333-6335.

(12) Sun, Y.; Xia, Y. *Science* **2002**, *298*, 2176 -2179.

(13) Swafford, L. A.; Weigand, L. A.; Bowers, M. J.; McBride, J. R.; Rapaport, J. L.; Watt, T. L.; Dixit, S. K.; Feldman, L. C.; Rosenthal, S. J. *J. Am. Chem. Soc.* **2006**, *128*, 12299-12306.

(14) Wang, C.; Chi, M.; Wang, G.; van der Vliet, D.; Li, D.; More, K.; Wang, H.; Schlueter, J. A.; Markovic, N. M.; Stamenkovic, V. R. *Adv. Funct. Mater.* **2011**, *21*, 147-152.

(15) Chen, W.; Kim, J.; Sun, S.; Chen, S. *J. Phys. Chem. C* **2008**, *112*, 3891-3898.

(16) Cheng, K.; Peng, S.; Xu, C.; Sun, S. *J. Am. Chem. Soc.* **2009**, *131*, 10637-10644.

(17) Yavuz, M. S.; Cheng, Y.; Chen, J.; Cobley, C. M.; Zhang, Q.; Rycenga, M.; Xie, J.; Kim, C.; Song, K. H.; Schwartz, A. G.; Wang, L. V.; Xia, Y. *Nat Mater* **2009**, *8*, 935-939.

(18) Wang, C.; van der Vliet, D.; More, K. L.; Zaluzec, N. J.; Peng, S.; Sun, S.; Daimon, H.; Wang, G.; Greeley, J.; Pearson, J.; Paulikas, A. P.; Karapetrov, G.; Strmcnik, D.; Markovic, N. M.; Stamenkovic, V. R. *Nano Lett.* **2011**, *11*, 919-926.

(19) Wang, C.; Daimon, H.; Sun, S. *Nano Lett.* **2009**, *9*, 1493-1496.

(20) Lim, B.; Jiang, M.; Camargo, P. H. C.; Cho, E. C.; Tao, J.; Lu, X.; Zhu, Y.; Xia, Y. *Science* **2009**, *324*, 1302-1305.

(21) Zhang, J.; Yang, H.; Fang, J.; Zou, S. *Nano Lett.* **2010**, *10*, 638–644.

(22) Sun, S. *Adv. Mater.* **2006**, *18*, 393-403.

(23) Mazumder, V.; Chi, M.; More, K. L.; Sun, S. *J. Am. Chem. Soc.* **2010**, *132*, 7848-7849.

(24) Stamenković, V.; Arenz, M.; Ross, P. N.; Marković, N. M. *J. Phys. Chem. B* **2004**, *108*, 17915-17920.

(25) Liu, Z.; Shamsuzzoha, M.; Ada, E. T.; Reichert, W. M.; Nikles, D. E. *J. Power Sources* **2007**, *164*, 472-480.

(26) Lee, Y. H.; Lee, G.; Shim, J. H.; Hwang, S.; Kwak, J.; Lee, K.; Song, H.; Park, J. T. *Chem. Mater.* **2006**, *18*, 4209-4211.

(27) Chen, W.; Kim, J.; Sun, S.; Chen, S. *Phys. Chem. Chem. Phys.* **2006**, *8*, 2779-2786.

(28) Xu, Z.; Shen, C.; Hou, Y.; Gao, H.; Sun, S. *Chem. Mater.* **2009**, *21*, 1778-1780.

(29) Chang, S.-C.; Weaver, M. J. *Surf. Sci.* **1990**, *238*, 142-162.

2.6 Supporting Information

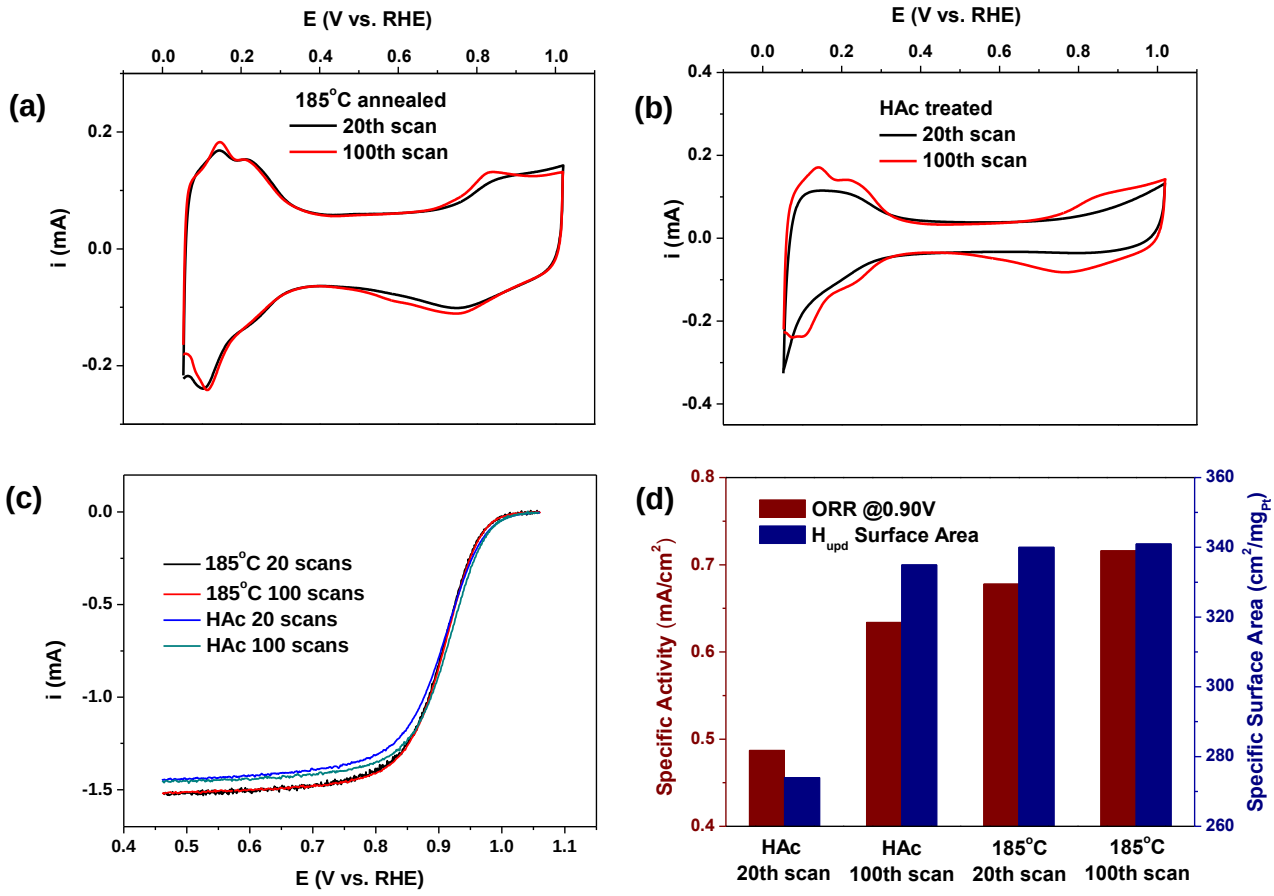

Figure S2-1. Cyclic voltammograms of (a) Annealed and (b) HAc treated recorded after different potential scans. Corresponding (c) ORR polarization curves, (d) specific activity at 0.90V and specific surface area after different potential scans

Further experiments have shown the cleaning effect of potential cycling (Fig. S2-1). For annealed sample, the voltammetric profiles in Figure S2-1a shows only slight changes in H_{upd} and oxide formation region. Nevertheless, there is little enhancement in ORR

activity after 100 sweeps between 0.05 V and 1.02 V at 50 mV/s scan rate (Fig. S2-1c,d). The contrast for acetic acid treated sample is sharp before and after same potential cycling. In Figure S2-1b, the CV developed to a platinum polycrystalline profile after 100 potential cycling, with growth in both H_{upd} and oxide formation regions. Positive shift of ORR polarization curves also suggests a cleaner surface (Fig. S2-1c). So the results prove that the HAc treatment can still be used combining with potential cycling. It should be noted that, in some cases when the NP catalysts are susceptible to the heat (e.g. core-shell nanoparticles in which thermal annealing may break the structure). Acetic acid treatment could be an alternative approach for the surface cleaning.

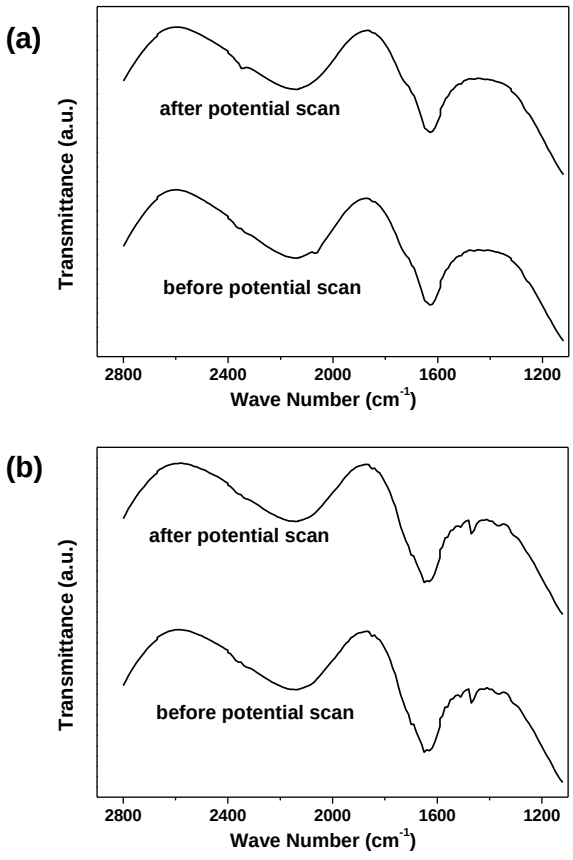

Figure S2-2. IR spectra of (a) annealed and (b) untreated sample recorded at 0.1 V and 0.9 V.

III. The Pt Particle Size and Shape Effects on Activity and Stability during the Oxygen Reduction Reaction Eletrocatalysis

3.1 Introduction

The last two decades have witnessed remarkable progress in our ability to chemically synthesize metal nanoparticles (NPs) ranging in size from 1-10 nm with unique electrocatalytic properties.[1–4] Because the electronic properties of metal NPs in this size range are not unique,[5] (electro)catalyst research with such materials has focused on the variations in the reaction rate or selectivity with characteristic dimensions of metallic catalysts. While Boronin and co-workers[6] pioneered this approach to understand the "crystalline size effect" in heterogeneous catalysis, Kinoshita[7] and others[8,9] used this tactic to understand the "particle size effect" in electrocatalysis. There is no simple ideal structure that will model all the aspects of NP catalysts, particularly in the configuration that are used in electrolytic cells. However, if one considers the equilibrium shape of a face-centered cubic (*fcc*) metal NP such as a cubo-octahedron, consisting of (111) and (100) facets bounded by edge atom rows that are like the top-most rows in the (110) surface, single-crystal surfaces may serve as a reasonable model for assessing the particle shape effects for reactions that present a certain structure sensitivity. By inference, if the reaction rate and/or selectivity display some dependence on the atomic surface geometry, then that reaction is expected to show a "particle shape effect" tied to the distribution of crystallographic faces exposed.

The effect of structure-function in electrocatalysis has long been recognized[10,11] and trends are beginning to emerge that give some predictive ability with respect to surface

structure assumed by the arrangement of surface atoms and their corresponding reactivity. One class of electrochemical reaction exhibiting strong structure sensitivity is the oxygen reduction reaction (ORR), the cathodic half-cell reaction in fuel cells.[12] The ORR on platinum (Pt) single crystals varies with crystal face in a different manner depending on the nature of solution. In "non-specifically adsorbing" perchloric acid electrolyte, the variation is relatively small between the three low index surfaces with the activity increasing in the order Pt(100)<Pt(111)≤Pt(110).[13] In sulfuric acid electrolyte, the activity variations on different crystal faces are much larger, with the difference between the most active Pt(110) and the least active Pt(111) being about two orders of magnitude and overall activity for all three crystallographic faces being lower than that in perchloric acid. The difference between these two electrolytes is attributed to an active site blocking effect caused by very strong adsorption of bisulfate anions.[14]

In contrast to structure-function relationships for the ORR on Pt(hkl), the Pt particle size effect on the ORR is still controversial. While some authors claim that there is a difference in activity between different particle sizes,[15–19] there are also reports claiming that little or no particle size effects exist for the ORR within specific size rage.[20–22] Even less is known about a functional link between surface structure sensitivity and the shape of Pt NPs,[18,23,24] a relationship that could potentially yield new design criteria for nanoparticulate based catalysts with improved catalytic activity and selectivity. In general, longstanding difficulty in resolving the particle size and shape effects can be attributed to a lack of methods suitable for syntheses of impurity-free Pt NPs that are uniform in size, equally dispersed on a conductive support and can be characterized at atomic and molecular levels. This situation is in sharp contrast to that for Pt single

crystals, for which the developments of surface preparation and characterization techniques have been well established over the last three decades.[25] Additionally, unlike Pt(hkl) single crystals where adsorption and catalytic properties can be obtained in the very first electrode potential sweep,[26] Pt NPs are often deactivated by the residual surfactants from the colloidal synthesis of Pt NPs poison the surface and are commonly removed by prolonged potential cycling in the potential region where an irreversible Pt-oxide is formed. Formation of irreversible oxide results in Pt dissolution followed by re-deposition at low electrode potentials. Consequently, subsequent potential cycling will inevitably lead to continual change in particle size and shape;[27–31] an issue which, especially when addressing any particle shape effects, has often been overlooked in electrocatalysis on metal NPs. Based on these and many other challenges, one may anticipate that depending on the experimental conditions and/or the physical properties of NPs, one may or may not find any correlation between the particle size and/or shape and activity for electrochemical reactions. However, finally resolving this controversial subject would be of fundamental and technological importance.

Here, we demonstrate that it is possible to develop a distinctive and systematic experimental strategy that reveals the inherently close ties between the structure sensitivity and the particle size/shape effects for the ORR ($O_2 + 4H^+ + 4e^- = 2H_2O$) on Pt single crystals and Pt NPs in acidic environments. By applying scanning tunneling microscopy (STM) in combination with electrochemical methods we establish, at atomic levels, the unique and symbiotic relationship between the oxide-induced morphological changes of Pt(111) and Pt(100) and the kinetics of the ORR. We use these results as a foundation for developing a new experimental protocol for resolving the particle size and

shape effects. By studying the ORR on four types of cubo-octahedral NPs with sizes ranging from 2.8-7.2 nm we establish that if the NPs are well dispersed and uniform in size then the ORR activity indeed depends on the size of Pt NPs. After examining the ORR on cubo-octahedral, cubic and octahedral NPs we found that the particle shape effect on the ORR is much smaller that the particle size effect, especially after moderate potential cycling. From analysis of transmission electron microscopy (TEM) images and cyclic voltammetry (CV) we learn that under ORR relevant conditions (electrode potential window, temperature and nature of electrolytes etc.) the particle size and shape effects are constantly evolving due to the oxide-induced transformations of both the smaller particles to larger particles as well as cubo-octahedral, cubic and octahedral NPs to round-like shaped NPs. Thus, while initially clearly observed, the particle size and shape effects diminish as the particles age to the point that it may appear that the ORR depends neither on the particle size nor particle shape.

3.2 Structure-function relationships: the ORR on Pt single crystal surfaces

It is well-established that the structure sensitivity of the ORR on Pt(hkl) is almost entirely controlled by the structure sensitive adsorption of spectator species and the reaction intermediates.[13,14,32,33] Although these studies have long captured the attention of experimentalists and theoreticians alike, no attempts have been made to resolve the fundamental link between the activity and potential-dependent changes in morphology of Pt single crystal surfaces, especially after introduction of an irreversible oxide (usually termed as a true “oxide”) and its subsequent reduction. As we present further below,

establishing such relations is one key in undertaking the particle size and particle shape effects in electrocatalysis.

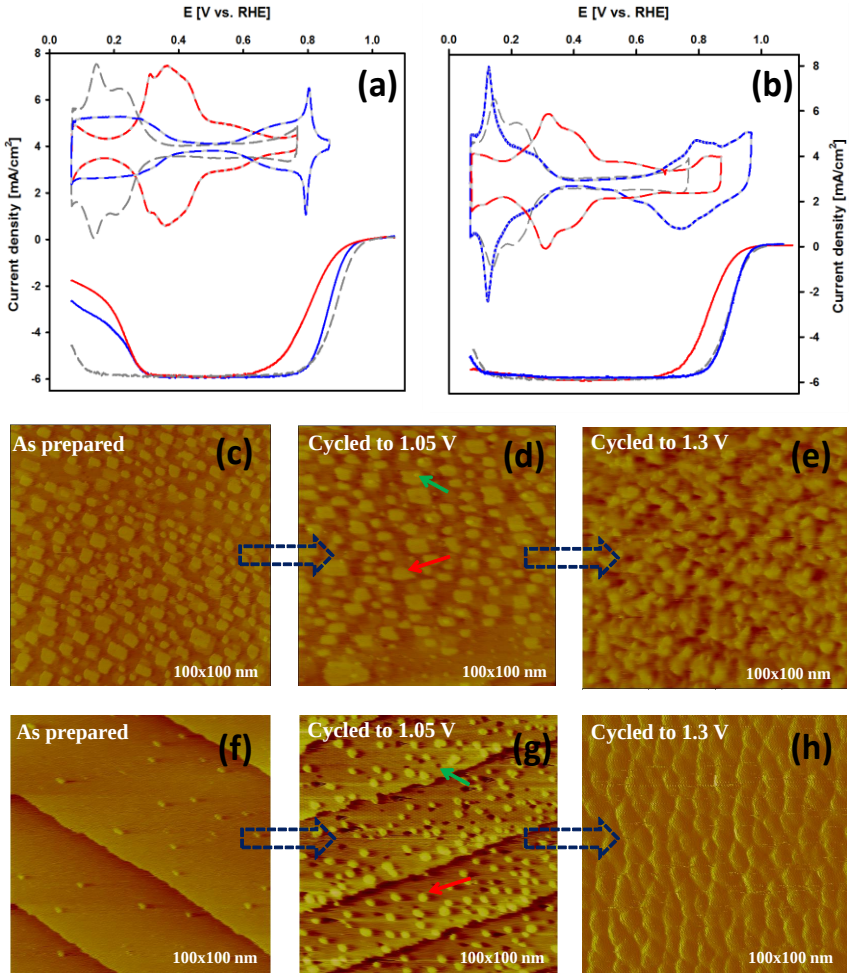

Figure 3-1. (a) Cyclic voltammograms and corresponding ORR polarization curves of as prepared Pt(100) (red line), Pt(110) (grey line) and Pt(111) (blue line). (b) Cyclic voltammograms and ORR polarization curves of Pt(100) (red line) and Pt(111) blue line after cycled to 1.3 V compared to as prepared Pt(110). STM images of Pt(100) (c) as prepared, cycled to 0.85 V, (d) after cycled to 1.05 V, additional ad-island is pointed out by the green arrow; red arrow indicates the loss of sharp corners from those square islands and (e) after cycled to 1.3V. STM images of Pt(111) (f) as prepared, cycled to

0.85 V (g) after cycled to 1.05V, red arrow points out ad-island; green arrow points out hole and (h) after cycled to 1.3V.

The basic experimental protocol introduced here is to acquire STM images first and then to analyze how the morphological changes induced by irreversible oxide formation affect the voltammetric features corresponding to the H_{upd} and OH_{ad} formation on Pt(100) and Pt(111). By relying on this approach, the importance of defects on the CO oxidation reaction has been resolved recently by comparing CO activity on Pt low index single crystal surfaces.[34] In line with this study, prior to presenting the potential-variations in surface morphology and related electrochemical activities it is convenient to consider the behavior of the "as-prepared" Pt single crystal surfaces (see also the Method Section). An STM image of the as-prepared Pt(111) electrode reveals that at 0.05 V the surface is composed of a flat terrace which is covered by few steps and Pt ad-islands with monatomic height (Figure 3-1f). In contrast to Pt(111), ad-islands with square shapes and monoatomic height are clearly evident on the as-prepared Pt(100) electrode (Figure 3-1c). The presence of such islands is due to "lifting" of a (100)-hex phase and the formation of a (100)-(1x1) surface with "well-ordered" defects.[35] The as-prepared surface morphology of these single-crystals remain unchanged after 100 cycles between 0.05 V and 0.85 V, confirming previous suggestions that the reversible adsorption of OH_{ad} does not result in Pt dissolution and consequently surface roughening (Fig. 3-1c, f). Typical CVs for Pt(100) and Pt(111) are summarized in Figure 3-1a revealing that while on Pt(100) adsorption of hydroxyl species overlaps with the adsorption of hydrogen below 0.45 V, the adsorption of OH_{ad} above 0.6 V on Pt (111) (usually termed as the "butterfly peak") is

clearly separated from the H_{upd} potential region.[26] Also worth noting here is that in electrochemical literature the type of CVs shown in Figure 3-1a have been used as a fingerprint for claiming that an electrochemical reaction is taking place on a clean and well-ordered Pt(111) and Pt(100) single crystals. However, by comparing the CVs with their corresponding STM images it is obvious that, in fact, there are no truly defect-free single-crystals and, thus, CVs are insensitive to the dispersed atomic scale morphology defects present on as-prepared single-crystal surfaces. (for more details see also reference [34,36]).

It is of fundamental importance to elucidate the onset potential at which morphological changes are first observed and how the changes in the characteristic CVs may be linked to the evolving surface structure induced by potential cycling. The importance of establishing such relationships is twofold: (i) during fuel cell operation under shut-down and start-up conditions the cathode potential can be pushed up to 1.5 V[37,38] ; and (ii) the irreversible oxide formation on Pt(100) and Pt(110) begins around 0.8 – 0.85 V[33] so that even around 0.9 V a slow Pt dissolution may take place during the ORR on these two low index facets. Certainly, since at these low potentials the kinetics of bulk oxide formation are rather slow, we introduced an accelerated test to establish relationships between the surface structure and reactivity. In these experiments the potential cycle above 1.0 V was undertaken by potential increments of 50-100 mV, employing 100 potential scans from 0.05 V to the targeted upper potential limit (1.0 to 1.3V. Inspection of STM images and CVs in Figure 3-1 reveal three key features: (i) visible roughening of the Pt(111) and Pt(100) surfaces initiates at E>1.0 V; (ii) surface disordering is accompanied by the formation of (111)-(111) and (111)-(100) step-terrace like structures; (iii) introduction of

steps on Pt(111) with the (110)-like symmetry is concomitant with the appearance of a sharp H_{upd} peak at 0.175 V and disappearance of the "butterfly feature"; and (iv) in the case of (100), enlargements in the density of (111)-(100) steps is accompanied by a concomitant enhancement in the H_{upd} peak at 0.35 V and reduction in the peak size at 0.4 V.

As discussed previously and demonstrated in the literature,[13,14,33] the ORR is a structure sensitive reaction, showing the variation in activity with the geometry of surface atoms in both the H_{upd} (below 0.4V) and OH_{ad} (between 0.75 and 0.9 V) potential regions, confirming that the ORR activity is controlled by the surface coverage of spectators such as H_{upd} and OH_{ad}. However, our goal is not to confirm previous findings related to ORR structure sensitivity but rather to understand relationships between the potential-dependent variations in surface morphology and reactivity. For example, the results in Figure 3-1 reveal that the activity of ORR is improving by systematic roughening of Pt(111) and Pt(100), to the point that the activity of both surfaces is approaching the activity of Pt(110) (See Figure 3-1). On the basis of these results, it is concluded that the oxide-induced roughening of Pt(111) and Pt(100) leads to narrowing differences in activity between Pt single crystal surfaces. In the following, the potential-dependent changes in surface morphology, adsorption, and reactivity properties observed on Pt(100) and Pt(111) will be used as a foundation for discussing the particle size and shape effects in the ORR.

3.3 Particle size effect: the ORR on cubo-octahedral NPs

We recall that there have been numerous studies aimed at establishing the particle size effects on the ORR in acidic environments.[7,15–17,19,39] However, the majority of attempts

to elucidate the particle size effect are not systematic, often relying on trends observed on ill-defined materials and failing to draw any comparison to well-defined surfaces and interfaces that are more readily controlled and understood. By drawing correlations to the potential dependent changes in surface morphology and adsorptive properties of Pt single-crystals, we are now able to acquire related potential-dependent variations in the size and shape of NPs and the concomitant variations in the adsorption of hydrogen and oxygenated species. Pt NPs of different sizes were synthesized by reduction of platinum acetylacetonate in the presence of surfactant using previously published methods with modification (See experimental methods section).The primary method for physical characterization of NPs is transmission electron microscopy (TEM) which gives an accurate determination of average particle size and dispersion of the nanoparticles on carbon support. TEM images at low magnification show that as-synthesized NPs with diameters of 2.8 ± 0.4 nm (Figure 3-2a), 4.1 ± 0.5 nm (Figure 3-2b), 5.1 ± 0.4 nm (Figure 3-2c) and 7.2 ± 0.6 nm (Figure 3-2d) have uniform size. Significantly, supported NPs on high surface area carbon remain well-dispersed (reducing the chance of coalescence) preserving uniform sizes even after surfactant removal (see the Method Section). For all as-synthesized NPs the same potential-cyclic protocol is used (adopted from single crystals experiments) entailing 50 potential cycles from 0.05 V to 1.0 V at 50 mV/s scan rate. For corresponding CVs, summarized in Figure 3-2e, two distinguished features are noteworthy. First, two clearly resolved reversible H_{upd} peaks are positioned at 0.1 V and 0.275 V. Based on CVs assessed for disordered Pt single crystals shown in Figure 3-1b, the H_{upd} peaks are assigned to hydrogen adsorption along (111)-(111) and (111)-(100) step-edges. Further inspection of Figure 3-2e indicates that typical irreversible oxide

formation/reduction peaks are recorded in CVs for all NPs. Second, while the position of H_{upd} is independent of particle size, the position the oxide formation/reduction peaks shifts systematically towards more positive potentials with increasing particle size. Behavioral differences in adsorption of oxygenated species have been attributed to variations in oxophilicity of NPs, increasing from 7.2 nm to 2.8 nm with increasing defect or low coordinated site density.[17,33] In addition, the specific surface area under the adsorption peaks is significantly enlarged for small NPs, reflecting a large surface to bulk ratio of Pt atoms for the 2.8 nm NPs. Similar results are also obtained from sputtered thin films where film thickness is directly related to the surface roughness and therefore average surface Pt atom coordination number. Film growth proceeds through initial islanding to eventual coalescence forming a continuous film, therefore, thinner films like smaller NPs are characterized by a surface that is atomically rougher with higher specific surface area (Fig. S3-1a) but lower specific activity for the ORR (Fig. S3-1b).

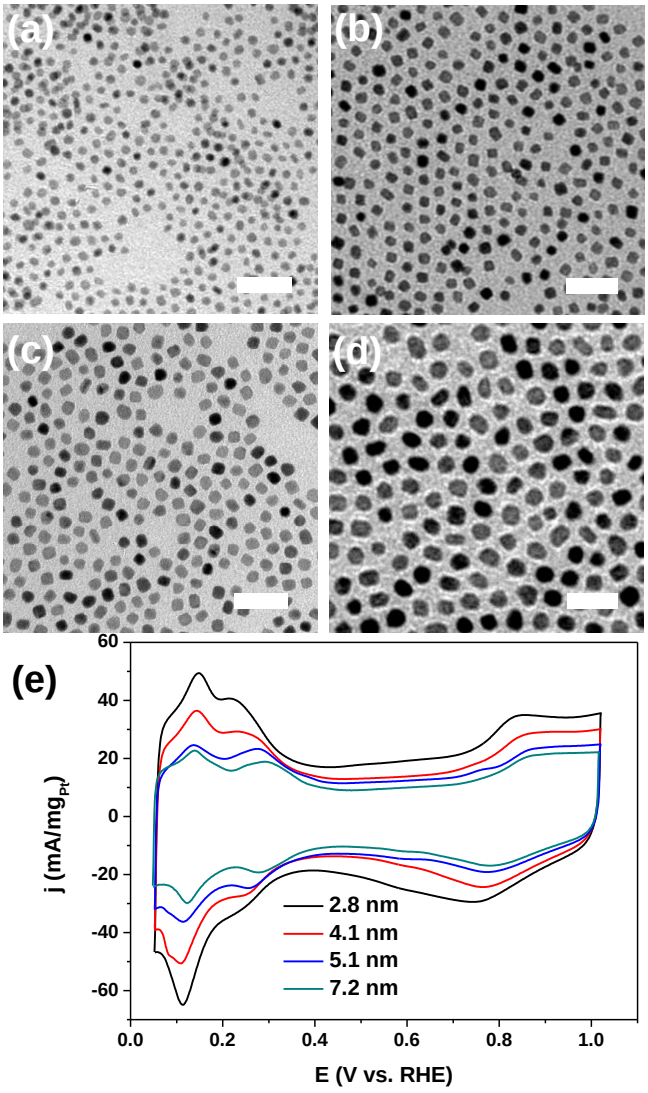

Figure 3-2. TEM images for the as-synthesized (a) 2.8 ± 0.4 nm, (b) 4.1 ± 0.5 nm, (c) 5.1 ± 0.4 nm, (d) 7.2 ± 0.6 nm Pt nanoparticles. Scale bar equals 20 nm. (e) Corresponding cyclic voltammograms recorded at 50mV/s scan rate in Ar purged 0.1 M perchloric acid.

It is important to note here, that in agreement with observations made with low index Pt-single crystals, prolonged cycling over potential regions between 0.05 and 0.8 V had no substantial effect on the shape of CVs, indicating that during the duration of our

experiment the NPs appear to be rather stable. Figure S3-2 shows that the CVs for Pt nanocubes in sulfuric acid are stable below 0.8 V evidenced by the negligible changes in the H_{upd} features (higher cycling potential and temperature lead to more prominent changes. See Figure S3-2). Recall that the first visible effects of the oxide-induced dissolution/re-deposition of Pt are observed for a potential cycling above 0.9 V. Here we have used an accelerated catalyst degradation protocol with an upper potential limit of 1.1 V in order to track morphological changes on a reasonable time scale (see the method section). We note that cycling to 1.0 V or even 0.9 V for Pt NPs will yield identical morphological changes to the ones observed through accelerated degradation but only after a considerably large number of cycles owing to the slower kinetics of surface oxide formation.

Analyses provided below for the oxide-induced variations in the particle size and corresponding CVs under the same conditions are summarized in Figure 3-3. For example, the resulting TEM images of 2.8 nm particles before and after cycling show that the extensive cycling up to 1.1 V causes a significant increase in the NPs average size. Figures 3-3a and 3-3b show that the average size increased from 2.8 nm to 7.3 nm with a concomitant increase in the polydispersity and a significant fraction of particles with diameters greater than 10 nm. This is indicative of an extensive dissolution of small nanoparticles above 1.0 V followed by re-deposition of Pt cations from solution as the potential moves below 1.0 V resulting in the growth of larger particles. Not surprisingly, the electrochemically active surface area (ECSA) under the H_{upd} and OH_{ad} peaks decreases significantly after the potential cycling, as shown in Figure 3-3c. In sharp contrast, a close inspection of Figures 3-3d and 3-3e reveal that under the same

experimental conditions, 7.2 nm NPs are rather stable which is confirmed by negligible changes in the CV after extended potential cycling. As anticipated, Figure 3-3c reveals that while the ECSA for small NPs (e.g., for 2.8 and 4.1 nm NPs) decreases dramatically even after moderate potential cycling, the ECSA changes observed for lager particles (5.1 and 7.2 nm) are rather modest, confirming that the latter are much more stable.

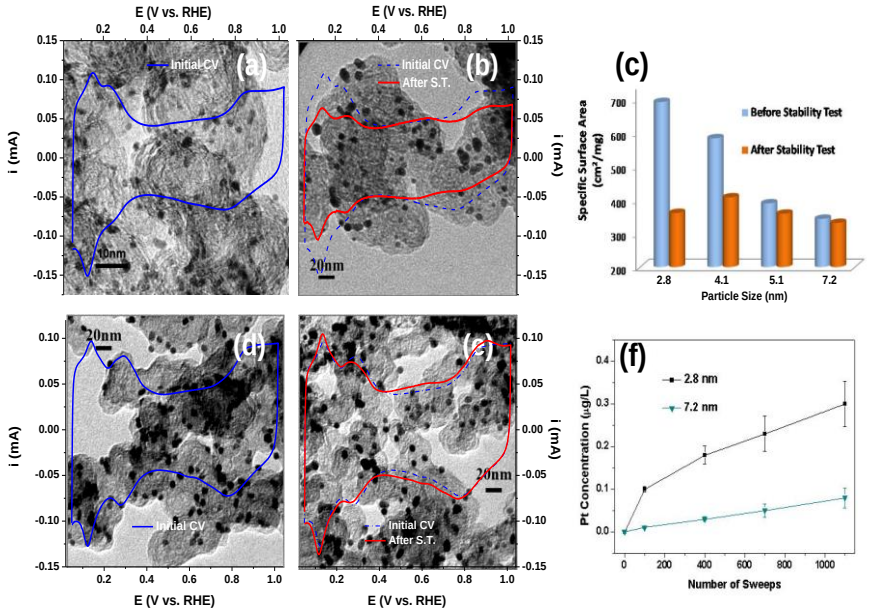

Figure 3-3. TEM images for the 2.8nm Pt NPs on carbon support (a) before, (b) after stability test. (c) Summary specific surface area of different sized NPs before (red bar) and after (blue bar) stability test. 7.2nm Pt NPs on carbon support (d) before, (e) after stability test. Corresponding cyclic voltammograms are shown in a, b, d, e. (f) Pt concentration in the electrolyte during potential cycling for 2.8 nm (black line) and 7.2 nm particles (cyan line).

Evidence pointing to the same conclusion is summarized in Figure 3-3f where the degree of dissolution (concentration of Pt cations found in a solution by ICP mass spectrometry under fuel cell operating conditions) is proportional to the oxophilicity of the respective Pt NPs (dissolved Pt content is four times higher for the 2.8 nm than for the 7.2 nm NPs). The corresponding changes of ECSA were recorded in Figure S3-3. Given that the density of low-coordinated Pt atoms affects the stability trends,[40,41] results in Figure 3-4 suggest that the density of defects on the surface play a significant role in the relationships between stability (dissolution of Pt) and changes in morphology. In contrast to Pt single crystals, however, for Pt NPs it is impossible to find a true correlation between the number of surface defects and the corresponding stability since in contrast to STM, TEM is not capable of providing detailed information on the nature and density of surface defects. However, on the basis of results for Pt(hkl) it is reasonable to expect that low coordinated Pt atoms along the step-edges are much less stable than more coordinated atoms that are part of (111) and (100) terraces.

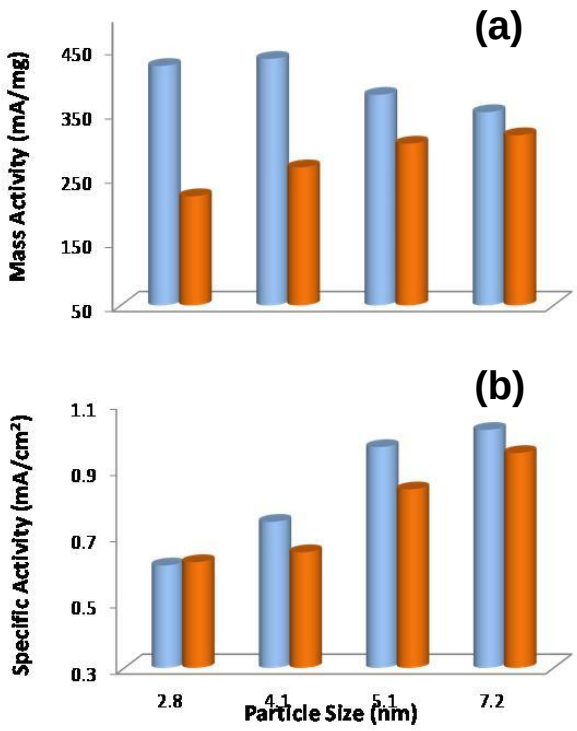

Figure 3-4. ORR performance summary of Pt NPs with different sizes before (blue bar) and after (red bar) stability test (a) Mass activity at 0.90V, (b) Specific activity at 0.90V.

The average potential induced morphological changes of a carbon supported NP sample are not only linked to the finite size of the NPs but may also be tied to the particle size uniformity. In order to probe how the size distribution may affect the average morphological stability of supported NPs, we mixed 2.8 nm and 7.2 nm Pt/C catalyst suspensions with approximately 1:3 mass ratios. From Figure S3-4, TEM and electrochemical analyses of NPs unambiguously show that the variation in size of lager particles is substantial. This is an important observation considering that commercially available Pt catalysts (usually prepared by the impregnation method) are not as uniform in size as NPs produced by colloidal method used in this work; therefore, any particle

size effects observed on catalysts of this nature are not reliable as the system is not sufficiently well defined. We also find that the rate of catalyst degradation in terms of specific surface area and mass activity loss is accelerated for non-uniform size distributions. Not surprisingly, the overall stability performance of this mixture, with an average particle size of 5 nm, is found to be worse than that for the monodisperse 5 nm catalyst. As a result, it is obvious that having uniform particle size is also instrumental in monitoring the durability and activity of supported NP catalysts and thus establishing the particle size effect for the ORR.

The potential-induced variations in the mass and specific activity of the ORR are presented in Figure 3-4 where three key features are noteworthy (i) at the same overpotentials, specific activity increases by increasing the particle size, with the same trend in activity observed before and after potential cycling to 1.1 V; (ii) while mass activity before cycling above 1.0 V is increasing from larger to a smaller NPs, an inverse trend is observed after cycling at high anodic potentials: and (iii) large variations in activity are observed between 2.8 nm to 5.1 nm and upon potential cycling the smaller particles suffer greater loss in mass activity (note that the particle size for an optimal mass activity is ~4 nm in diameter). In addition, based on the knowledge from single crystals it is reasonable to suggest that the observed particle size effect is governed by the correlation between particle size and surface coverage of OH_{ad}, which decreases with an increase in the "size" of ordered low index facets and a decrease in the defect/low coordinated site density (see also Figure 3-2e and 3-3). Thus, in harmony with structure sensitivity it is reasonable to propose that at the same overpotentials an increase in activity by increasing the NPs size can be attributed to an increase in availability of bare

Pt sites required for adsorption of O_2 and the formation of reactive intermediates. Although there is no one to one correspondence between the potential-dependent variations in adsorption proprieties of single crystals and high surface area materials, for establishing the experimental protocol and understanding behavioral differences between various NPs, it is crucial to understand the evolution of well-defined interfaces under the same experimental conditions and operational protocols. As summarized further below the same applies to the particle shape effects.

3.4 Particle shape effects: the ORR on nano-cubes and nano-octahedrons

The particle shape effect on the ORR is even less certain than the particle size effect because the preparation of catalysts with dispersed metal particles of well defined shapes is not straightforward, but has been helped recently by development of novel synthetic techniques based on the solvothermal colloidal method[1,3,4]. It is difficult to prepare NPs of different shapes while maintaining the same average particle size and size distribution. To overcome this limitation we synthesized 7-8 nm Pt NPs with the cubic and octahedral shapes as we found previously that above 7 nm Pt NPs tended to be more stable than the smaller diameter NPs, in order to compare stability of these NPs with 7 nm cubo-octahedral NPs. TEM images of these NPs are summarized in Supplementary Section Figure S3-6. High-resolution TEM (HRTEM) and scanning transmission electron microscope (STEM) images for octahedral and cubic NPs are depicted in Figures 3-5. Analysis of TEM images reveals that the NPs with cubic (7.3 ± 0.6nm in edge length, Fig. S3-5a) and octahedron shapes (8.6 ± 0.8 nm in edge length, Fig. S3-5c) have similar size range when compared to the cubo-octahedral NPs (Fig. 3-2d). Therefore we are not expecting to have a significant impact from the particle size effect. It is interesting to

note that the shape of the as-synthesized cubic NPs supported on carbon, Figure 3-5a, bears a striking resemblance to the square-shaped ad-islands observed on the as-prepared Pt(100) in Figure 3-1c. This interim similarity in the particle shapes, however, has a tendency to mask the inherent differences in the density and nature of surface defects present on NPs and single crystal surfaces. Furthermore, close inspection of the STEM image in Figure 3-5a reveals that the corners of a considerable fraction of the cubic particles are truncated with the (110) crystallographic face. This in turn, limits our ability to find true relationships between the structure/shape of NPs and their corresponding reactivity.

One way to overcome this limitation is to compare CVs of Pt(110) and Pt(100) single crystals with cubic NPs, taking advantage of characteristic positions of the H_{upd} peaks on Pt(110) and Pt(100). CVs for the cubic NPs are recorded in sulfuric acid, (Figure 3-5a), where due to concomitant adsorption/desorption of H_{upd} and desorption/adsorption of bisulfate anions the "H_{upd}" peaks recorded on Pt(110) and Pt(100) are much more pronounced than in perchloric acid electrolytes. We recall that the reversible peaks positioned at 0.125 V and 0.3 V correspond to the competitive adsorption of hydrogen and anions along (111)-(111) and (100)-(111) step-sites present on Pt(110) and Pt(100), respectively. On the other hand, a sharp peak at 0.4 V can be assigned to concomitant adsorption of hydrogen and desorption of anions from (100) sites, which typically are considered to be "flat" terraces of Pt(100). In the case of cubic NPs, a sequence of three reversible H_{upd} peaks are found; two sharp peaks centered at 0.15 and 0.275 V and a broad peak between 0.3 and 0.4 V. The peak around 0.4 V can be further enhanced by CO annealing (Fig. S3-6), since it is well established that CO_{ad} removes some surface

defects from Pt NPs[42] and single crystals.[25] Notice that the large double layer capacitance for the high surface area carbon support complicates the CV analysis as it tends to mask features associated with lower faradaic currents. Nevertheless, based on the position of the H_{upd} peaks on Pt(110) and Pt(100), the cubic NPs dispersed on a carbon support contain some sites with the (100) geometry (broad peak between 0.3 to 0.4 V) and many more defects with both (111)-(100) (sharp peak centered at 0.275 V) and (111)-(111) (a peak at 0.15 V) symmetry.[25] The strong structure sensitivity of adsorptive processes such as H_{upd} and bisulfate adsorption, as shown in the CVs for the different shaped NPs, are in many ways a better indication of the true effect of shape and surface structure on electrochemical properties than the perceived reactivity changes for the ORR. While oxygen adsorption and consequent reduction is limited to a small portion of unblocked surface sites where high turnover frequencies limit real-time observation of surface structure related adsorption geometry, hydrogen and specifically adsorbing anions sample the entire surface providing an intimate knowledge of surface structure.

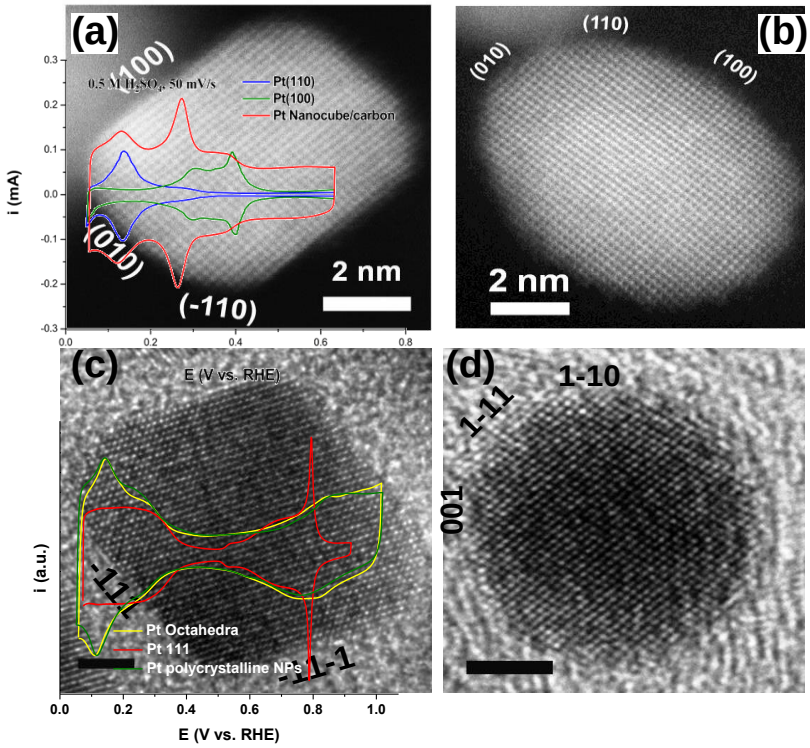

Figure 3-5. Representative STEM images of Pt nanocube (a) before and (b) after potential cycling. HRTEM images of Pt nano-octahedron (c) before and (d) after potential cycling. Cyclic voltammograms in (a) designate Pt nanocubes (red line) and corresponding Pt(110) (blue line), Pt(100) (green line) surfaces from 0.5 M H_2SO_4. Cyclic votammograms in (c) designate Pt nano-octahedrons (yellow line) compared with Pt polycrystalline nanoparticles (green line) and Pt(111) (red line) from 0.1 M $HClO_4$.

For octahedral NPs, adsorption related electrochemical features are supposed to bear some resemblance to those of the Pt(111) single crystal surface. While the HRTEM in Figure 3-5c representing a selected fraction of the NP population shows NPs with hexagonal shape, close inspection of TEM of lower magnification unambiguously reveals that a portion of supported NPs deviate from octahedral shape (some taking on an

icosahedral shape[43,44]) (Fig. S3-5c), signaling that adsorption of H_{upd} and OH_{ad} will deviate significantly from a CV recorded for the Pt(111) in perchloric acid. Indeed, evident in the CV of the octahedral NPs is the presence of a pronounced (110)-like peak at 0.15 V and a broad H_{upd} peak at more positive potentials (Fig. 3-5c). As stated above for cubo-octahedral and cubic NPs, it can be concluded that an average distribution of Pt atoms within the octahedral NPs is rather irregular, i.e., they are more Pt-poly-like than Pt(111)-like. This is expected as even well prepared Pt single crystals contain a moderate amount of surface defects and therefore it is even less feasible to have perfect faceted NPs. Taken together, results in Figure 3-5 reveal that both cubic and octahedral NPs are decorated with many defects which, as we learned from single crystals, play an inherently synergistic role in controlling the potential-dependent stability and reactivity of surface atoms.

Any chance of elucidating a NP shape effect for the ORR relies on the potential-dependent stability of these shapes; if the shape is lost at potentials relevant for PEMFC cathodes than it would be difficult to correlate any activity differences to the initial NP shape. The loss of cubic and octahedral shapes after applying 4000 potential cycles to 1.1 V was confirmed by HRTEM images such as those shown in Figure 3-5 as well as by TEM in Figure S3-5. Namely, after the potential cycling both the as-prepared cubic (changes of [100] facet by germanium adsorption is shown in Figure S3-7) and octahedral NPs are converted to the round-like shape, signifying that under irreversible oxide formation/reduction cycles it is very difficult to preserve the particle shapes. This can be correlated to the morphological changes of single crystal surfaces upon potential cycling (Fig. 3-1), though higher potentials are used for bulk single crystals since they are

more stable than small NPs. We notice, the same is true if the potential is cycled to 1 V, the only deference being that the observed transformation requires more potential cycles. The potential-dependent shape transformation of Pt NPs can be considered to be guided by both thermodynamics (the driving force for an irreversible oxide formation) as well as kinetics (the rate of oxide formation which is, at the same electrode potential, mainly controlled by the density of surface defects). Although it is been suggested that reactivity and selectivity of metal catalysts for the ORR can be tailored by controlling NP shape, our results show that this would be extremely difficult for long-term catalytic performance as the NPs will eventually be exposed to electrode potentials at which an irreversible oxide would slowly, but persistently, transform any shape-controlled activity to activity that is determined by thermodynamically stable rounded-like NPs.[45] The study of NP shape affected electrochemistry is better suited for reactions that take place within the potential window of NP stability, below 0.8 V, and is of fundamental importance for design of next generation, nanoparticulate based electrocatalysts.

3.5 Conclusion

In summary, by comparing morphological, adsorption and catalytic properties of Pt single crystals to those of Pt NPs before and after the ORR we conclude that without understanding relationships between activity and stability of Pt single crystal surfaces it would be impossible to resolve complexities associated with the ORR on Pt NPs. NPs, by the nature of their geometry, are defined by a distribution of crystallographic surface orientations that may be related to their size and radius of curvature. As this distribution

and the density of defects vary with NP size, it is expected that the "particle shape effect" should be linked to a "particle size effect." Caution must be exercised, especially in the case of NPs, when attempting to find a correlation between activity and structure related to particle shape and size, as this structure is often metastable and may easily evolve to some thermodynamically equilibrated shape/size even at moderate reaction conditions. Using insight gained from the characteristic response of Pt single crystals to adsorption of species such as H_{upd} and OH_{ad}, we have been able to elucidate intimate details of the surface structure of NPs with varying size and shape and track the evolution of that surface structure under ORR conditions. From the results presented here, it is clear that in establishing the particle size effect for the ORR, or any electrochemical reaction, one must take into consideration at least three important factors: (i) NPs must be uniform in size; (ii) dispersion of NPs on conductive support must be uniform; (iii) electrochemical experimental conditions (potential window, number of cycles, temperature etc.) used to "pre-condition" NPs for establishing the ECSA and the specific activity must follow the same protocol. With these stipulations in mind, we have shown that there is indeed a particle size effect with specific activity increasing with increasing NP diameter. This increase in activity is directly related to the change in adsorption properties of species such as OH_{ad}, with coverage increase as defect density increases and particle size decreases. However, the particle size effect begins to lose its clarity as catalyst age, especially at the smaller particles sizes, where Pt dissolution initiated by the formation of irreversible surface oxides results in dissolution/redeposition and a broadening of the particle size distribution. These same stability issues are evident when exploring the particle shape effect. We found that structural evolution under moderate reaction

conditions yielded particles of a rounded geometry, indiscriminate to the initial particle shape. While there may in fact be a shape effect for the ORR electrocatalysis on the Pt NP, the main challenge should be placed on how to stabilize particular shape that could be associated with certain architecture of nanoparticles.[46–48]

3.6 Experimental Methods

The Pt based NPs of varied sizes were synthesized using solvo-thermo method adopted from previous publications with modifications. The detailed synthesis of 2.8 nm Pt was recorded elsewhere.[49] The synthesis of 7.2 nm cubo-octahedral Pt NPs started by mixing 0.08 g $Pt(acac)_2$ 1.0 mL oleic acid, 5.0 mL oleylamine and 10 mL benzyl ether in a three-necked flask. The solution was stirred under Ar flow for 30 minutes and was subsequently heated to 160 ˚C at 10 ˚C/min. In the meantime, 0.2 mL iron pentacarbonyl $Fe(CO)_5$ was dissolved in 4 mL chloroform $CHCl_3$ to make 5% $Fe(CO)_5$ solution. 0.5 mL of this $Fe(CO)_5$ solution was injected to the flask at 160˚C. The temperature was then raised to 210 ˚C at 15 ˚C/min and kept for one hour. The as-synthesized Pt NPs were precipitated out by adding ethanol with centrifugation. The washed NPs were subsequently collected and re-dispersed in hexane. Cubo-octahedral Pt NPs of 4 and 5 nm were synthesized by similar methods expect that the $Fe(CO)_5$ solution was introduced at 170 ˚C and 180 ˚C, respectively. The synthesis details were recorded in previous publications for Pt cubic NPs[18] and octahedral NPs.[43,44] The NPs were anchored onto carbon support (Tanaka 902.4 m^2/g) in chloroform by sonicating. The mass ratio of particle versus carbon was approximately 1:1. After that, the catalyst was annealed in air at 185 ˚C to clean the surface.[47] Pt thin films of varied thickness were deposited onto the surface of glassy carbon.[50] Pt(111), Pt(100) and Pt(100) single crystalline electrodes were

prepared by inductive heating for 10 minutes at about 1100 K under gentle flow of forming gas (3% H_2 in Ar). These electrodes were subsequently cooled down to room temperature under the same atmosphere. The surface of the electrodes was covered by a droplet of Milli-Q water before they were transferred to the electrochemical cell in hanging meniscus mode.

The electrochemical characterizations of the Pt NP catalysts were carried out in a standard three-compartment electrochemical cell using 0.1 M perchloric acid ($HClO_4$) as the electrolyte. A Ag/AgCl electrode was used as the reference electrode and a Pt wire served as the counter electrode. The treated catalysts were dispersed in Milli-Q water under sonication to make ~0.5 mg/mL catalyst ink. 20-30 uL catalyst ink was pipetted onto the glassy carbon electrode surface (0.283 cm^2 geometrical surface area) to make the working electrode. The catalyst loadings were between 15 and 19 ug/cm^2. An autolab 302 potentiostat was used to conduct the electrochemical measurement. An initial cyclic voltammogram (CV) was recorded after cycling between 0.05V and 1.0V for 50 sweeps at 50 mV/s under argon atmosphere. The oxygen reduction reaction (ORR) polarization curves were obtained at 20mV/s scan rate and 1600 rpm rotation with iR drop correction when the electrolyte was saturated with oxygen. For the CO stripping experiment, the electrolyte was purged by carbon monoxide to have the surface of Pt fully covered by CO at 0.05V. After that, the electrolyte was purged with argon to remove CO. The electrode was cycled between 0.05V and 1.07V at 50mV/s for four scans. The electrochemically active surface area (ECSA) of the catalyst was calculated from CO stripping peak area. The reference electrode was calibrated by hydrogen oxidation/evolution reaction at the end of each measurement. All potential shown in this paper are versus reversible

hydrogen electrode (RHE). All above mentioned electrochemical measurements were conducted at room temperature (20˚C). Stability test was carried out at elevated temperature (60˚C), by scanning between 0.6V and 1.1V for 4000 sweeps at 50mV/s in 0.1 M $HClO_4$ unless otherwise specified.

For germanium adsorption,[51] GeO_2 was dissolved in 1.0 M NaOH to form ~10^{-2} M Ge solution. After a clean CV was recorded in 0.5 M H_2SO_4, the surface of electrode was rinsed by Milli-Q water and dipped into the Ge solution for two minutes. The electrode was subsequently suspended in the cell with a droplet of Ge solution attached to the glassy carbon disc. The cell was purged with Ar for 10 minutes. Then the electrode was put in contact with the 0.5 M H_2SO_4 electrolyte at 0.1 V.

The Inductively coupled plasma mass spectrometry (ICP-MS) analysis was performed on a Perkin-Elmer/SCIEX spectrometer (model Number: ELAN DRC-II). The sample flow rate is 0.83 mL/min. Transmission electron microscopy (TEM) analysis was performed on a Philips EM 30 at 200 kV. HRTEM images were collected on a FEI Tecnai F20ST AEM (200 kV). STEM images were carried out on a JEOL 2200FS TEM/STEM (200 kV) with a CEOS aberration (probe) corrector.

Acknowledgement

The single crystal work was supported by the U.S. Department of Energy, Basic Energy Sciences, Materials Sciences and Engineering Division. The portion of work related to nanoparticle syntheses and characterization was supported by the office Energy efficiency and Renewable Energy, Fuel Cells Technologies Program and Toyota motor Engineering & Manufacturing North America. The electron microscopy was

accomplished at the Electron Microscopy Center at Argonne National Laboratory, a U.S. Department of Energy Office of Science Laboratory operated under Contract No. DE-AC02-06CH11357 by UChicago Argonne, LLC. STEM studies were accomplished at the Center for Nanophase Materials Sciences at Oak Ridge National Laboratory, which is sponsored by the Scientific User Facilities Division, Office of Basic Energy Sciences, U.S. Department of Energy.

3.7 References

(1) Chen, J.; Lim, B.; Lee, E. P.; Xia, Y. *Nano Today* **2009**, *4*, 81–95.

(2) Cuenya, B. R. *Thin Solid Films* **2010**, *518*, 3127–3150.

(3) Guo, S.; Zhang, S.; Sun, S. *Angewandte Chemie International Edition* **2013**, *52*, 8526–8544.

(4) Wu, J.; Yang, H. *Acc. Chem. Res.* **2013**, *46*, 1848–1857.

(5) Hammer, B.; Nørskov, J. K. *Advances in Catalysis* **2000**, *45*, 71–129.

(6) Poltorak O. M.; Boronin V. S. *Russ. J. Phys. Ch.* **1966**, *40*, 1436.

(7) Kinoshita, K. *J. Electrochem. Soc.* **1990**, *137*, 845–848.

(8) Sattler, M. L.; Ross, P. N. *Ultramicroscopy* **1986**, *20*, 21–28.

(9) Markovic, N.; Gasteiger, H.; Ross, P. N. *J. Electrochem. Soc.* **1997**, *144*, 1591–1597.

(10) Hammer, B.; Nørskov, J. K. *Surface Science* **1995**, *343*, 211–220.

(11) Mukerjee, S.; Srinivasan, S.; Soriaga, M. P.; McBreen, J. *J. Electrochem. Soc.* **1995**, *142*, 1409–1422.

(12) Gasteiger, H. A.; Marković, N. M. *Science* **2009**, *324*, 48–49.

(13) Marković, N. M.; Adžić, R. R.; Cahan, B. D.; Yeager, E. B. *Journal of Electroanalytical Chemistry* **1994**, *377*, 249–259.

(14) Markovic, N. M.; Gasteiger, H. A.; Ross, P. N. *J. Phys. Chem.* **1995**, *99*, 3411–3415.

(15) Bregoli, L. J. *Electrochimica Acta* **1978**, *23*, 489–492.

(16) Gasteiger, H. A.; Kocha, S. S.; Sompalli, B.; Wagner, F. T. *Applied Catalysis B: Environmental* **2005**, *56*, 9–35.

(17) Mayrhofer, K. J. J.; Blizanac, B. B.; Arenz, M.; Stamenkovic, V. R.; Ross, P. N.; Markovic, N. M. *J. Phys. Chem. B* **2005**, *109*, 14433–14440.

(18) Wang, C.; Daimon, H.; Onodera, T.; Koda, T.; Sun, S. *Angewandte Chemie* **2008**, *120*, 3644–3647.

(19) Shao, M.; Peles, A.; Shoemaker, K. *Nano Lett.* **2011**, *11*, 3714–3719.

(20) Watanabe, M.; Sei, H.; Stonehart, P. *Journal of Electroanalytical Chemistry and Interfacial Electrochemistry* **1989**, *261*, 375–387.

(21) Nesselberger, M.; Ashton, S.; Meier, J. C.; Katsounaros, I.; Mayrhofer, K. J. J.; Arenz, M. *J. Am. Chem. Soc.* **2011**, *133*, 17428–17433.

(22) Sheng, W.; Chen, S.; Vescovo, E.; Shao-Horn, Y. *J. Electrochem. Soc.* **2012**, *159*, B96–B103.

(23) Tian, N.; Zhou, Z.-Y.; Sun, S.-G.; Ding, Y.; Wang, Z. L. *Science* **2007**, *316*, 732 – 735.

(24) Yu, T.; Kim, D. Y.; Zhang, H.; Xia, Y. *Angewandte Chemie International Edition* **2011**, *50*, 2773–2777.

(25) Marković, N. M.; Ross Jr., P. N. *Surface Science Reports* **2002**, *45*, 117–229.

(26) Clavilier, J. *Journal of Electroanalytical Chemistry and Interfacial Electrochemistry* **1979**, *107*, 211–216.

(27) Kinoshita, K.; Lundquist, J. T.; Stonehart, P. *Journal of Electroanalytical Chemistry and Interfacial Electrochemistry* **1973**, *48*, 157–166.

(28) Ferreira, P. J.; La O', G. J.; Shao-Horn, Y.; Morgan, D.; Makharia, R.; Kocha, S.; Gasteiger, H. A. *J. Electrochem. Soc.* **2005**, *152*, A2256–A2271.

(29) Shao-Horn, Y.; Sheng, W. C.; Chen, S.; Ferreira, P. J.; Holby, E. F.; Morgan, D. *Topics in Catalysis* **2007**, *46*, 285–305.

(30) Tang, L.; Han, B.; Persson, K.; Friesen, C.; He, T.; Sieradzki, K.; Ceder, G. *J. Am. Chem. Soc.* **2010**, *132*, 596–600.

(31) Yang, Z.; Ball, S.; Condit, D.; Gummalla, M. *J. Electrochem. Soc.* **2011**, *158*, B1439–B1445.

(32) El Kadiri, F.; Faure, R.; Durand, R. *Journal of Electroanalytical Chemistry and Interfacial Electrochemistry* **1991**, *301*, 177–188.

(33) Marković, N. M.; Gasteiger, H. A.; Ross, P. N. *J. Phys. Chem.* **1996**, *100*, 6715–6721.

(34) Strmcnik, D. S.; Tripkovic, D. V.; Van der Vliet, D.; Chang, K.-C.; Komanicky, V.; You, H.; Karapetrov, G.; Greeley, J. P.; Stamenkovic, V. R.; Marković, N. M. *J. Am. Chem. Soc.* **2008**, *130*, 15332–15339.

(35) Wagner, F. T.; Ross Jr., P. N. *Journal of Electroanalytical Chemistry and Interfacial Electrochemistry* **1983**, *150*, 141–164.

(36) Subbaraman, R.; Tripkovic, D.; Strmcnik, D.; Chang, K.-C.; Uchimura, M.; Paulikas, A. P.; Stamenkovic, V.; Markovic, N. M. *Science* **2011**, *334*, 1256–1260.

(37) Reiser, C. A.; Bregoli, L.; Patterson, T. W.; Yi, J. S.; Yang, J. D.; Perry, M. L.; Jarvi, T. D. *Electrochemical and Solid-State Letters* **2005**, *8*, A273.

(38) Siroma, Z.; Fujiwara, N.; Ioroi, T.; Yamazaki, S.; Senoh, H.; Yasuda, K.; Tanimoto, K. *Journal of Power Sources* **2007**, *172*, 155–162.

(39) Takasu, Y.; Ohashi, N.; Zhang, X.-G.; Murakami, Y.; Minagawa, H.; Sato, S.; Yahikozawa, K. *Electrochimica Acta* **1996**, *41*, 2595–2600.

(40) Komanicky, V.; Chang, K. C.; Menzel, A.; Markovic, N. M.; You, H.; Wang, X.; Myers, D. *J. Electrochem. Soc.* **2006**, *153*, B446–B451.

(41) Jinnouchi, R.; Toyoda, E.; Hatanaka, T.; Morimoto, Y. *J. Phys. Chem. C* **2010**, *114*, 17557–17568.

(42) Arenz, M.; Mayrhofer, K. J. J.; Stamenkovic, V.; Blizanac, B. B.; Tomoyuki, T.; Ross, P. N.; Markovic, N. M. *Journal of the American Chemical Society* **2005**, *127*, 6819–6829.

(43) Kang, Y.; Li, M.; Cai, Y.; Cargnello, M.; Diaz, R. E.; Gordon, T. R.; Wieder, N. L.; Adzic, R. R.; Gorte, R. J.; Stach, E. A.; Murray, C. B. *J. Am. Chem. Soc.* **2013**, *135*, 2741–2747.

(44) Kang, Y.; Pyo, J. B.; Ye, X.; Diaz, R. E.; Gordon, T. R.; Stach, E. A.; Murray, C. B. *ACS Nano* **2013**, *7*, 645–653.

(45) Tripković, V.; Cerri, I.; Bligaard, T.; Rossmeisl, J. *Catal Lett* **2014**, *144*, 380–388.

(46) Zhang, J.; Sasaki, K.; Sutter, E.; Adzic, R. R. *Science* **2007**, *315*, 220–222.

(47) Wang, C.; Van der Vliet, D.; More, K. L.; Zaluzec, N. J.; Peng, S.; Sun, S.; Daimon, H.; Wang, G.; Greeley, J.; Pearson, J.; Paulikas, A. P.; Karapetrov, G.; Strmcnik, D.; Markovic, N. M.; Stamenkovic, V. R. *Nano Lett.* **2011**, *11*, 919–926.

(48) Chen, C.; Kang, Y.; Huo, Z.; Zhu, Z.; Huang, W.; Xin, H. L.; Snyder, J. D.; Li, D.; Herron, J. A.; Mavrikakis, M.; Chi, M.; More, K. L.; Li, Y.; Markovic, N. M.; Somorjai, G. A.; Yang, P.; Stamenkovic, V. R. *Science* **2014**, 1249061.

(49) Li, D.; Wang, C.; Tripkovic, D.; Sun, S.; Markovic, N. M.; Stamenkovic, V. R. *ACS Catal.* **2012**, *2*, 1358–1362.

(50) Van der Vliet, D. F.; Wang, C.; Tripkovic, D.; Strmcnik, D.; Zhang, X. F.; Debe, M. K.; Atanasoski, R. T.; Markovic, N. M.; Stamenkovic, V. R. *Nat Mater* **2012**, *11*, 1051–1058.

(51) Rodríguez, P.; Herrero, E.; Solla-Gullón, J.; Vidal-Iglesias, F. J.; Aldaz, A.; Feliu, J. M. *Electrochimica Acta* **2005**, *50*, 4308–4317.

3.8 Supporting Information

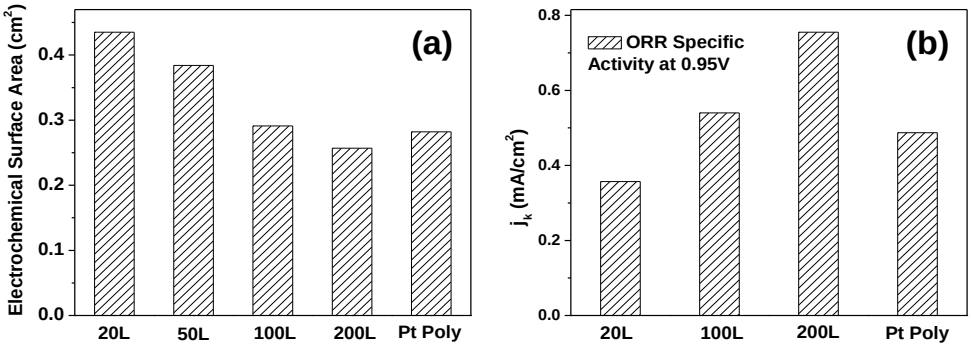

Figure S3-1. Summary of electrochemical properties of sputtered Pt film on the glassy carbon electrode with controlled atomic layers: (a) Electrochemical surface area and (b) ORR specific activity at 0.95V. Pt poly crystal of same geometric surface area (~0.283 cm^2) is used for comparison.

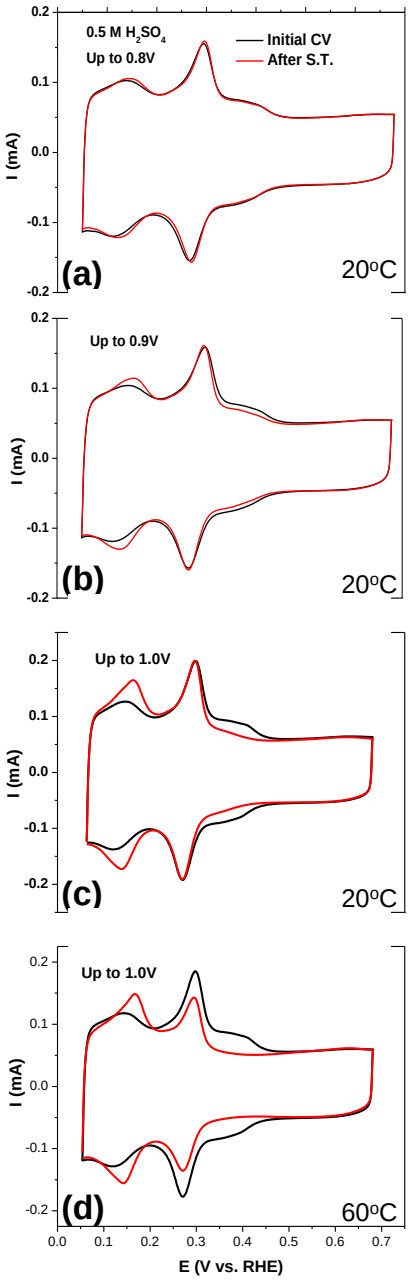

Figure S3-2. Cyclic voltammograms (CVs) of Pt nanocubes on carbon support before and after 4000 potential cyclings from 0.6V to (a) 0.8 V (b) 0. 9V (c) 1.0 V (d) 1.0 V. (a) to (c) were conducted at room temperature (20 ˚C). (d) was conducted at 60 ˚C. All the CVs were recorded in 0.5 M H_2SO_4. The potential cycling was conducted in 0.1 M $HClO_4$.

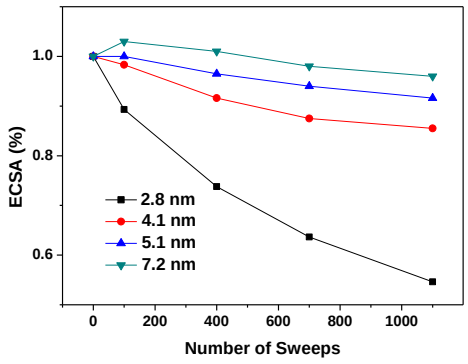

Figure S3-3. Changes of electrochemically active surface area (ECSA) during potential cycling between 0.6V and 1.1V at 50mV/s, 60˚C in 0.1 M perchloric acid.

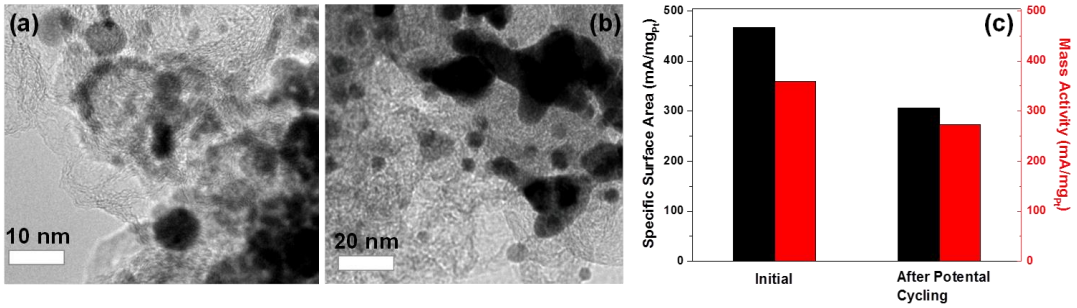

Figure S3-4. Mixed 2.8 nm and 7.2 nm catalyst suspension: TEM images (a) before and (b) after stability test, (c) Specific surface area (black) and ORR mass activity at 0.90V (Red) before and after stability test. Same stability test protocol was used. (i.e. 60˚C, scan between 0.6V and 1.1V for 4000 sweeps at 50mV/s in 0.1M perchloric acid).

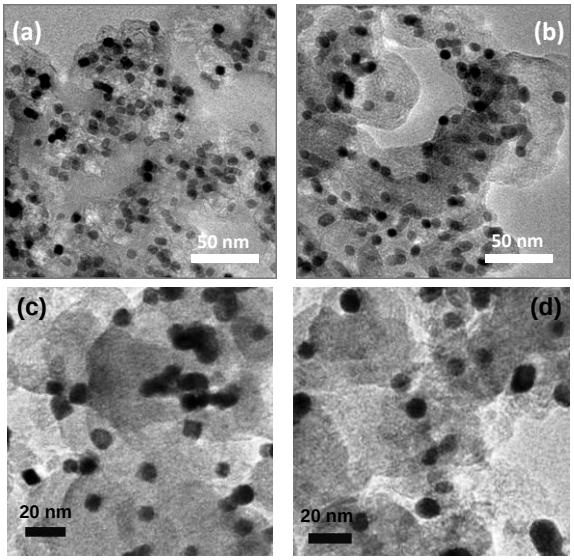

Figure S3-5. TEM images of nanocubes (a) before and (b) after stability test. TEM images of nano-octahedrons (c) before and (d) after stability test. Stability test protocol is the same as in Figure S3-4.

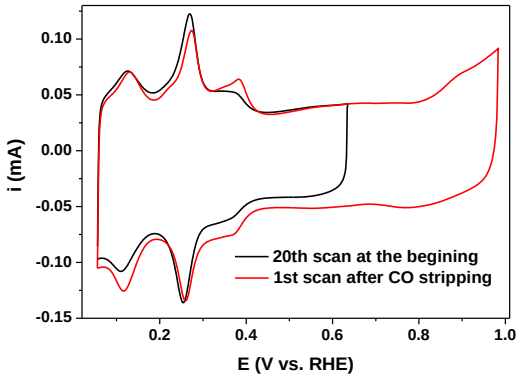

Figure S3-6. Pt nanocubes, initial (black line) and CV after CO stripping (red line) in 0.5 M H_2SO_4 at 50mV/s, room temperature. The black line was recorded after first 20 scans between 0.05 V and 0.65 V. The red line was recorded after the CO adsorbed on the surface was oxidized.

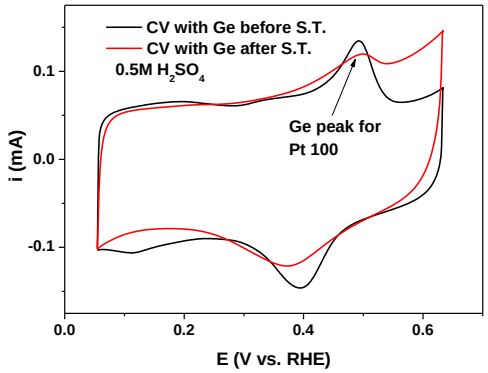

Figure S3-7. CVs of 7 nm Pt nanocubes covered with adsorbed germanium before and after stability test (S.T., 4000 scans between 0.6V and 1.0V, at 50mV/s, room temperature, in 0.1 M $HClO_4$) in 0.5 M H_2SO_4, at 50 mV/s, room temperature.

IV. Design and Synthesis of Bimetallic Electrocatalyst with Multilayered Pt-Skin Surfaces

4.1 Introduction

The foreground of sustainable energy is built up on a renewable and environmentally compatible scheme of chemical-electrical energy conversion. One of the key processes for such energy conversion is the electrocatalytic reduction of oxygen, the cathode reaction in fuel cells[1] and metal air batteries,[2,3] where an electrocatalyst is used to accelerate the course of ORR. Current electrocatalysts used for this reaction are typically in the form of dispersed Pt nanoparticles (NPs) on amorphous high-surface-area carbon. Considering the high cost and limited resource of Pt, large-scale applications of these renewable energy technologies demand substantial improvement of the catalyst performance so that the amount of Pt needed can be significantly reduced. For example, a 5-fold improvement of catalytic activity for the ORR is required for the commercial implementation of fuel cell technology in transportation.[4]

The recent work on well-defined extended surfaces has shown that high catalytic activity for the ORR can be achieved on Pt bimetallic alloys (Pt_3M,M= Fe, Co, Ni, etc.), due to the altered electronic structure of the Pt topmost layer and hence reduced adsorption of oxygenated spectator species (e.g., OH^-) on the surface.[5,6] It was also found that in an acidic electrochemical environment the non-noble 3d transition metals are dissolved from the near surface layers, which leads to the formation of Pt-skeleton

surfaces. Moreover, the thermal treatment of Pt_3M alloys in ultra high vacuum (UHV) has been shown to induce segregation of Pt and formation of a distinctive topmost layer that was termed Pt-skin surface. However, the same treatment did not cause Pt to segregate over PtM alloys with high content (≥50%) of non-Pt elements.[6,7] Recently, we further demonstrated the surfacing of an ordered Pt(111)-skin over Pt_3Ni(111) single crystal with 50% of Ni in the subsurface layer. This unique nanosegregated composition profile was found to be responsible for the dramatically enhanced ORR activity.[8]

On the basis of these findings, it could be envisioned that the most advantageous nanoscale architecture for a bimetallic electrocatalyst would correspond to the segregated Pt-skin composition profile established on extended surfaces. A lot of effort has thus been dedicated,[9–13] but it still remains elusive, to finely tune the Pt-bimetallic nanostructure to achieve this desirable surface structure and composition profile. Major obstacles reside not only in the difficulty to manipulate elemental distribution at the nanoscale, but also in the fundamental differences in atomic structures, electronic properties, and catalytic performance between extended surfaces and confined nanomaterials. For example, in an attempt to induce surface segregation, high-temperature (>600 °C) annealing is typically applied for Pt-based alloy nanocatalysts. While improvement in specific activity is obtained, such treatment usually causes particle sintering and loss of electrochemical surface area (ECSA).[10,14,15] Besides that, the surface coordination of nanomaterials is quite different from that of bulk materials; that is, the surface of NPs is rich in corner and edge sites, which have a smaller coordination number than the atoms on longrange ordered terraces of extended surfaces.[16,17] These low-coordination surface atoms are considered as preferential sites for the adsorption of oxygenated spectator species (e.g.,

OH^-)[18,19] and thus become blocked for adsorption of molecular oxygen and inactive for the ORR.[17,20,21] Additionally, due to strong Pt-O interaction, these sites are more vulnerable for migration and dissolution, resulting in poor durability and fast decay of the catalyst.[22,23] The latter effect is even more pronounced in Pt bimetallic systems, considering that more undercoordinated atoms are present on the skeleton surfaces formed after the depletion of nonprecious metals from near-surface regions.[5,24] Therefore, a systematic approach with all of these factors integrally considered becomes necessary to pursue the design and synthesis of advanced bimetallic catalysts.

Our focus in this study has been placed on the fine-tuning of Pt-bimetallic nanostructure aiming to achieve the advantageous Pt-skin surface structure and composition profile established on extended surfaces. We started with Pt thin films of controlled thickness deposited over PtNi substrate to explore the correlation between the surface composition profile and catalytic performance. These findings were then applied for guiding the synthesis of nanocatalysts with the optimized structure. The outcome of such effort is an advanced Pt-bimetallic catalyst with altered nanoscale architecture that is highly active and durable for the ORR.

4.2 Results and Discussion

4.2.1 *Sputtered PtNi Thin films.* Pt films of various thicknesses, that is, 1-7 atomic monolayers (ML), were deposited in a vacuum by sputtering on PtNi (Pt:Ni = 1:1) substrate and then transferred to an electrochemical cell for further characterizations (see the Experimental Section). The as-sputtered Pt films consist of randomly distributed Pt nanoclusters (<1 nm), which mimic the Ni depleted Pt-skeleton structures.4a The film

thickness was varied to explore the dependence of catalytic activity on the surface depletion depth in Pt-skeleton type of surfaces.[24] The choice of PtNi substrate was based on our previous results from nanosegregated extended surfaces6 and most recent findings related to composition-dependent electrochemical properties of Pt_xNi_{1-x} NPs,[24] which had confirmed the superior catalytic properties of systems with 50% of Ni in subsurface layers. Figure 4-1 summarizes the results of electrochemical studies for these thin films by rotating disk electrode (RDE). Cyclic voltammograms (CVs, Figure 4-1a) of the as-sputtered films correspond to polycrystalline Pt (poly-Pt) with similar, but slightly enlarged, underpotentially deposited hydrogen (H_{upd}) regions (E < 0.4 V) due to the rougher surfaces. Consistent with our previous findings,[8] the onset of Pt-OH_{ad} formation has anodic shifts for most of the Pt films (≤5 ML) as compared to poly-Pt (more visible in the CVs shown in the Supporting Information, Figure S4-1, with currents normalized by the electrochemical surface area (ECSA) obtained from integrated Hupd region). Correspondingly, similar positive shifts are also present in the polarization curves for the ORR (Figure 4-1b). The largest shift of ~30 mV was obtained for the Pt films with thicknesses of three atomic layers. Measured specific activities at 0.95 V, expressed as kinetic current normalized by the ECSA, show that the thinner films (≤3 ML) have improvement factors of ~2.5 versus poly-Pt surface, which is in line with the previous results on polycrystalline Pt_3M bulk alloys with the skeleton type of surfaces.[6] Reduced enhancement was observed for thicker Pt films, for example, improvement factor of 1.7 for 5 ML of Pt, while the specific activity measured for the 7 ML film was close to that of poly-Pt. It should be noted here that for the as-sputtered films, 1 ML of Pt may not be able to entirely cover Ni atoms in the alloy substrate and protect them from dissolution,

whereas addition of a second and/or third layer can effectively diminish this process. Along the same lines, this may also be the reason that the surfaces with 2 or 3 ML of Pt were found to be more active than that with 1 ML. These findings revealed that bimetallic systems with Pt-skeleton near-surface formation of up to three atomic layers in thickness are also capable of efficiently harvesting the beneficial properties of bimetallic alloys, while protecting the subsurface Ni from leaching out.

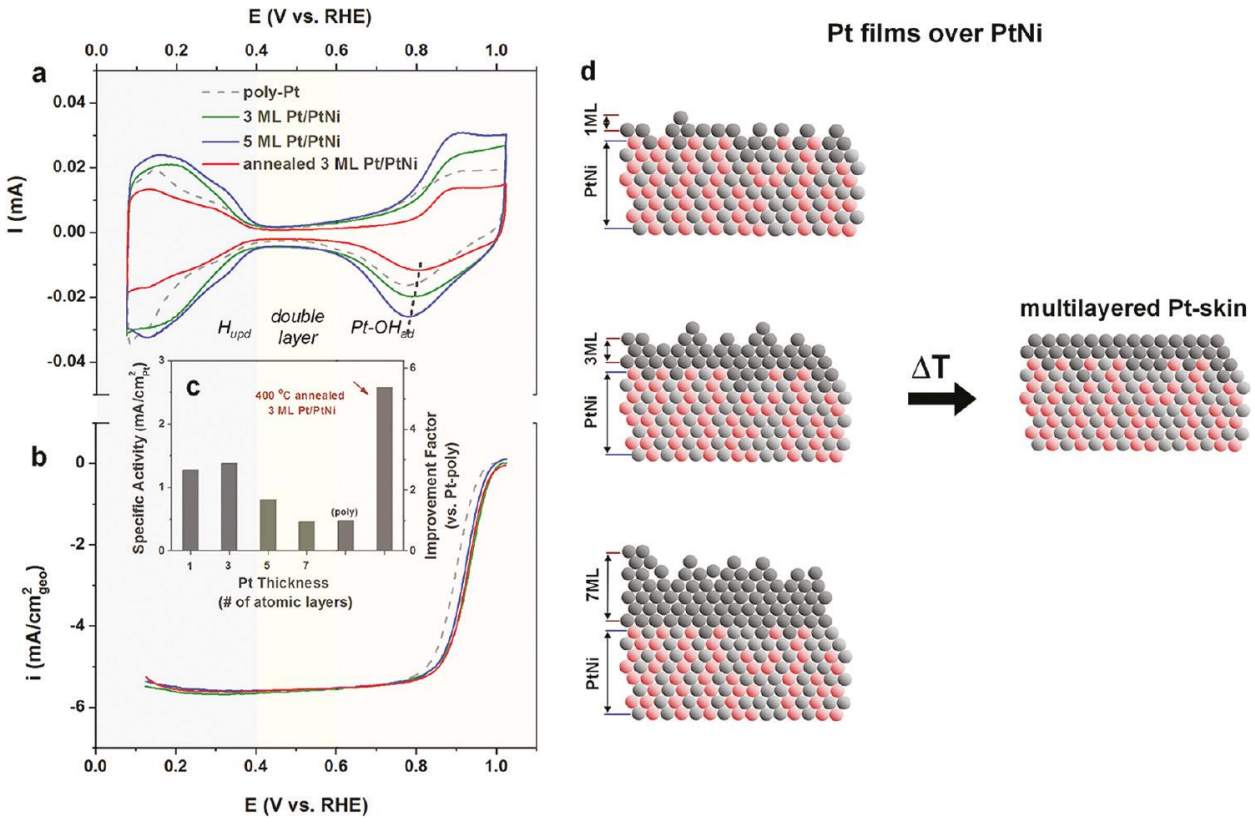

Figure 4-1. Electrochemical studies on the Pt thin films deposited over PtNi substrate by RDE: (a) cyclic voltammograms, (b) polarization curves, and (c) summary of specific activities and corresponding improvement factors (vs. polycrystalline Pt surface) for the Pt films of various thicknesses. Cyclic voltammograms were recorded in Ar saturated

0.1M $HClO_4$ electrolyte with a sweeping rate of 50 mV/s. Polarization curves were recorded in the same electrolyte under O_2 saturation with a sweep rate of 20 mV/s. Specific activities were presented as kinetic currents normalized by ECSAs obtained from integrated H_{upd}, except that for the annealed 3 ML Pt/PtNi surface which was based on CO_{ad} stripping polarization curve.

Because the as-sputtered skeleton type of surfaces have abundant low-coordination sites[5] that are detrimental to the ORR, we have applied thermal treatment to investigate potential surface restructuring and further catalytic improvement. A moderate temperature of ~400 °C was chosen as it was determined to be optimal for Pt bimetallic nanocatalysts.[14] In Figure 4-1a, the CV of annealed 3ML Pt/PtNi surface is also shown. The suppressed H_{upd} region and an even larger positive shift of the Pt-OH_{ad} peak (Figure S4-1) indicates the formation of Pt-skin type of surface e, which is smoother and less oxophilic with significantly reduced number of low coordination surface atoms.[7,8] Additional proof of the transitiontoward Pt-skin is provided by the measured boost in specific activity for the ORR (Figure 4-1c), reaching an improvement factor of more than 5 with respect to poly-Pt (Figure 4-1d). Moreover, this high catalytic activity was based on the ECSA estimated from CO stripping polarization curves, not Hupd. The ECSA estimated from integrated H_{upd} charge was found to be substantially smaller than that obtained from the electrochemical oxidation of adsorbed CO monolayer (Figure S4-2), which was not observed on unannealed Pt-skeleton surfaces. Such a difference can only be interpreted in terms of the altered electronic properties of the Pt-skin surface that have affected the adsorption of hydrogenated species, but not the Pt-CO_{ad} interaction.[8]

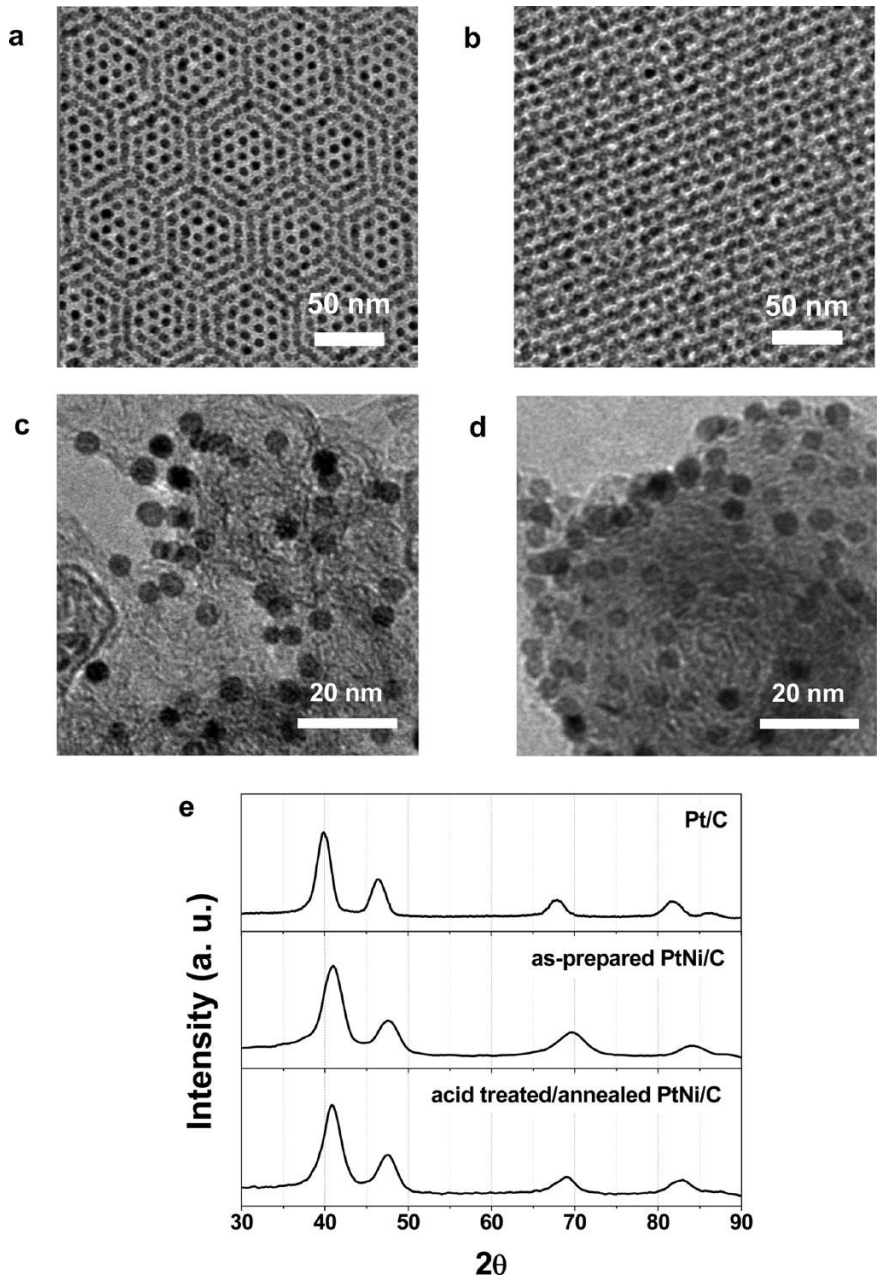

Figure 4-2. Representative transmission electron microscopy (TEM) images for (a,b) the as-synthesized PtNi NPs, (c) the as-prepared, and (d) the acid treated/annealed PtNi/C catalysts. (d) X-ray diffraction (XRD) patterns for the PtNi/C catalysts in comparison with commercial Pt/C (~6 nm in particle size).

4.2.2 *As-synthesized PtNi nanoparticles*. The above studies of Pt thin films over PtNi substrate, as well as the knowledge previously acquired from poly-/single-crystalline surfaces[5–8] and nanocatalysts,[14,21,24] have led us to a novel approach toward the design and synthesis of Pt bimetallic catalysts with Pt terminated surfaces. The initial step in this approach should involve the synthesis of monodisperse and homogeneous PtNi NPs followed by intentional depletion of Ni from the surface, producing a skeleton type of surface structure. The final step is supposed to be the thermal treatment aimed to induce the transition from Pt-skeleton into Pt-skin type of structure by surface relaxation and restructuring. For that purpose, PtNi NPs were synthesized by simultaneous reduction of platinum acetylacetonate, $Pt(acac)_2$, and nickel acetate, $Ni(ac)_2$, in an organic solution (see the Experimental Section).[24,25] Figure 4-2a and b shows representative transmission electron microscopy (TEM) images of the as-synthesized PtNi NPsprepared with a molar ratio of 1:2 between the Pt and Ni precursors. The NP size was controlled to be ~5 nm[21] with a very narrow size distribution, as evidenced by the formation of various types of super lattices after drying the nanoparticle suspension (in hexane) under ambient conditions.[26] The final composition was characterized by energy-dispersive X-ray spectroscopy (EDX), which confirmed an atomic ratio of Pt/Ni ≈ 1/1 (Figure S4-3). The as-synthesized NPs were incorporated into carbon black (~900 m^2/g) via a colloidal-deposition method, and the organic surfactants were efficiently removed by thermal treatment.[21] Such as-prepared PtNi/C catalyst was first treated by acid to dissolve the surface Ni atoms[24] (Figure S4-3) and then annealed at 400 °C. These consecutive treatments were expected to bring on the Pt-skin type of surface over the substrate with

50% of Ni, which otherwise would not be possible because complete segregation of Pt only takes place in Pt_3M systems.[7] TEM images of the acid treated/annealed catalyst do not show notable changes in morphology (Figure 4-2c and d), except a slight decrease (~0.3 nm) in average particle size (Figures S4-4). Additionally, X-ray diffraction (XRD) analysis was used to characterize the crystal structure of the NPs. As compared to the commercial Pt/C catalyst (Tanaka, ~6 nm), both the as-prepared and the acid treated/annealed PtNi/Csystems show a face-centered cubic (fcc) pattern with noticeable shifts [e.g., ~1° for (111) peak] toward high angle (Figure 4-2e), corresponding to a decrease of lattice constant due to alloying between Pt and Ni.[27] The XRD pattern of the acid treated/annealed NPs has sharper peaks as compared to the as-prepared one, which indicates the increased crystallinity after annealing. These observations, in addition to the absence of peaks for separate Pt or Ni phases, show that the bimetallic catalyst preserved the alloy properties after the applied treatments.

The nanostructures and composition profiles of the PtNi/C catalysts were characterized by atomically resolved aberrationcorrected high angle annular dark field-scanning transmission electron microscopy (HAADF-STEM) in combination with energy dispersive X-ray spectroscopy (EDX). Figure 4-3a shows representative HAADF-STEM images taken along the [110] zone axis of the as-prepared (left), acid treated (middle), and acid treated/annealed (right) PtNi/C catalysts, with the intensity profiles along [001] directions across the single particles shown in Figure 4-3b. As compared to the benchmark intensity profiles calculated for ideal octahedral alloy NPs of the same size and orientation (see the Supporting Information), NP exposed to acid shows 3-4 peaks on each side stretching above the standards, indicating the formation of a Pt-rich overlayer.

This feature was preserved after annealing, but with 2-3 Pt-rich peaks on each side, corresponding to a reduced Pt overlayer thickness due to restructuring and smoothing (Figure 4-3b). These findings were further confirmed by EDX analysis. By scanning the e-beam across the particle while simultaneously analyzing the generated X-rays, composition line profiles were obtained for the NPs (Figure 4-3c). It can be seen that the distribution of Pt and Ni in the as-prepared catalyst was highly intermixed and the sketched trend lines were almost identical, indicating a homogeneous alloy nature of the catalyst particles. The treated catalysts have substantially broader distribution of Pt than Ni, with a difference of ~1 nm (at the half-maximum of the trend lines) for the acid treated and ~0.6 nm for the acid treated/annealed catalyst. Hence, both the intensity and the composition line profiles show that multilayered Pt-rich surface structure was formed by acid treatment and preserved after annealing.

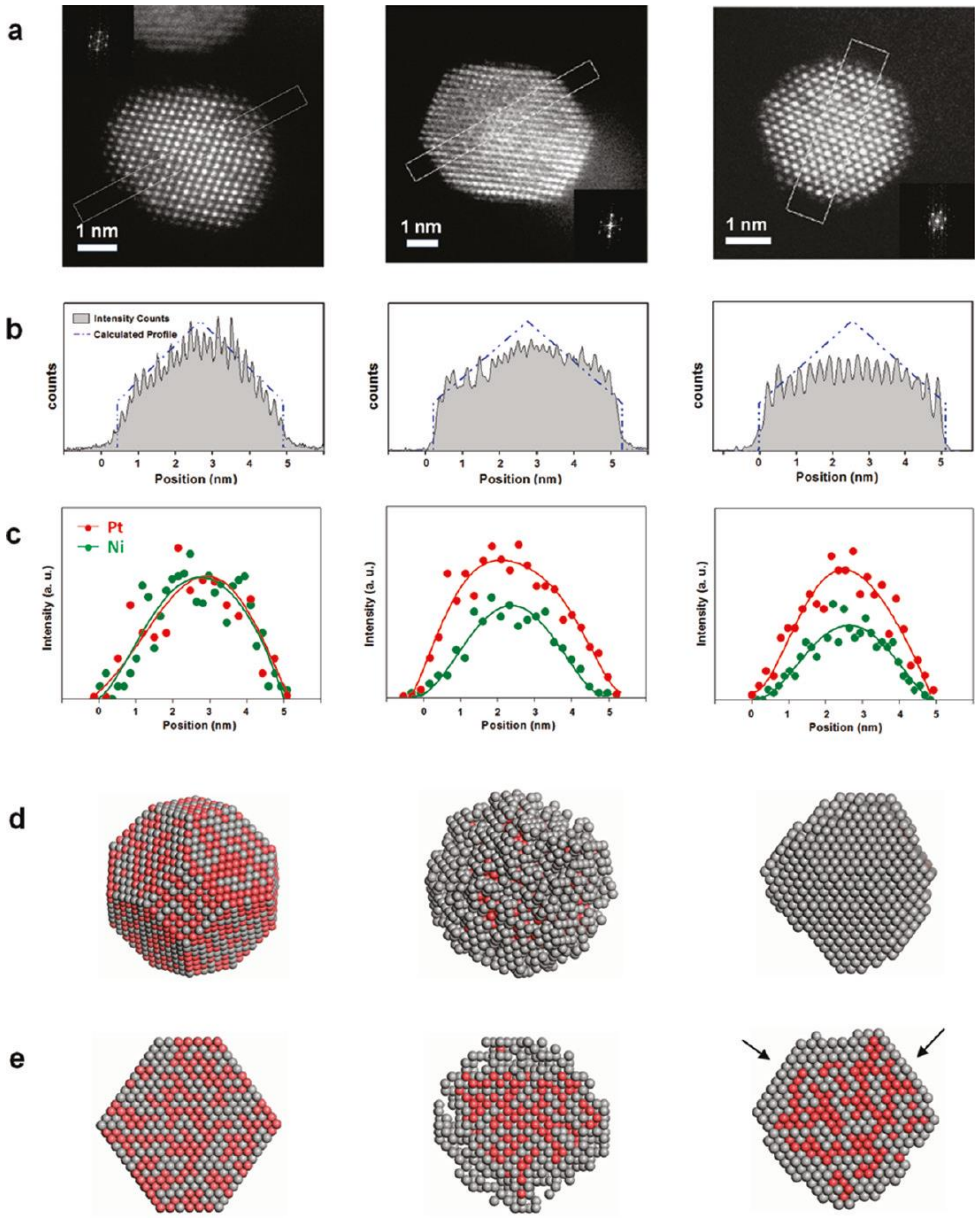

Figure 4-3. Microscopic characterization and theoretical simulation of nanostructure evolution in the PtNi/C catalysts: (a) Representative high-angle annular dark-field scanning transmission electron microscopy (HAADF-STEM) images taken along the zone axis [110], as confirmed by the fast Fourier transfer (FFT) patterns of the STEM images (shown as insets); (b) background subtracted, normalized intensity line profiles extracted for the regions marked in (a); (c) composition line profiles (normalized for PtL

peaks) obtained by energy-dispersive X-ray spectroscopy (EDX) with an electron beam (~2 Å in spot size) scanning across individual catalyst particles; (d) overview; and (e) cross-section views of the nanostructures depicted by atomistic particle simulation. The figure is also organized in columns for the as-prepared (left), acid treated (middle), and acid treated/annealed (right) PtNi/C catalysts, respectively.

The microscopic characterizations strongly point toward surface restructuring in the bimetallic catalyst upon annealing. This was additionally depicted by atomistic simulation of the nanostructure evolution subject to the acid and annealing treatments (Figure 4-3d for overviews and Figure 4-3e for cross-section views; see the Supporting Information for more details). It shows that removing Ni atoms from the surface led to the formation of a Pt-skeleton overlayer with a thickness of up to 3 atomic layers. Further relaxation of low-coordination surface atoms resulted in a multilayered Pt-skin surface, whereas the PtNi core was barely affected. It is important to mention that the relaxation process is expected to induce preferential formation of highly active (111) surface[8] (labeled by arrows in Figure 4-3e), due to the higher atomic coordination, that is, lower surface energy, of this facet as compared to others.

To gain more insights into the nanostructure evolution, especially the correlation of surface structures to their electrochemical properties, we have carried out in situ X-ray absorption near edge structure (XANES) studies of the nanocatalysts (see the Experimental Section and Supporting Information for details). Figure 4-4a and b shows the normalized XANES spectra collected at Ni K and Pt L_3 edges, under the ORR-relevant conditions (~1.0 V). As compared to the spectra of reference foils, Pt and Ni

edge positions were found to correspond to the bulk oxidation state of zero for both elements in the treated catalysts.[28] It is intriguing to see that the acid treated catalyst shows higher white line intensity than does the acid treated/annealed catalyst at the Ni edge, which is caused by the presence of a small amount of NiO underlying the highly corrugated Pt-skeleton surface morphology in the acid treated catalyst,[29,30] whereas subsurface Ni in the acid treated/annealed catalyst was well protected. The distinction in surface structure between the two treated catalysts is even more visible at the Pt edge, where a slightly lower white line intensity for the acid treated/annealed catalyst corresponds to a reduced amount of platinum oxides under the same conditions, and, more fundamentally, less oxophilic surface with larger average surface coordination number.[7,29,31–33] The findings from XANES provide additional evidence for the formation of surface relaxed multilayered Pt-skin in the acid treated/annealed catalyst and its superiority in protecting the inner Ni from leaching out.

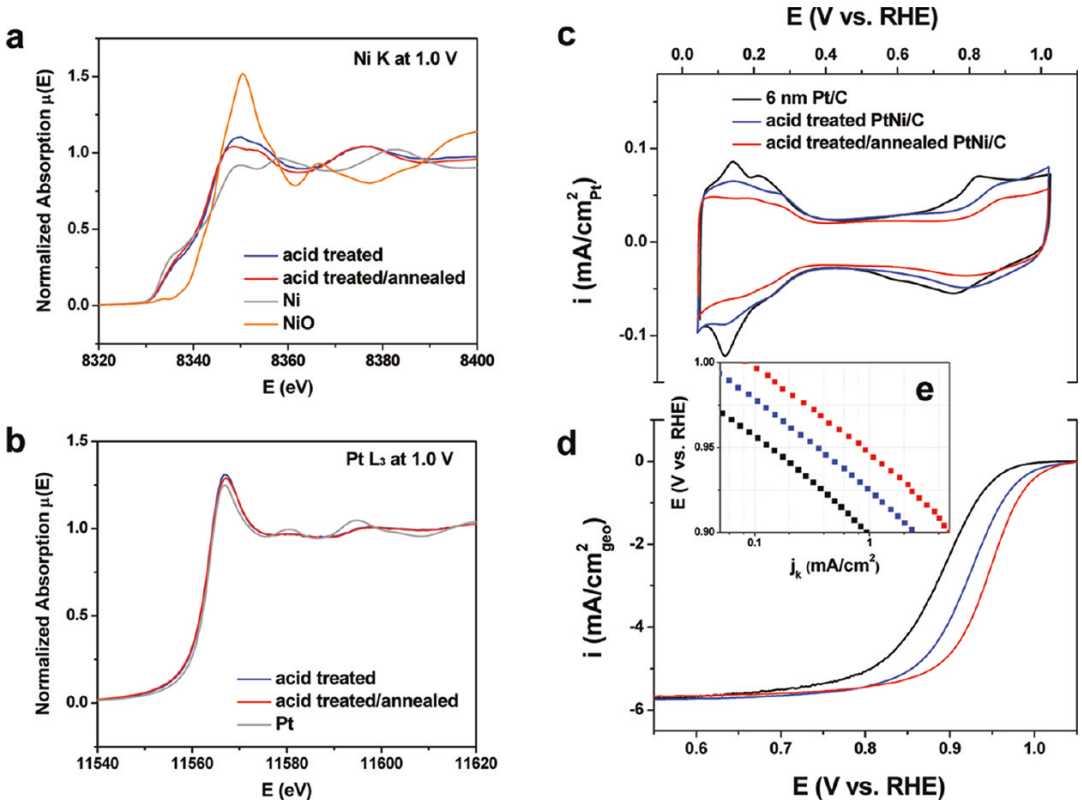

Figure 4-4. In situ X-ray absorption and electrochemical studies of the PtNi/C catalysts. (a,b) XANES spectra for the PtNi/C catalysts recorded at Ni K and Pt L_3 edges with an electrode potential of 1.0 V, in comparison with standard spectra of Ni, NiO, and Pt. (c) Cyclic voltammograms, (d) polarization curves, and (e) Tafel plots with the specific activity (j_k, kinetic current density) as a function of electrode potential, in comparison with the commercial Pt/C catalyst. Estimation of ECSA was based on integrated Hupd for the Pt/C and acid treated PtNi/C catalysts, and CO_{ad} stripping polarization curve for the acid treated/annealed PtNi/C catalyst.

On the basis of these results, we have managed to achieve the desirable nanoscale architecture established on PtNi supported Pt films, that is, multilayered Pt-skin over a

particle core with 50% of Ni. Considering what was revealed from the studies on extended surfaces, the obtained nanocatalyst should show superior catalytic performance for the ORR, which was examined by RDE measurements (see the Experimental Section). Figure 4c-e summarizes the electrochemical studies for the three types of nanocatalysts. It can be seen from the voltammograms (Figure 4-4c) that the H_{upd} region ($E < 0.4$ V) of the acid treated/annealed catalyst is largely suppressed versus the acid treated sample. On the positive side of the potential scale, the onset of oxide formation for the acid treated/annealed catalyst is shifted positively by about 20 mV versus that for the acid treated catalyst, and more than 50 mV with respect to Pt/C. Similar shifts are also seen for the reduction peaks in the cathodic scans. Such peak shifts are representative of a less oxophilic catalyst surface due to the formation of multilayered Pt-skin structure, and further corresponding to remarkable enhancement in the ORR activity as evidenced by the polarization curves shown in Figure 4-4d and the Tafel plots, Figure 4-4e. These findings are reminiscent of those on extended surfaces (Figure 4-1) and from in situ XANES studies (Figure 4-4b). At 0.95 V, the specific activity of the acid treated/annealed PtNi/C reaches 0.85 mA/cm^2, as compared to 0.35 mA/cm^2 for the acid treated specimen and 0.13 mA/cm^2 for Pt/C. This translates into improvement factors versus Pt/C of 3 and over 6 for the acid treated and acid treated/annealed PtNi/C catalysts, respectively, which is also in line with the results obtained on extended surfaces (Figure 4-1c). Therefore, the electrochemical studies of nanocatalysts validated that the scheme of the near surface architecture established on extended surfaces had been successfully applied to nanocatalysts by forming a multilayered Pt-skin surface. Remarkably, the ECSA of this catalyst obtained from integrated H_{upd} region was over

30% lower than that from CO stripping (Figure S4-2), which also confirms the formation of Pt-skin type of surface in the nanocatalyst.

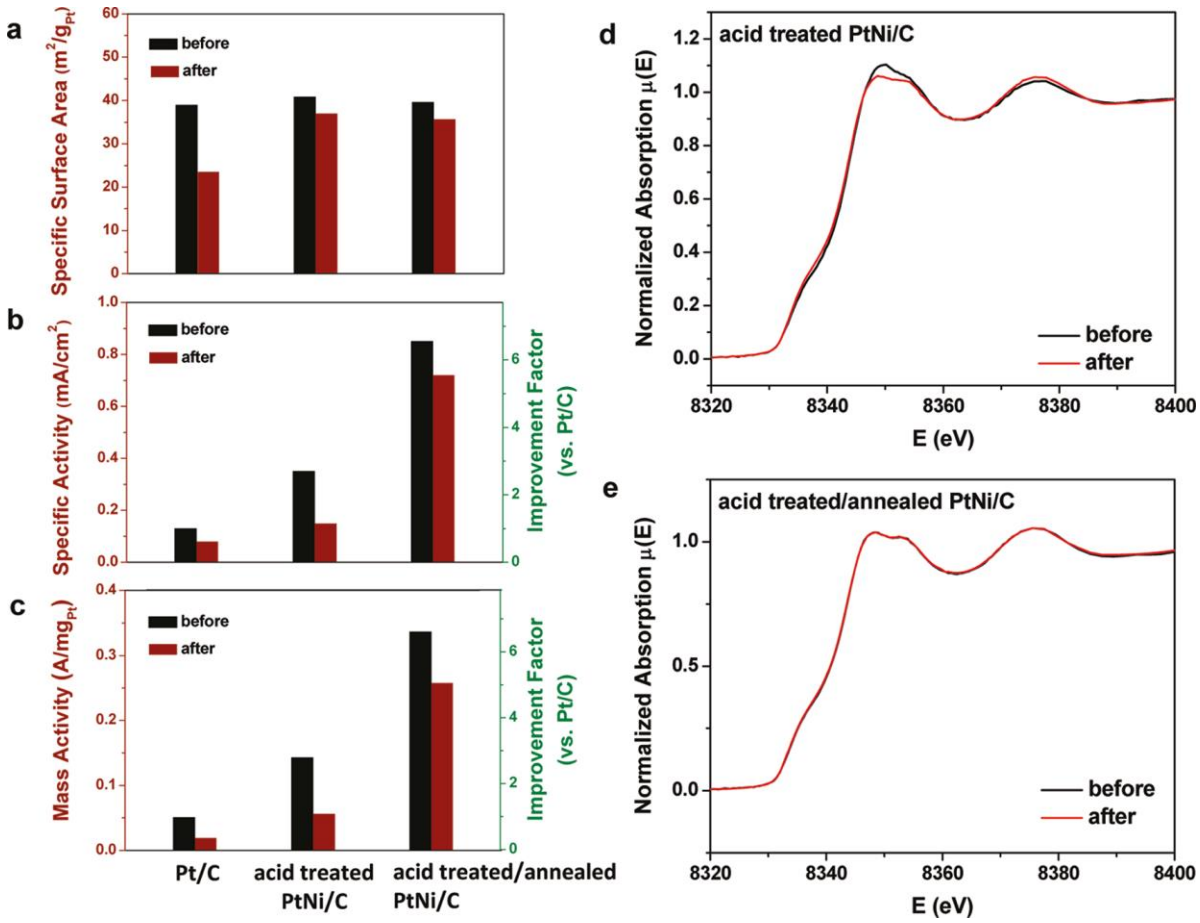

Figure 4-5. Summary of electrochemical durability studies obtained by RDE before and after 4000 potential cycles between 0.6 and 1.1 V for the Pt/C and PtNi/C catalysts in 0.1M $HClO_4$ at 0.95 V and 60 °C: (a) specific surface area, (b) specific activity, and (c) mass activity. Activity improvement factors versus Pt/C before and after cycling were also shown for specific and mass activities in (b) and (c). Parts (d) and (e) show the XANES spectra recorded for the acid treated and acid treated/annealed PtNi/C catalysts at Ni K edge, at 1.0 V before and after potential cycling. Estimation of ECSA was based

on integrated Hupd for the Pt/C and acid treated PtNi/C catalysts, and CO_{ad} stripping polarization curve for the acid treated/annealed PtNi/C catalyst.

Moreover, the developed Pt bimetallic catalyst with the unique nanoscale architecture does not only show enhanced catalytic activity, but also improved catalyst durability for the ORR. Figure 4-5 summarizes the electrochemical results for the PtNi/C catalysts before and after 4000 potential cycles between 0.6 and 1.1 V at 60 °C. Both the acid treated and the acid treated/ annealed PtNi/C catalysts had minor losses (~10%) in ECSA after cycling, in comparison to a substantial drop (~40%) for Pt/C (Figure 4-5a). An additional observation was that the acid treated/annealed PtNi/C had only 15% loss in specific activity, in contrast to 57% for the acid treated catalyst and 38% for Pt/C (Figure 4-5b). We have also applied in situ XANES to monitor the catalyst structures in the durability studies (Figure 4-5d and e, and more details in the Supporting Information). Not surprisingly, the acid treated/annealed PtNi/C does not show visible changes, whereas reduction of absorption at the Ni edge was observed for the acid treated PtNi/C during and after potential cycling. These findings are in line with the elemental analysis of the PtNi/C catalysts after the durability experiments, which indicate no loss for the Ni content in the acid treated/annealed catalyst in contrast to the significant loss of Ni in the acid treated catalyst (Figures S4-5). It is thus assured that the multilayered Pt-skin formation has indeed provided complete protection of the Ni inside the catalyst and enabled the sustained high catalytic activity under fuel cell operating conditions. On the basis of that, in addition to diminished number of vulnerable undercoordinated Pt surface atoms after annealing, multilayered Pt-skin formation is also thick enough to protect

subsurface Ni from dissolution that otherwise occurs through the place exchange mechanism[22] (Figures 4-5 and S4-5). At the same time, the multilayered Pt-skin is thin enough to maintain typical skin-like properties (discussed above), which originates from altered electronic structures due to the presence of a desirable amount of subsurface Ni. As a result, the PtNi/C catalyst with multilayered Pt-skin surfaces exhibited improvement factors in mass activity of more than one order of magnitude after elongated potential cycling versus the Pt/C catalyst (Figure 4-5c).

4.3 Summary

We have demonstrated the design and synthesis of an advanced Pt-bimetallic catalyst, which simultaneously achieves high catalytic activity and superior durability for the ORR. The developed catalyst contains unique nanoscale architecture with a PtNi core of 50 at% Ni and multilayered Pt-skin surfaces. This structure was built up through synergistic studies of extended surfaces and nanocatalysts, with critical parameters such as particle size, thermal treatment, particle sintering, alloy composition, and elemental composition profile integrally designed and optimized. Delicate structure-function correlation in the bimetallic electrocatalysts with composite nanostructures has been comprehensively resolved by employing state-of-the-art electron microscopy and in situ X-ray spectroscopy characterization. Our findings have immense implications for the development of heterogeneous catalysts and nanostructure engineering toward advanced functional materials.

4.4 Experimental Section

4.4.1 *Thin Film Preparation.* Pt films were deposited at room temperature on PtNi substrates (6 mm in diameter), which were set 125 mm away from DC sputter magnetrons in 4 mTorr argon gas (base vacuum 1_10_7 Torr). The Pt source rate (0.32 Å/s) was determined by quartz crystal microbalance, and an exposure duration of 7.0 s was calibrated for the nominal thickness of 2.2-2.3 Å for a monolayer of Pt. The film thickness was derived from the exposure time of computer-controlled shutters during sputtering.

4.4.2 *NP and Catalyst Synthesis.* In a typical synthesis of PtNi NPs, 0.67 mmol of $Ni(ac)_2 \bullet 4H_2O$ was dissolved in 20 mL of diphenyl either in the presence of 0.4 mL of oleylamine and 0.4 mL of oleic acid. 0.33 mmol of 1,2-tetradodecanediol was added, and the formed solution was heated to 80 °C under Ar flow. After a transparent solution formed, the temperature was further raised to 200 °C, where 0.33 mmol of $Pt(acac)_2$ dissolved in 1.5 mL of dichlorobenzene was injected. The solution was kept at this temperature for 1 h and then cooled to room temperature. An amount of 60 mL of ethanol was added to precipitate the NPs, and the product was collected by centrifuge (6000 rpm, 6 min). The obtained NPs were further washed by ethanol two times and then dispersed in hexane. The as-synthesized PtNi NPs were deposited on high surface area carbon (~900 m^2/g) by mixing the NPs with carbon black (Tanaka, KK) in hexane or chloroform with a 1:1 ratio in mass. This mixture was sonicated for 1 h and then dried under nitrogen flow.

The organic surfactants were removed by thermal treatment at 150-200 °C in an oxygenated atmosphere. The obtained catalyst is denoted as "as-prepared PtNi/C". For the acid treatment, ~10 mg of the as-prepared PtNi/C catalyst was mixed with 20 mL of 0.1M $HClO_4$ that has been used as electrolyte in electrochemical measurements. After overnight exposure to the acidic environment, the product was collected by centrifuge and washed three times by deionized water. Such NPs are named as "acid treated PtNi/C". The acid treated PtNi/C was further annealed at 400 °C to reduce low-coordinated surface sites, and the obtained catalyst is termed as "acid treated/annealed PtNi/C".

4.4.3 *Microscopic Characterization*. TEM images were collected on a PhilipsEM30 (200 kV) equipped with EDX functionality. XRD patterns were collected on a Rigaku RTP 300 RC machine. STEM and elemental analysis were carried out on a JEOL 2200FS TEM/STEM with a CEOS aberration (probe) corrector. The microscope was operated at 200 kV in HAADF-STEM mode equipped with a Bruker-AXS X-Flash 5030 silicon drift detector. The probe size was ~0.7 Å and the probe current was ~30 pA during HAADF-STEM imaging. When accumulating EDX data, the probe current was increased to ~280 pA and the probe size was ~2 Å. The presented EDX data were confirmed to be from "e-beam damage-free" particles by comparing STEM images before and after EDX acquisition.

4.4.4 *X-ray Absorption Spectroscopy*. X-ray fluorescence spectra of at the Ni K and Pt L3 edges were acquired at bending magnet beamline 12-BM-B at the Advanced Photon Source (APS), Argonne National Laboratory. The incident radiation was filtered by a Si(111) double-crystal monochromator (energy resolution $\Delta E/E = 14.1 \times 10^{-5}$) with a

double mirror system for focusing and harmonic rejection.[34] All of the data were taken in fluorescence mode using a 13-element Germanium array detector (Canberra), which was aligned with the polarization of the X-ray beam to minimize the elastic scattering intensity. Co and Ge filters (of 6 absorption length in thickness) were applied in front of the detector to further reduce the elastic scattering intensity for the Ni K and Pt L_3 edges, respectively. The Ni K and Pt L_3 edge spectra were calibrated by defining the zero crossing point of the second derivative of the XANES spectra for Ni and Pt reference foils as 8333 and 11564 eV, respectively. The background was subtracted using the AUTOBK algorithm,[35] and data reduction was performed using Athena from the IFEFFIT software suite.[36,37] A scheme of the homemade in situ electrochemical cell and setup at beamline was shown in the Supporting Information, Figure S4-9.

4.4.5 *Electrochemical Characterization*. The electrochemical measurements were conducted in a three-compartment electrochemical cell with a rotational disk electrode (RDE, 6 mm in diameter) setup (Pine) and a Autolab 302 potentiostat. A saturated Ag/AgCl electrode and a Pt wire were used as reference and counter electrodes, respectively. 0.1 M $HClO_4$ was used as electrolyte. The catalysts were deposited on glassy carbon electrode substrate and dried in Ar atmosphere without using any ionomer. The loading was controlled to be 12 $\mu g_{Pt}/cm^2_{disk}$ for PtNi/C nanocatalysts. All of the potentials given in the discussion were against reversible hydrogen electrode (RHE), and the readout currents were recorded with ohmic iR drop correction during the measurements.[38,39]

4.5 References

(1) Vielstich, W.; Lamm, A.; Hubert A., G. *A. Handbook of Fuel Cells: Fundamentals, Technology And Applications*; Willey.

(2) Abraham, K. M.; Jiang, Z. *J. Electrochem. Soc.* **1996**, *143*, 1–5.

(3) Armand, M.; Tarascon, J.-M. *Nature* **2008**, *451*, 652–657.

(4) Gasteiger, H. A.; Kocha, S. S.; Sompalli, B.; Wagner, F. T. *Applied Catalysis B: Environmental* **2005**, *56*, 9–35.

(5) Stamenkovic, V.; Mun, B. S.; Mayrhofer, K. J. J.; Ross, P. N.; Markovic, N. M.; Rossmeisl, J.; Greeley, J.; Nørskov, J. K. *Angewandte Chemie International Edition* **2006**, *45*, 2897–2901.

(6) Stamenkovic, V. R.; Mun, B. S.; Arenz, M.; Mayrhofer, K. J. J.; Lucas, C. A.; Wang, G.; Ross, P. N.; Markovic, N. M. *Nat Mater* **2007**, *6*, 241–247.

(7) Stamenkovic, V. R.; Mun, B. S.; Mayrhofer, K. J. J.; Ross, P. N.; Markovic, N. M. *J. Am. Chem. Soc.* **2006**, *128*, 8813–8819.

(8) Stamenkovic, V. R.; Fowler, B.; Mun, B. S.; Wang, G.; Ross, P. N.; Lucas, C. A.; Marković, N. M. *Science* **2007**, *315*, 493–497.

(9) Mani, P.; Srivastava, R.; Strasser, P. *J. Phys. Chem. C* **2008**, *112*, 2770–2778.

(10) Chen, S.; Sheng, W.; Yabuuchi, N.; Ferreira, P. J.; Allard, L. F.; Shao-Horn, Y. *J. Phys. Chem. C* **2009**, *113*, 1109–1125.

(11) Chen, J.; Lim, B.; Lee, E. P.; Xia, Y. *Nano Today* **2009**, *4*, 81–95.

(12) Zhang, J.; Yang, H.; Fang, J.; Zou, S. *Nano Lett.* **2010**, *10*, 638–644.

(13) Strasser, P.; Koh, S.; Anniyev, T.; Greeley, J.; More, K.; Yu, C.; Liu, Z.; Kaya, S.; Nordlund, D.; Ogasawara, H.; Toney, M. F.; Nilsson, A. *Nat Chem* **2010**, *2*, 454–460.

(14) Wang, C.; Wang, G.; Vliet, D. van der; Chang, K.-C.; Markovic, N. M.; Stamenkovic, V. R. *Phys. Chem. Chem. Phys.* **2010**, *12*, 6933–6939.

(15) Schulenburg, H.; Müller, E.; Khelashvili, G.; Roser, T.; Bönnemann, H.; Wokaun, A.; Scherer, G. G. *J. Phys. Chem. C* **2009**, *113*, 4069–4077.

(16) Van Hardeveld, R.; Hartog, F. *Surface Science* **1969**, *15*, 189–230.

(17) Kinoshita, K. *J. Electrochem. Soc.* **1990**, *137*, 845–848.

(18) Han, B. C.; Miranda, C. R.; Ceder, G. *Phys. Rev. B* **2008**, *77*, 075410.

(19) Strmcnik, D. S.; Tripkovic, D. V.; Van der Vliet, D.; Chang, K.-C.; Komanicky, V.; You, H.; Karapetrov, G.; Greeley, J. P.; Stamenkovic, V. R.; Marković, N. M. *J. Am. Chem. Soc.* **2008**, *130*, 15332–15339.

(20) Mayrhofer, K. J. J.; Blizanac, B. B.; Arenz, M.; Stamenkovic, V. R.; Ross, P. N.; Markovic, N. M. *J. Phys. Chem. B* **2005**, *109*, 14433–14440.

(21) Wang, C.; Van der Vliet, D.; Chang, K.-C.; You, H.; Strmcnik, D.; Schlueter, J. A.; Markovic, N. M.; Stamenkovic, V. R. *J. Phys. Chem. C* **2009**, *113*, 19365–19368.

(22) Komanicky, V.; Chang, K. C.; Menzel, A.; Markovic, N. M.; You, H.; Wang, X.; Myers, D. *J. Electrochem. Soc.* **2006**, *153*, B446–B451.

(23) Borup, R.; Meyers, J.; Pivovar, B.; Kim, Y. S.; Mukundan, R.; Garland, N.; Myers, D.; Wilson, M.; Garzon, F.; Wood, D.; Zelenay, P.; More, K.; Stroh, K.; Zawodzinski, T.; Boncella, J.; McGrath, J. E.; Inaba, M.; Miyatake, K.; Hori, M.; Ota, K.; Ogumi, Z.; Miyata, S.; Nishikata, A.; Siroma, Z.; Uchimoto, Y.; Yasuda, K.; Kimijima, K.; Iwashita, N. *Chem. Rev.* **2007**, *107*, 3904–3951.

(24) Wang, C.; Chi, M.; Wang, G.; Van der Vliet, D.; Li, D.; More, K.; Wang, H.-H.; Schlueter, J. A.; Markovic, N. M.; Stamenkovic, V. R. *Adv. Funct. Mater.* **2011**, *21*, 147–152.

(25) Ahrenstorf, K.; Heller, H.; Kornowski, A.; Broekaert, J. A. C.; Weller, H. *Adv. Funct. Mater.* **2008**, *18*, 3850–3856.

(26) Kiely, C. J.; Fink, J.; Brust, M.; Bethell, D.; Schiffrin, D. J. *Nature* **1998**, *396*, 444–446.

(27) Li, Y.; Zhang, X. L.; Qiu, R.; Qiao, R.; Kang, Y. S. *J. Phys. Chem. C* **2007**, *111*, 10747–10750.

(28) Bunker, G. *Introduction to XAFS: A Practical Guide to X-ray Absorption Fine Structure Spectroscopy*; Cambridge University Press.

(29) Mukerjee, S.; Srinivasan, S.; Soriaga, M. P.; McBreen, J. *J. Electrochem. Soc.* **1995**, *142*, 1409–1422.

(30) Rodriguez, J. A.; Hanson, J. C.; Frenkel, A. I.; Kim, J. Y.; Pérez, M. *J. Am. Chem. Soc.* **2002**, *124*, 346–354.

(31) Imai, H.; Izumi, K.; Matsumoto, M.; Kubo, Y.; Kato, K.; Imai, Y. *J. Am. Chem. Soc.* **2009**, *131*, 6293–6300.

(32) Friebel, D.; Miller, D. J.; O'Grady, C. P.; Anniyev, T.; Bargar, J.; Bergmann, U.; Ogasawara, H.; Wikfeldt, K. T.; Pettersson, L. G. M.; Nilsson, A. *Phys. Chem. Chem. Phys.* **2010**, *13*, 262–266.

(33) Russell, A. E.; Rose, A. *Chem. Rev.* **2004**, *104*, 4613–4636.

(34) Beno, M. A.; Engbretson, M.; Jennings, G.; Knapp, G. S.; Linton, J.; Kurtz, C.; Rütt, U.; Montano, P. A. *Nuclear Instruments and Methods in Physics Research Section*

A: Accelerators, Spectrometers, Detectors and Associated Equipment **2001**, *467–468, Part 1*, 699–702.

(35) Newville, M.; Līviņš, P.; Yacoby, Y.; Rehr, J. J.; Stern, E. A. *Phys. Rev. B* **1993**, *47*, 14126–14131.

(36) Newville, M. *Journal of Synchrotron Radiation* **2001**, *8*, 322–324.

(37) Ravel, B.; Newville, M. *Journal of Synchrotron Radiation* **2005**, *12*, 537–541.

(38) Newman, J. *J. Electrochem. Soc.* **1966**, *113*, 501–502.

(39) Van der Vliet, D.; Strmcnik, D. S.; Wang, C.; Stamenkovic, V. R.; Markovic, N. M.; Koper, M. T. M. *Journal of Electroanalytical Chemistry* **2010**, *647*, 29–34.

4.6 Supporting Information

4.6.1. *Material Characterization and Electrochemical Studies*

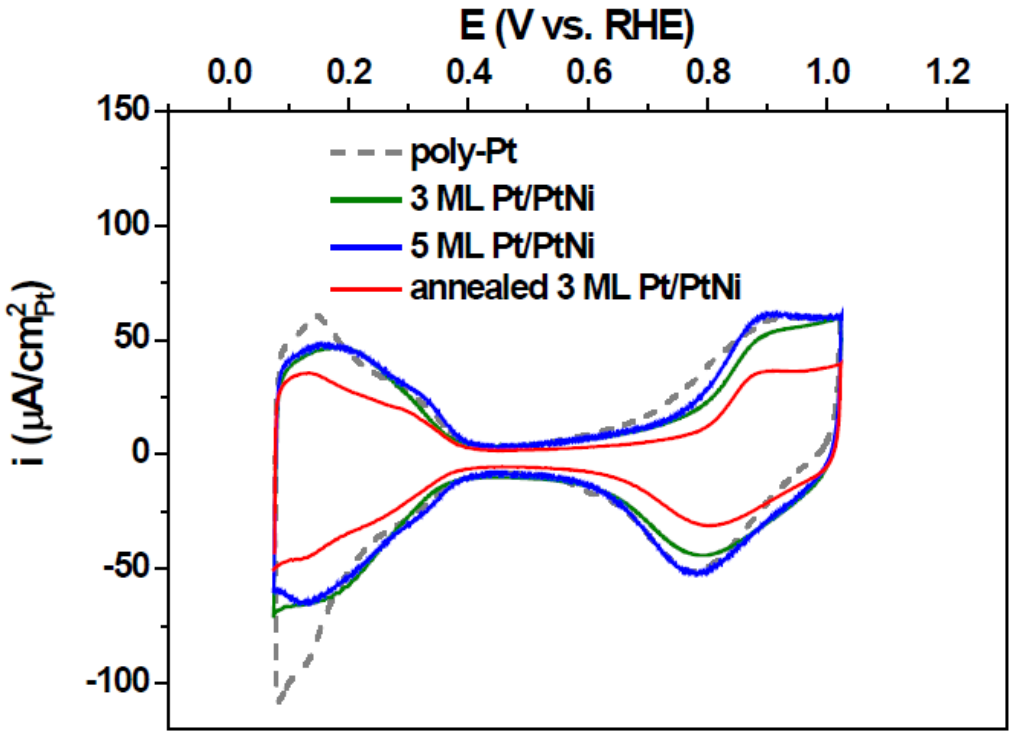

Figure S4-1. Cyclic voltammetries of the Pt/PtNi films of various thicknesses with current normalized by the ECSAs. The ECSAs were estimated from integrated H_{upd}, except that for the annealed 3ML Pt/PtNi surface which was based on integrated CO_{ad} stripping polarization curve. Cyclic voltammetries were recorded in Ar saturated 0.1 M $HClO_4$ electrolyte with a sweep rate of 50 mV/s.

The onset of Pt-OH_{ad} formation for the Pt/PtNi films shows anodic shifts (e.g., ~30 mV for 3 ML Pt) versus polycrystalline Pt surface (poly-Pt). Similar shifts are also seen for

the reduction peaks in the cathodic scans. Such shifts correspond to altered electronic/adsorption properties of the surface and they are in line with substantial improvement in ORR catalytic activity.[1]

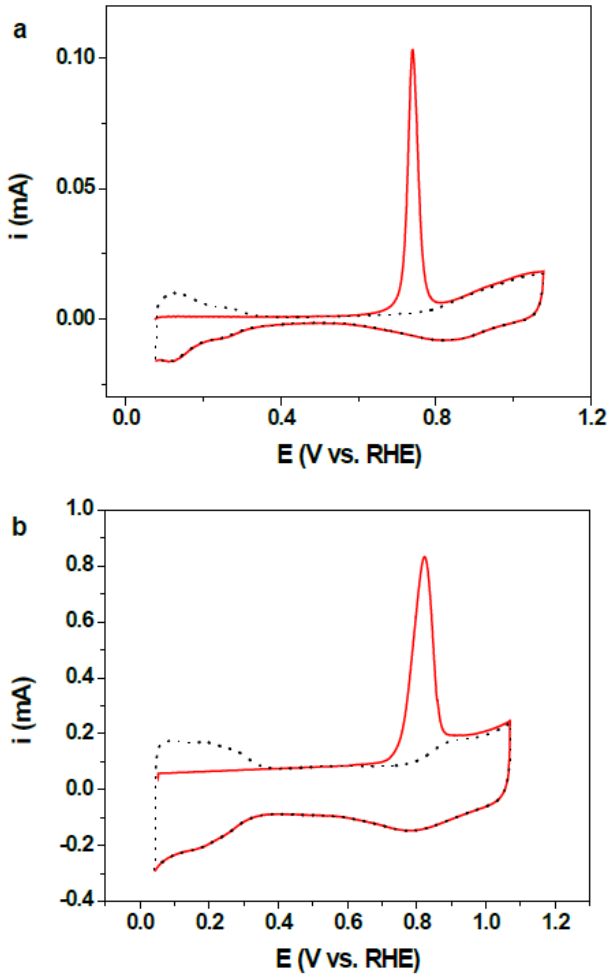

Figure S4-2. Representative CO stripping curves recorded for electrochemical oxidation of adsorbed CO monolayer obtained from RDE in hanging meniscus configuration in 0.1M $HClO_4$ on (a) 400 °C annealed 3 ML Pt/PtNi film and (b) acid treated/annealed PtNi/C. The following up scans for blank CV are also shown for comparison. The charge calculated by integration of the area under the CO stripping peak was used to estimate

ECSA in order to diminish the underestimation from H_{upd} due to the altered electronic/adsorption properties of Pt-skin surface.

Integrated charges can be translated into surface area based on assumption that 1 cm^2 of polycrystalline Pt surface corresponds to ~210 μC in case of one electron process (~420 μC for two electron process). For Pt surfaces, the surface area estimated from integrated polarization curves of underpotentially adsorbed hydrogen Hupd and electrooxidized CO_{ad} monolayer should be the same. However, in the case of bimetallic alloys with Pt-skin type of surfaces, adsorption of H_{upd} can be greatly suppressed by altered electronic properties of Pt-skin surfaces, and therefore, the H_{upd} surface coverage is much lower, while estimated surface area is underestimated and inaccurate.[1] Contrary to that, CO adsorption is not affected due to the strong Pt-CO interaction, and the estimation based on integrated CO stripping curve provides more accurate values for surface area. In the figure above, the ECSA of annealed 3 ML of Pt over PtNi substrate was estimated from CO stripping and H_{upd} polarization curves and obtained values are 0.18 and 0.12 cm^2, respectively. The substantially reduced ECSA (~33%) based on H_{upd} vs. CO_{ad} is indicative of the formation of Pt-skin type of surface, which was not observed on unannealed thin film surfaces. Similar findings were also obtained for the acid treated/annealed PtNi/C catalyst, but not for the Pt/C and acid treated PtNi/C catalysts. This approach should be used not only to get accurate surface area, but also as a proof for the formation of Pt-skin type of surface over Pt-bimetallic system.

	Pt/C		acid treated PtNi/C		acid treated/annealed PtNi/C	
	H_{upd}	CO_{ad}	H_{upd}	CO_{ad}	H_{upd}	CO_{ad}
C (μC)	277	542	292	613	193	563
ECSA (cm^2)	1.3	1.3	1.4	1.5	0.9	1.3

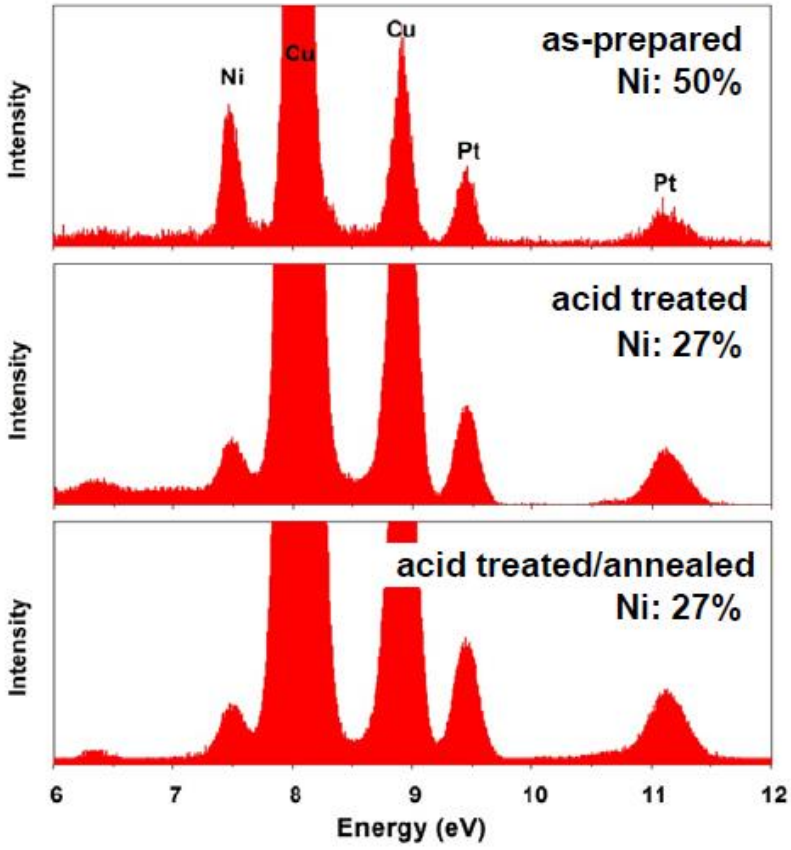

Figure S4-3. EDX spectra for the as-prepared, acid leached and acid leached/annealed PtNi/C catalysts, respectively.

These spectra were collected on a Philips EM 30 (200 kV) equipped with EDX functionality. A large assembly (a few hundred) of nanoparticles/catalyst particles was analyzed. The overall ratio of Ni was determined to be 50%, 27%, and 27% in the three PtNi/C catalysts, respectively. The decrease of Ni content was due to the depletion of Ni from near-surface layers by acid treatment. It is important to emphasize that the content of Ni in the center of the particles, however, remains unchanged (~50%) after the treatments.

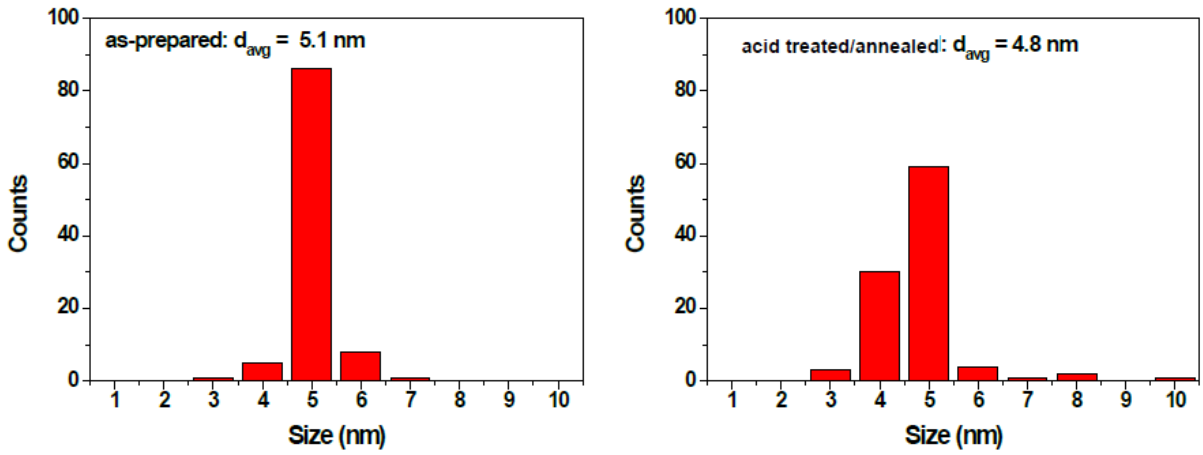

Figure S4-4. Statistical results of the particle sizes for the as-prepared and acid leached/annealed PtNi/C catalysts. Particle sizes were obtained by counting 100 nanoparticles from representative TEM images.

The average particle size decreased by 0.3 nm after the acid and annealing treatments. This was due to the depletion of surface Ni by acid treatment and subsequent surface relaxation/smoothening by annealing (see the following Theory and Simulation section). It has to point out, that the applied treatments, in particular annealing at the moderate temperature (400 °C) did not induce agglomeration of the catalyst particles. Remarkably, both the as-prepared and treated catalysts show monodisprse particle size distribution. The consistent control in particle size has enabled the systematic study of electrocatalytic properties of the bimetallic catalysts with particle size effect[2–4] excluded.

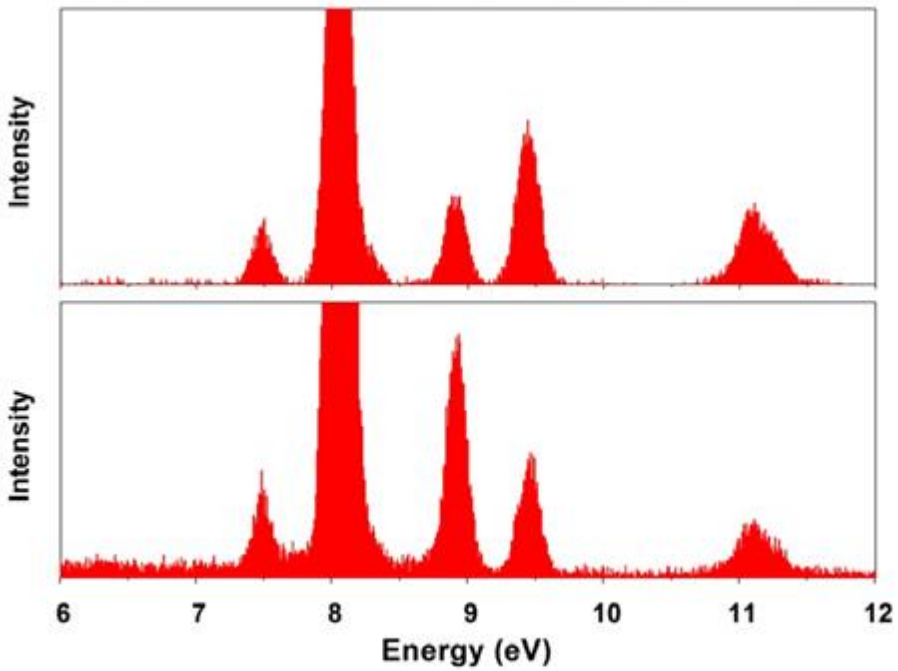

Figure S4-5. EDX spectra for the acid leached and acid leached/annealed PtNi/carbon catalysts after the durability studies (4,000 cycles between 0.6 and 1.1 V at 60 °C).

It is shown that 23% Ni (overall composition in the catalyst) was left in the acid leached/annealed catalyst, versus only 13% for the acid leached one. Compared with the same initial Ni content (~27%) in these two catalysts, these results demonstrated the substantially improved durability of the bimetallic catalyst after additional annealing treatment which had the multilayered Pt-skin formed to protect the subsurface Ni from leaching out.

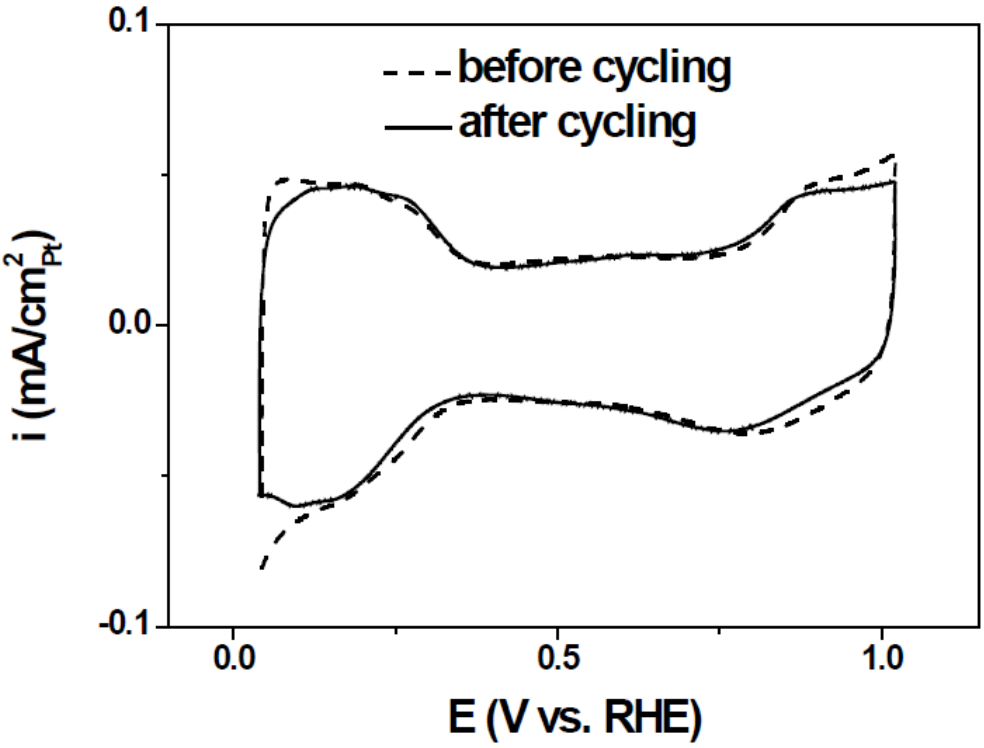

Figure S4-6. CVs of the acid treated/annealed PtNi/C catalyst before and after potentially cycling.

4.6.2. *STEM Analysis*

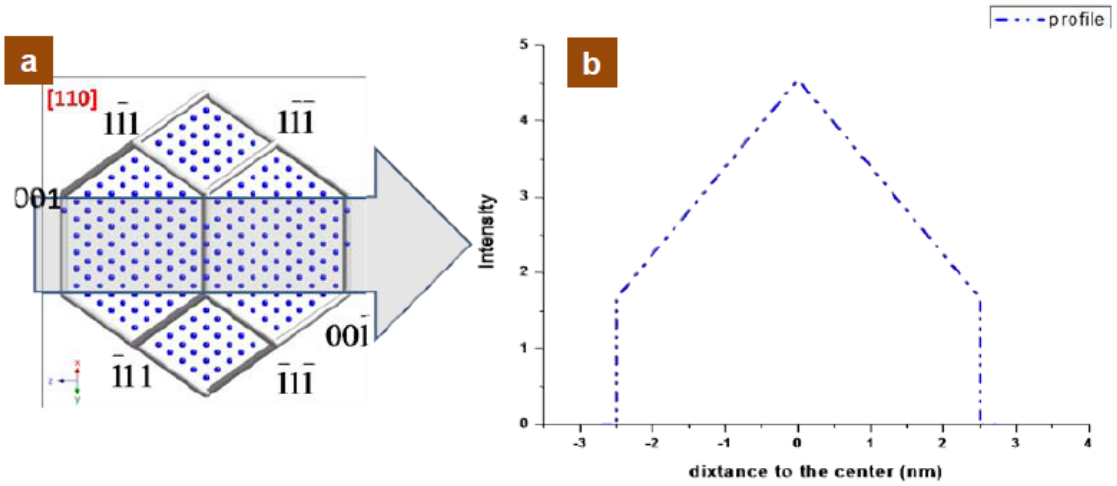

Figure S4-7. (a) Schematic illustration of a cubo-octahedral particle viewed along [110], and (b) is the ideal thickness profile along the arrow direction.

According to the geometry of the cubo-octahedron, the thickness profile along [001] direction while crossing the two edge-on (001) surfaces (shown as the shadowed arrow in Fig. S4-7a) should follow the equation:

$$y = \frac{D}{3} + \frac{\sqrt{3}}{3}D - \frac{2}{\sqrt{3}}|x|$$

where x≤ D/2. Here we define the diameter of the particle D is the interval between surface (001) and $(00\bar{1})$, y is the thickness, and x is the distance to the center along [001]. The line profiles calculated in this way does not count the contrast between Pt and Ni, and thus can be viewed as the intensity profiles for homogeneous alloy NPs.

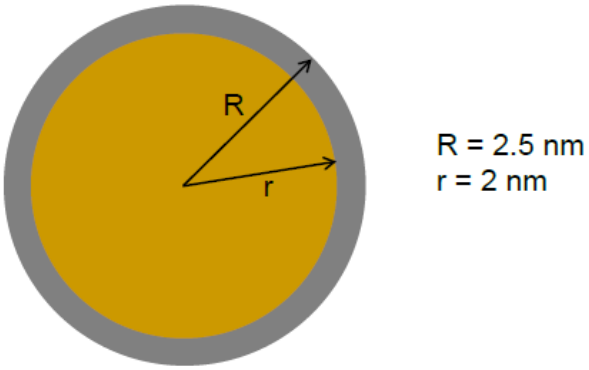

Both intensity and composition line profiles revealed a Pt-overlayer thickness of ~2 atomic layers in the acid treated/annealed PtNi/C catalyst particles (Fig. 4-3 in the text). This corresponds to a S10 multilayered Pt-skin of ~0.5 nm thick. Considering an ideal model of the Pt/PtNi particle (5 nm in diameter, see the structure illustrated on the left), it is also plausible to deduce through calculation that the central part (~4 nm in diameter) of the particle preserved ~50% of Ni after the treatments.

The amount of Ni in the particle can be written as

$$N_{Ni} = N_{total} C_{Ni,overal}$$

where Ntotal and $C_{Ni,\ overall}$ are the total number of atoms and overall ratio of Ni in the particle. From EDX analysis we have known that $C_{Ni,\ overall}$ is about 27%. Since the Pt-skin does not contribute any Ni, NNi can also be expressed as

$$N_{Ni} = N_{center} C_{Ni,center}$$

The numbers of atoms (N_{total} and N_{center}) are proportional to the volumes (V_{total} and V_{center}), respectively. For fcc crystals each unit cell contains 4 atoms, we write

$$N_{center} = 4V_{center}/a_{PtNi}^3$$

$$N_{total} = 4V_{skin}/a_{Pt}^3 + 4V_{center}/a_{PtNi}^3$$

where a_{Pt} and a_{PtNi} are the lattice parameter for the unit cells of Pt and PtNi, respectively. Due to the rather small difference between a_{Pt} and a_{PtNi}, we treat $a_{Pt} = a_{PtNi} = a$ for simplicity and write

$$N_{center} = 4V_{center}/a^3$$

$$N_{total} = 4V_{skin}/a^3 + 4V_{center}/a^3 = 4V_{total}/a^3$$

Combining above equations we obtain

$$4V_{total}/a^3 \bullet C_{Ni,overal} = 4V_{center}/a^3 \bullet C_{Ni,center}$$

and

$$C_{Ni,center} = \frac{V_{total}}{V_{center}} \bullet C_{Ni,overal} = (\frac{R}{r})^3 \bullet C_{Ni,overal} = (\frac{2.5}{2})^3 \bullet 27\% \approx 53\%$$

This result is also consistent with that obtained from atomistic simulation in the following.

4.6.3 *Theory and Simulation*

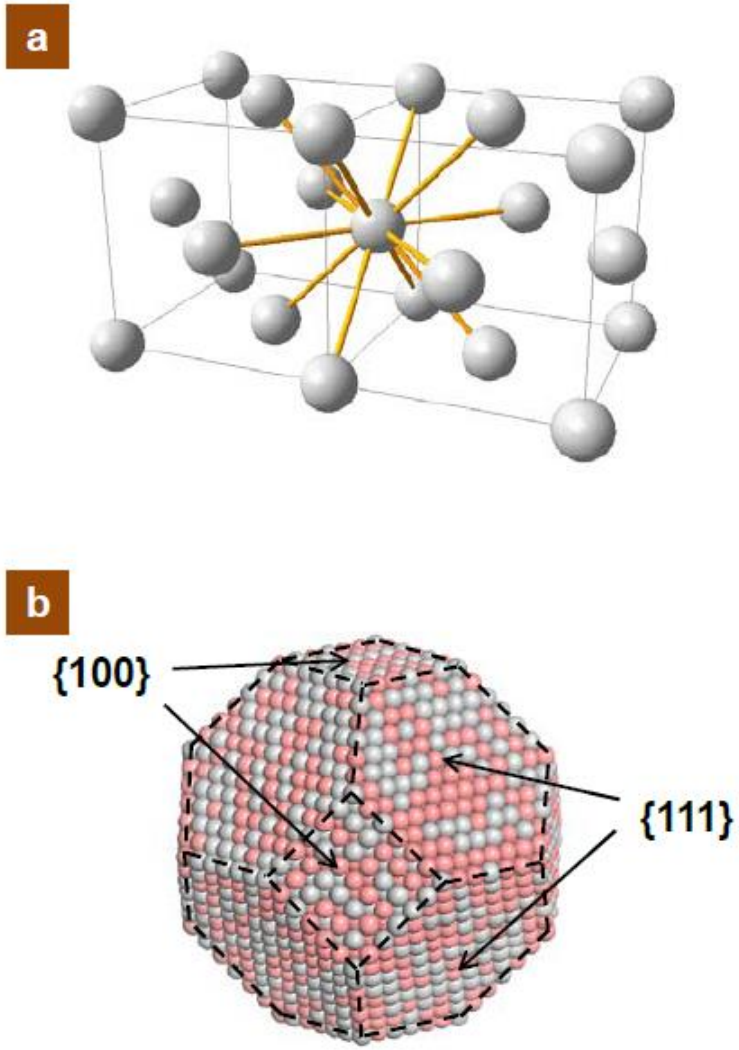

Figure S4-8. Illustration of (a) fcc lattice structure showing the coordination number of 12 for each atom, and (b) a perfect fcc cubo-octahedral PtNi nanoparticle with Pt and Ni randomly distributed. Edges are marked by dashed lines, while {111} and {100} facets are labeled by arrows in (b).

In the simulation of particle structure, a perfect cubo-octahedral PtNi alloy nanoparticle (containing 4033 atoms) with a face-centered cubic (fcc) lattice and a diameter of 4.99 nm was constructed at first. In this $Pt_{50}Ni_{50}$ model particle, 2017 Pt atoms and 2016 Ni atoms were randomly distributed. Surface atoms in this cubo-octahedral nanoparticle refer to those atoms with coordination number less than or equal to 9. We made this definition based on the fact that the atoms inside a cubo-octahedral particle of fcc phase have a coordination number of 12 while the atoms on the surface have coordination numbers of 9 on {111} facets, 8 on {100} facets, 7 at edges, and 6 at vertices.[5]

To simulate the acid leaching process, we iteratively removed all the Ni surface atoms from the particle until the coordination number of all the remaining Ni atoms were larger than 9. With leaching out Ni surface atoms, the Pt surface atoms have lowering coordination numbers. We further relocated the low-coordinated Pt atoms to the high-coordinated vacancies left by the removed Ni atoms for minimizing the total energy of the PtNi particle. In the resultant particle (Fig. 4-3 in text), all the Ni atoms have coordination number larger than 9 and all the Pt atoms have coordination number larger than 6. Our simulation shows that the final particle had 2017 Pt atoms and 822 Ni atoms (namely, overall Pt concentration of ~71.0 at.%) and a size of about 4.76 nm (4.7 % reduction in size compared with the initial particle). It is also found that the resulted particle core possesses a nearly unaltered composition of Pt/Ni ≈ 1/1 (ref 6) and a Pt-overlayer of an average thickness of 2 atomic layers.

4.6.4. *X-ray Absorption Spectroscopy*

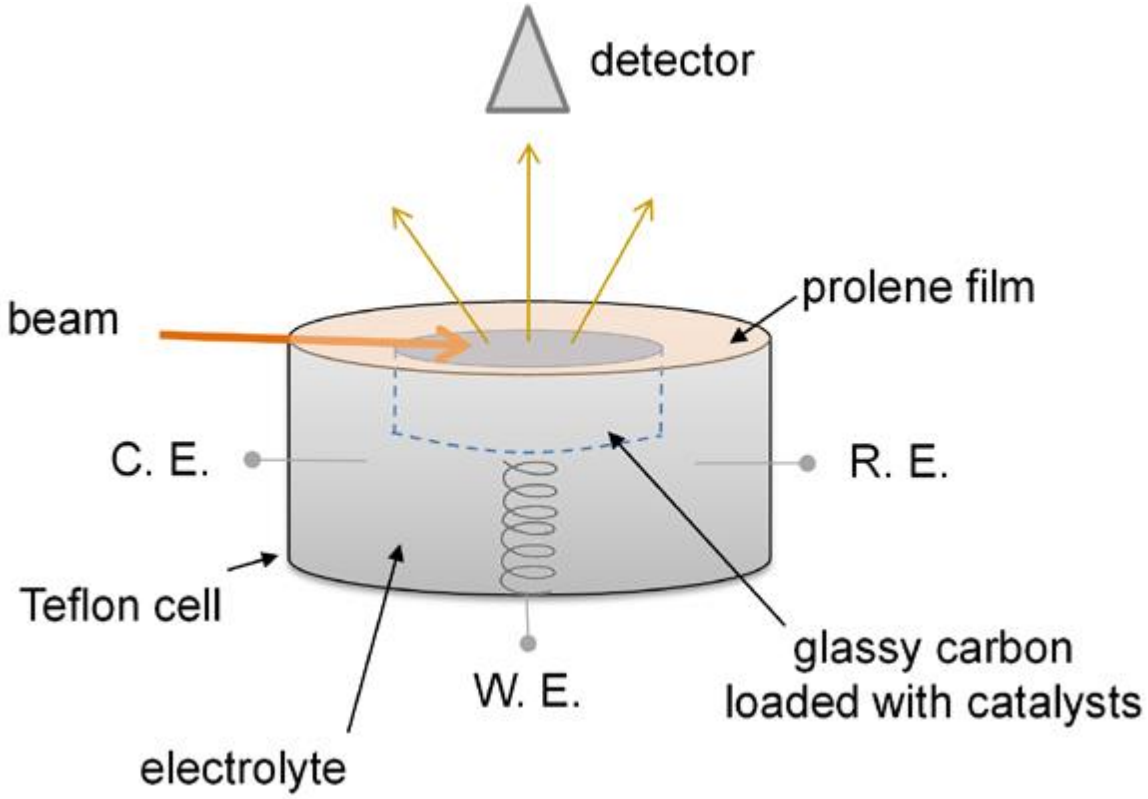

Figure S4-9. The electrochemical cell setup for *in situ* XAS

Catalysts were loaded on a glassy carbon disk which served as the working electrode in a home-made *in situ* electrochemical cell (Fig. S4-9). A saturated Ag/AgCl electrode and a Pt wire were used as reference and counter electrodes, respectively. 0.1M $HClO_4$ with oxygen removed by Ar bubbling was used as electrolyte. The cell was sealed by a prolene film and further wrapped by a plastic bag which was continuously filled in with nitrogen (or oxygen for durability studies) to control the gaseous conditions inside the cell. The X-

ray beam was set to glancing incidence to the working electrode surface to maximize fluorescence and minimize elastic scattering.

References

(1) Stamenkovic, V. R.; Fowler, B.; Mun, B. S.; Wang, G.; Ross, P. N.; Lucas, C. A.; Marković, N. M. *Science* **2007**, *315*, 493–497.

(2) Kinoshita, K. *J. Electrochem. Soc.* **1990**, *137*, 845–848.

(3) Mayrhofer, K. J. J.; Blizanac, B. B.; Arenz, M.; Stamenkovic, V. R.; Ross, P. N.; Markovic, N. M. *J. Phys. Chem. B* **2005**, *109*, 14433–14440.

(4) Wang, C.; Van der Vliet, D.; Chang, K.-C.; You, H.; Strmcnik, D.; Schlueter, J. A.; Markovic, N. M.; Stamenkovic, V. R. *J. Phys. Chem. C* **2009**, *113*, 19365–19368.

(5) Wang, G.; Hove, M. A. V.; Ross, P. N.; Baskes, M. I. *The Journal of Chemical Physics* **2004**, *122*, 024706.

(6) Wang, C.; Chi, M.; Wang, G.; Van der Vliet, D.; Li, D.; More, K.; Wang, H.-H.; Schlueter, J. A.; Markovic, N. M.; Stamenkovic, V. R. *Adv. Funct. Mater.* **2011**, *21*, 147–152.

V. Rational Development of Ternary Alloy Electrocatalysts

5.1 Introduction

Highly efficient catalysts for the oxygen reduction reaction (ORR) have been studied for the development of renewable energy technologies such as fuel cells[1] and metal− air batteries.[2,3] The current state-of-the-art electrocatalyst for this reaction is Pt in the form of nanoparticles (NPs) supported on high-surface-area carbon. Even though Pt is considered to be the catalyst of choice, the kinetic limitation for the ORR is substantial, resulting in loss of potential at which this reaction is taking place. In addition, the high cost and scant availability of Pt have further limited commercial applications of technologies that rely on precious metal catalysts with high rates for the ORR. Hence, one of the major efforts in the development of renewable energy technologies is to improve the performance of ORR catalysts and reduce the amount of Pt needed.

Alloying has been shown to be a promising approach to producing advanced catalytic materials.[4–10] Previous work on extended surfaces (bulk electrodes) has demonstrated that bimetallic Pt_3M (M = Fe, Co, Ni, etc.) alloys are superior for the ORR when compared to Pt, with the enhanced catalytic activity arising from the altered electronic structures of the topmost Pt atoms.[8,11,12] This modification has been found to reduce the surface coverage by oxygenated spectator species (e.g., OH^-) and thus increase the number of active sites accessible for molecular oxygen.[8,12]

So far, the focus has been largely placed on Pt-bimetallic catalysts, but other systems, such as ternary alloys, have also attracted substantial interest due to the potential for fine-tuning of the electronic structures and further improving the catalytic activity.[13–26]

Though high-surface-area nanocatalysts have been intensively studied,[19–22] extended surfaces of Pt-ternary alloys have not been thoroughly investigated for the ORR,[23–26] and the trend of catalytic activity for the Pt-ternary catalysts has not been established yet. Moreover, the correlation between electronic structures and surface adsorption/catalytic properties still remains elusive for such multimetallic systems, which however is important for fundamental understanding of the enhanced catalysis and achieving rational catalyst design. Therefore, more systematic studies are needed for full exploration of Pt-based multimetallic systems in electrocatalysis.

Here we focus on $Pt_3(MN)_1$ alloy catalysts for electrocatalytic reduction of oxygen. The main objective of this study is to perform systematic evaluation of Pt-ternary alloys versus Pt-bimetallic systems. For that purpose, we first investigate well-defined extended surfaces of ternary thin-film alloys to examine their electrocatalytic activities and then develop a NP synthesis for the ternary system of choice. In addition, we also performed theoretical simulations based on density functional theory (DFT) and have been able to extend previously established relationships between electronic structures and catalytic performance from Pt-bimetallic to Pt-ternary systems.

5.2 Results and Discussion

Polycrystalline ternary films of 50 nm in thickness were prepared by confocal magnetron sputtering. Different targets of pure metals were used for sputtering over a mirror polished glassy carbon substrate of 6 mm in diameter. The obtained films were

subjected to annealing to induce a homogeneous elemental distribution and subsequent surface analyses in order to explore the existence of Pt-skin formation in ternary systems (see the Methods in the Supporting Information (SI)).[27,28]

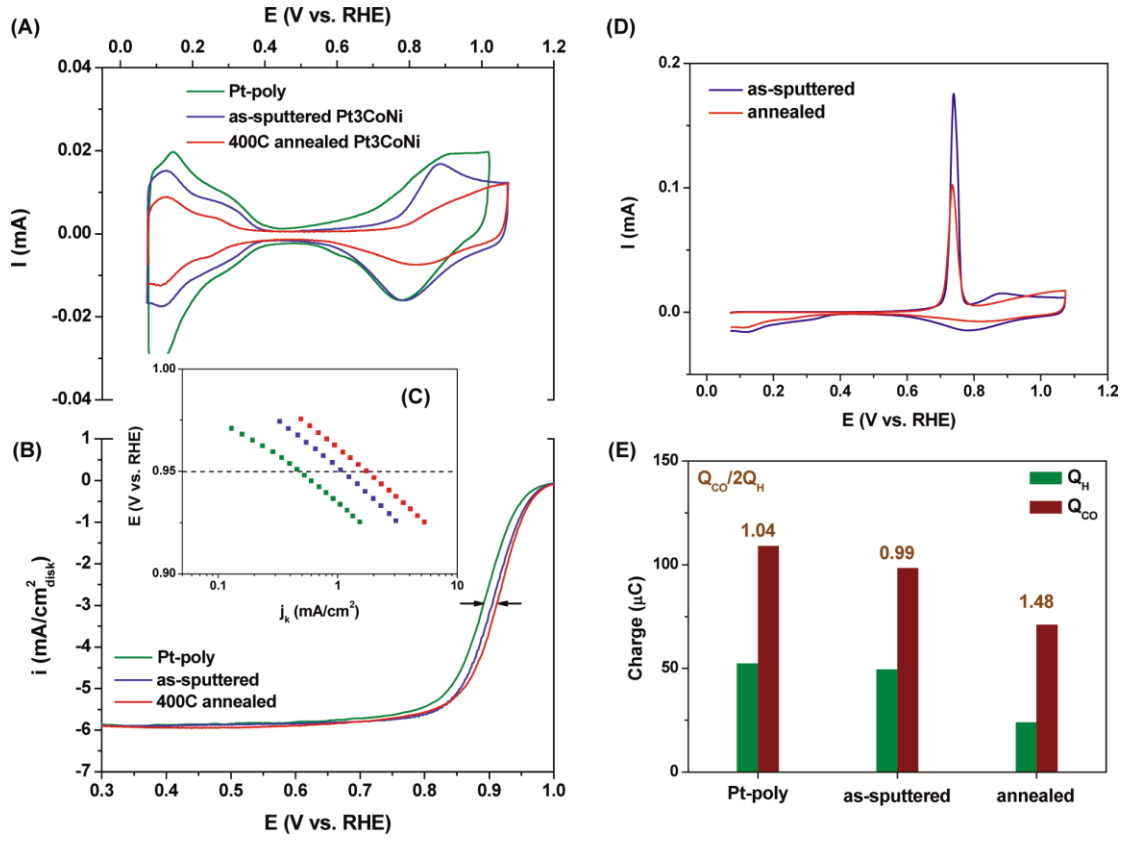

Figure 5-1. Electrochemical characterization of the extended $Pt_3(CoNi)_1$ thin-film surfaces. (A) Cyclic voltammograms (CVs), (B) polarization curves, and (C) Tafel plots. Specific activities for the ternary systems were presented as kinetic currents normalized by ECSAs obtained from CO_{ad} stripping curves. (D) CO stripping curves of the as-sputtered and annealed $Pt_3(CoNi)_1$ surfaces. (E) H_{upd} (Q_H) and CO stripping (Q_{CO}) integrated charges from (A) and (D), with the ratio of $Q_{CO}/2Q_H$ labeled above the histogram bars.

Figure 5-1 summarizes the results of electrochemical studies for these thin films acquired by a rotating disk electrode (RDE). Compared to polycrystalline Pt (Pt-poly), cyclic voltammograms (CVs, Figure 5-1A) of the as-sputtered films have similar features in the underpotentially deposited hydrogen (H_{upd}) region (E < 0.4 V) with slightly suppressed peaks. In the ORRrelevant region (E > 0.6 V), the ternary alloy surfaces exhibit positive shifts for the onset of $Pt{-}OH_{ad}$ formation compared to Pt-poly, indicating weaker chemisorptions of oxygenated species on these surfaces. After annealing at 400 °C, the H_{upd} peaks of ternary systems are additionally suppressed, while the onset of $Pt{-}OH_{ad}$ formation is shifted to even more positive potentials. Even though both effects can also be assigned to altered surface morphology upon thermal annealing, in what follows we prove that they are predominantly associated with the formation of a Pt-skin structure due to Pt segregation.[8,28] The surfaces of the annealed ternary thin films were examined by electrooxidation of adsorbed CO molecules. Figure 5-1D shows the CO stripping curves for the two types of $Pt_3(CoNi)_1$ surfaces, as sputtered and annealed. Both curves have a sharp peak at ~0.74 V, but the annealed surface exhibits lower peak intensity than the as-sputtered surface due to smoother morphology. The integrated charge of the CO stripping curves that are associated with electrooxidation of adsorbed CO are summarized in Figure 5-1E. The as-sputtered $Pt_3(CoNi)_1$ surface has a CO stripping charge of 98.4 μC, which is close to the value obtained for Pt-poly (109 μC) of the same geometric size (d = 6 mm). The charge of CO stripping for the annealed surface is 71.0 μC, which is about 30% lower than that of the as-sputtered surface and polycrystalline Pt. However, integration of the corresponding Hupd region revealed that

the annealed ternary thin film exhibits suppression of Hupd of about ~50% after annealing (from 49.6 to 24.0 μC), as depicted in Figure 5-1E. Consequently, the calculated ratio $Q_{CO}/ 2Q_H$ increased from 0.99 to 1.48 upon annealing. This behavior is typical for the Pt-skin surface formation due to the unique electrochemical adsorption properties associated with these surfaces (Figure S5-1). As shown in our recent studies, the ratio between CO stripping and Hupd charges, $Q_{CO}/2Q_H$, is a good descriptor of the surface compositional profile in the case Figure 5-1. Electrochemical characterization of the extended Pt3(CoNi)1 thin-film surfaces. (A) Cyclic voltammograms (CVs), (B) polarization curves, and (C) Tafel plots. Specific activities for the ternary systems were presented as kinetic currents normalized by ECSAs obtained from COad stripping curves. (D) CO stripping curves of the as-sputtered and annealed $Pt_3(CoNi)_1$ surfaces. (E) H_{upd} (Q_H) and CO stripping (Q_{CO}) integrated charges from (A) and (D), with the ratio of $Q_{CO}/2Q_H$ labeled above the histogram bars of Pt alloys, with the value close to 1 for Pt and Pt-skeleton surfaces, and higher values revealing the formation of a Pt-skin surface due to the suppressed surface coverage by H_{upd}.[29] The formed Pt-skin surface is expected to possess enhanced ORR catalytic activity, which was validated by polarization curves recorded by rotating disk electrode (RDE) measurements (Figure 5-1B). Compared to the Pt-poly surface, the assputtered and annealed $Pt_3(CoNi)_1$ surfaces show positive shifts of half-wave potentials, 12 and 22 mV, respectively. The specific activity at 0.95 V of the annealed surface reaches 1.75 mA/cm^2, whereas the as-sputtered surface achieves 1.12 mA/cm^2 (Figure 5-1C). These values correspond to improvement factors of 4 and 2.5 compared to Pt-poly (0.45 mA/cm^2), respectively.

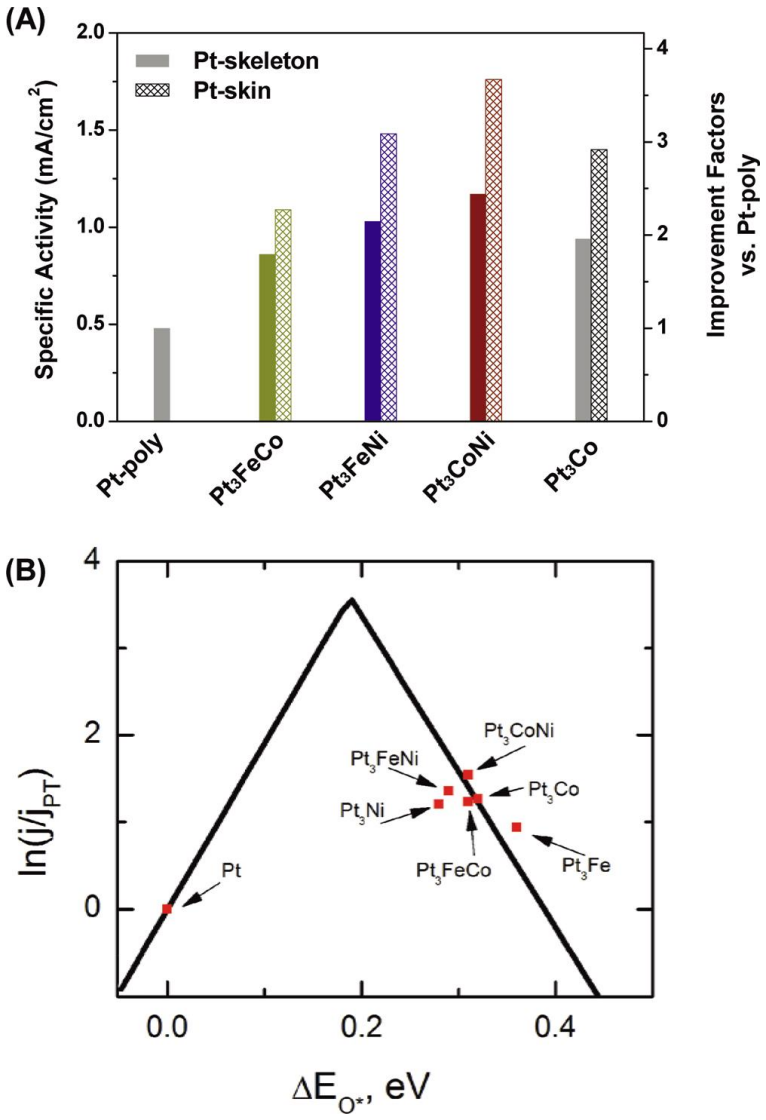

Figure 5-2. (A) Summary of the ORR catalytic activities for the Ptbimetallic and Pt-ternary thin films compared to that of Pt-poly. Activities of as-sputtered (Pt-skeleton) and annealed (Pt-skin) surfaces are represented by solid and net-filled bars, respectively, with the improvement factors labeled by the right axis. (B) Volcano plot relationship of measured catalyst performance versus the DFT calculated oxygen binding energy. The adsorption energy of oxygen (ΔE_{O*}) is calculated relative to Pt(111); activities are scaled by values measured for Pt. (Solid black activity lines are taken from DFT calculations used for Pt-based bimetallic catalysts.[11,30]

The same strategy was employed to investigate other binary and ternary systems, and hence, a trend in the ORR activity has been established. Figure 5-2A shows a summary of the ORR catalytic activities of the ternaries in comparison to Pt-poly and Pt_3Co. All of the as-sputtered thin-film surfaces show higher activities than Pt-poly, with the improvement factors ranging from 1.7 to 2.5. Further improvement was consistently achieved by thermal annealing, which confirms Pt-skin surface formation for each ternary system. For the annealed surfaces, $Pt_3(CoNi)_1$ shows an improvement factor of ~4 versus Pt-poly, compared to ~2.2 and ~3.0 for $Pt_3(FeCo)_1$ and $Pt_3(FeNi)_1$, respectively.

Figure 5-2B shows the relationship between the measured and predicted ORR activities based on the DFT-determined oxygen binding energies (see SI for additional details). It has been previously shown that the DFT approach can be utilized to generate volcano plots relating catalyst activity to a few key catalytic descriptors.[11,30,31] For the ORR, these and other related studies have shown that the binding energy of atomic oxygen, ΔE_{O*}, serves as a reliable descriptor. The volcano relationship in Figure 5-2B shows that, as is the case with binary Pt alloys, the ternary systems exhibit weaker oxygen binding compared to pure Pt. The weakening of the oxygen binding energy actually induces a change in the predicted rate-limiting step of the ORR ($O_2(g) + H^+ + e^- + * \rightarrow OOH*$ on the weak-binding side of the volcano, as opposed to $OH* + H^+ + e^- \rightarrow H_2O(l) + *$ on the strong-binding side), and both binaries and ternaries thus fall on the opposite side of the volcano from pure Pt. The net activity of the binaries and ternaries, however, is still higher than that of Pt, which is in good agreement with our experimental results. Though it remains unclear why $Pt_3(CoNi)_1$ is the most active based on the current

simulations, it is evident that the employment of multimetallic Pt-based alloys can serve to additionally tune the oxygen binding energies of Pt-based catalysts, which in turn results from corresponding changes in the electronic structures of platinum surface sites.[11]

On the basis of the established trend on extended surfaces, we aimed toward the synthesis of the most active $Pt_3(CoNi)_1$ nanocatalysts. Considering that conventional impregnation methods rely on precipitation from the aqueous solutions and usually do not provide NPs with homogeneous compositions, we developed an organic solvothermal approach for the synthesis of ternary alloy NPs.[32,33] In general, Pt in solution tends to nucleate faster than the 3d transition metals and forms unalloyed Pt NPs due to the higher reduction potential of Pt^{2+} (+1.2 V) versus those of 3d metals (−0.2 to −0.4 V). However, we managed to achieve simultaneous growth for ternary alloy NPs by injection of the Pt precursor to a hot solution of the 3d transition-metal acetates (see the Methods in the SI), where 3d metal precursors could already be reduced to form metallic species and thus be able to match the fast reduction of Pt^{2+} to form uniform ternary alloy NPs.[34]

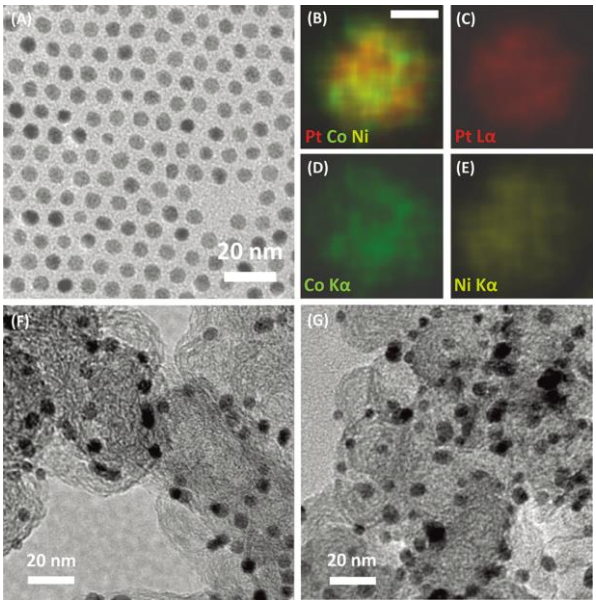

Figure 5-3. (A) TEM image of the as-synthesized $Pt_3(CoNi)_1$ alloy NPs. (B−E) Representative elemental maps from EDS analysis based on STEM for (B) overlapping of Pt, Co, and Ni, (C) Pt, (D) Co, and (E) Ni. The scale bar in (B) is equal to 2 nm, and it also applies for (C)−(E). (F, G) TEM images of the ternary catalyst before (F) and after (G) surfactant removal and thermal treatment.

Figure 5-3A shows a representative transmission electron microscopy (TEM) image of the as-synthesized $Pt_3(CoNi)_1$ NPs. The monodisperse particles have an average particle size of ~6 nm, which is close to the optimal size for Pt alloy catalysts established before.[35] Elemental composition was analyzed by energy-dispersive X-ray spectroscopy (EDX), showing a composition of $Pt_{0.72}Co_{0.11}N_{i0.17}$ close to the expected Pt/M/N = 3:0.5:0.5 ratio. In addition, distribution of elements in the ternary NPs was mapped by

EDX based on high-angle annular dark field scanning transmission electron microscopy (HAADF-STEM). Figure 5-3B−E presents overlapped and separate maps of the elements in a typical $Pt_3(CoNi)_1$ particle. It is obvious that all of the constituents, Pt, Co, and Ni, are uniformly distributed across the particle and well intermixed in the overlapping map (Figure 5-3B). The observations here are consistent with our recent findings on Pt-bimetallic NPs prepared by similar methods,[33] confirming the highly homogeneous nature of the ternary alloy NPs obtained by organic solution synthesis.

To prepare electrocatalysts, the as-synthesized NPs were mixed with high-surface-area carbon black (see the SI for experimental details). The previously established protocol for thermal treatment was applied to remove the surfactants and induce beneficial surface segregation for best catalytic performance.[36,37] TEM images (Figure 5-3F and G) show that no significant size or morphology change happened after these treatments. A catalyst suspension was prepared by sonication of the catalyst in deionized water, and a drop of that suspension was deposited on a polished glassy carbon (GC) disk (6 mm in diameter). The content of Pt in the catalyst was adjusted to ∼25%, and the loading of Pt on the GC electrode was ∼12 μg/cm^2.

Figure 5-4 summarizes electrochemical results for the Pt3(CoNi)1 nanocatalysts and commercial Pt/carbon of a similar size (6 nm, Tanaka), which was used as a reference. The measured CVs have Hupd peaks at E < 0.4 V and Pt oxidation/ reduction peaks at 0.8−0.9 V. Similar to the results on extended surfaces (Figure 5-1A), the onset of Pt−OHad on the ternary catalyst was shifted positively by >25 mV versus Pt/C (Figure 5-4A), confirming altered electronic structures and surface adsorption properties of ternary alloy NPs. Consequently, the corresponding polarization curves exhibit similar shifts in

halfwave potentials and show substantially enhanced catalytic activities (Figure 5-4B). At 0.95 V, the as-prepared and annealed Pt3(CoNi)+/C catalysts have achieved improvement factors of 2.3 and 4.2 in specific activity versus Pt/C (Figure 5-4C), with the annealed catalyst reaching 0.55 mA/cm2 (versus 0.13 mA/ cm^2 for Pt/C). The level of catalytic activity improvement is consistent with the trend established on extended thin-film surfaces. Similar improvement factors were also present in mass activity, with the annealed $Pt_3(CoNi)_1$/C achieving 183 A/g in comparison to 49 A/g for Pt/C.

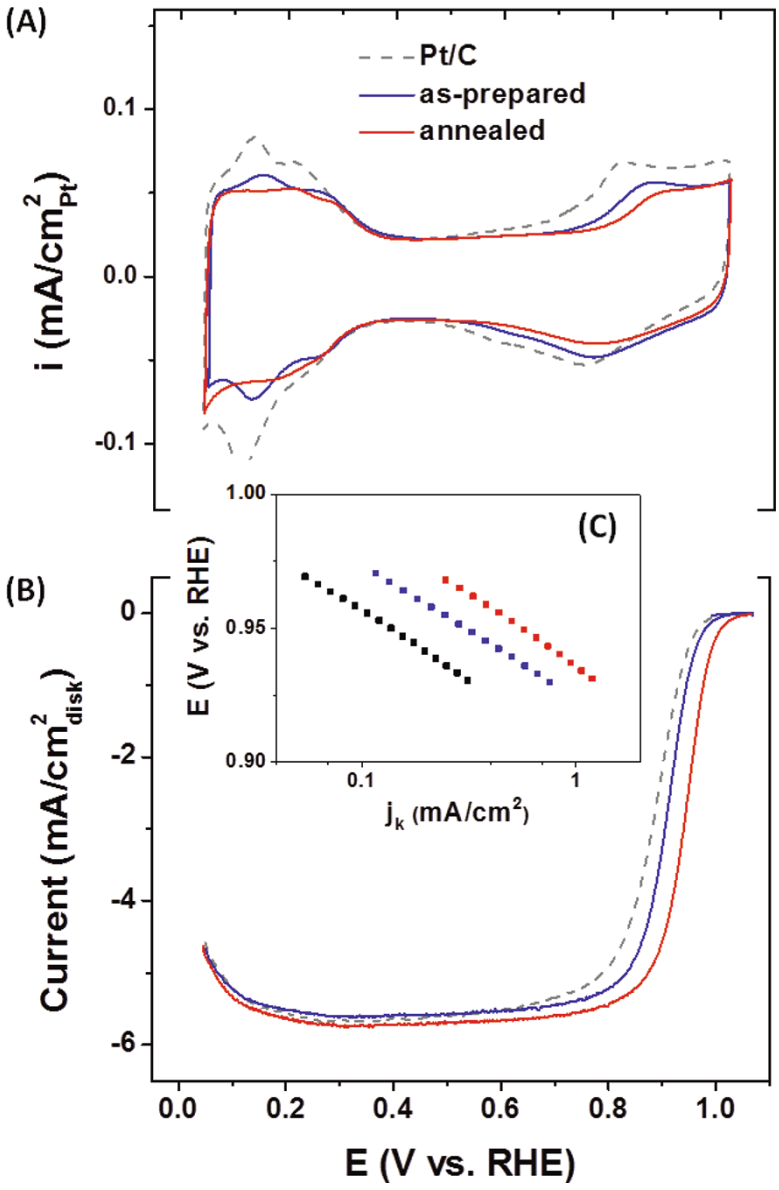

Figure 5-4. Electrochemical characterization of the $Pt_3(CoNi)_1$/C catalysts. (A) CVs recorded at 50 mV/s in Ar-saturated 0.1 M $HClO_4$. (B) Polarization curves for the ORR with the iR drop correction recorded in O_2-saturated 0.1 M $HClO_4$. (C) Tafel plots of the kinetic current densities depending on electrode potentials.

5.3 Conclusion

Ternary alloys of Pt and 3d transition metals were investigated as catalysts for the ORR. Systematic studies on extended surfaces of Pt-based ternary thin films revealed a volcano-type dependence between the measured catalytic activities and DFT-predicted oxygen-binding energies of corresponding model ternary alloy surfaces. On the basis of this trend, we have synthesized the catalyst of choice with the highest activity based on monodisperse and homogeneous ternary alloy NPs from organic solution synthesis. Our comparative studies show that the ternary alloy catalysts possess enhanced catalytic activities for the ORR when compared to Pt or Pt-bimetallic alloys. The most active system was found to be $Pt_3(CoNi)_1$, which exhibits an improvement factor of ~4 versus Pt.

Acknowledgements

This work was conducted at Argonne National Laboratory, a U.S. Department of Energy, Office of Science Laboratory, operated by UChicago Argonne, LLC, under Contract No. DEAC02- 06CH11357. This research was sponsored by the U.S. Department of Energy, Office of Energy Efficiency and Renewable Energy, Fuel Cell Technologies Program. Other components of the research, including a DOE Early Career Award (J.G.) and use of the Center for Nanoscale Materials, was supported by the U.S. Department of Energy, Office of Science, Office of Basic Energy Sciences. Microscopy research was conducted at the Electron Microscopy Center for Materials Research at Argonne. STEM and element mapping were done at ORNL's SHaRE User Facility sponsored by the Scientific

User Facilities Division, Office of Basic Energy Sciences, the U.S. Department of Energy.

5.4 References

(1) Vielstich, W.; Lamm, A.; Hubert A., G. *A. Handbook of Fuel Cells: Fundamentals, Technology And Applications*; Willey.

(2) Abraham, K. M.; Jiang, Z. *J. Electrochem. Soc.* **1996**, *143*, 1.

(3) Armand, M.; Tarascon, J.-M. *Nature* **2008**, *451*, 652.

(4) Besenbacher, F.; Chorkendorff, I.; Clausen, B. S.; Hammer, B.; Molenbroek, A. M.; Nørskov, J. K.; Stensgaard, I. *Science* **1998**, *279*, 1913.

(5) Diemant, T.; Hager, T.; Hoster, H. E.; Rauscher, H.; Behm, R. J. *Surf. Sci.* **2003**, *541*, 137.

(6) Greeley, J.; Mavrikakis, M. *Nat. Mater.* **2004**, *3*, 810.

(7) Chen, M.; Kumar, D.; Yi, C.-W.; Goodman, D. W. *Science* **2005**, *310*, 291.

(8) Stamenkovic, V. R.; Mun, B. S.; Arenz, M.; Mayrhofer, K. J. J.; Lucas, C. A.; Wang, G.; Ross, P. N.; Markovic, N. M. *Nat. Mater.* **2007**, *6*, 241.

(9) Strasser, P.; Koh, S.; Anniyev, T.; Greeley, J.; More, K.; Yu, C.; Liu, Z.; Kaya, S.; Nordlund, D.; Ogasawara, H.; Toney, M. F.; Nilsson, A. *Nat. Chem.* **2010**, *2*, 454.

(10) Tao, F.; Grass, M. E.; Zhang, Y.; Butcher, D. R.; Aksoy, F.; Aloni, S.; Altoe, V.; Alayoglu, S.; Renzas, J. R.; Tsung, C.-K.; Zhu, Z.; Liu, Z.; Salmeron, M.; Somorjai, G. A. *J. Am. Chem. Soc.* **2010**, *132*, 8697.

(11) Stamenkovic, V.; Mun, B. S.; Mayrhofer, K. J. J.; Ross, P. N.; Markovic, N. M.; Rossmeisl, J.; Greeley, J.; Nørskov, J. K. *Angew. Chem. Int. Ed.* **2006**, *45*, 2897.

(12) Stamenkovic, V. R.; Fowler, B.; Mun, B. S.; Wang, G.; Ross, P. N.; Lucas, C. A.; Marković, N. M. *Science* **2007**, *315*, 493.

(13) Seo, A.; Lee, J.; Han, K.; Kim, H. *Electrochimica Acta* **2006**, *52*, 1603.

(14) Antolini, E. *Appl. Catal. B Environ.* **2007**, *74*, 324.

(15) Antolini, E. *Appl. Catal. B Environ.* **2007**, *74*, 337.

(16) Neyerlin, K. C.; Srivastava, R.; Yu, C.; Strasser, P. *J. Power Sources* **2009**, *186*, 261.

(17) Srivastava, R.; Mani, P.; Hahn, N.; Strasser, P. *Angew. Chem. Int. Ed.* **2007**, *46*, 8988.

(18) Mani, P.; Srivastava, R.; Strasser, P. *J. Power Sources* **2011**, *196*, 666.

(19) Neyerlin, K. C.; Bugosh, G.; Forgie, R.; Liu, Z.; Strasser, P. *J. Electrochem. Soc.* **2009**, *156*, B363.

(20) Fang, B.; Luo, J.; Chen, Y.; Wanjala, B. N.; Loukrakpam, R.; Hong, J.; Yin, J.; Hu, X.; Hu, P.; Zhong, C.-J. *ChemCatChem* **2011**, *3*, 583.

(21) Datta, J.; Dutta, A.; Mukherjee, S. *J. Phys. Chem. C* **2011**, *115*, 15324.

(22) Wanjala, B. N.; Loukrakpam, R.; Luo, J.; Njoki, P. N.; Mott, D.; Zhong, C.-J.; Shao, M.; Protsailo, L.; Kawamura, T. *J. Phys. Chem. C* **2010**, *114*, 17580.

(23) Miura, A.; Tague, M. E.; Gregoire, J. M.; Wen, X.-D.; van Dover, R. B.; Abruña, H. D.; DiSalvo, F. J. *Chem. Mater.* **2010**, *22*, 3451.

(24) He, T.; Kreidler, E. *Phys. Chem. Chem. Phys.* **2008**, *10*, 3731.

(25) Hwang, S.-M.; Lee, C. H.; Kim, J. J.; Moffat, T. P. *Electrochimica Acta* **2010**, *55*, 8938.

(26) Prochaska, M.; Jin, J.; Rochefort, D.; Zhuang, L.; DiSalvo, F. J.; Abruna, H. D.; van Dover, R. B. *Rev. Sci. Instrum.* **2006**, *77*, 054104.

(27) Stamenkovic, V. R.; Mun, B. S.; Mayrhofer, K. J. J.; Ross, P. N.; Markovic, N. M. *J. Am. Chem. Soc.* **2006**, *128*, 8813.

(28) Wang, C.; Chi, M.; Li, D.; Strmcnik, D.; van der Vliet, D.; Wang, G.; Komanicky, V.; Chang, K.-C.; Paulikas, A. P.; Tripkovic, D.; Pearson, J.; More, K. L.; Markovic, N. M.; Stamenkovic, V. R. *J. Am. Chem. Soc.* **2011**, *133*, 14396.

(29) Van der Vliet, D. F.; Wang, C.; Li, D.; Paulikas, A. P.; Greeley, J.; Rankin, R. B.; Strmcnik, D.; Tripkovic, D.; Markovic, N. M.; Stamenkovic, V. R. *Angew. Chem. Int. Ed.* **2012**, *51*, 3139.

(30) Greeley, J.; Stephens, I. E. L.; Bondarenko, A. S.; Johansson, T. P.; Hansen, H. A.; Jaramillo, T. F.; Rossmeisl, J.; Chorkendorff, I.; Nørskov, J. K. *Nat. Chem.* **2009**, *1*, 552.

(31) Greeley, J.; Nørskov, J. K. *J. Phys. Chem. C* **2009**, *113*, 4932.

(32) Sun, S.; Murray, C. B.; Weller, D.; Folks, L.; Moser, A. *Science* **2000**, *287*, 1989.

(33) Wang, C.; Chi, M.; Li, D.; van der Vliet, D.; Wang, G.; Lin, Q.; F. Mitchell, J.; More, K. L.; Markovic, N. M.; Stamenkovic, V. R. *ACS Catal.* **2011**, *1*, 1355.

(34) Wang, C.; Markovic, N. M.; Stamenkovic, V. R. *ACS Catal.* **2012**, *2*, 891.

(35) Wang, C.; van der Vliet, D.; Chang, K.-C.; You, H.; Strmcnik, D.; Schlueter, J. A.; Markovic, N. M.; Stamenkovic, V. R. *J. Phys. Chem. C* **2009**, *113*, 19365.

(36) Wang, C.; Wang, G.; Vliet, D. van der; Chang, K.-C.; Markovic, N. M.; Stamenkovic, V. R. *Phys. Chem. Chem. Phys.* **2010**, *12*, 6933.

(37) Li, D.; Wang, C.; Tripkovic, D.; Sun, S.; Markovic, N. M.; Stamenkovic, V. R. *ACS Catal.* **2012**, *2*, 1358.

5.5 Supporting Information

5.5.1 Material Preparation

Extended Surfaces. $Pt_3(MM')_1$ films of 50 nm in thickness were prepared by physical deposition on glassy carbon substrates. The composition was controlled to be Pt : M : M′ = 3 : 0.5 : 0.5. During sputtering, the substrates were set 125mm away from DC sputter magnetrons in 4 mTorr Argon gas (base vacuum 1×10^{-7} Torr). Metal source rate was determined by quartz crystal microbalance, and the film thickness was derived from exposure time of computer controlled shutters during sputtering. The sputtered films were annealed at 400 °C in a forming gas (Ar + 3% H_2) for 2 hours before electrochemical studies.

Nanocatalysts. $Pt_3(CoNi)_1$ NPs were synthesized by co-reduction of the corresponding metal salts in organic solution. In a typical synthesis, 0.2 mmol of $Ni(ac)_2$ and 0.4 mmol of $Co(ac)_2$ were dissolved in 10 ml of diphenylether in the presence of 0.5 ml of oleic acid, 0.5 ml of oleylamine and 2 mmol of tetradecanediol. After heating up to 200oC, 0.33 mmol of $Pt(acac)_2$ dissolved in 1 ml of 1,2-dichlorobenzene was injected into this solution. The solution was kept at this temperature for 1 hour and then cooled down to room temperature. The product was separated by adding 30 ml of ethanol and centrifuging (6,000 rpm). The collected NPs were re-dispersed in hexane for further applications.

5.5.2 Material Characterization

TEM images were taken on a Philips EM 30 (200 kV) equipped with EDS functionality. STEM and elemental analysis were carried out on JEOL 2200FS TEM/STEM with a CEOS aberration (probe) corrector. The microscope was operated at 200kV in HAADF-STEM mode equipped with a Bruker-AXS X-Flash 5030 silicon drift detector. The probe size was ~0.7 Å and the probe current was ~30 pA during HAADF-STEM imaging. When accumulating EDS data, the probe current was increased to ~280 pA and the probe size was ~2 Å. The presented EDS data were confirmed to be from "e-beam damage-free" particles by comparing STEM images before and after EDS acquisition.

5.5.3 Electrochemical Studies

The as-synthesized NPs were mixed with carbon black (Tanaka, ~900 m2/g) by sonication. After drying, the mixture was subjected to thermal treatment at 185 °C in air to remove the surfactants.[1] The obtained catalyst was further annealed at 400 °C in Ar + 3% H_2.[2] Electrochemical measurements were conducted in a three-compartment electrochemical cell with a rotational disc electrode (RDE) setup (Pine) and a Autolab 302 potentiostat. A glassy carbon disk (6 mm in diameter) was used as working electrode. A saturated Ag/AgCl electrode and a Pt wire were used as reference and counter electrodes, respectively. 0.1 M $HClO_4$ was used as electrolyte. The loading was controlled to be 12 μgPt/cm^2 disk for $Pt_3(CoNi)_1$/C nanocatalysts. The catalysts were cycled in the electrolyte until stable CVs were collected with a scanning rate of 50 mV/s in 0.1 M $HClO_4$ under Ar saturation at room temperature (20 °C), and polarization curves for the ORR were measured with a scanning rate of 20 mV/s in the same electrolyte under O_2 saturation at 1,600 rpm and 60 °C. All the potentials given in the discussion were against reversible hydrogen electrode (RHE), and the readout currents are recorded

with ohmic iR drop correction during the measurements. The electrochemical results reported in the text were based on average of three independent measurements and the values were within ±15% error.

5.5.4 Theory and Simulation

Density Functional Theory (DFT) calculations were performed using the DACAPO[3] software package. Pt, and the binary and ternary Pt-based alloy surfaces, are represented using periodically repeated slabs of four close-packed layers with approximately 16 Å of vacuum between slabs. A p(2x2) surface unit cell is employed. The bottom two layers of the slabs are kept fixed in their bulk geometries, while the top two layers are fully relaxed. Atomic relaxations are performed with the Quasi-Newton scheme until the Cartesian forces in any given direction converge to less than 0.04 eV/Å. Ionic cores are described by ultrasoft pseudopotentials,[4] and the Kohn-Sham one-electron valence states are expanded in a basis of plane waves with kinetic energy below 340 eV; a density cutoff of 500 eV is used. The surface Brillouin zone was sampled by an 18(1x1) Chadi-Cohen *k*-point grid; in all cases, convergence with respect to the number of k-points and the slab layers is confirmed. The exchange-correlation energy and potential are described by the generalized gradient approximation (GGA-RPBE).[3] The self-consistent RPBE density is determined by iterative diagonalization of the Kohn-Sham Hamiltonian, Fermi population of the Kohn-Sham states (kBT = 0.1 eV), and Pulay mixing of the resulting electronic density.[5] Calculations were performed spin-polarized to account for magnetic effects in the Pt-based alloys containing Fe, Co or Ni. Adsorption is allowed on only one of the two exposed surfaces of the metal slabs, and the electrostatic potential is adjusted accordingly.[6]

The Pt_3XY ternary alloys are constructed in a manner very similar to that employed previously for Pt_3X binary alloys with Pt surface skins.[7,8] The overall alloy structure (and location of heteroatom sites) is the same in both the binaries and ternaries, but the positions of the X and Y heteroatoms in the ternaries are permutted with one another (but not with Pt atoms) to find a lowest energy structure. The surface layer is composed of a pure Pt skin, while the Pt concentration in the first subsurface layer is 50%, and the concentration of each heteroatom in the first subsurface layer is 25%. Deeper layers have their bulk concentration profiles. Lattice constants are determined by averaging the corresponding binary alloy lattice constants. A schematic is shown in Figure S5-1.

For comparison relative to Pt(111), the relative binding energy of atomic oxygen, ΔE_{O*}, is calculated per the following equation:

$$\Delta E_{O*} = E_{O/alloy} - E_{O/Pt} + E_{Pt} - E_{alloy}$$

In this equation, $E_{O/alloy}$ represents the total energy of the adsorbed oxygen/alloy surface system, $E_{O/Pt}$ that of oxygen/platinum, E_{Pt} that of the bare platinum surface, and E_{alloy} that of the bare alloy surface.

The DFT-based predicted activity lines in Fig. 5-2B are taken from related previous work.[8]

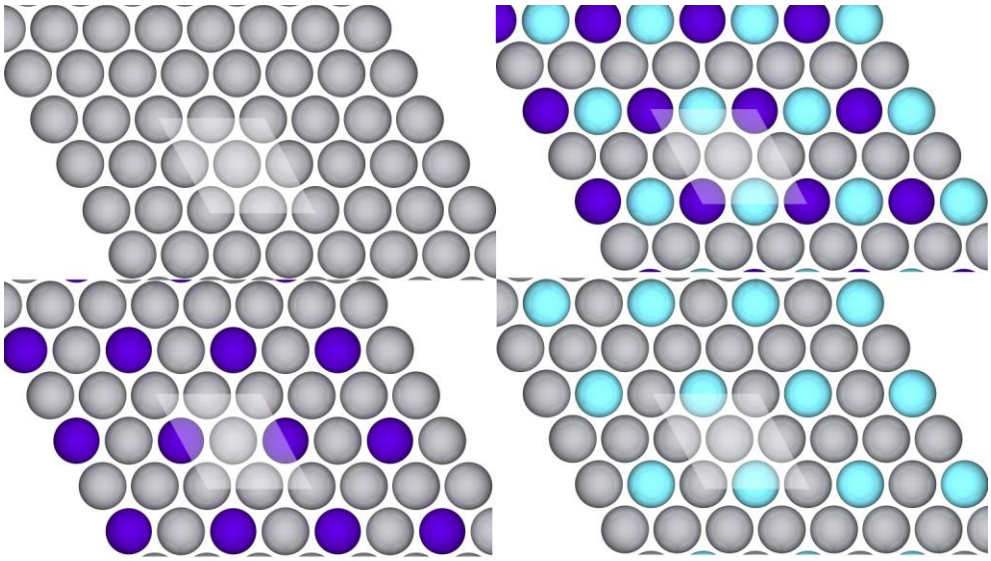

Figure S5-1. Description given below is given in the order of top-left, top-right, bottom-left, bottom-right. Top-down plan view through $Pt_3(XY)_1$ ternary alloy surface structure, close packed layers 1-4 (a)-(d). The p(2x2) surface cell boundaries are denoted by the half transparent white parallelogram overlay. Platinum atoms shown as light gray, X atoms as dark blue, Y atoms as light blue.

References

(1) Li, D.; Wang, C.; Tripkovic, D.; Sun, S.; Markovic, N. M.; Stamenkovic, V. R. *ACS Catal.* **2012**, *2*, 1358.

(2) Wang, C.; Wang, G.; Vliet, D. van der; Chang, K.-C.; Markovic, N. M.; Stamenkovic, V. R. *Phys. Chem. Chem. Phys.* **2010**, *12*, 6933.

(3) Hammer, B.; Hansen, L. B.; Nørskov, J. K. *Phys. Rev. B* **1999**, *59*, 7413.

(4) Vanderbilt, D. *Phys. Rev. B* **1990**, *41*, 7892.

(5) Kresse, G.; Furthmüller, J. *Comput. Mater. Sci.* **1996**, *6*, 15.

(6) Bengtsson, L. *Phys. Rev. B* **1999**, *59*, 12301.

(7) Stamenkovic, V.; Mun, B. S.; Mayrhofer, K. J. J.; Ross, P. N.; Markovic, N. M.; Rossmeisl, J.; Greeley, J.; Nørskov, J. K. *Angew. Chem. Int. Ed.* **2006**, *45*, 2897.

(8) Greeley, J.; Stephens, I. E. L.; Bondarenko, A. S.; Johansson, T. P.; Hansen, H. A.; Jaramillo, T. F.; Rossmeisl, J.; Chorkendorff, I.; Nørskov, J. K. *Nat. Chem.* **2009**, *1*, 552.

VI. Ultrathin MPt (M = Fe, Co) Nanowires as Efficient Catalysts for Oxygen Reduction Reaction

6.1 Introduction

Oxygen reduction reaction (ORR) is an important cathode reaction used in fuel cells and metal-air batteries for renewable energy applications.[1–3] Platinum (Pt) has been studied extensively as an essential catalytic component to reduce undesired overpotentials observed in ORR.[4–6] Previous experimental and computational investigations have revealed that once alloyed with first-row transition metals, especially with Fe, Co and Ni, Pt can show dramatic activity enhancement in ORR catalysis.[7–13] This enhancement is believed to originate from the downshift of the d-band center of the Pt in the alloy structure, weakening the bonding strength between Pt and oxygenated species (often called blocking species or spectators) and facilitating oxygen binding to Pt sites for its activation and reduction.[7,8] Recent experiments further indicate that one-dimensional (1D) Pt nanostructures, either nanowires (NWs) or nanotubes (NTs), are less subject to dissolution, Ostwald ripening and aggregation than the zero-dimensional Pt NPs in acidic conditions,[14–18] and may represent a new class of catalysts for catalyzing ORR with high activity and durability. In these studies, Pt NW catalysts were made either by reduction of H_2PtCl_6 with formic acid,[14] or by assembly of Pt NWs.[16] Pt NTs were prepared via galvanic reaction of between Ag and Pt^{2+} ($2Ag + Pt^{2+} \rightarrow 2Ag^{+} + Pt$) by refluxing the aqueous solution containing Ag NWs and $Pt(CH_3COOH)_2$.[17] These previous studies infer that if 1D Pt alloy nanostructures can be prepared to serve as catalysts, then the combined shape and alloy effects provided by the 1D structure may lead to further enhancement in both ORR activity and stability.

Herein, we report an improved organic phase synthesis of ultrathin FePt and CoPt alloy NWs with controllable compositions for enhanced ORR catalysis. We recently developed a facile synthesis of 2-3 nm thick FePt NWs via decomposition of iron pentacarbonyl, $Fe(CO)_5$, and reduction of platinum acetylacetonate, $Pt(acac)_2$, in oleylamine (OAm).[19] We found that NW aspect ratio could be tuned by adding 1-octadecene (ODE) in OAm with more ODE leading to shorter NWs. By adding sodium oleate in the reaction condition, we succeeded in producing both FePt and CoPt NWs with the desired alloy composition control and good synthetic yield. These NWs showed the composition-dependent ORR catalysis with FePt NWs being more active than CoPt NWs. The specific and mass activities of the FePt NWs reached as high as 1.53 mA/cm^2 and 844.0 mA/mg Pt at 0.9 V (vs. reversible hydrogen electrode, RHE) while those of the benchmark Pt catalyst valued at 0.325 mA/cm^2 and 155.0 mA/mg Pt. These NWs are a new class of catalyst suitable for enhanced ORR catalysis.

6.2 Results and Discussion

The FePt or CoPt NWs were prepared by thermal decomposition of $Fe(CO)_5$ or $Co_2(CO)_8$ and reduction of $Pt(acac)_2$. Different from the previous approach to FePt NPs[20,21] and FePt NWs,[19] the current synthesis was performed in the ODE and OAm solution containing sodium oleate, which could improve the yield of NWs. $Fe(CO)_5$ or $Co_2(CO)_8$ was added to serve both as a reducing agent and as a Fe or Co precursor for its alloying with Pt. For example, to make $Fe_{56}Pt_{44}$ or $Co_{63}Pt_{37}$, 0.3 g of sodium oleate was dissolved in 12 mL of ODE by heating the mixture to 180 ^oC. After the solution was cooled to 60 ^oC, 0.2 g of $Pt(acac)_2$ (0.5 mmol) and 8 mL of OAm were added and the

solution was further heated to 115ºC at the heating rate of 10 ^{o}C/min. Immedicately, $Fe(CO)_5$ (0.14 mL) or $Co_2(CO)_8$ (0.182 g) dissolved in dichlorobenzene (DCB) was injected and the resultant solution was heated to 240 ºC at a heating rate of 4-5 ºC/min and kept at 240 ºC for 25 min.

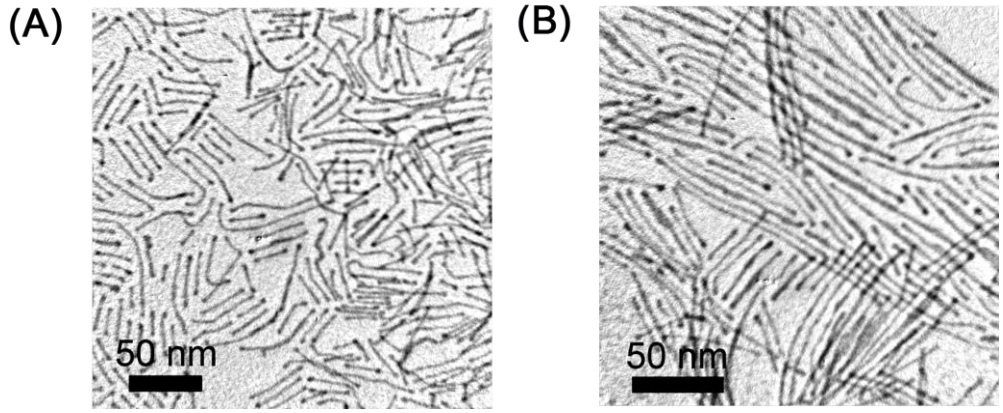

Figure 6-1 TEM images of (A) $Fe_{56}Pt_{44}$ and (B) $Co_{63}Pt_{37}$ NWs.

Inductively coupled plasma-atomic emission spectroscopy (ICP-AES) was used to analyze the composition of the as-prepared FePt and CoPt NWs. We found that the molar ratio of Fe/Pt or Co/Pt was important for tuning the composition of FePt or CoPt NWs. 0.2 g $Pt(acac)_2$ (0.5 mmol) and 0.14 mL $Fe(CO)_5$ (1 mmol) led to $Fe_{68}Pt_{32}$ NWs. With a fixed amount of $Pt(acac)_2$ at 0.2 g (0.5 mmol), 0.08 (0.57 mmol) and 0.045 mL (0.32 mmol) of $Fe(CO)_5$ resulted in $Fe_{56}Pt_{44}$ and $Fe_{42}Pt_{58}$ NWs, respectively. Under the same reaction conditions as in the synthesis of FePt NWs, 180 mg (0.53 mmol) and 136 mg $Co_2(CO)_8$ (0.4 mmol) produced $Co_{63}Pt_{37}$ and $Co_{32}Pt_{68}$ NWs. In the synthesis of CoPt NWs, the amount of $Co_2(CO)_8$ added in the reaction mixture was key to the formation of NW product. Increasing the amount of $Co_2(CO)_8$ to 270 mg would yield a mixture of NPs

and thick NWs (Figure S6-1A) whereas reducing the amounts of $Co_2(CO)_8$ to 90 or 63 mg gave either the mixture of NPs and thin NWs (Figure S6-1B), or NPs as the main product (Figure S6-1C). Figure 6-1&S6-2 show the representative transmission electron microscopy (TEM) images of FePt NWs and CoPt NWs with diameters at 2.5 ± 0.3 nm. The length of FePt NWs is in 30-100 nm range and that of CoPt NWs in 50-500 nm range. The FePt and CoPt NWs were further characterized by X-ray diffraction (XRD) (Figure S6-3). The broadened diffraction peaks from these NWs reveal the small dimension of the chemically disordered face centered cubic crystal domains, further proving their ultrathin character.[22,23]

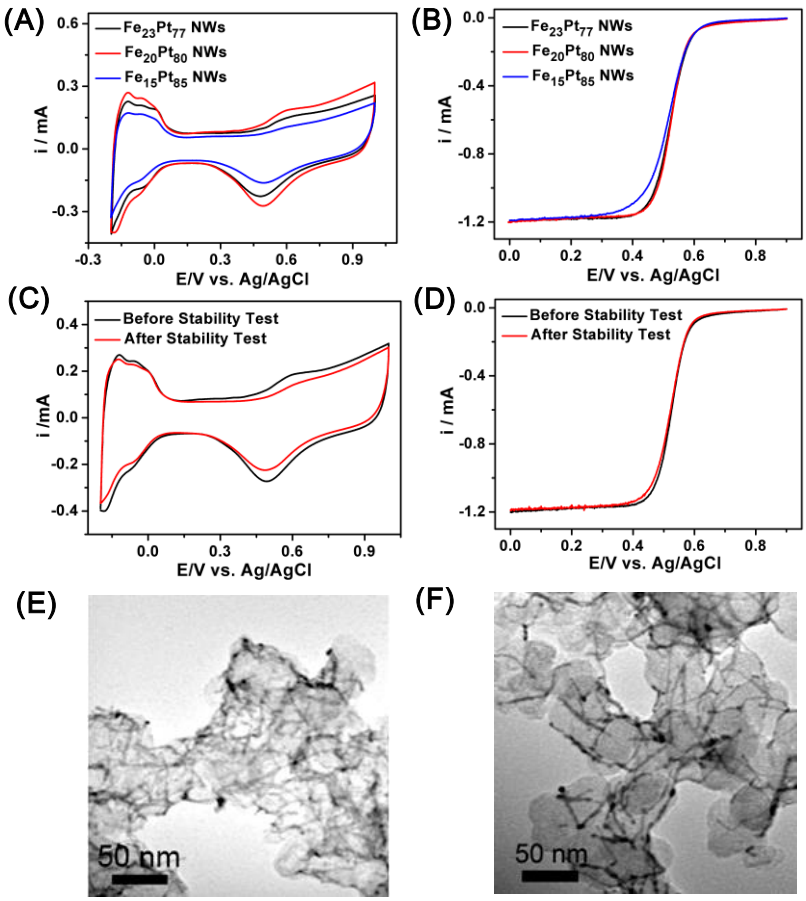

Figure 6-2 (A) CVs of FePt NWs with different compositions in N_2-saturated 0.1 M $HClO_4$ solution at a scan rate of 50 mV/s, (B) their polarization curves for ORR in O_2-saturated 0.1 M $HClO_4$ solution at 293 K. (C) CVs and (D) polarization curves of the $Fe_{20}Pt_{80}$ NWs before and after 5000 potential cycles between 0.4-0.8 V (vs. Ag/AgCl). (E,F) TEM images of the $Fe_{20}Pt_{80}$/C NWs before (E) and after (F) stability test.

The as-synthesized FePt and CoPt NWs with different compositions were studied for ORR. To perform the tests, the NWs were first deposited on a carbon (C) support (Ketjen EC-300J) via sonicating the mixture of NWs and C in hexane/acetone (v/v =2:1) (NW:C = 4:6 by weight) and then washed with acetic acid (AA, 99%) at 70 ºC to remove the surfactant.[24,25] Upon this acid wash, part of Fe in FePt NWs was etched away, as confirmed by the composition change from $Fe_{42}Pt_{58}$, $Fe_{56}Pt_{44}$, $Fe_{68}Pt_{32}$ to $Fe_{15}Pt_{85}$, $Fe_{20}Pt_{80}$ and $Fe_{23}Pt_{77}$, respectively. After the same AA treatment, larger portion of Co in CoPt NWs was lost and less than 10% Co was retained in the NW structure. This indicates that CoPt NWs are chemically less stable than FePt NWs and Co is less contained in CoPt NWs than Fe in FePt NWs after AA treatment. Figure 6-2A shows the typical cyclic votammograms (CVs) of the FePt NWs with different compositions in N_2-saturated 0.1 M $HClO_4$ with a sweep rate of 50 mV/s. The corresponding CV curves exhibit strong peaks associated with hydrogen adsorption/desorption at -0.2-0 V and Pt oxidization/reduction at above 0.4 V. With increasing the amount of Fe in FePt NWs, the reduction peak potential of FePt NWs in the cathodic scan is slightly negatively shifted, indicating the difficulty in reducing the oxidized FePt species on the FePt NW surface.

Figure 6-2B shows typical ORR polarization curves of FePt NWs catalysts obtained at room temperature in O_2-saturated 0.1 M $HClO_4$ at a sweep rate of 10 mV/s and a rotation speed of 1600 rpm. $Fe_{20}Pt_{80}$ NWs have a slightly higher half-wave potential than other two kinds of FePt NWs. We should note that composition dependent ORR activity is not well represented by these FePt NWs due to the loss of Fe in AA treatment. However, more Fe in FePt NWs does show higher activity. Using $Fe_{20}Pt_{80}$ NWs as an example, we further studied the stability of $Fe_{20}Pt_{80}$ NWs by scanning the potential between 0.4 and 0.8 V (vs. Ag/AgCl) in the O_2-saturated 0.1 M $HClO_4$ at the scan rate of 100 mV/s. Figure 6-2C, D shows the CVs and ORR polarization curves of the $Fe_{20}Pt_{80}$ NWs before and after 5000 potential cycles. We can see that $Fe_{20}Pt_{80}$ NWs lose slightly their initial electrochemically active surface area, ECASA, after the stability test. However, their ORR polarization curves overlap with the Fe/Pt ratio changed only from 17/83 to 16/84. TEM analysis shows that there is no visible morphology change for $Fe_{20}Pt_{80}$ NWs after 5000 potential cycles (Figure 6-2E, F). Similarly, CoPt NWs with different compositions were studied for ORR. The corresponding CVs, ORR polarization curves and stability tests are shown in Figure S6-4. CoPt NWs tested have generally lower ORR catalytic activity than the FePt NWs. This is likely caused by the heavier loss of Co from CoPt than of Fe from FePt in acid solution. Importantly, the Co_8Pt_{92} NWs have the ORR stability as good as the FePt NWs.

The electrocatalytic activities of these NWs were further studied with RHE as the reference electrode and were compared with the common BASF 3.2 nm Pt catalyst supported on carbon (C-Pt). Figure 6-3A, B shows the Tafel plots (A) with the specific activities (j_k, kinetic current density) as a function of electrode potential, and specific

activity comparisons (B) of $Fe_{20}Pt_{80}$ NWs, Co_8Pt_{92} NWs and commercial Pt catalysts at 0.9 V. The specific activity of $Fe_{20}Pt_{80}$ NWs reaches 1.53 mA/cm^2, which is higher than that of Co_8Pt_{92} NWs (0.639 mA/cm^2) and Pt catalyst (0.325 mA/cm^2). The present FePt NWs have the highest specific activity for ORR in all the reported 1D Pt-based NW or NT ORR catalysts such as starlike Pt NWs (0.611 mAcm^{-2}),[14] Pt NTs (0.38 mAcm^{-2})[17] and Pd-Pt core-shell NWs (0.77 mAcm^{-2}).[18] Moreover, the mass activity of $Fe_{20}Pt_{80}$ NWs is 844.0 mA/mg Pt, exceeding the DOE 2015 target at 440 mA/mg Pt.[26] The enhancement in both ORR activity and stability observed in FePt NWs arises very likely from the Pt-alloy effect and the strong interaction between NWs and the carbon support, which prevents these NWs from easy dissolution, Ostwald ripening, and aggregation in ORR conditions.[14,17,18]

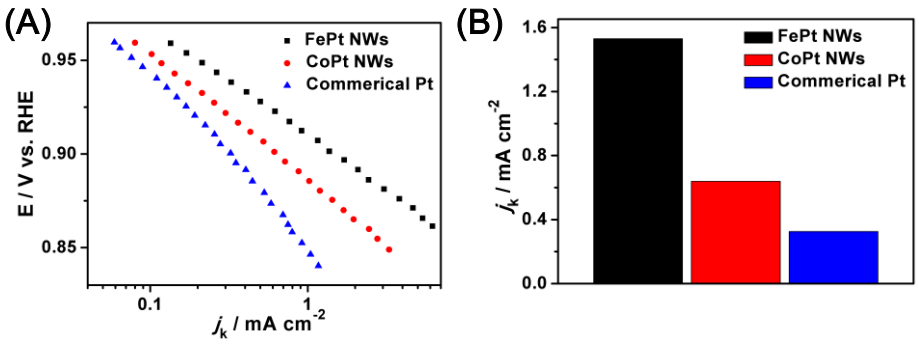

Figure 6-3 (A) Specific activities for ORR on different catalysts at different electrode potentials at 1600 rpm (Tafel plot), and (B) summary of specific activities for ORR at 0.9 V vs. RHE.

Thicker (6.3 nm) FePt NWs showed even better specific ORR catalysis in the current detection condition. The thicker NWs were synthesized by growing FePt over the pre-formed 2.5 nm $Fe_{56}Pt_{44}$ NWs (Experimental Section). Using this seed mediated growth, we could easily tune the diameter of FePt NWs from 2.5 nm to 6.3 nm with the nearly precise composition control at $Fe_{56}Pt_{44}$. TEM images (Figure S6-5) prove that these NWs are fairly uniform. XRD of these NWs (Figure S6-6) show diameter-dependent line broadening diffraction patterns, indicating that thicker NWs have larger crystal domains. Recent experiments demonstrate that acid treatment followed by thermal annealing is an important step to activate MPt NP catalyst for ORR.[27,28] We found that annealing the AA-treated NWs at 400 ^{o}C under Ar + 5% H_2 for 2 h was essential to further activate the NWs. However, none of the NWs thinner than 4 nm could survive such a combined treatment – they were broken down into irregular particulate structure (Figure S6-7). In contrast, the morphology of the 6.3 nm FePt NWs was nearly unchanged after this AA plus annealing treatment (Figure 6-4A) (their composition was at $Fe_{18}Pt_{82}$). These treated 6.3 nm $Fe_{18}Pt_{82}$ NWs were further studied as catalysts for ORR in 0.1 M $HClO_4$. From ORR activity comparisons of different catalysts (Figure S6-8A), we can see that the 6.3 nm FePt NWs treated by AA plus annealing have the best ORR specific activity at 3.9 mA cm^{-2}. The ORR stability of the annealed 6.3 nm FePt NWs was also studied in O_2-saturated 0.1 M $HClO_4$ by cycling the potentials between 0.6-1.0 V (vs. RHE) for 4000 cycles. As shown in the CVs (Figure 6-4B) and ORR polarization curves (Figure S6-8B), the annealed 6.3 nm FePt NWs have no ECASA drop and ORR polarization shift. We should note that under the same testing condition, the mass activity of these 6.3 nm FePt NWs is lower than the 2.5 nm FePt NWs due to the larger percentage Pt embedded inside

the 6.3 nm FePt NWs. Nonetheless, the results indicate that Pt alloy NWs can indeed be used to tune ORR catalysis.

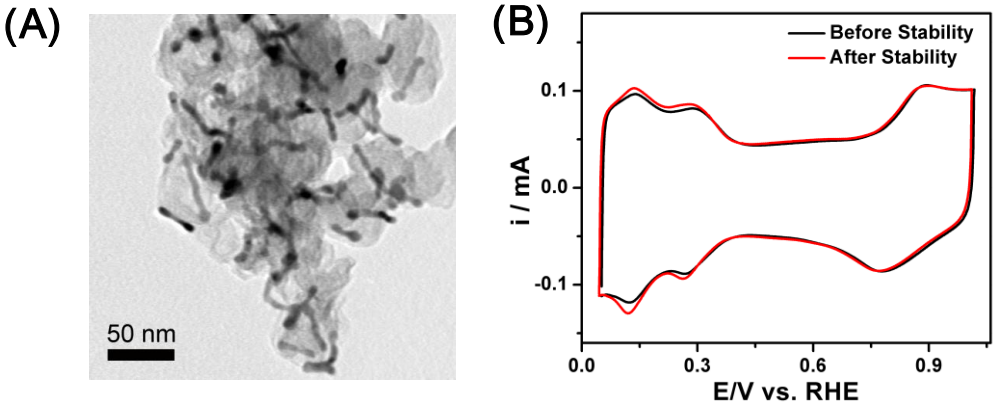

Figure 6-4 (A) TEM image of C-FePt NWs after annealing at 400 ^{o}C for 2 h in 95% Ar + 5% H_2. (B) CVs of the 6.3 nm annealed FePt NWs before and after 4000 potential cycles between 0.6-1.0 V vs. RHE.

In summary, FePt (or CoPt) NWs have been synthesized in high yield via a simple organic phase decomposition of $Fe(CO)_5$ (or $Co_2(CO)_8$) and reduction of $Pt(acac)_2$ in the 1-octadecene and oleylamine solution containing sodium oleate. Through controlling the molar ratio of $Fe(CO)_5$ or $Co_2(CO)_8$ to $Pt(acac)_2$, FePt (or CoPt) NW composition can be readily tuned. Treated with acetic acid, these FePt (or CoPt) NWs become active and stable for ORR in $HClO_4$ solution. The activity is dependent on the Fe or Co retention in FePt or CoPt NWs, and the stability is mostly decided by the NW shape. The specific and mass activities of the FePt NWs reach 1.53 mA/cm^2 and 844.0 mA/mg Pt, while those of

the common BASF 3.2 nm Pt catalyst is at 0.325 mA/cm^2 and 155.0 mA/mg Pt. These NWs represent a class of new catalyst that is capable of optimizing ORR catalysis and may be more applicable in practical energy devices.

6.3 Experimental Section

Synthesis of 2.5 nm FePt NWs. Under a gentle nitrogen flow and a magnetic stirring, 0.3 g of sodium oleate was dissolved in 12 mL of ODE by heating the suspension to 180 ºC. The solution was cooled down to 60 ºC, followed by adding 0.2 g of $Pt(acac)_2$ and 8 mL OAm, and further re-heating to 115 °C. 0.14 mL (or 0.08 mL, or 0.045 mL) of $Fe(CO)_5$ was injected into the reaction solution and the solution was further heated to 240 °C at a heating rate of 4-5 °C/min and kept at this temperature for 25 min to make $Fe_{68}Pt_{32}$ (or $Fe_{56}Pt_{44}$, or $Fe_{42}Pt_{58}$) NWs. 30 mL of hexane and then 50 mL of ethanol were added to precipitate out the product. The product was separated by centrifugation at 9500 rpm for 10 min. The NWs were dispersed in hexane for future use.

Synthesis of 2.5 nm CoPt NWs. For the synthesis of $Co_{63}Pt_{37}$ and $Co_{32}Pt_{68}$ NWs, the same recipe as the synthesis of FePt NWs was used except that $Co_2(CO)_8$ (180 mg or 136 mg) DCB solution was injected into the solution containing $Pt(acac)_2$. After the reaction, 44 mL hexane and 36 mL ethanol were consecutively added to precipitate out NWs.

Seed-Mediated Synthesis of FePt NWs thicker than 2.5 nm. 0.08 g $Pt(acac)_2$ was dissolved in 10 mL ODE, 1.4 mL OAm and 1.4 mL OA by heating the mixture to 115 ^oC under N_2 protection. 30 mg $Fe_{56}Pt_{44}$ NWs dispersed in 2 mL ODE and 0.032 mL $Fe(CO)_5$ were added under N_2 blanket, then the temperature was raised to 240 ^oC and kept at this temperature for 25 min. The solution was cooled down to room temperature,

and 25 mL ethanol was added to precipitate the NWs and the product was collected by centrifuge (8500 rpm, 8 min). The product (3.7 nm FePt NWs) was dispersed in 25 mL hexane and precipitated out by adding 25 mL ethanol. It was redispersed in 10 ml hexane for either catalytic use or for further NW growth. Under the same condition as the synthesis of 3.7 nm FePt NWs, 40 mg $Pt(acac)_2$ and 0.016 mL $Fe(CO)_5$ led to 4.6 nm FePt NWs, whereas 60 mg $Pt(acac)_2$ and 0.024 mL $Fe(CO)_5$, 80 mg $Pt(acac)_2$ and 0.032 mL $Fe(CO)_5$ yielded 5.5 and 6.3 nm FePt NWs, respectively.

NW Activation for ORR. 20 mg of NWs (20 mL) was added into 30 mg Ketjen carbon support suspended in a mixture of hexane/acetone (v/v 2/1, 30 mL) and further sonicated for 1 h. The obtained NW/C catalyst was separated by centrifugation, and washed with hexane for two times, and mixed with 30 mL of AA. The suspension was heated to 70 °C for overnight.[24,25] For the preparation of acid+annealed C-FePt NWs, according to the previous report on treating C-NiPt NPs,[27,28] the as-prepared C-FePt NWs were first thermally treated in the air at 200 ^oC overnight, and then mixed with 20 mL 0.1 M $HClO_4$ overnight to remove Fe on the surface of FePt NWs. Finally, the acid-treated C-FePt NWs were annealed in the forming gas (volume ratio: 5/95 H_2/N_2) at 400 ^oC for 2 h. All the catalysts were dispersed in a mixture containing water, isopropanol and Nafion (5%) (v:v:v 4:1:0.05) to form a 2 mg/mL suspension.

Electrochemical Test. 10 or 20 μL of catalyst ink was casted on the new polished glassy carbon (GC) electrode and dried at ambient condition. The test solution was 0.1 M $HClO_4$. The catalysts were cycled in the electrolyte until stable CVs were collected with a scanning rate of 50 mV/s in 0.1 M $HClO_4$ under N_2 or Ar saturation at room temperature,

and polarization curves for the ORR were measured with a scanning rate of 10 or 20 mV/s in the same electrolyte under O_2 saturation at 1600 rpm.

6.4 References

(1) Liang, Y.; Li, Y.; Wang, H.; Zhou, J.; Wang, J.; Regier, T.; Dai, H. *Nat Mater* **2011**, *10*, 780–786.

(2) Suntivich, J.; Gasteiger, H. A.; Yabuuchi, N.; Nakanishi, H.; Goodenough, J. B.; Shao-Horn, Y. *Nat Chem* **2011**, *3*, 546–550.

(3) Lu, Y.-C.; Xu, Z.; Gasteiger, H. A.; Chen, S.; Hamad-Schifferli, K.; Shao-Horn, Y. *J. Am. Chem. Soc.* **2010**, *132*, 12170–12171.

(4) Bing, Y.; Liu, H.; Zhang, L.; Ghosh, D.; Zhang, J. *Chem. Soc. Rev.* **2010**, *39*, 2184–2202.

(5) Wang, Y.-J.; Wilkinson, D. P.; Zhang, J. *Chem. Rev.* **2011**, *111*, 7625–7651.

(6) Mazumder, V.; Lee, Y.; Sun, S. *Adv. Funct. Mater.* **2010**, *20*, 1224–1231.

(7) Stamenkovic, V. R.; Mun, B. S.; Arenz, M.; Mayrhofer, K. J. J.; Lucas, C. A.; Wang, G.; Ross, P. N.; Markovic, N. M. *Nat Mater* **2007**, *6*, 241–247.

(8) Stamenkovic, V. R.; Fowler, B.; Mun, B. S.; Wang, G.; Ross, P. N.; Lucas, C. A.; Marković, N. M. *Science* **2007**, *315*, 493–497.

(9) Wu, J.; Zhang, J.; Peng, Z.; Yang, S.; Wagner, F. T.; Yang, H. *J. Am. Chem. Soc.* **2010**, *132*, 4984–4985.

(10) Wu, J.; Qi, L.; You, H.; Gross, A.; Li, J.; Yang, H. *J. Am. Chem. Soc.* **2012**, *134*, 11880–11883.

(11) Kim, J.; Lee, Y.; Sun, S. *J. Am. Chem. Soc.* **2010**, *132*, 4996–4997.

(12) Wang, C.; Van der Vliet, D.; Chang, K.-C.; You, H.; Strmcnik, D.; Schlueter, J. A.; Markovic, N. M.; Stamenkovic, V. R. *J. Phys. Chem. C* **2009**, *113*, 19365–19368.

(13) Wu, J.; Gross, A.; Yang, H. *Nano Lett.* **2011**, *11*, 798–802.

(14) Sun, S.; Zhang, G.; Geng, D.; Chen, Y.; Li, R.; Cai, M.; Sun, X. *Angew. Chem. Int. Ed.* **2011**, *50*, 422–426.

(15) Koenigsmann, C.; Zhou, W.; Adzic, R. R.; Sutter, E.; Wong, S. S. *Nano Lett.* **2010**, *10*, 2806–2811.

(16) Xia, B. Y.; Ng, W. T.; Wu, H. B.; Wang, X.; Lou, X. W. (David) *Angew. Chem. Int. Ed.* **2012**, *51*, 7213–7216.

(17) Chen, Z.; Waje, M.; Li, W.; Yan, Y. *Angewandte Chemie International Edition* **2007**, *46*, 4060–4063.

(18) Koenigsmann, C.; Santulli, A. C.; Gong, K.; Vukmirovic, M. B.; Zhou, W.; Sutter, E.; Wong, S. S.; Adzic, R. R. *J. Am. Chem. Soc.* **2011**, *133*, 9783–9795.

(19) Wang, C.; Hou, Y.; Kim, J.; Sun, S. *Angew. Chem. Int. Ed.* **2007**, *46*, 6333–6335.

(20) Sun, S.; Murray, C. B.; Weller, D.; Folks, L.; Moser, A. *Science* **2000**, *287*, 1989–1992.

(21) Sun, S. *Adv. Mater.* **2006**, *18*, 393–403.

(22) Guo, S.; Zhang, S.; Sun, X.; Sun, S. *J. Am. Chem. Soc.* **2011**, *133*, 15354–15357.

(23) Chen, M.; Kim, J.; Liu, J. P.; Fan, H.; Sun, S. *J. Am. Chem. Soc.* **2006**, *128*, 7132–7133.

(24) Mazumder, V.; Sun, S. *J. Am. Chem. Soc.* **2009**, *131*, 4588–4589.

(25) Guo, S.; Sun, S. *J. Am. Chem. Soc.* **2012**, *134*, 2492–2495.

(26) *U. S. Department of Energy, Technical Plan: Fuel Cells, 2007 (www1.eere.energy.gov/hydrogenandfuelcells/mypp/pdfs/fuel_cells.pdf).*

(27) Wang, C.; Chi, M.; Li, D.; Strmcnik, D.; Van der Vliet, D.; Wang, G.; Komanicky, V.; Chang, K.-C.; Paulikas, A. P.; Tripkovic, D.; Pearson, J.; More, K. L.; Markovic, N. M.; Stamenkovic, V. R. *J. Am. Chem. Soc.* **2011**, *133*, 14396–14403.

(28) Gan, L.; Heggen, M.; Rudi, S.; Strasser, P. *Nano Lett.* **2012**, *12*, 5423–5430.

6.5 Supporting Information

6.5.1 *Materials*. Oleylamine **(**OAm, >70%), Oleic acid (OA, 90%), 1-octadecene (ODE, 90%), $Fe(CO)_5$ (99.9+% trace metals basis), hexane (98.5%), ethanol (100%), acetic acid (AA, 99%) and 1,2-dichlorobenzene (DCB) were purchased from Sigma-Aldrich. $Pt(acac)_2$ (99.99%) was purchased from Strem. Sodium oleate (97%) was obtained from Tokyo Chemical Industry CO., LTD. The commercial C-Pt catalyst (46% loading) was purchased from BASF Company. The deionized water was obtained from a Millipore Autopure system. All the reagents were of analytical grade and used without further purification.

6.5.2 *Characterization*. The Inductively coupled plasma-atomic emission spectroscopy (ICP-AES) measurements were carried on a JY2000 Ultrace ICP Atomic Emission Spectrometer equipped with a JY AS 421 autosampler and 2400g/mm holographic grating. TEM were conducted on a Philips CM 20 operating at 200 kV. X-ray diffraction (XRD) characterization was carried out on a Bruker AXS D8-Advanced diffractometer with Cu Kα radiation (λ =1.5418 Å). The electrochemical measurements on GC electrode using Ag/AgCl as reference electrode and platinum wire as counter electrode, respectively, were performed on a Pine Electrochemical Analyzer, Model AFCBP1 (5 mm GC) and a Autolab 302 potentiostat (6 mm GC).

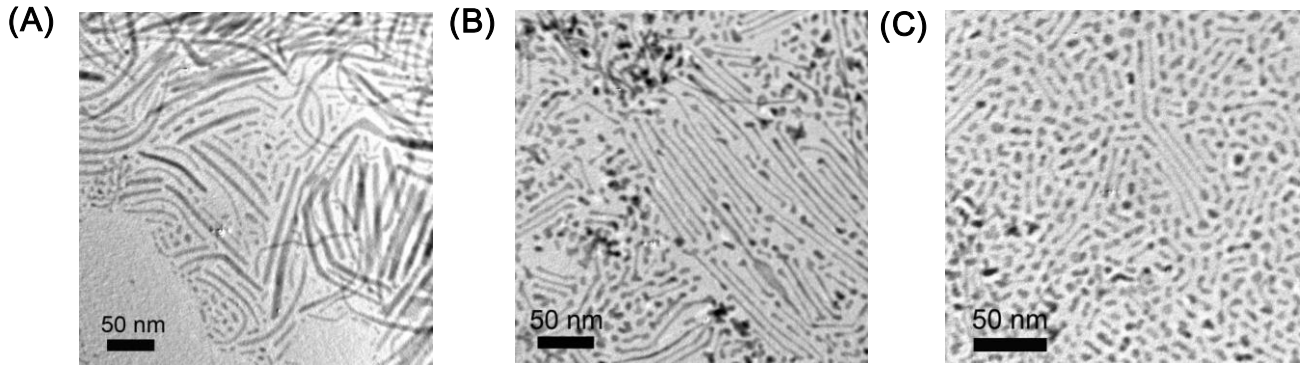

Figure S6-1. TEM images of different CoPt nanomaterials obtained through adding (A) 270, (B) 90 and (C) 63 mg $Co_2(CO)_8$ into the mixture containing $Pt(acac)_2$.

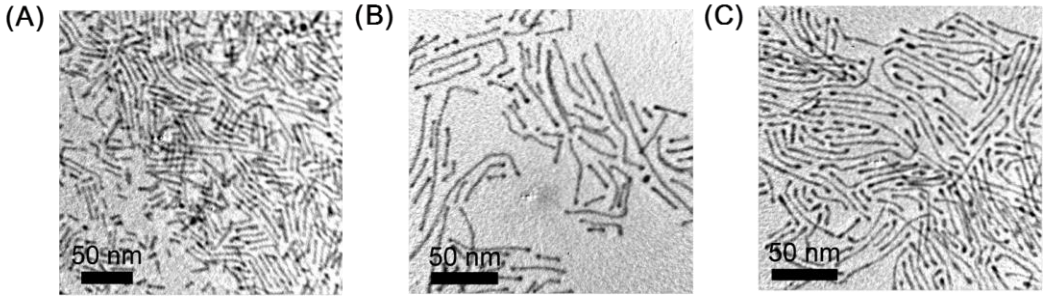

Figure S6-2. TEM images of (**A**) $Fe_{42}Pt_{58}$, (**B**) $Fe_{68}Pt_{32}$, and (**C**) $Co_{32}Pt_{68}$ NWs.

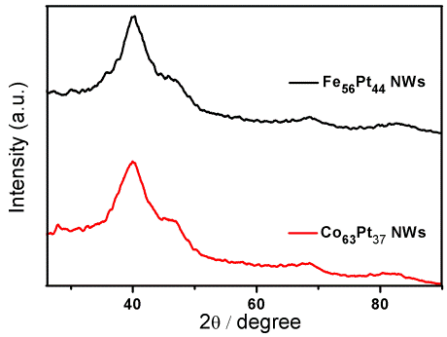

Figure S6-3. XRD patterns of $Fe_{56}Pt_{44}$ and $Co_{63}Pt_{37}$ NWs

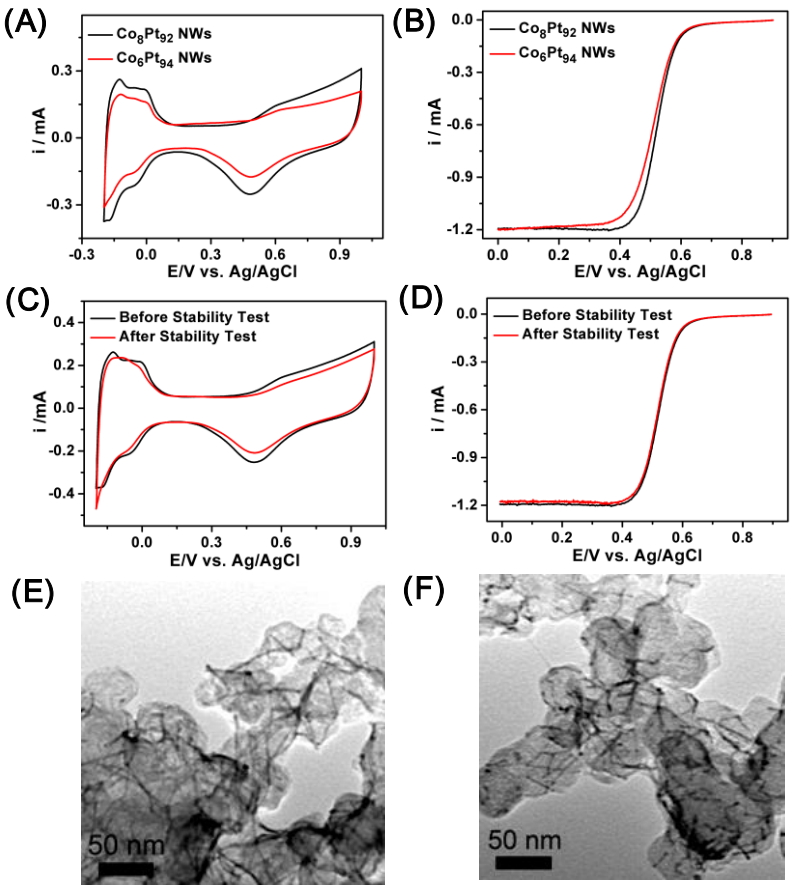

Figure S6-4. (**A**) CVs of CoPt NWs with different compositions in N_2-saturated 0.1 M $HClO_4$ at a scan rate of 50 mV/s, (**B**) their polarization curves for ORR in O_2-saturated 0.1 M $HClO_4$ at 293 K (The potential scan rate was 10 mV/s and the electrode rotation speed was 1600 rpm). The CVs (**C**) and polarization curves (**D**) of Co_8Pt_{92} NWs before and after 5000 potential cycles between 0.4-0.8 V vs. Ag/AgCl. TEM images of C-Co_8Pt_{92} NWs before (**E**) and after stability test (**F**).

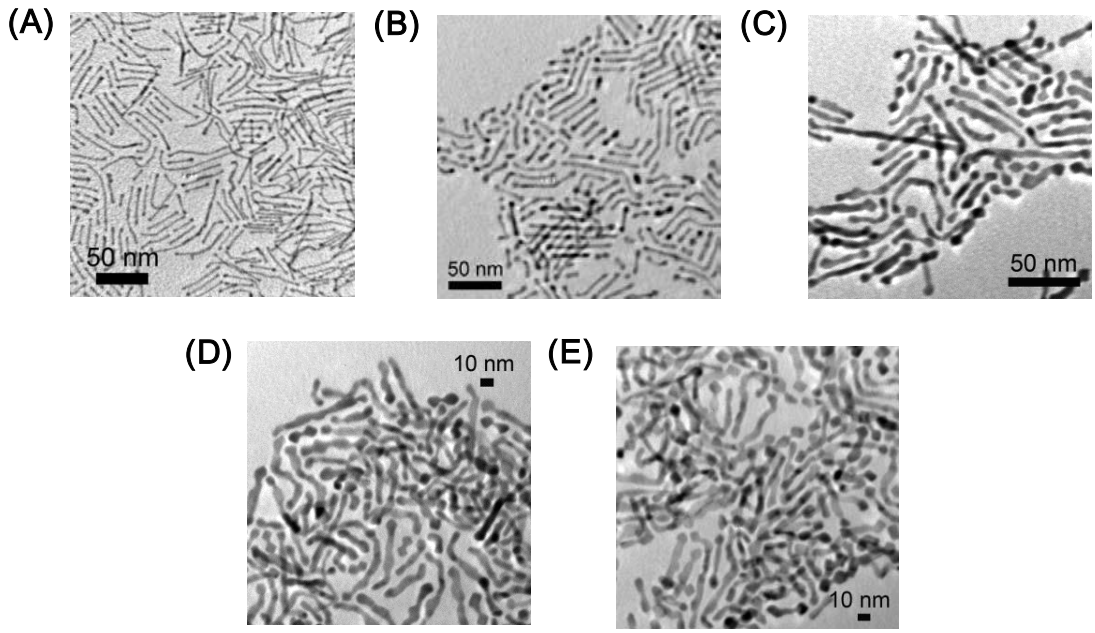

Figure S6-5. TEM images of FePt NWs with different diameters. (A) 2.5 nm, (B) 3.7 nm, (C) 4.6 nm, (D) 5.5 nm and (E) 6.3 nm.

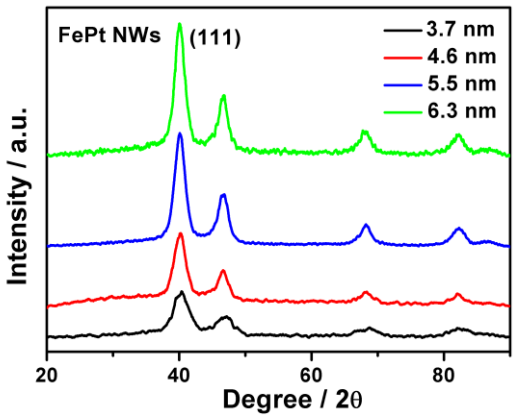

Figure S6-6. XRD pattern of FePt NWs with different diameters. The XRD results show the line broadening change with the change of the FePt NW diameters, indicating the crystal domain size increase with the increase in NW diameter.

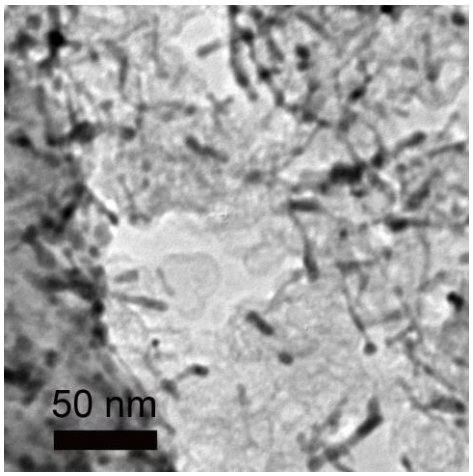

Figure S6-7. TEM image of 3.7 nm FePt NWs annealed at 400 ^{o}C for 2 h in the forming gas.

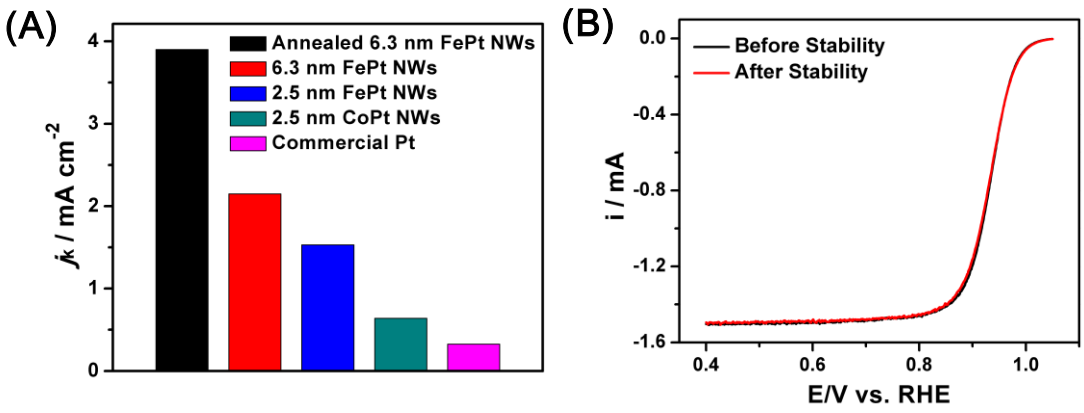

Figure S6-8. (A) Summary of specific activities for ORR on the 6.3 nm annealed FePt NWs, 6.3 nm FePt NWs, 2.5 nm FePt NWs, 2.5 nm CoPt NWs and commercial Pt at 0.9 V (vs. RHE). (B) ORR polarization curves of the 6.3 nm annealed FePt NWs before and after 4000 potential cycles between 0.6-1.0 V (vs. RHE).

VII. Core/Shell Au/PtCu Nanoparticles and Their Dual Electrocatalysis for Both Reduction and Oxidation Reactions

7.1 Introduction

Coupling fuel oxidation and oxygen reduction reactions at or near ambient conditions is an important approach to covert chemical energy stored in fuel to electric energy.[1] To ensure easy electron flow from fuel (via fuel oxidation) to oxygen (via oxygen reduction) at lower oxidation and reduction overpotentials, an efficient catalyst must be present to catalyze each of the two reactions.[2] Traditionally, nanoparticles (NPs) of Pt and its alloys with Ru are selected as such catalysts due to their relatively high activity and durability for both reactions in acidic media. Recently, the need to minimize the use of Pt has motivated the extended search for more efficient Pt NP catalysts with parameters tuned specifically in NP shapes,[3] Pt alloying with other early transition metals[4] and core/shell structures.[5] Among these three classes of catalysts studied, shape and alloy composition controlled catalysts often show some impressive enhancement in initial activity but have very limited improvement in stability unless the catalyst is prepared to have one-dimensional (1D) nanostructure.[6] Core/shell NPs, on the other hand, are found to be more promising as a robust catalyst. These Pt-based core/shell NPs with non-Pt core not only maximize Pt exposure to reactants, but also enhance Pt catalysis via strong core/shell interactions.[7] However, due to the difference in chemical reaction nature between oxygen reduction and fuel oxidation reactions, these core/shell catalysts are often applied to a specific one. Therefore, different kinds of Pt catalysts have to be developed to improve efficiency of these two reactions.

Herein we report a controlled synthesis of core/shell Au/PtCu NPs and demonstrate their enhanced dual catalysis for both oxygen reduction reaction (ORR) and methanol oxidation reaction (MOR) in 0.1 M $HClO_4$ solution. In studying core/shell NPs as robust catalyst for fuel cell reactions, we noticed that Au/$FePt_3$ NPs with 1.5 nm $FePt_3$ shell showed much improved activity and durability in catalyzing ORR in 0.1 M $HClO_4$ solution[5a] while PtFe/PtAu with PtFe in face centered tetragonal structure and Au segregating around the Pt shell were highly efficient for formic acid oxidation reaction (FAOR) and MOR.[8] However, they became ineffective if their role was switched. Interestingly, core/shell PtCu/Pt NPs made from controlled dealloying of Cu from PtCu NPs showed the enhanced ORR catalysis[7a] and cubic PtCu NPs were found to be active for FAOR and MOR with enhanced CO tolerance.[9] This indicated that PtCu as a catalyst component was capable of serving as a catalyst for both ORR and fuel oxidation reactions. Therefore, we synthesized core/shell Au/PtCu NPs *via* a seed-mediated growth method and expected that PtCu shell would exhibit dual catalysis and Au core would further enhance the catalysis by stabilizing the PtCu shell. Our tests showed that these Au/PtCu NPs were indeed efficient in its dual catalysis for both ORR and MOR. Its ORR and MOR specific (mass) activities reached 2.72 mA/cm^2 (1500 mA/mg_{Pt}) at 0.9 V and 0.755 mA/cm^2 (441 mA/mg_{Pt}) at 0.8 V (*vs* reversible hydrogen electrode, RHE) respectively.

7.2 Results and Discussion

The core/shell Au/PtCu NPs were prepared by simultaneous reduction of $Pt(acac)_2$ and $Cu(acac)_2$ in the mixture of 5 nm seeding Au NPs, HDD, OAm, OA and ODE at 200 °C.

In the synthesis, Au NPs were pre-made and coated with OAm. HDD served as a reducing agent and OA/OAm as surfactants. This seed mediated growth condition facilitated PtCu deposition around each Au NP, forming core/shell Au/PtCu with a uniform shell of PtCu. PtCu compositions were controlled by the molar ratio of $Cu(acac)_2$ to $Pt(acac)_2$ and analyzed by ICP-MS and EDS. For example, $Pt_{65}Cu_{35}$, $Pt_{50}Cu_{50}$ and $Pt_{36}Cu_{64}$ were obtained from 3:2, 1:1 and 3:5 Pt/Cu ratios respectively.

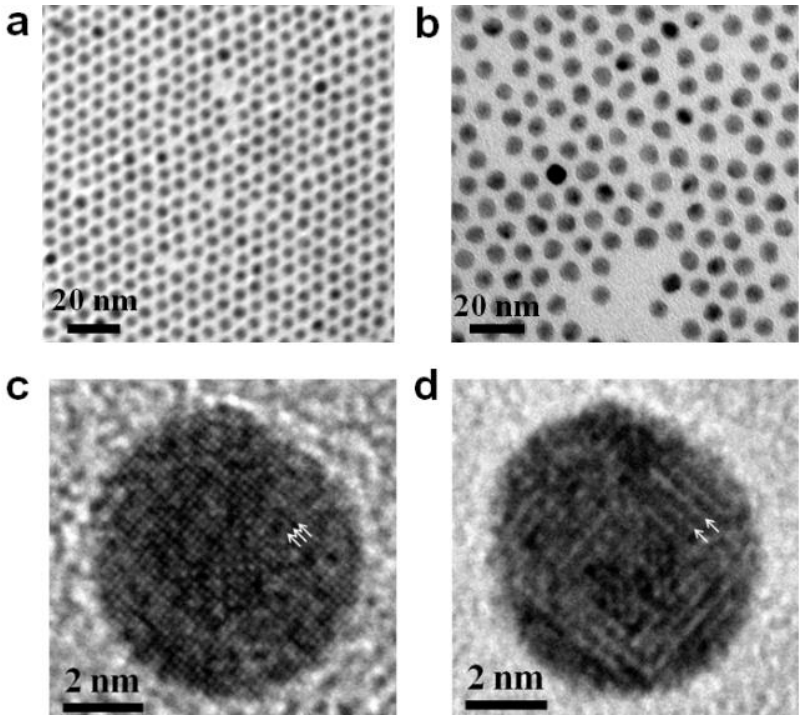

Figure 7-1. TEM images of (a) 5 nm Au NPs, (b) 7.5 nm Au/$Pt_{65}Cu_{35}$ NPs. (c,d) HRTEM images of a single Au/$Pt_{65}Cu_{35}$ NP acquired at different focus condition.

Figure 7-1a&b show the typical TEM images of the seeding 5 nm Au NPs and the core/shell NPs. After PtCu coating, the average size of the core/shell NPs was increased from 5 ± 0.5 nm (Au NPs) to 7.5 ± 0.5 nm (Au/PtCu), indicating the coating thickness was at 1.3 nm. High-resolution TEM (HRTEM) was used to analyze the detailed structure of a single NP, as shown in Figure 7-1c&d. The interface between Au core and Pt shell cannot be clearly seen due to the close scattering power and lattice paramter of Au and Pt in core and shell structure. There is also no clear evidence of the existence of misfit dislocation, as observed in the Au/PtFe system.[11] However, the HRTEM image of the same NP (Figure 7-1c) recorded at different focus condition (Figure 7-1d) **s**hows a long-range ordered structure as highlighted by the arrowheads, which must come from the PtCu alloy structure. The formation of the ordered structure indicates that PtCu is successfully coated over the Au core. The core/shell structure was further confirmed by the linear EDS scan across a single particle (Figure 7-2). Operated at 300 kV, the EDS revealed that the Au peak was 1 nm narrower than the Pt peak at the begining of the scan (the left side of the line scan, Figure 7-2a&b), indicating that the coating thickness was around 1 nm. However, at the end of the scan, the NP showed an alloy-type structure (Figure 7-2b). We also obtained the image of the NP we scanned and noticed the morphology change upon electron beam irradiation (Figure 7-2c). However, when the operation voltage was decreased to 200 kV, the EDS analysis showed clearly the core/shell structure (Figure 7-2d). This indicates that the core/shell Au/PtCu is indeed formed and high voltage electron beam used for EDS analysis can trigger the core/shell diffusion into the solid solution structure.

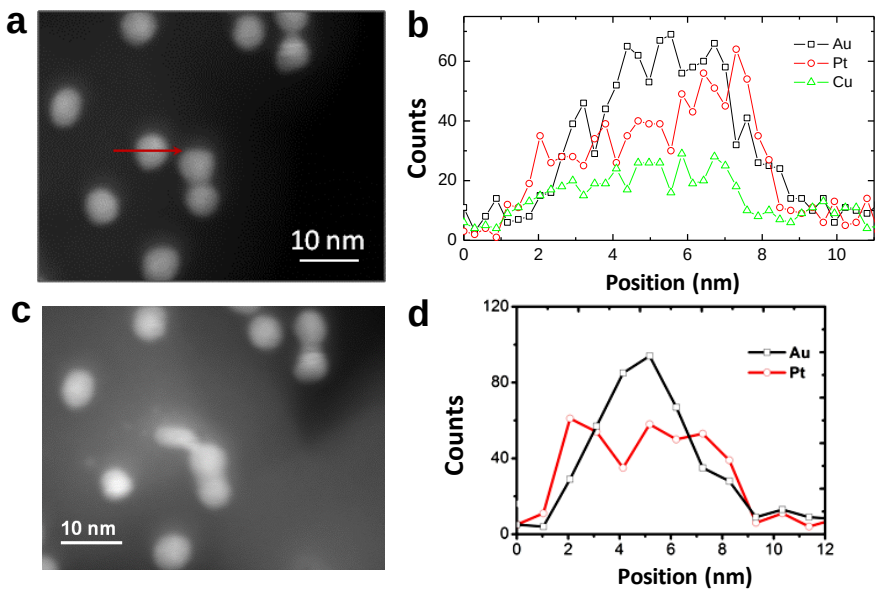

Figure 7-2. (a) HAADF-STEM image of the Au/PtCu NPs before the EDS scan at 300 kV, (b) line-scan EDS analysis across a single Au/PtCu NP indicated in (a), (c) HAADF-STEM image of the same Au/PtCu NPs shown in (a) after the EDS scan at 300 kV, indicating the diffusion between the core and shell, and (d) line-scan EDS analysis across a single Au/PtCu NP at 200 kV.

In the synthesis, the ratio of Au seeds over $Pt(acac)_2$ was kept the same and the amount of $Cu(acac)_2$ was used to control Cu/Pt compositions. Figure 7-3a is the plot of atomic % of Cu in PtCu shell *vs*. mol% $Cu(acac)_2$ used to react with 0.25 mmol $Pt(acac)_2$ in coating PtCu over Au NPs. The molar percentage of Cu in the shell structure (y-axis) is nearly the same as that of $Cu(acac)_2$ in the two precursors ($Cu(acac)_2$ and $Pt(acac)_2$) (x-axis), which indicates the Cu/Pt compositions are carried over to the final PtCu shell in our synthetic condition. Figure 7-3b shows the XRD patterns of the Au/Cu_xPt_{1-x} (x= 35,

50, 64) core/shell NPs and pure PtCu NPs. The (111) diffraction of the Au NPs appears at 38º while that of the $Cu_{50}Pt_{50}$ NPs at 41.4°. Once PtCu shell is coated on Au, the PtCu (111) peak appears between Au (111) and PtCu (111) peaks, indicating that the (111) lattice in the PtCu shell is increased compared to that in pure PtCu NPs due to the Au core effect. With more Cu present in the PtCu structure, the (111) peak shifts from 39.5º ($Au/Cu_{35}Pt_{65}$), 40.2º ($Au/Cu_{50}Pt_{50}$) to 40.8º ($Au/Cu_{64}Pt_{36}$), which follows the Vegard's law[12] and proves the formation of PtCu alloy structure. Incorportating more Cu in the PtCu shell led to a slight increase in shell thickness. For example, $Au/Cu_{35}Pt_{65}$ has a 1 nm shell, $Au/Cu_{64}Pt_{36}$ has 1.5 nm shell. The PtCu coating was further characterized by UV-Vis spectroscopy and electrochemical redox properties. The surface plasmonic absorption peak of the 5 nm Au NPs in hexane dispersion appeared at 520 nm. UV-Vis spectra of the core/shell NP dispersion in hexane showed no plasmonic absorption (Figure 7-3c). To test the electrochemical properties of these NPs, we first deposited the NPs on the Ketjen carbon support by sonicating for 1 h a mixture of NPs and carbon support in 5 mL hexane at a weight ratio of 1:2. We then used acetic acid and 0.1 M $HClO_4$ solution to wash the C-NP composite to remove the surfactants around each NP.[13] This combined acid treatments did not change either Au/Pt ratio or Cu composition. Cyclic voltammgrams (CVs) of the NPs recorded from 0.02 V to 1.61 V in N_2 saturated 0.1 M $HClO_4$ is given in Figure 7-3d. We can see that the C-Au NPs have a Au-O-related reduction peak at 1.08 V, while C-Au/PtCu NPs show only PtCu-O, no Au-O reduction peak, indicating that Au is embedded under the PtCu shell.

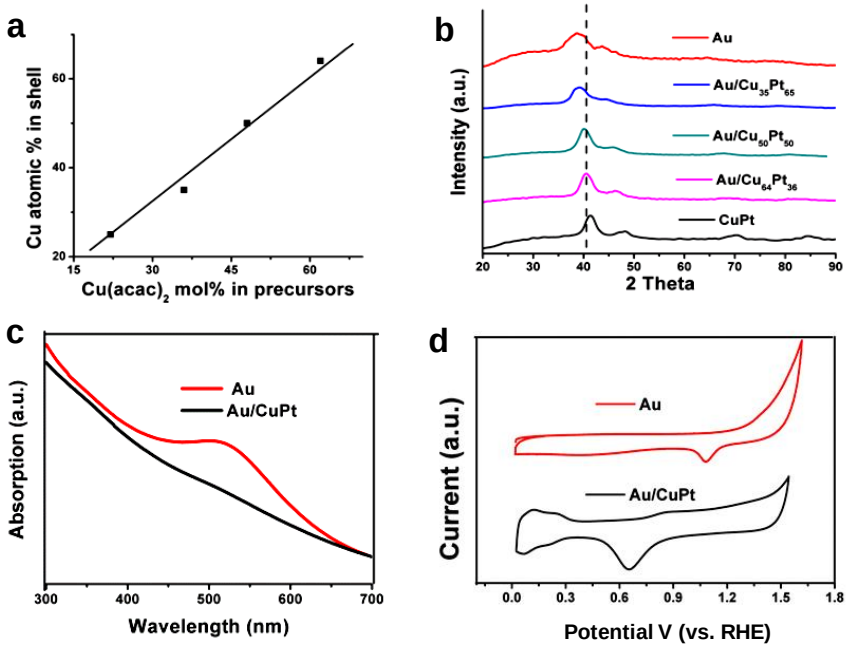

Figure 7-3. (a) Correlation between the amount of $Cu(acac)_2$ added and the amount of Cu obtained in the final PtCu shell (b) XRD pattern of Au/Cu_xPt_{1-x} (x= 35, 50, 64) core/shell NPs. (c) UV-Vis spectra of the 5 nm Au NPs and Au/PtCu NPs in hexane. (d) CVs of the C-Au and C-Au/PtCu in N_2-saturated 0.1 M $HClO_4$ solution

Cu in the Au/PtCu NPs could be further etched away electrochemically, forming Au/PtCu/Pt core/shell NPs. This was similar to electrochemically dealloying of Cu observed in PtCu NPs.[7a,14] Figure 7-4a lists several rounds of CV scans for the $Au/Cu_{64}Pt_{36}$ NPs. In the first anodic scan, there is a broad peak near 0.6-0.7 V which is referred to Cu dissolving process from the PtCu shell. In the backward cathodic scan, there are two peaks related to the reduction of Pt-O (0.8 V) and Cu-O oxide (0.6 V). During the second scan, the area of Cu dissolving peak decreased dramatically and the hydrogen desorption peak (0.04-0.4 V) increased, indicating the removal of surface Cu

and the formation of Pt layer. Once the dealloying reached equilibrium and there was no hydrogen desorption peak increase (after 50 cycles), Au/ $Pt_{50}Cu_{50}$ and Au/$Pt_{36}Cu_{64}$ were converted to Au/$Pt_{64}Cu_{36}$, and Au/$Pt_{65}Cu_{35}$ was turned to Au/ $Pt_{71}Cu_{29}$. The CO stripping peak of the dealloyed Au/$Pt_{64}Cu_{36}$ (Figure 7-4b) resembled the pure Pt[5a] and core/shell FePtCu/Pt nanorods,[15] confirming that Au/$Pt_{64}Cu_{36}$ NPs have a smooth Pt shell, forming Au/PtCu/Pt.

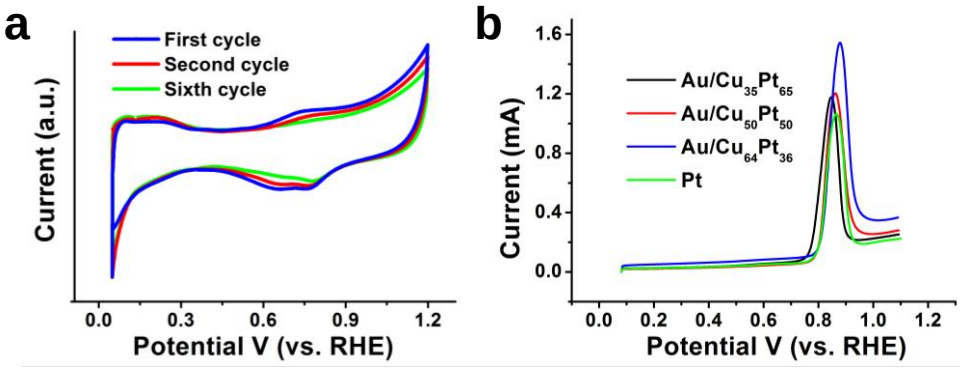

Figure 7-4. (a) CV curves of the C-Au/$Pt_{36}Cu_{64}$ catalyst during electrochemical dealloying at 100 mV/s. (b) CO stripping curves of the C-Au/Pt_xCu_{100-x} and C-Pt catalysts in 0.1 M $HClO_4$.

The electrocatalytic activity of these Au/PtCu (Au/PtCu/Pt) NPs for the ORR was studied. Figure 7-5a shows the representative CV curves obtained in N_2-saturated 0.1 M $HClO_4$ solution. The ORR polarization curves were obtained in O_2-saturated 0.1 M $HClO_4$ solution. The Tafel plots of three C-NPs (Au/$Pt_{65}Cu_{35}$, Au/$Pt_{50}Cu_{50}$ and Au/$Pt_{36}Cu_{64}$) were given in (Figure 7-5b). By comparing CV and ORR curves of different

Au/PtCu NPs, we noticed that the specific activities of the core/shell NPs were not Cu composition dependent. This is likely caused by the dealloying of Cu (leaving only 25-36% Cu present in the final core/shell structure) and the formation of Pt shell. The specific activities of the Au/PtCu reach as high as 2.75 mA/cm^2 at 0.9 V which is nearly five times higher than that from the 5 nm commercial Pt (commercial TKK TEC10E50E-HT 5 nm Pt 50.5% wt. Pt loading) (0.58 mA/cm^2). Figure 7-5c lists the specific and mass activities of the core/shell NPs and Pt NPs for ORR. The core/shell NPs have the mass activity up to 1700 mA/mg_{Pt} at 0.9 V (from the $Au/Pt_{36}Cu_{64}$ NPs), six times higher than that of the commercial 5 nm Pt (270 mA/mg_{Pt}). The stability of the Au/PtCu NPs was also tested by performing 5000 potential sweeps between 0.60 V and 1.10 V at 100 mV/s in O_2-saturated 0.1 M $HClO_4$ solution. Figure 7-5a show the CV s of the $Au/Pt_{65}Cu_{35}$ NPs before and after the test. The ECASA of the Au/PtCu dropped only 7.8% after this stability test while that of the commercial Pt reduced by 20%. TEM analysis further confirmed the stability of the Au/PtCu NPs as they showed little morphology change after the stability test (Figure 7-5d).

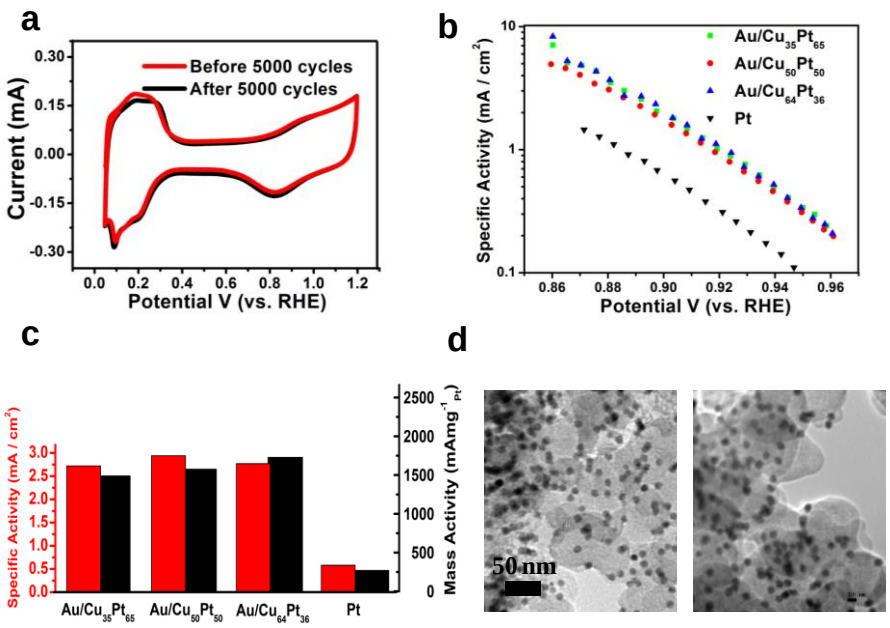

Figure 7-5. (a) CVs of C-Au/$Pt_{65}Cu_{35}$ NPs before and after 5000 potential cycles between 0.6 and 1.0 V. (b) Activity-potential plots of C-Au/Pt_xCu_{100-x} and C-Pt catalysts. (c) Specific and Pt mass activities of C-Au/Pt_xCu_{100-x} and C-Pt catalysts at 0.9 V. (d) TEM of C-Au/$Pt_{65}Cu_{35}$ NPs before (left) and after (right) 5000 potential cycles.

The Au/PtCu NPs were also active catalyst for MOR. Figure 7-6 summarizes the CV oxidation and stability test results. Among all core/shell NPs studied, the Au/$Pt_{36}Cu_{64}$ NPs showed the highest catalytic activity (Figure 7-6a). Even after 1 h of stability test, the catalytic activity of the Au/$Pt_{36}Cu_{64}$ NPs was still much higher than Pt (Figure 7-6b). This high activity is attributed to the high CO tolerance of the Au/PtCu NPs as characterized by the current ratio change between two peaks in forward (I_f) and backward (I_b) scans in the CV - the larger the ratio is, the better the CO removal activity of the

catalyst.[16] The mass activity of the $Au/Cu_{64}Pt_{36}$ NPs was calculated to be around 441 mA/mg_{Pt}, four times higher than Pt NPs at 0.8 V.

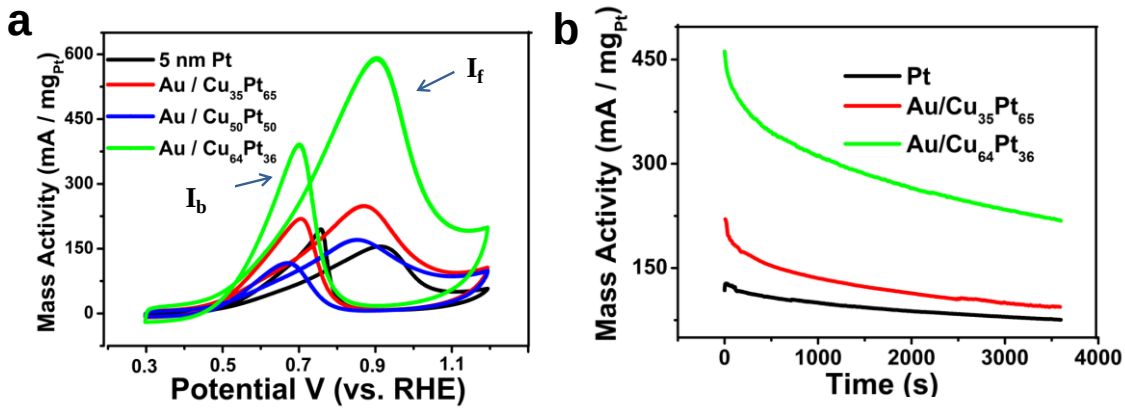

Figure 7-6 (a) MOR curves and (b) catalyst stability test at 0.8 V in 0.1 M $HClO_4$ + 0.1 M methanol.

The observed enhancement of the Au/PtCu NPs on both ORR and MOR catalysis is likely caused by the combination of alloy and strain effects present in the core/shell structure. Similar to what has been predicted and observed, alloying Pt with an early transition metal lowers the Pt *d*-band level, weakening the binding of oxygenated spectator (blocking) species (e.g., OH^-) to Pt and increasing the number of active Pt sites that are accessible to oxygen.[17] The formation of Au/PtCu/Pt may also have the surface Pt lattice compressed, further favoring ORR.[7a] The presence of electropositive Au in the core can prevent Pt from easy oxidation,[5a, 18] stabilizing the Pt shell in the ORR condition. The Au core and Cu alloying effects must also help methanol

adsorption/activation on Pt with high CO tolerance, rendering the Au/PtCu/Pt NPs equally effective in catalyzing MOR.

7.3 Conlcusion

We have reported a facile synthesis of monodisperse 5/1.5 nm Au/PtCu NPs by co-reduction of $Pt(acac)_2$ and $Cu(acac)_2$ in the mixture of 5 nm seeding Au NPs, HDD, OAm, OA and ODE at 200 °C. The Au core provides the proper nucleation sites for PtCu alloy formation and, as a result, the nucleation/growth of the PtCu shell occurs at a lower temperature without the formation of free PtCu NPs. Due to the PtCu alloy effect and core/shell interactions, these Au/PtCu NPs show promising dual catalysis for both ORR and MOR in 0.1 M $HClO_4$ solution with their ORR specific (mass) activities reaching 2.72 mA/cm^2 (1500 mA/mg_{Pt}) at 0.9 V and MOR specific (mass) activities at 0.755 mA/cm^2 (441 mA/mg_{Pt}) at 0.8 V. Our tests prove that the existence of Au NP core not only minimizes the Pt usage in its catalysis for fuel cell reactions, but also improve drastically the stability of the core/shell catalyst. The results suggest that the core/shell design is indeed effective for optimizing NP catalysis. The same concept may be extended to other multimetallic NP system, making it possible to tune NP catalysis for many different chemical reactions.

7.4 Experimental Section

7.4.1 *Materials***.** 1-Octadecene (ODE), borane t-butylamine complex (BBA), oleic acid (OA), 1,2,3,4-tetrahydronaphthalene (tetralin), platinum acetylacetonate ($Pt(acac)_2$),

copper acetylacetonate ($Cu(acac)_2$), 1,2-hexadecanediol (HDD) and Nafion 117, carbon black (Kejen EC 300J) were all from Sigma Aldrich. Oleylamine (OAm) was from Acros Organics. $HAuCl_4 \bullet 3H_2O$ was from Strem Chemicals. All chemicals were used as received.

7.4.2 *Instruments*. Transmission electron microscopy (TEM) images were acquired on a Philips EM 420 (120 kV). High resolution TEM (HRTEM) images were obtained on a JEOL 2010 TEM (200 kV). High resolution high-angle annular dark-field scanning TEM (HAADF-STEM) and elemental mapping images were obtained on a JEOL 2200FS microscope with a beam size of ~0.8 Å for imaging and ~ 2 Å for chemical analysis. All TEM samples were prepared by depositing a drop of diluted NP dispersion in hexane on copper grid coated with amorphous carbon. X-ray diffraction (XRD) patterns were collected on a Bruker AXS D8-Advanced diffractometer with Cu Kα radiation (λ=1.5418 Å). The inductively coupled plasma mass spectrometry (ICP-AES) analyses were performed on a JY2000 Ultrace ICP Atomic Emission Spectrometer equipped with a JY AS 421 autosampler and 2400 g/mm holographic grating. Energy dispersive X-ray spectroscopy (EDS) was carried out on a Joel JSM-6060 scanning electron microscopy (SEM). Samples for EDS were deposited on a graphitized porous carbon support. UV-Vis spectra were recorded on a Perkin Elmer Lambda 35 spectrometer. Electrochemical measurements were carried out on a Pine Electrochemcial Analyzer, model AFCBP1. Ag/AgCl (filled with 0.1 M KNO_3) and Pt wire were used as reference and counter electrodes respectively. All potentials were calibrated against reversible hydrogen electrode (RHE).

7.4.3 *Synthesis of Au NPs*. Au NPs were synthesized through adopting the previous protocol.[10] $HAuCl_4 \cdot 3H_2O$ (0.2 g) was dissolved in tetralin (10 mL) and OAm (10 mL), and the solution was cooled in ice bath (0 °C). BBA (1 mmol), tetralin (1 mL), and OAm (1 mL) were mixed by sonication and quickly injected into the above solution. The reaction mixture was further stirred at room temperature for 3 h. Au NPs were precipitated by adding acetone and collected by centrifugation. The product was re-dispersed in hexane and separated by adding ethanol and centrifugation. The final product was dispersed in hexane.

7.4.4 *Synthesis of Au/PtCu core/shell NPs*. $Cu(acac)_2$ (0.25 mmol) $Pt(acac)_2$ (0.25 mmol) and HDD (2 mmol) were dissolved in 10 mL ODE with 1.2 mL OA and 1.6 mL OAm before Au NPs (35 mg) in hexane (1 mL) were added. The mixture was heated to 120 °C under a gentle N_2 flow to remove hexane before it was heated to 200 °C at a heating rate of 2 °C/min and kept at this temperature for 30 min. The reaction mixture was cooled down to room temperature. The product was precipitated by isopropanol and collected by centrifugation. The product was re-dispersed in hexane and separated by adding ethanol and centrifugation. The final product was dispersed in hexane.

7.4.5 *Electrochemical measurements*. 10 mg of the as-synthesized NPs and 20 mg Ketjen-300J carbon support were mixed in 10 ml hexane and sonicated with a Fischer Scientific FS 110 for 60 min. The product was then suspended in 20 mL acetic acid at 60 °C overnight under a mild N_2 flow. The catalyst (C-NPs) was separated by centrifugation and washed with ethanol three times before it was suspended in de-ionized water at a concentration of 2 mg/mL. 0.5% (v/v) nafion was added and the suspension was sonicated for 1 h.

10 μL of C-NPs in water was dropped on a rotation disk electrode (RDE) with a glassy carbon surface (5 nm in diameter from Hokuto Denko Corp., Japan). Water was slowly evaporated in the air and another 10 μL of C-NPs was dropped on the electrode and dried to ensure a complete coverage of electrode surface.

Surface cleaning process was carried out by CV scanning in N_2 saturated 0.1 M $HClO_4$ at room temperature between 0.05 V and 1.20 V at a scan rate of 50 mV/s for 100 scans. CO stripping voltammetry was performed by scanning between 0.05 and 1.10 V in the Ar purged 0.1 M $HClO_4$ at 50 mV/s after a $CO_{adlayer}$ was formed on the NP surface in the CO saturated 0.1 M $HClO_4$ at 0.10 V. Oxygen reduction reaction (ORR) catalyzed by C-NPs was measured by rotation disk electrode at 1600 rpm and 20 mV/s. The catalyst stability was checked by scanning between 0.60 V and 1.10 V at 100 mV/s for 5000 sweeps. Methanol oxidation reaction (MOR) catalyzed by the same C-NPs was evaluated in the N_2 saturated 0.1 M $HClO_4$ containing 0.1 M methanol at room temperature. The CV scan was carried out between 0.3-1.2 V with a scan rate of 20 mV/s. The stability was tested by chronoamperometry at 0.8 V for 1 h.

Acknowledgement

This work was supported by the U.S. Army Research Laboratory and the U.S. Army Research Office under the Multi University Research Initiative (MURI, grant number W911NF-11-1-0353) on "Stress-Controlled Catalysis via Engineered Nanostructures".

7.5 References

(1) a) Reed, T. B.; Lerner, R. M. *Science* **1973**, *182*, 1299-1304. b) Barbir, F. *PEM Fuel Cells: Theory and Practice*, Academic Press, **2005**, p. 1-38.

(2) a) Mark, K. D. *Nature* **2012**, *486*, 43-51. b) Zhang, J. *PEM Fuel Cell Electrocatalysts and Catalyst Layers: Fundamentals and Applications*, Springer, **2008**, p. 355-373. c) Wieckowski, A. *Fuel Cell Catalysis: A Surface Science Approach*, WILEY-VCH, Weinheim, **2008**, p. 271-375.

(3) a) Wang, C.; Daimon, H.; Onodera, T.; Koda, T.; Sun, S. *Angew. Chem. Int. Ed.* **2008**, *47*, 3588-3591. b) Porter, N. S.; Wu, H.; Quan, Z.; Fang, J. *Acc. Chem. Res.* **2013**, *46*, 1867-1877. c) Kang, Y.; Li, M.; Cai, Y.; Cargnello, M.; Diaz, R. E.; Gordon, T. R.; Wieder, N. L.; Adzic, R. R.; Gorte, R. J.; Stach, E. A.; Murray, C. B. *J. Am. Chem. Soc.* **2013**, *135*, 2741-2747.

(4) a) Wang, C.; Markovic, N. M.; Stamenkovic, V. R. *ACS Catal.* **2012**, *2*, 891-898. b) Zhang, J.; Fang, J. *J. Am. Chem. Soc.* **2009**, *131*, 18543-18547. c) Wu, J.; Qi, L.; You, H.; Gross, A.; Li, J.; Yang, H. *J. Am. Chem. Soc.* **2012**, *134*, 11880-11883.

(5) a) Wang, C.; Vliet, D.; More, K. L.; Zaluzec, N. J.; Peng, S.; Sun, S.; Daion, H.; Wang, G.; Greeley, J.; Pearson, J.; Paulikas, A. P.; Karapetrov, G.; Strmcnik, D.; Markovic, N. M.; Stamenkovic, V. R. *Nano Lett.* **2011**, *11*, 919-926. b) Mazumder, V.; Chi, M.; More, K. L.; Sun, S. *J. Am. Chem. Soc.* **2010,** *132*, 7848-7849. c) Gong, K.; Su, D.; Adzic, R. R. *J. Am. Chem. Soc.* **2010**, *132*, 14364-14366. d) Koenigsmann, C.; Santulli, A. C.; Gong, K.; Vukmirovic, M. B.; Zhou, W.; Sutter, E.; Wong, S. S.; Adzic, R. R. *J. Am. Chem. Soc.* **2011**, *133*, 9783-9795.

(6) Guo, S.; Li, D.; Zhu, H.; Zhang, S.; Markovic, N. M.; Stamenkovic, V. R.; Sun, S. *Angew. Chem. Int. Ed.* **2013**, *52*, 3465-3468.

(7) a) Strasser, P.; Koh, S.; Anniyev, T.; Greeley, J.; More, K.; Yu, C.; Liu, Z.; Kaya, S.; Nordlund, D.; Ogasawara, H.; Toney, M. F.; Nilsson, A. *Nat. Chem.* **2010**, *2*, 454-460. b) Hwang, S.; Yoo, S.; Shin, J.; Cho, Y.; Jang, J.; Cho, E.; Sung, Y.; Nam, S.; Lim, T.; Lee, S.; Kim, S. *Sci. Rep.* **2012**, *3*, 1309.

(8) Zhang, S.; Guo, S.; Zhu, H.; Su, D.; Sun, S. *J. Am. Chem. Soc.* **2012**, *134*, 5060-5063.

(9) a) Xu, D.; Liu, Z.; Yang, H.; Liu, Q.; Zhang, J.; Fang, J.; Zhou, S.; Sun, S. *Angew. Chem. Int. Ed.* **2009**, *48*, 4217-4221. b) Xu, D.; Bliznakov, S.; Liu, Z.; Fang, J.; Dimitrov. N. *Angew. Chem.* **2010**, *122*, 1304-1307.

(10) Peng, S.; Lee, Y.; Wang, C.; Yin, H.; Dai, S.; Sun, S. *Nano Res.* **2008**, *1*, 229-234.

(11) Ding, Y.; Sun, X.; Wang, Z. L.; Sun, S. *Appl. Phys. Lett.* **2012.** *100*, 111603.

(12) Denton, A. R.; Ashcroft, N. W. *Phys. Rev. A* **1991**, *43*, 3161-3164.

(13) Mazumder, V.; Sun, S. *J. Am. Chem. Soc.* **2009**, *131*, 4588-4589.

(14) a) Koh, S.; Strasser, P. *J. Am. Chem. Soc.***2007**, *129*, 12624-12625. b) Gupta, G.; Slanac, D. A.; Kumar, P.; Wiggins-Camacho, J. D.; Wang, X.; Swinnea, S.; More, K. L.; Dai, S.; Stevenson, K. J.; Johnston, K. P. *Chem. Mater.* **2009**, *21*, 4515-4526.

(15) Zhu, H.; Zhang, S.; Guo, S.; Su, D.; Sun, S. *J. Am. Chem. Soc.* **2013**, *135*, 7130-7133.

(16) Sharma, S; Ganguly, A.; Papakonstantinou, P.; Miao, X.; Li, M.; Hutchison, J. L.; Delichatsios, M.; Ukleja, S. J. *J. Phys. Chem. C.* **2010**, *114*, 19459-19466.

(17) a) Stamenkovic, V. R.; Fowler, B.; Mun, B. S.; Wang, G. F.; Ross, P. N.; Lucas, C. A.; Markovic, N. M. *Science* **2007**, *315*, 493-497. b) Wang, C.; Markovic, N. M.; Stamenkovic, V. R. *ACS Catal.* **2012**, *2*, 891-898; c) Greeley, J.; Stephens, I. E. L.; Bondarenko, A. S.; Johansson, T. P.; Hansen, H. A.; Jaramillo, T. F.; Rossmeisl1, J.; Chorkendorff , I.; Nørskov, J. K. *Nat. Chem.* **2009**, *1*, 552-556.

(18) Zhang, J.; Sasaki, K.; Sutter, E.; Adzic, R. R. *Science*, **2007**, *315*, 220-222.

VIII. A General Approach to Multimetallic Core/Shell Nanoparticles for Oxygen Reduction Reaction

8.1 Introduction

In recent search for highly efficient catalysts applicable to commercially viable fuel cells and other energy conversion devices, Pt-based core/shell nanoparticles (NPs) are found to show much improved activity and durability in catalyzing oxygen reduction reaction (ORR).[1-7] In this core/shell NP structure, core can be made from non-Pt metals and shell consists of either elemental Pt or its alloys. When used as ORR catalyst, such a core/shell structure has some distinct advantages over the conventional single component PtM alloy catalysts: 1) with Pt only present in thin shell, Pt amount is greatly reduced; 2) intimate contact and crystal lattice mismatch between the core and Pt shell may lead to a better control of strain (geometric) effect of the Pt shell on catalysis;[1-5] 3) Pt alloying with other early transition metals and the induced strain in Pt shell also cause the shift of its *d*-band center, further affecting its redox properties, its interaction with reaction species, and its catalysis.[6-10] Despite the fact that recent catalytic demonstrations focus mostly on ORR, such core/shell structures can be applied easily to catalyze many other chemical reactions, providing an advanced catalyst system for chemical reactivity tuning and optimization. The key to the success of developing these core/shell NP catalysts is in the synthesis with precise controls on dimensions and compositions of both core and shell.

Core/shell structures are often prepared by galvanic replacement reaction.[2, 4, 5] In this approach, a Cu monolayer is first coated over a core metal and this Cu monolayer is then subject to the galvanic replacement by Pt *via* the reaction $Cu + Pt^{2+} \rightarrow Cu^{2+} + Pt$. This technique has been used to coat an atomic layer of Pt onto many different metallic NPs. Core/shell NPs can also be prepared by surface dealloying. In this method, alloy PtM NPs are prepared and top surface layers of M in the alloy structure are removed by electrochemical etching, producing PtM/Pt-type core/shell structures.[1, 11] More recently, core/shell NPs are found to be well prepared by seed-mediated growth via growing Pt shell over the monodisperse NPs. In this synthesis, core NPs are first prepared and shell material is controlled to nucleate and grow around the core NPs, as demonstrated in the synthesis of Pd/PtFe,[7] Au/PtFe,[6] AuCu/Pt,[12] as well as Pd/Au and Pd/Au/FePt NPs.[13] Such seed-mediated growth provides the necessary controls on both core dimensions and shell thickness so that the catalytic properties of the core/shell NPs is better controlled by the core/shell interactions and by shell thickness.[6, 7]

Since the core/shell NPs have shown great advantages over the single component and alloy NP catalyst in NP catalysis tuning, it is important to develop a general approach to prepare multimetallic core/shell NPs so that electronic and geometric (strain) effects of the core/shell NPs can be rationally controlled and their catalysis be tuned to optimization. Recently, we demonstrated that the seed-mediated growth method could be used to prepare Au/PtFe, Pd/PtFe, Pd/Au, Pd/Au/PtFe with controlled shell thickness, composition and ORR catalysis.[6, 7, 13] We further studied the synthesis and found that monodisperse core/shell Au/PtM NPs with M = Fe, Co, Cu, Mn, Ag could be readily prepared. We noticed that PtM shell thicker than 1 nm was key to the formation of

uniform PtM coating over the Au NP core and the resultant core/shell NPs with shell around 1 nm thick show much enhanced catalytic activity and durability for ORR. Our seed-mediated synthesis can be extended to other metal cores (such as Pd or Ag core) and alloy shells, providing a general approach to multimetallic core/shell NPs with tunable catalysis not only for ORR, but also for many other important chemical reactions.

8.2 Experimental Section

8.2.1 *Materials*. Oleylamine (80-90%, OAm), oleic acid (OA), 1-octadecene (ODE), iron pentacarbonyl ($Fe(CO)_5$), cobalt carbonyl ($Co_2(CO)_8$), manganese carbonyl ($Mn_2(CO)_{10}$), 1,2,3,4-Tetrahydronaphthalene (tetralin), borane t-butylamine complex (TBB), 1,2-hexadecandiol, 1-adamantanecarboxylic acid, dichlorobenzene (DCB) were purchased from Sigma Aldrich. Platinum acetylacetonate ($Pt(acac)_2$), hydrogen tetrachloroaurate (III) hydrate ($HAuCl_4 \cdot 3H_2O$), copper(II) acetylacetonate ($Cu(acac)_2$), silver nitrate ($AgNO_3$), palladium(II) acetylacetonate ($Pd(acac)_2$) were purchased from Strem. The deionized water was from a Millipore Autopure system. All the reagents were of analytical grade and used without further purification.

8.2.2 *Synthesis of Au Seed NPs*.[16] To synthesize 4-5 nm Au NPs, 0.2 g $HAuCl_4$ was dissolved in 10 ml tetralin and 10 ml OAm under N_2 flow at 15 °C with vigorous magnetic stirring. 0.5 mmol TBB was dissolved in 1 ml tetralin and 1 ml OAm by sonicating, and was injected into the precursor solution. The mixture was stirred for 1 h before 40 ml acetone was added and Au NPs were collected by centrifugation (8500 rpm, 8 min). The product was dispersed in 20 ml hexane and precipitated by 40 ml ethanol before it was redispersed in hexane for further use.

8.2.3 *Synthesis of Au/CoPt core/shell NPs*. In a typical synthesis of 4/1.5 nm Au/$Pt_{75}Co_{25}$ core/shell NPs, 0.25 mmol $Pt(acac)_2$ and 36 mg Au NPs were mixed with 3 mmol adamantanecarboxylic acid and 16 mmol hexadecylamine (or OAm) in 10 ml ODE solvent. The mixture was heated to 100 °C under N_2 flow for 10 min to remove air/moisture. Under a blanket of N_2 atmosphere, 0.25 mmol $Co_2(CO)_8$ dissolved in DCB was injected into the solution. The solution was then further heated to 200 °C at a heating rate of 2 °C /min and kept at this temperature for 1 h before it was cooled to room temperature. The product was collected by centrifugation after adding 40 ml isopropanol. The product was dispersed in 20 ml hexane and precipitated with 40 ml ethanol. The final product was re-dispersed in hexane for further use.

To synthesize Au/$Pt_{75}Co_{25}$ core/shell NPs with different PtCo shell thickness, Au seed amount and Co, Pt precursor amount were carefully tuned. 36 mg 4 nm Au, 0.13 mmol $Pt(acac)_2$, 0.13 mmol $Co_2(CO)_8$ resulted in 4/0.8 nm Au/ $Pt_{75}Co_{25}$ NPs. 36 mg 4 nm Au, 0.25 mmol $Pt(acac)_2$, 0.25 mmol $Co_2(CO)_8$ gave 4/1.5 nm Au/$Co_{25}Pt_{75}$ NPs. To further increase the PtCo shell thickness to 2.5 nm, 36 mg 4/1.5 nm Au/$Co_{25}Pt_{75}$ NPs, instead of 36 mg Au NPs, were used as seeds.

The Co compositions in the Au/PtCo NPs were controlled by reaction temperatures. $Pt_{75}Co_{25}$, $Pt_{65}Co_{35}$ and $Pt_{50}Co_{50}$ shell were formed from 200 °C, 220 °C and 250 °C heating respectively.

8.2.4 *Synthesis of Au/Pt NPs and Au/$Mn_{50}Pt_{50}$ NPs*. In a typical synthesis of 4/1.5 nm Au/Pt NPs, 0.25 mmol $Pt(acac)_2$ and 36 mg Au NPs were mixed with 20 mmol OAm and 5 mmol OA in 10 ml ODE solvent. The mixture was heated to 100 °C under N_2 for 10 min to remove moisture. Under a blanket of N_2 atmosphere, 0.25 mmol $Mn_2(CO)_{10}$

dissolved in DCB was injected. The reaction was further heated to 200 °C at a heating rate of 2 °C /min and kept at this temperature for 30 min before it was cooled down to room temperature. The workup process was same as that in the synthesis of Au/PtCo NPs. Under this condition, only less than 1% Mn was present in the final product.

To make Au/$Mn_{50}Pt_{50}$ NPs, the reaction temperature was simply increased to 250 °C.

8.2.5 *Synthesis of Au/PtCu NPs*. In a typical synthesis of 4/1.5 nm Au/$Cu_{25}Pt_{75}$ NPs, 0.25 mmol $Pt(acac)_2$ and 0.08 mmol $Cu(acac)_2$ were mixed with 3 mmol OAm and 3 mmol OA in 10 ml ODE solvent in presence of 2 mmol 1,2-hexanediol. The mixture was heated to 100 °C to obtain a clear solution before 36 mg Au seeds were added. The solution was further heated to 200 °C at a heating rate of 2 °C /min and kept at this temperature for 30 min before it was cooled to room temperature. The workup process was same as that in the synthesis of Au/CoPt NPs.

The Cu composition was controlled from $Pt_{50}Cu_{50}$ to $Pt_{35}Cu_{65}$ simply by tuning the $Cu(acac)_2$ from 0. mmol to 0.46 mmol while keeping the other parameters similar with that of the synthesis of $Pt_{75}Cu_{25}$.

8.2.6 *Synthesis of Au/AgPt NPs*. In a typical synthesis of 4/1.5 nm Au/$Pt_{50}Ag_{50}$ NPs, 30 mg Au seeds were mixed with 2 mmol 1,2-hexanediol in 10 ml ODE in presence of 3 mmol OAm and 3 mmol OA. The solution was heated to 100 °C under N_2 for 10 min. 0.25 mmol $Pt(acac)_2$ and 0.25 mmol $AgNO_3$ were dissolved in 3 ml DCB in presence of 1 ml OAm and injected in the above solution. The reaction and workup process was same as that in the synthesis of Au/PtCu NPs.

8.2.7 *NP Deposition on Carbon and NP Activation*. The as-synthesized NPs were deposited on carbon black (Kejen EC 300J) support by mixing the NPs with carbon black

in hexane with a 1:2 ratio in mass and sonicating with a Fisher Scientific FS 110 for 1 h. To remove the surfactants, the mixture was first dried under N_2 and then suspended in 20 mL of acetic acid. The suspension was heated to 70 °C for 10 h. The C-NPs were separated by centrifugation and re-dispersed in de-ionized (DI) water + isopropanol + 5% Nafion (volume ratio:4/1/0.025) to reach a concentration of 2 mg/mL. After sonicating for 1 h, 20 μl of the C-NPs was dropped on a glassy carbon (GC) electrode and dried overnight under ambient conditions.The Pt loading amount was between 3.5 to 5.3 μg.

8.2.8 *NP Characterization*. Transmission electron microscopy (TEM) image of NPs was acquired on a Philips EM 420 (X120kV). High resolution TEM (HRTEM) images were obtained from a JEOL 4000EX transmission electron microscope with the accelerating voltage of 380 kV and point to point resolution close to 0.17 nm. High resolution aberration-corrected high-angle annular dark-field scanning TEM (HAADF-STEM) and elemental mapping images were obtained on an aberration corrected JEOL 2200FS microscope with a beam size of ~0.8Å for imaging and ~ 2Å for chemical analysis. All TEM samples were prepared by depositing a drop of diluted NP dispersion on carbon-coated copper grids. X-ray diffraction (XRD) patterns were collected on a Bruker AXS D8-Advanced diffractometer with Cu Kα radiation (λ=1.5418 Å). The elemental weight ratios of the NPs were first measured by inductively coupled plasma atomic emission spectroscopy (ICP-AES) from a JY2000 Ultrace ICP Atomic Emission Spectrometer equipped with a JY AS 421 autosampler and 2400 g/mm holographic grating and converted into atomic ratios. The elemental atomic ratios of the NPs were also analyzed by Energy-dispersive X-ray spectroscopy (EDX) on a Joel JSM-6060 scanning electron microscopy (SEM). Samples for EDX were deposited on a graphitized porous carbon

support. UV/vis spectra of the NP dispersions were recorded on a Perkin Elmer Lambda 35 spectrometer.

8.2.9 *Electrochemical Characterization*. Electrochemical measurements were conducted in a three-compartment electrochemical cell with a rotational disk electrode (RDE, 6 mm glassy carbon in diameter) setup (Pine) and an Autolab 302 potentiostat. A saturated Ag/AgCl electrode and a Pt wire were used as reference and counter electrodes, respectively. 0.1 M $HClO_4$ was used as electrolyte. All the potentials given in the discussion were against reversible hydrogen electrode (RHE).

8.3 Results and Discussion

To make Au/PtM NPs, Au NPs were first prepared by reducing $HAuCl_4$ with t-butylamine-borane in presence of OAm. Among numerous methods developed for the syntheses of Au NPs, we chose this one to prepare Au NPs because it gave monodisperse and OAm-coated NPs that were suitable as seeds for the core/shell formation. These Au NPs initiated PtM nucleation and growth at temperate lower than that required for preparation of PtM single component NPs. Therefore, in the current synthetic condition, separate nucleation and growth of PtM was inhibited and core/shell Au/PtM NPs with uniform PtM coating were obtained.

Using 4 nm Au-OAm NPs seeds, we produced Au/Pt_3Fe NPs via thermal decomposition of $Fe(CO)_5$ and reduction of $Pt(acac)_2$, similar to what was reported in the synthesis of 7/1.5 nm Au/$FePt_3$ NPs.[6] Depending on the amount of Au seeds and Fe, Pt precursors added, we could tune the FePt shell thickness from 0.5 to 2 nm. In addition to conventional TEM, HRTEM and elemental mapping analyses,[6] we further characterized

these core/shell NPs with XRD and with their properties in electrochemical oxidation of CO (also called CO stripping). Figure 8-1A lists the XRD patterns of the 4 nm Au and 4/1.5 nm Au/FePt NPs. We can see that with the coating, the (111) peak of the face-centered cubic (fcc) structure shift to higher angles and the (111) peak from the 2 nm FePt shell is close to the one from the pure FePt NPs, indicating that FePt shell at 2 nm thick is structurally similar to the FePt NPs. Figure 8-1B gives the characteristic CO stripping peaks of the Au/FePt NPs. Pt surface is known to bind to CO strongly. The bound CO can be oxidized electrochemically and this oxidation peak is dependent on chemical environment of the surface Pt, giving typical CO stripping peak. In our test, after CO was adsorbed on the surface of Au/FePt NP at 0.05V, the electrolyte was pured with Ar to make it CO free. CO stripping was then performed by scanning from 0.05V to 1.1V. From Figure 8-1B, we can see that the core/shell NPs with 0.5 nm FePt shell have two broad CO stripping peaks at >1 nm thick coating, the core/shell NPs have a smooth single stripping peak.

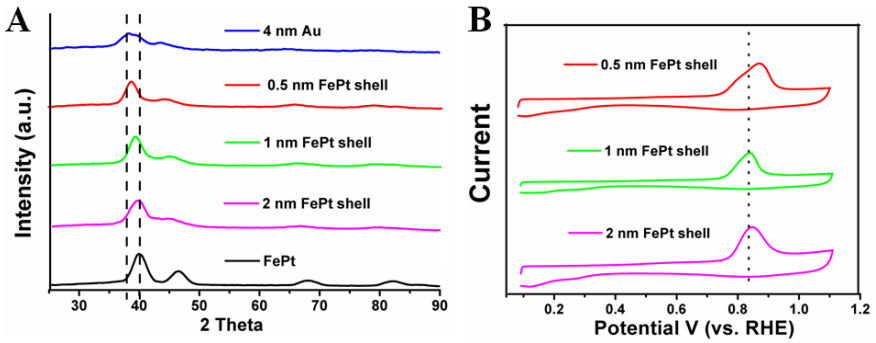

Figure 8-1. (A) XRD patterns of Au NPs, Au/FePt core/shell NPs with 0.5, 1, 2 nm shell and FePt NPs. (B) CO stripping peaks from Au/FePt core/shell NPs with different FePt shell thickness. CO adsorption on the surfaces was done by holding the electrode in CO

saturated $HClO_4$ solution at a constant potential of 0.05 V. The CO stripping curves were acquired at 50 mV/s sweep rate.

The thermal decomposition and metal salt reduction could be readily extended to prepare other new core/shell Au/PtM NPs. Au/CoPt NPs were synthesized by thermal decomposition of $Co_2(CO)_8$ and reduction of $Pt(acac)_2$ in the presence of Au NPs. In the synthesis, we replaced OA with 1-adamantanecarboxylic acid for the better formation of PtCo alloys.[14] The CoPt shell thickness was controlled by the amount of Au NPs and the Co, Pt precursor added. For example, 36 mg Au NPs reacting with 0.13 mmol of $Pt(acac)_2$ and 0.13 mmol of $Co_2(CO)_8$ at 200 °C gave ~0.8 nm $Pt_{75}Co_{25}$ shell while mixing 0.25 mmol $Pt(acac)_2$ and 0.25 mmol $Co_2(CO)_8$ at the same temperature yielded a 1.5 nm $Pt_{75}Co_{25}$ shell. When $Pt(acac)_2$ and $Co_2(CO)_8$ were less than 0.13 mmol, heating the reaction solution at 200 °C led to Au NP aggregation. It seems that the presence of more than 0.13 mmol each of $Pt(acac)_2$ and $Co_2(CO)_8$ helped to stabilize Au NPs at 200 °C temperature. However, when too much $Pt(acac)_2$ and $Co_2(CO)_8$ (above 0.3 mmol) were used to react with 36 mg Au seeds, PtCo tended to self-nucleate. This indicated that there was a dynamic balance among Au NP stability, PtCo coating over Au NPs and PtCo self-nucleation/growth. Our experiments showed that as long as Au and (Co+Pt) were between 1: 1.2 to 1 : 2.8 molar ratio (based on 36 mg Au), PtCo preferred to grow around Au, efficiently stabilizing Au NPs and preventing PtCo from self-nucleation and growth. However, this reaction condition could not be applied to coat PtCo shell thicker than 1.5 nm. To make shell thicker than 1.5 nm, 36 mg of 4/1.5 nm Au/$Pt_{75}Co_{25}$ NPs were used as seeds to grow $Pt_{75}Co_{25}$. Also, in the current coating condition, the final PtCo

composition seemed to be independent on the ratios of $Pt(acac)_2$ and $Co_2(CO)_8$ used in the reaction – the $Pt_{75}Co_{25}$ shell was always formed. To control Co/Pt in different ratio, higher reaction temperature could be applied. For example, when 0.25 mmol $Pt(acac)_2$ and 0.25 mmol $Co_2(CO)_8$ reacted at 200 °C, 220 °C to 250 °C, the composition of PtCo shell could be tuned from $Co_{25}Pt_{75}$, $Co_{35}Pt_{65}$ to $Co_{50}Pt_{50}$ and the thickness of these shells was decreased from 1.5 nm, 1.0 nm to 0.8 nm correspondingly. This shell thickness is likely caused by high temperature induced partial diffusion between Au core and PtCo shell, leading to the "shrink" of the PtCo shell.

Figure 8-2A shows the TEM image of Au/$Pt_{75}Co_{25}$ NPs. The average size of the NPs were measured to be 5.7$\pm$0.2 nm (Au/Pt_{75} Co_{25} NPs), indicating a 0.8 nm $Pt_{75}Co_{25}$ shell was deposited onto the Au seeds. Figure 8-2B is the HRTEM image of a typical Au/ $Pt_{75}Co_{25}$ NP. Due to the close scattering power of Au and Pt, it is difficult to distinguish the core-shell interface from the image. However, the misfit dislocations (pointed out by the red arrows) can be seen. This misfit has been observed in Au/PtFe and is attributed to the tendency to release the strain caused by interface mismatch between the core and shell.[15] The composition profile of a representative Au/$Pt_{75}Co_{25}$ NP was further confirmed by the elemental analysis, as seen in the HAADF-STEM image (Figure 8-2C) and the related elemental mapping of Pt and Au (Figure 8-2D), in which the Au (yellow) is surrounded by Pt (red). The Pt peak is nearly 1.6 nm wider than the Au peak, further confirming that the shell thickness is around 0.8 nm. The signal of Co is weak due to the limited sensitivity of the mapping technique. ICP-AES and EDX were used to measure the element composition quantitatively. These 4/0.8 nm core/shell NPs has the Pt to Au molar ratio around 1.1:1 and the Co to Pt molar ratio around 1:3. TEM images of other

Au/PtCo NPs, and PtCo NPs prepared following similar method in absence of Au seeds, are given in Figure S8-1.

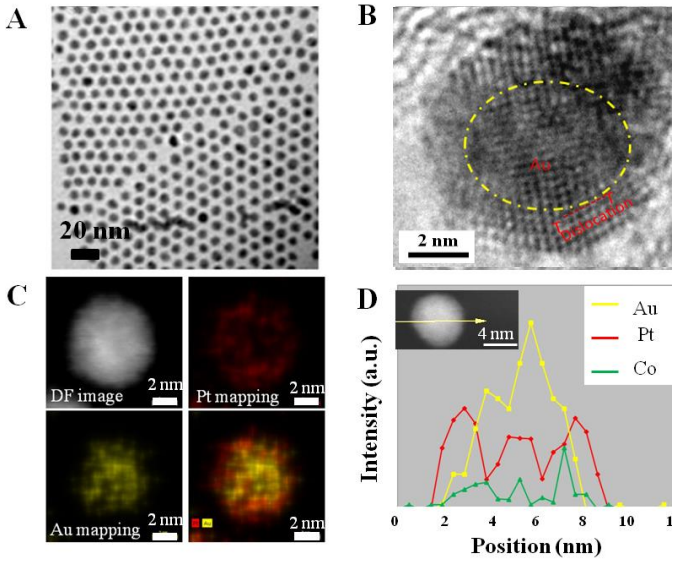

Figure 8-2. (A) TEM image and (B) HRTEM image of 4/0.8 nm Au/$Pt_{75}Co_{25}$ core/shell NPs (red arrows point out the dislocation), (C) HAADF-STEM-EDS mapping of a typical Au/ $Pt_{75}Co_{25}$ core/shell NPs (D) Cross-sectional compositional line profiles of the arrow area in insert picture.

Figure 8-3A shows the XRD patterns of the Au NPs, Au/ $Pt_{75}Co_{25}$ core/shell NPs with different shell thickness and $Pt_{75}Co_{25}$ NPs. All these samples have typical *fcc* structure. As the shell thickness increases, the (111) peaks shift to higher angles towards the one from $Pt_{75}Co_{25}$ NPs. The (111) spacing of Au (38.7), 0.8 nm shell (39.1), 1.5 nm shell (39.3), 2.5 nm shell (40.0), as well as $Pt_{75}Co_{25}$ (40.2) were calculated to be 0.258, 0.255, 0.253, 0.249 and 0.248 nm respectively according to Bragg's law. This indicates

that in presence of Au core, the (111) spacing in the $Pt_{75}Co_{25}$ shell is increased due to the lattice mismatch between the Au core and $Pt_{75}Co_{25}$ shell. As the shell thickness increases, the Au effect is diminished and the 2.5 nm $Pt_{75}Co_{25}$ shell has the (111) spacing similar to that from the $Pt_{75}Co_{25}$ NPs. The coating uniformity in the Au/PtCo can be further characterized by the redox property change of the Au and Au/PtCo NPs in 0.1 M $HClO_4$ solution, as seen in Figure 8-3B. The oxidized Au is reduced at 1.08 V. 0.8 nm PtCo coating reduce much of the Au peak, but small peak can still be seen, indicating the misfit dislocation observed in 0.8 nm PtCo coating (Figure 8-2B) led to incomplete Au coverage by PtCo. At 1.5 nm PtCo coating, the core/shell NPs show only the reduction peak of the oxidized PtCo at 0.68 V, demonstrating a uniform PtCo coating.

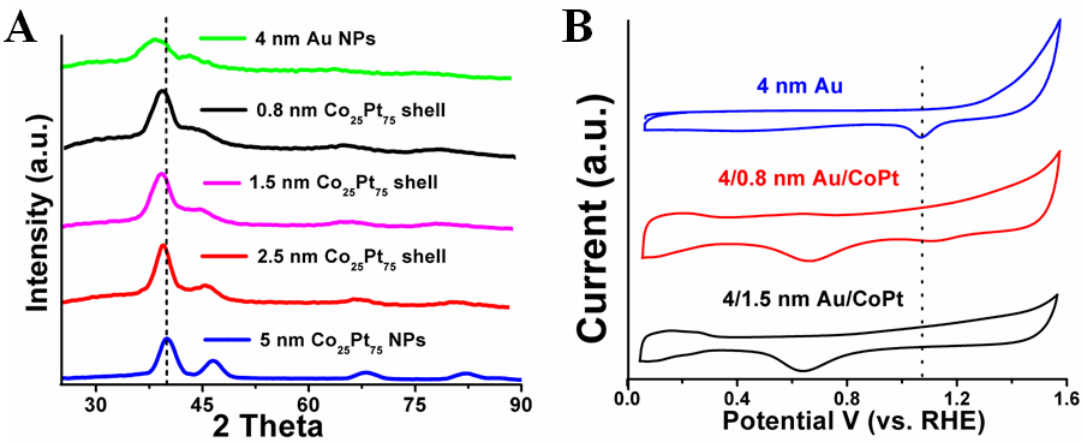

Figure 8-3**.** (A) XRD patterns of Au NPs, Au/ $Pt_{75}Co_{25}$ core/shell NPs with 0.8, 1.5, 2.5 nm shell and $Pt_{75}Co_{25}$ NPs. (B) CVs of Au NPs and Au/ $Pt_{75}Co_{25}$ core/shell NPs with 0.8 or 1.5 nm shell.

MnPt shell was coated onto Au NPs by decomposing $Mn_2(CO)_{10}$ and $Pt(acac)_2$ in the presence of OAm and OA. Such a reaction has been used to make MnPt or Pt with

shape control.[16, 17] The solvents used to dissolve the $Mn_2(CO)_{10}$ can determine whether the final product is pure Pt or MnPt alloy NPs. Here, we used the dichlorobenzene solution of $Mn_2(CO)_{10}$ to control the coating of Pt shell and MnPt shell onto the Au seeds. In the coating experiment, if the reaction temperature was set at 190 °C, 4/1.5 nm Au/Pt NPs were obtained with Mn in less than 1% (Figure S8-2B). It seems that this reaction temperature is too low for $Mn_2(CO)_{10}$ to decompose in the rate that is comparable with that of the Pt-salt reduction. However, this slow decomposition of $Mn_2(CO)_{10}$ is essential for Pt shell formation, giving the Au/Pt with very small amount of Mn present in the structure. Without $Mn_2(CO)_{10,}$ Au/Pt NPs cannot be formed, instead, the synthesis led to the formation of branched Pt structure (Figure S8-2A). A reasonable assuPtMion here is that trace Mn helps to release the strain caused by the lattice mismatch between Au and Pt. If the reaction temperature was raised to 250 °C and the reaction time was extended to 1 h, more Mn (56%) could be alloyed with Pt (Figure S8-2C). As a comparison, if the synthesis was conducted in the absence of Au seeds, only $Mn_{25}Pt_{75}$ NPs were obtained.[16, 18]

Au/PtM NPs could also be prepared by co-reduction of metal salts in the presence of Au NPs. This was seen in the controlled synthesis of 4/1.5 nm Au/PtCu (or Au/AgPt). In the condition similar to the synthesis of Au/FePt NPs, Au/PtM (M = Cu or Ag) NPs were prepared by co-reduction of $Cu(acac)_2$ or $AgNO_3$ together with $Pt(acac)_2$. The PtCu shell was coated on Au NPs by co-reduction of $Cu(acac)_2$ and $Pt(acac)_2$ with 1,2-hexanediol. Such a co-reaction has been used to produce a mixture of spherical PtCu and PtCu nanorods.[19] Figure 8-4A&B show the TEM images of $Au/Cu_{35}Pt_{65}$ and $Au/Cu_{64}Pt_{36}$ NPs. $Au/Cu_{35}Pt_{65}$ NPs have a 1 nm shell, while the $Au/Cu_{64}Pt_{36}$ ones have a 1.5 nm shell - the

presence of more Cu leads to a thicker PtCu shell. The composition of the PtCu shell was controlled by the precursor ratios. Figure 8-4C is the plot of atomic % of Cu in PtCu shell vs. mol% $Cu(acac)_2$ reacted with 0.25 mmol $Pt(acac)_2$. The molar percentage of Cu in the shell is nearly the same with that from the $Cu(acac)_2$ and $Pt(acac)_2$ mixture, indicating the atomic ratio of two precursors are carried over to the final PtCu shell. Figure 8-4D shows XRD patterns of Au/Cu_xPt_{1-x} (x= 35, 50, 64) core/shell NPs. As the Cu composition increases, the patterns shift to wider angles, which is in agreement with Vegard's law.[20]

To synthesize Au/AgPt NPs (Figure S8-3), a mixture of Ag and Pt precursors were injected at 100 °C into 10 ml ODE in presence of 3 mmol OAm, 3 mmol OA and 2 mmol 1,2-hexanediol containing Au NPs. This injection process was essential for the formation of uniform AgPt shell, without which the mixture of Ag NPs and Pt NPs was formed due to the easy reduction of Ag salt. The composition of the AgPt was also controlled by the precursor ratios.

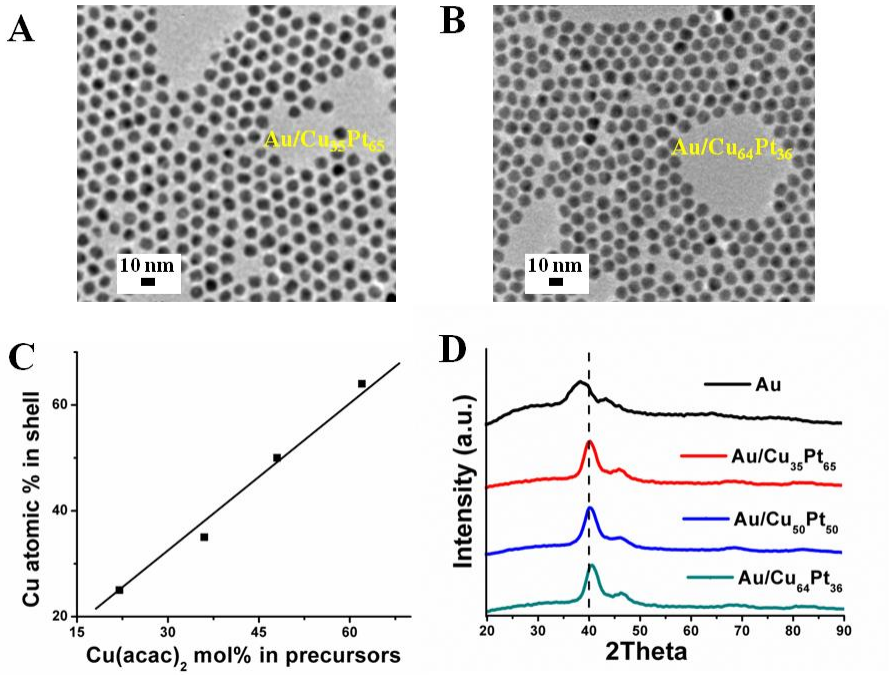

Figure 8-4. TEM images of (A) Au/$Pt_{65}Cu_{35}$ and (B) Au/$Pt_{36}Cu_{64}$ core/shell NPs. (C) Correlation between the amount of $Cu(acac)_2$ added and the amount of Cu obtained in the final PtCu shell (D) XRD patterns of the Au/PtCu core/shell NPs.

The core/shell structure was active and durable catalyst for ORR in 0.1 M $HClO_4$ as demonstrated by Au/Pt_3Fe NPs.[6] With Au induced stability, our Au/PtM NPs provide more versatile NP platforms for ORR studies. Our testes showed that when the shell was thinner than 1 nm, surface coverage was incomplete and ORR activity was not enhanced, while too thick a coating (over 2 nm) made the Au/PtM NPs with the ORR activity close to the single component PtM NPs. We found 1.5 nm shell coating gave the NPs the highest activity without losing the desired stability.

The electrocatalytic trends established for extended surface pointed out that Fe and Co are two of the most favorable transition metals for Pt alloy catalyzed ORR.[10] Thus, we first compared the ORR electrocatalytic performance of 4/1.5 nm Au/Pt and Au/PtM (M = Fe, Co) core/shell NPs. Figure 8-5 summarizes the electrochemical characterization of Au/Pt and Au/$Pt_{75}M_{25}$ (M = Fe, Co) core/shell NPs. All the samples show the similar CVs with a underpotentially deposited hydrogen (H_{upd}) peaks at E < 0.4 V and Pt oxidation/reduction peaks at 0.8-0.9 V in the anodic/cathodic scans (Figure 8-5A). For C-Au/$Pt_{75}M_{25}$, we observed a positive shift of the reduction peaks in the cathodic scans compared with C-Au/Pt. Such a peak shift represents a less oxophilic catalyst surface due to the addition of transition metals. CO stripping curves (Figure 8-5B) of all the core/shell catalysts also confirm a similar Pt-rich surface with a negative shift of the CO_{ad} oxidation peak in the presence of transition metals. The electrochemically active surface

area (ECASA) was calculated from CO-stripping area.[21] The control of the size and shape of the core/shell NPs led to consistent values for the specific surface area (between 700 and 750 $cm^2mg^{-1}_{Pt}$). The specific activities of the AA-treated C-Au/Pt, C-Au/$Pt_{75}Fe_{25}$ and C-Au/$Pt_{75}Co_{25}$ normalized by the ECASA were recorded as a function of potential in Figure 8-5C and the specific activities at 0.9 V vs. RHE were 0.34, 0.90, 1.49 mA/cm^2 respectively, as summarized in Figure 8-5D. The measured catalytic specific activity of C-Au/$Pt_{75}Co_{25}$ is around 1.5 times versus that of C-Au/$Pt_{75}Fe_{25}$ and nearly five times higher than that of C-Au/Pt for ORR, which is consistent with the previous model catalyst studies for $Pt_{75}M_{25}$ alloys on extended surface.[6,10] We noticed a significant loss of Fe and Co after acid treatment ($Pt_{75}Fe_{25}$ or $Pt_{75}Co_{25}$ shell had only 5% Fe or Co left after acetic acid wash (Table S8-1). However, compared with pure Pt, the presence of 5% Fe or Co in the PtM shell still plays an important role in the ORR catalytic improvement via ligand effect and geometric effect.[10] After confirming the superiority of C-Au/PtCo catalysts, we then compare the ORR electrocatalytic performance of C-Au/PtCo catalysts with different Co composition The most active catalyst among all these core/shell NPs studied was 4/1.5 nm C-Au/$Pt_{50}Co_{50}$. After acetic acid treatment, the C-Au/$Co_{50}Pt_{50}$ was converted into C-Au/$Pt_{75}Co_{25}$. Its initial specific activity reached 3.0 mA/cm^2 at 0.9 V (vs. RHE) (Figure S8-4).

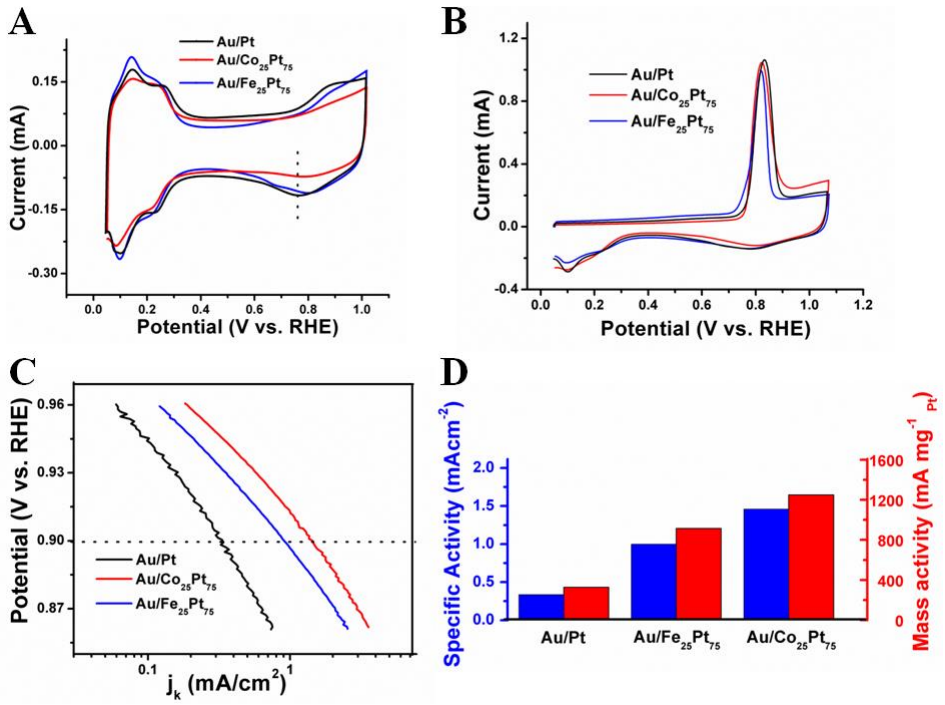

Figure 8-5. (A) CVs and (B) CO strippings of Au/Pt and Au/PtM (M=Fe, Co)/C catalysts in 0.1 M $HClO_4$. (C) Specific activities at 1600 rpm, 20mV/s and room temperature of Au/Pt and Au/PtM (M=Fe, Co)/C catalysts in 0.1 M $HClO_4$ for the ORR at different electrode potential (Tafel plot). (D) Specific activity and mass activity of Au/Pt and Au/PtM (M= Fe, Co) for the ORR@ 0.9 V (vs RHE).

The C-Au/PtM NPs were much more stable than C-Pt NPs in catalyzing ORR. This has been demonstrated in Au/PtFe NPs.[6] Here we selected $Au/Pt_{50}Co_{50}$ NPs as an example. After acetic acid, we further annealed the samples at 300 °C for 2 h to stabilize the transition metal. The stability test was performed in oxygen-saturated 0.1 M $HClO_4$ with the potential scanned from 0.6 V to 1 V for 8000 scans at 50 mV/s, room temperature. After that, their CV and ORR activity were re-evaluated. Figure 8-6 summarizes the test. The CVs by opening the potential to 1.6 V (Figure 8-6A) demonstrated the core/shell structures are well-maintained after the treatment and 8000

sweeps. The changes in CO stripping feature (Figure 8-6B) are not significant. From the TEM images of the core/shell NPs obtained before and after the stability test (Figure S8-5), we observed that the NPs are nearly intact after the test. These all confirmed that the Au/PtCo core/shell morphology is stable in ORR reaction condition. However, the ORR specific activity dropped after the first 4000 sweeps (Figure 8-6C&D), from 2.2 mA/cm^2 to 1.6 mA/cm^2 at 0.9 V vs. RHE, but kept stable for the next 4000 sweeps with only less than 5% lost. A reasonable explanation is that although the Pt shell is stabilized by the Au core, the etching of Co near the surface of the core/shell NPs has led to the decrease of ORR activity during initial stage. After that, a platinum rich shell formed, preventing further cobalt dissolution. This could be seen in figure 8-6B, the CO stripping in the cathodic sweep increased from 1.94 cm^2 to 2.06 cm^2 after first 4000 scans, which indicated more Pt on the surface as cobalt leached out. Almost no change in the CO stripping was seen at the end of 8000 scans, showing the surface became stable. This has been further confirmed by the ICP analysis with an increase of Co amount in the electrolyte after the first 4000 sweeps but a negligible amount of Co detection in the next 4000 sweeps. Further study on how to stabilizing transition metal with Pt is still going on.

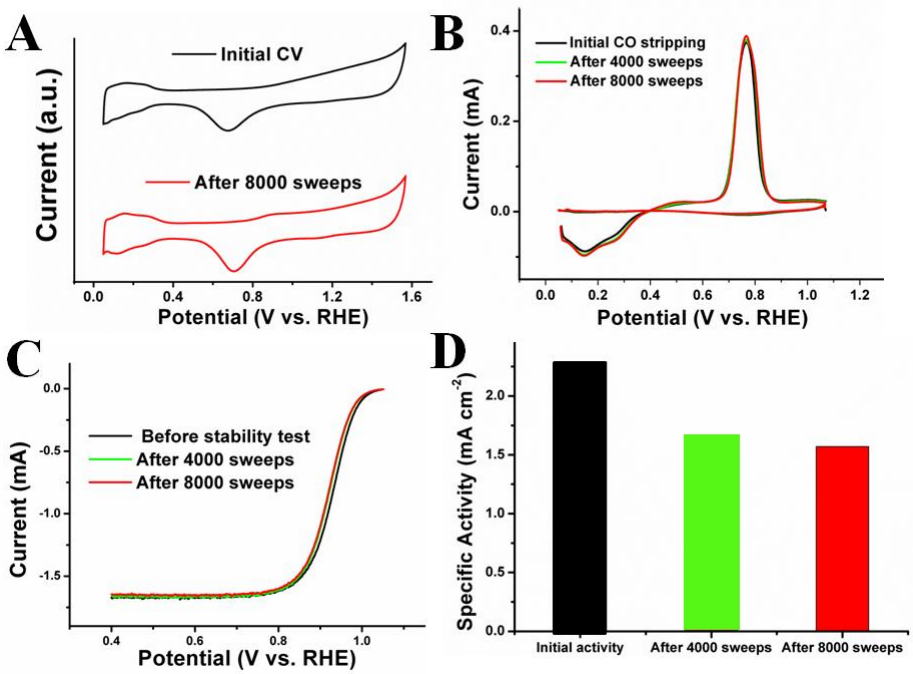

Figure 8-6. (A) CVs (B) CO strippings (C) polarization curves and (D) Specific activity of C-Au/$Pt_{50}Co_{50}$ before and after stability test by 8000 potential cycles between 0.6 and 1.1 V in oxygen-saturated 0.1 M $HClO_4$ at 20 °C with a sweep rate of 50 mV/s.

8.4 Conclusion

In summary, we have reported a facile and reliable approach to monodisperse core/shell Au/PtM (M = Fe, Co, Cu, Mn, Ag) NPs. The key step of the synthesis is first to prepare the oleylamine-coated Au NPs to initiate the PtM nucleation and growth at a temperature that is generally lower than that for the formation of PtM NPs. As a result, monodisperse Au/PtM NPs with controlled PtM coating (thickness and composition) are synthesized. To have a uniform PtM coating and enhanced catalysis, PtM shell thickness should be thicker than 1 nm but thinner than 2 nm. PtM shell thinner than 1 nm cannot form a uniform layer of coating around the 4 nm Au core and that thicker than 2 nm tends

to make the Au/PtM NPs behave more like a large PtM NPs. Using 1.5 nm PtM coating as an example, we have demonstrated that the Au/PtM NPs show the M-dependent activity for catalyzing ORR. The highest initial specificity activity of 3.0 mA/cm^2 (at 0.9 V vs. RHE) is achieved when $Au/Pt_{50}Co_{50}$ NPs are used as the catalyst. M in PtM is subject to acid-etching in the tested 0.1 M $HClO_4$ solution, leading to the activity drop. Nonetheless, the Au/PtM NPs are generally stabilized and the resultant Au/PtM NPs are much more efficient than Pt NPs in catalyzing ORR. The synthetic strategy applied in this report is not limited to the Au/PtM NPs but can be extended to other core/shell NPs. With the controls in dimension, composition and core-shell interactions achieved in the structure, these core/shell NPs should serve as a much better catalyst system for studying electronic and geometric (strain) effects on various chemical reactions with NP catalysis being tuned to optimization.

8.5 References

1 Strasser, P.; Koh, S.; Anniyev, T.; Greeley, J.; More, K.; Yu, C.; Liu, Zengcai; Kaya, S.; Nordlund, D.; Ogasawara, H.; Toney, M. F. *Nat. Chem.* **2010**, *2*, 454-460.

2 Wang, J.; Inada, H.; Wu, L.; Zhu, Y.; Choi, Y.; Liu, P.; Zhou, W.; Adzic, R. R. *J. Am. Chem. Soc.* **2009**, *131*, 17298-17302.

3 Zhou, W.; Yang, X.; Vukmirovic, M. B.; Koel, B. E.; Jiao, J.; Peng, G.; Mavrikakis, M.; Adzic, R. R. *J. Am. Chem. Soc.* **2009**, *131*, 12755 -12762. 4 Xing, Y.; Cai, Y.; Vukmirovic, M. B.; Zhou, W.; Karan, H.; Wang, J.; Adzic, R. R. *J. Phys. Chem. Lett.* **2010**, *1*, 3238-3242.

5 Sasaki, K.; Naohara, H.; Cai, Y.; Choi, Y. M.; Liu, P.; Vukmirovic, M. B.; Wang, J. X.; Adzic, R. R. *Angew. Chem. Int. Ed.* **2010**, 49, 8602-8607.

6 Wang, C.; Vliet, D.; More, K. L.; Zaluzec, N. J.; Peng, S.; Sun, S.; Daion, H.; Wang, G.; Greeley, J.; Pearson, J.; Paulikas, A. P.; Karapetrov, G.; Strmcnik, D.; Markovic, N. M.; Stamenkovic, V. R.; *Nano Lett.* **2011**, *11*, 919-926.

7 Mazumder, V.; Chi, M.; More, K. L.; Sun, S. *J. Am. Chem. Soc.* **2010**, *132*, 7848-7849.

8 Greeley. J.; Mavrikakis, M. *Nat. Mater.* **2004**, 3, 810

9 Stamenkovic, V. R.; Fowler, B.; Mun, B.S.; Wang, G.; Ross, P. N.; Lucas, C. A.; Markovic, N. M. *Science* **2007**, 315, 493

10 Stamenkovic, V. R.; Mun, B. S.; Arenz, J. J.; Mayrhofer, M.; Lucas, C. A.; Wang, G.; Ross, P. N.; Markovic, N. M. *Nat. Mater.* **2007**, *6*, 241-247.

11 Chen, S.; Ferreira, P. J.; Sheng, W.; Yabuuchi, N.; Allard, L. F.; Shao-Horn, Y. *J. Am. Chem. Soc.* **2008**, *130*, 13818-13819.

12 Yang, J.; Chen, X.; Yang, X.; Ying, J. Y. *Energy Environ. Sci.* **2012**, 5, 8976-8981.

13 Mazumder, V.; Chi, M.; More, K. L.; Sun, S. *Angew. Chem. Int. Ed.* **2010**, 49, 9368-9372.

14 Shevchenko, E. V.; Talapin, D. V.; Rogach, A. L.; Kornowski, A.; Haase, M.; Weller, H. *J. Am. Chem. Soc.* **2002**, 124, 11480-11485.

15 Ding, Y.; Sun, X.; Wang, Z.; Sun, S. *Appl. Phys. Lett.* **2012**, *100*, 111603.

16 Kang Y.; Murray, C. B. *J. Am. Chem. Soc.* **2010**, 132, 22, 7568-7569.

17 Kang Y.; Li, M.; Cai, Y.; Cargnello, M.; Diaz, R. E.; Gordon, T. R.; Wieder, N. L.; Adzic, R. R.; Gorte, R. J.; Stach, E. A.; Murray, C. B. *J. Am. Chem. Soc.* **2013**, 135, 2741-2747.

18 Lee, D. C.; Ghezelbash, A.; Stowell, C. A.; Korgel, B. A. *J. Phys. Chem. B.* **2006**, 110, 20906-20911.

19 Liu, Q.; Yan, Z.; Henderson, N. L.; Bauer, J. C.; Goodman, D. W.; Batteas, J. D.; Schaak, R. E. *J. Am. Chem. Soc.* **2009**, 131, 5720-5721.

20 Denton, A. R., Ashcroft, N. W. *Phys. Rev. A* **1991**, 43, 3161-3164.

21 Mayrhofer, K. J. J.; Strmcnik, D.; Blizanac, B. B.; Stamenkovic, V.; Arenz, M.; Markovic, N. M. *Electrochimi. Acta.* **2008**, 53, 3181–3188.

8.6 Supporting Information

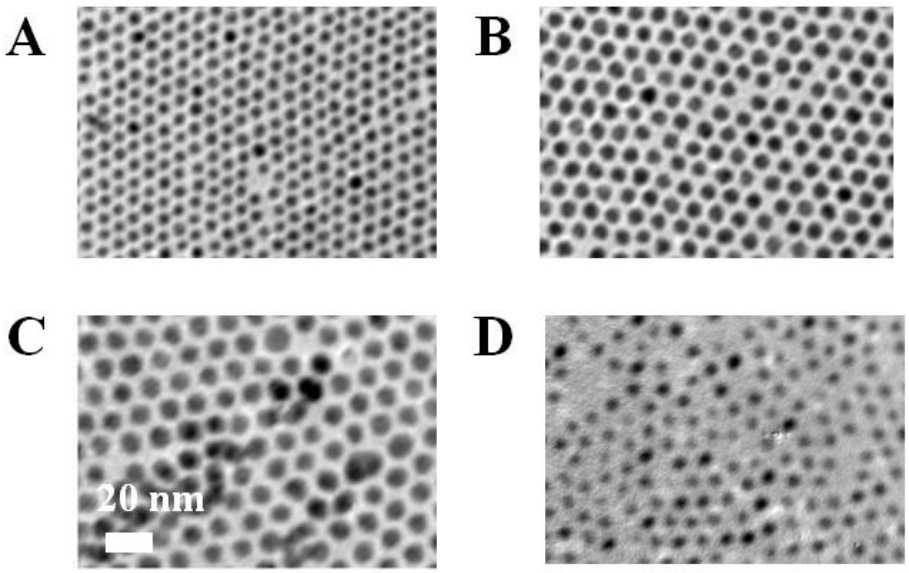

Figure S8-1 TEM images of (A) 4 nm Au NPs (B) 4/1.5 nm Au/$Co_{25}Pt_{75}$ (C) 4/2.5 nm Au/$Co_{25}Pt_{75}$ core shell NPs and $Co_{25}Pt_{75}$ NPs.

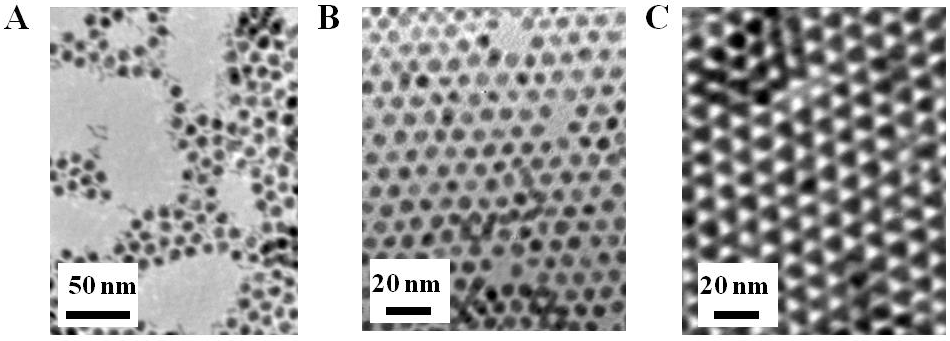

Figure S8-2. TEM images of (A) Au/Pt synthesized without $Mn_2(CO)_{10}$ (B) Au/Mn_1Pt_{99} (C) Au/$Mn_{56}Pt_{44}$

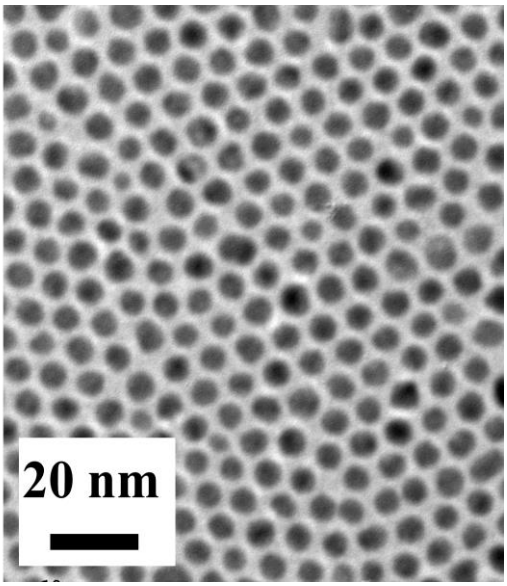

Figure S8-3. TEM of Au/AgPt core/shell NPs.

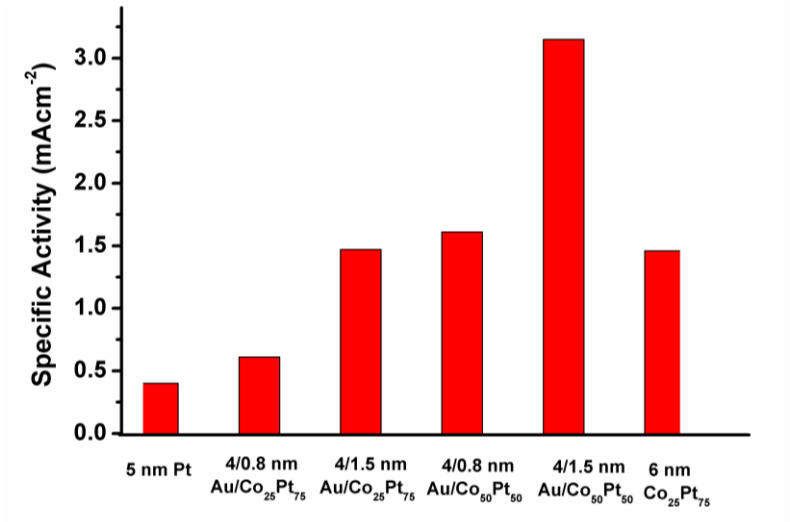

Figure S8-4. Specific activities of Au/PtCo catalysts with different Co composition and PtCo shell thickness in 0.1 M $HClO_4$ for the ORR @ 0.9 V vs RHE.

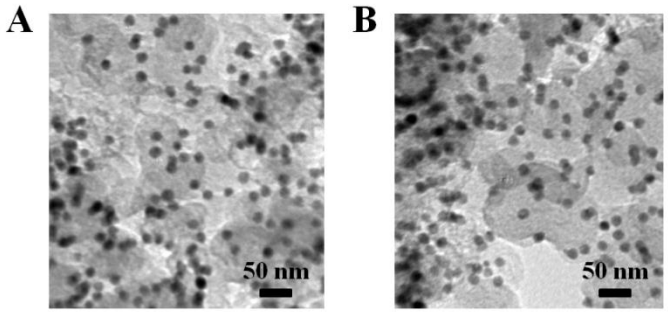

Figure S8-5. TEM images of the C-Au/CoPt NPs (**A**) before and (**B**) after ORR stability test.

Table S8-1. Au/PtM composition before and after acetic acid treatment

As-synthesized NPs	After acetic acid treatment
$Au/Fe_{26}Pt_{74}$	Au/Fe_4Pt_{96}
$Au/Co_{25}Pt_{75}$	Au/Co_5Pt_{95}
$Au/Cu_{25}Pt_{75}$	$Au/Cu_{25}Pt_{75}$

IX. Synthesis of Pt_3Sn Alloy Nanoparticles and Their Catalysis for Electro-Oxidation of CO and Methanol

9.1 Introduction

Alloying a non-noble metal (M) with Pt has become a popular approach to Pt-based catalysts with much reduced Pt usage and enhanced Pt activity.[1-7] Depending on the chemical nature of M, PtM can be made highly active for either electrochemical oxidation or reduction.[5-8] Among various PtM alloys studied thus far, PtSn alloys represent an interesting group of catalysts not only for hydrogenation[9-11] and dehydrogenation reactions,[12-14] but also for electro-oxidation of carbon monoxide (CO),[15-20] methanol,[21-23] ethanol,[23-26] and ethylene glycol.[27] Previous evaluations on single crystals and thin films of Pt_3Sn for catalytic CO oxidation suggest that Sn as an alloy component can enhance CO oxidation on Pt by promoting H_2O dissociation on Sn to form Sn-OH and by altering electronic properties of Pt through its bonding with Pt, weakening the CO adsorption on Pt.[15-19] These experimental observations are further supported by the first-principle and density function theory calculations.[8, 28] The activation energies for CO oxidation on Pt_3Sn/Pt (111), Pt_3Sn (111) and Pt (111) surfaces are 0.64 eV, 0.68 eV and 0.82 eV, respectively,[28] and water dissociation energy is lower on Sn (0.44 eV) than on Pt (0.67 eV).[8] These studies indicate that PtSn alloys in a nanoparticle (NP) form should be a more promising catalyst for CO and other small organic molecule oxidizations.

Here we report a high temperature organic phase synthesis of monodisperse Pt_3Sn alloy NPs by co-reduction of Pt and Sn salts and study their enhanced catalysis for CO and methanol oxidation reaction (MOR) in acid solutions. Previously, Pt_3Sn NPs were synthesized directly on carbon supports from reduction of the absorbed Pt salt and Sn salt.[20] Recently, Pt_3Sn NPs were prepared by room temperature H_2 reduction of Pt(dibenzylidene acetone)$_2$ with (n-Bu)$_3$SnH,[29] or made by high temperature co-reduction of Pt(acac)$_2$ (acac = acetylacetonate) and Sn(acac)$_2$ with 1,2-hexandecanediol.[21] These Pt_3Sn NPs were examined for CO oxidation and MOR catalysis and were found to be unstable in acidic electrolyte and oxidative conditions.[21] By carefully optimizing the synthesis conditions, we succeeded in synthesizing monodisperse Pt_3Sn NPs with controlled sizes, compositions and alloy structure. These Pt_3Sn NPs were highly active for CO and methanol oxidation in 0.1 M $HClO_4$ solutions and their activity and stability were further improved by a post-synthesis thermal treatment. These Pt_3Sn NPs could serve as a promising new CO tolerant catalyst for oxidation of small organic molecules.

9.2 Results and Discussion

Monodisperse Pt_3Sn alloy NPs were synthesized by high temperature reduction of Pt(acac)$_2$ and Sn(acac)$_2$. In the synthesis, oleylamine (OAm), as well as the solution of Pt(acac)$_2$ and Sn(acac)$_2$ in benzyl ether (BE) was injected into the solution of oleic acid (OA) in 1-octadecene (ODE) at 220˚C. The reaction temperature was subsequently raised to 280˚C and kept at this temperature for 1 h to complete the reduction. Transmission electron microscopy (TEM) analysis shows that the as-synthesized Pt_3Sn alloy NPs are monodisperse with their diameter measured to be 5.2 ± 0.4 nm (Figure 9-1A). Selected

area diffraction pattern (SAED) of a group of NPs (Figure 9-1B) and high resolution TEM (HRTEM) of a representative single NP (Figure 9-1C) indicate that the NPs are single crystalline. The crystalline fringe shown in Figure 9-1C is measured to be ~0.23 nm, corresponding to the (111) interplanar spacing of the face centered cubic (fcc) Pt_3Sn alloy structure (0.231 nm). Figure 9-1D is the X-ray diffraction (XRD) pattern of the as-synthesized Pt_3Sn NPs. The XRD peaks match with the fcc Pt_3Sn standard, and shift to lower diffraction angles compared to the fcc Pt peaks, indicating that alloying Pt with Sn results in a crystal lattice expansion in Pt_3Sn NPs. The composition of the Pt_3Sn NPs was measured to be 71/29 (atomic ratio) by both inductively coupled plasma-atomic emission spectrometry (ICP-AES) and Energy Dispersive X-ray Spectroscopy (EDS) (Figure S9-1).

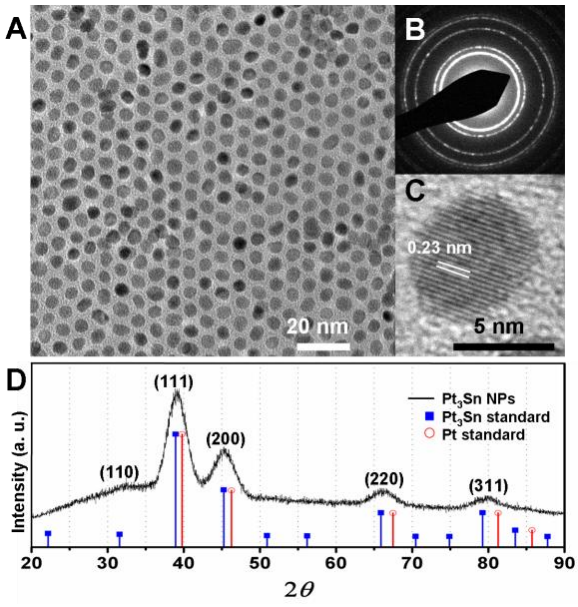

Figure 9-1. (A) TEM image, (B) SAED pattern, (C) HRTEM image, (D) XRD pattern of the as-synthesized 5.2 ± 0.4 nm Pt_3Sn NPs. The drop lines are the standard peaks for Pt_3Sn (■, PDF 03-065-0958) and Pt (○, PDF 01-084-0646).

In the synthesis, the size of the Pt_3Sn NPs was tuned by controlling the precursor injection temperatures. Injection at 180˚C resulted in 3.6 ± 0.3 nm NPs while at 240˚C led to 6.6 ± 0.9 nm NPs (Figure S9-2). We should emphasize that injection of $Pt(acac)_2$ and $Sn(acac)_2$ at higher temperatures and the use of OAm as the reducing agent are essential for the successful synthesis of monodisperse Pt_3Sn alloy NPs. Since $Sn(acac)_2$ is moisture sensitive, injecting $Sn(acac)_2$ and $Pt(acac)_2$ together at high temperatures can inhibit the hydrolysis of $Sn(acac)_2$ and promote the alloy formation. If $Sn(acac)_2$ was added before the reaction solution was heated, the side reaction of hydrolysis would lead to much less control in NP composition and morphology (Figure S3A). OAm served as a mild reducing agent for co-reduction of Pt and Sn salts at high temperatures. A stronger reducing agent, such as morphine borane, tended to reduce Pt selectively, producing non-uniform Pt-rich PtSn (Figure S9-3B). In a control experiment, we found that the presence of $Pt(acac)_2$ and $Sn(acac)_2$ in the injection solution could actually facilitate the reduction of these two salts for the formation of PtSn alloy. Without $Pt(acac)_2$, $Sn(acac)_2$ could not be reduced completely to its metallic state. Instead, a mixture of Sn and SnO NPs was separated (Figure S9-3C and Figure S9-3D&E). On the other hand, $Sn(acac)_2$ also helped Pt nucleation and growth. Without $Sn(acac)_2$, the reaction at the same condition could only lead to the formation of sub-nanometer Pt NPs which were difficult to precipitate from the reaction solution. Our synthesis indicates that the co-existence of $Sn(acac)_2$ and

$Pt(acac)_2$ is important for the metal salt co-reduction, metal co-nucleation and growth into Pt_3Sn NPs.

The Pt_3Sn NPs were deposited on carbon black (Ketjen EC-300J) for catalytic studies as described in the experimental section. Figure 9-2 shows the TEM images of two kinds of Pt_3Sn catalysts studied in this work. By comparing the Pt_3Sn as prepared (Figure 9-2A), and Pt_3Sn annealed (Figure 9-2B), we can see that the NPs have no obvious change in particle size during the acetic acid and the thermal treatment. XRDs of the Pt_3Sn as prepared and Pt_3Sn annealed (Figure S9-4) suggest a slight crystalline size increase from 3 nm to 3.6 nm. This crystalline size increase is due to the crystalline domain growth within a single NP, not the NP aggregation/sintering.

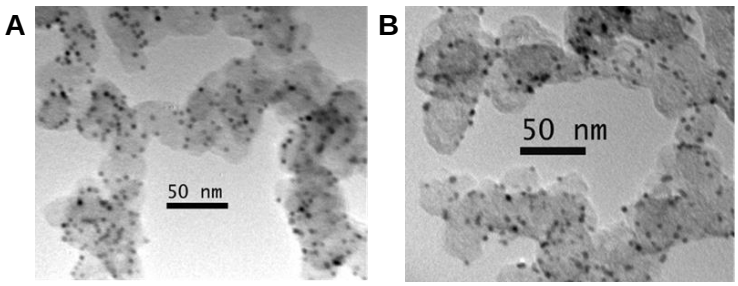

Figure 9-2. TEM images of (A) the Pt_3Sn as prepared and (B) the Pt_3Sn annealed. The catalysts were deposited on carbon black (Ketjen EC-300J) and washed with acetic acid (A) and annealed under Ar + 5% H_2 at 400 °C for 1 h (B).

CO electro-oxidation serves as a model system in understanding electro-oxidation of methanol.[30, 31] CO stripping voltammograms were used to probe oxidation potentials of

the adsorbed CO on catalyst surface. Figure 9-3A-C summarizes the results on CO stripping experiments. The commercial Pt has a sharp oxidation peak at 0.61 V, and the as-prepared and as-annealed Pt_3Sn show broader peaks at 0.50 V and 0.47 V. These broader oxidation peaks infer the lower onset potential for electro-oxidation of "weakly adsorbed" CO.[19-21] Figure 9-3D shows the CO oxidation curves in which the onset potentials are ~ 0 V for both Pt_3Sn NP catalysts and 0.25 V for the Pt catalyst. The annealed Pt_3Sn/C has the slightly higher activity than the as prepared one as indicated by the slightly negative shift of the CO stripping peak and higher CO oxidation current density. The enhanced CO oxidation activity of the Pt_3Sn alloy NPs over Pt NPs is consistent with what has been reported in the single crystal and thin film studies.[15-19] In the PtSn alloy structure, Sn weakens the CO adsorption on Pt and promotes water dissociation to form Sn-OH_{ad} near Pt-CO, facilitating the fast CO oxidation.[15]

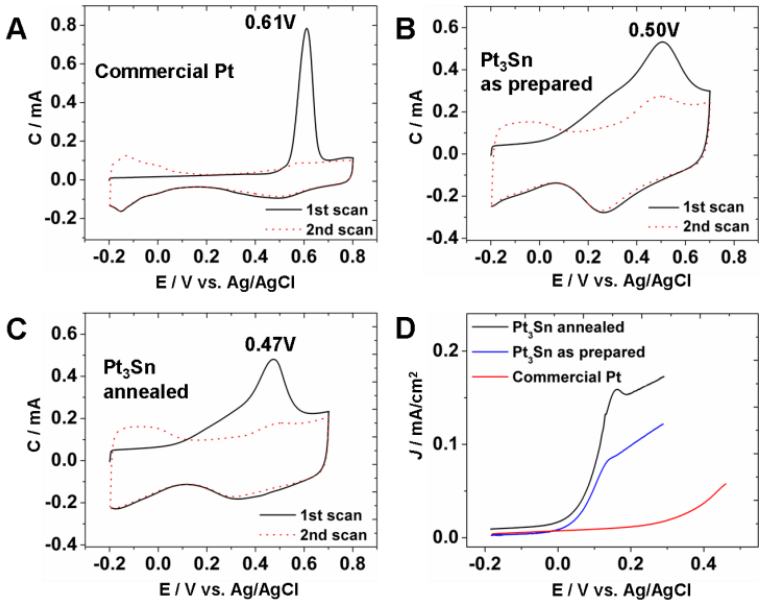

Figure 9-3. CO strippings of (A) the commercial Pt, (B) the Pt_3Sn as prepared, (C) the Pt_3Sn annealed. (D) J-V curves reflecting CO oxidation catalyzed by different catalysts in CO saturated 0.1 M $HClO_4$. The curves were obtained at a potential sweeping rate of 20 mV/s and RDE rotation speed of 1600 rpm.

The cyclic voltammograms (CVs) (Figure 9-4A-C) were recorded in 0.1 M $HClO_4$. The hydrogen under potential desorption area (H_{upd}) was used to estimated the electrochemically active surface areas (ECASAs) of the catalysts. The ECASA is comparably small for the as-prepared Pt_3Sn (1.99 cm^2). This is further reduced to 1.14 cm^2 for the annealed Pt_3Sn due likely to the increase of Sn on the alloy NP surface and the non-adsorption of H_{upd} on Sn.

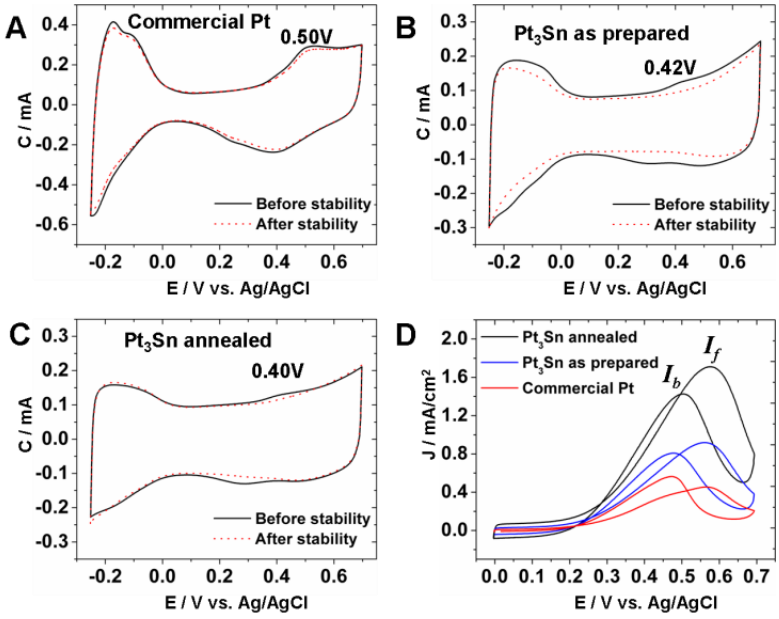

Figure 9-4. CVs of (A) the commercial Pt, (B) the Pt_3Sn as prepared and (C) the Pt_3Sn annealed. (D) J-V curves reflecting MOR catalysis in 0.1 M $HClO_4$ and 0.1 M methanol with a potential sweeping rate at 50 mV/s.

The CO stripping experiments indicate that monodisperse Pt_3Sn alloy NPs are active for CO oxidation and should be a good catalyst for MOR. The MOR activity was measured by sweeping the potentials from 0 – 0.7 V in a solution of 0.1 M $HClO_4$ and 0.1 M methanol, and the current density was normalized by dividing the raw current with the ECASAs, as shown in Figure 9-4D. We can see that the annealed Pt_3Sn has the highest oxidation peak current density in the forward scan (I_f). The I_f (mA/cm^2) decreases from the as-annealed Pt_3Sn (1.71) to the as-prepared Pt_3Sn (0.92) and further to the commercial Pt (0.45). The CO tolerance of the catalyst can be evaluated by the ratio of the oxidation peak current densities in the forward and backward scans (I_f/I_b). Larger I_f/I_b represents a more complete MOR, less accumulation of CO_{ads}, and a better CO-poisoning tolerance.[32] I_f/I_b ratios are calculated from the MORs in Figure 9-4D to be 1.20, 1.14 and 0.80 for the annealed Pt_3Sn, as-prepared Pt_3Sn and commercial Pt, respectively. The MOR currents normalized to Pt weight are given in Figure S9-5. The mass current densities follow the order of Pt_3Sn annealed > Pt > Pt_3Sn as prepared. The lower mass activity of the as-prepared Pt_3Sn is likely caused by their larger size (5.2 nm) and less perfect alloy structure. Once annealed, these Pt_3Sn NPs form a better alloy structure and may show more synergetic effect from Pt-Sn for MOR, leading to higher activity.

Stability of the catalyst in the oxidation conditions has long been a concern in developing Pt alloy catalysts for practical applications. The stability of the Pt_3Sn NP

catalysts were evaluated by the chronoamperometric curves in 0.1 M $HClO_4$ + 0.1 M methanol at 0.3 V for 1 h (Figure 9-5). The Pt_3Sn annealed shows less degradation in current density compared to the Pt_3Sn as-prepared, and both kinds of Pt_3Sn NPs have higher current density than the commercial Pt throughout the 1 h test period. The CVs of the catalysts in 0.1 M $HClO_4$ before and after the 1 h stability test are compared in Figure 9-4A-C. The commercial Pt has an ECASA decrease from 5.15 cm^2 to 4.55 cm^2 (-11.7%), which agrees with the NP aggregation observed after catalysis (Figure S9-6A&B). The as-prepared Pt_3Sn NPs are unstable and show certain degree of aggregation (Figure S9-6C) with ECASA changing from 1.99 cm^2 to 1.54 cm^2 (-22.6%). Their composition is changed from Pt/Sn = 70/30 to 77/23 (Figure S9-1). In contrast, the annealed Pt_3Sn NPs show a much improved stability without obvious change in both NP morphology (Figure S9-6D**)** and composition (from Pt/Sn = 70/30 to 72/28, Figure S9-1). Their ECASA area is actually increased from 1.14 to 1.27 cm^2 (+11.4%) due most likely to the more efficient H_2 adsorption/desorption on the better ordered PtSn alloy structure.

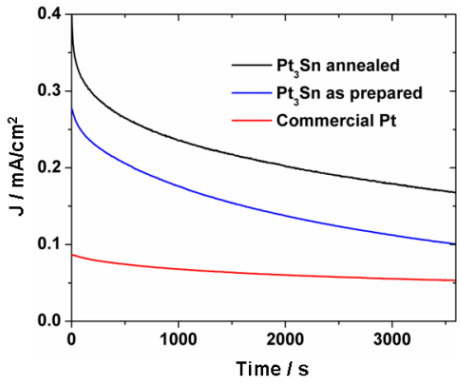

Figure 9-5. Chronoamperometric curves reflecting stability of the NP catalysts in 0.1 M $HClO_4$ and 0.1 M methanol at constant voltage 0.3 V for 1 h.

9.3 Conclusion

We have developed a high temperature organic phase synthesis of monodisperse Pt_3Sn alloy NPs by a controlled co-reduction of $Pt(acac)_2$ and $Sn(acac)_2$ at 180-280˚C in 1-octacdecene. In the synthesis, oleylamine was used as a reducing agent and oleylamine/oleic acid served as surfactants. The key to the successful synthesis of Pt_3Sn NPs was the co-injection of $Pt(acac)_2$ and $Sn(acac)_2$ at high temperatures. The size of the Pt_3Sn NPs was tuned from 4-7 nm by controlling the metal-injection temperatures. The Pt_3Sn alloy NPs were catalytically more active for CO and methanol oxidations than the pure Pt NP catalyst and their activity and stability could be further improved by the thermal treatment in Ar + 5% H_2 at 400˚C for 1 h. The Pt_3Sn NPs are a promising group of new catalysts for electro-oxidation of CO, methanol and other small organic molecules.

9.4 Experimental Section

9.4.1 *Chemicals*. $Pt(acac)_2$ (acac = acetylacetonate), $Sn(acac)_2$ (98%, Strem), oleylamine (OAm, technical grade, 70%, Aldrich), oleic acid (OA, technical grade, 90%, Aldrich), 1-octadecene (ODE, technical grade, 90%, Aldrich), benzyl ether (BE, 98%, Aldrich), carbon black (Kejen EC 300J), acetic acid (ACS reagent, ≥ 99.7%, Aldrich). E-TEK Pt (20% Pt loading, Fuel Cell Store), TANAKA Pt (TEC10E50E-HT, 50.5% Pt loading,

TANAKA KIKINZOKU KOGYO K. K.), perchloric acid ($HClO_4$, 70-72%, J. T. Baker), methanol (≥99.8%, Mallinckrodt Chemicals) were purchased and used as received.

9.4.2 *Synthesis of Pt_3Sn NPs*. Under an argon (Ar) gas flow and magnetic stirring, 2 ml of OA and 15 ml of ODE were mixed in a reaction flask and degassed at room temperature and 120˚C for 0.5 h each. At the same time, a 5 ml BE solution of 0.15 mmol $Pt(acac)_2$ and 0.05 mmol $Sn(acac)_2$ was prepared separately by first dissolving 0.059 g of $Pt(acac)_2$ in 5 ml of BE with sonication, followed by addition of 0.11 ml of $Sn(acac)_2$ stock solution (0.5 ml $Sn(acac)_2$ in 4.5 ml BE). The OA and ODE mixture was heated up to 220˚C when 3 ml of OAm was added by syringe. Once the reaction temperature reached 220˚C again, the BE solution of $Pt(acac)_2$ and $Sn(acac)_2$ was injected immediately to initiate the burst nucleation, which was indicated by the solution color change from light yellow to black for about 60 sec after injection. Then the temperature was raised to 280˚C at a heating rate of 2˚C/min, and kept at this temperature for 1 h. After cooled down to room temperature, the Pt_3Sn NPs were separated by adding isopropanol and centrifugation. The Pt_3Sn NPs were washed twice by a mixture of hexane and isopropanol and finally dispersed in hexane. The size of as prepared Pt_3Sn was around 5.2 nm.

To prepare smaller (3.6 nm) and larger (6.6 nm) Pt_3Sn NPs, OAm and the metal precursor solution were injected at 180˚C and 240˚C respectively while other reaction conditions were kept same.

9.4.3 *Preparation of carbon supported Pt_3Sn NPs (Pt_3Sn/C as prepared).* 10 mg of Pt_3Sn NPs in 15 ml of hexane were mixed with 30 mg of carbon black (Ketjen EC-300J) and sonicated for 1 h. The Pt_3Sn NPs loaded on carbon was separated by centrifugation and

then heated in acetic acid at 70˚C for 12 h and washed with ethanol. After surfactant (25% wt of the NPs) removal, the total metal loading calculated was 20% wt, and the Pt loading was 16% wt. Finally, the Pt_3Sn as prepared was dried under a controlled flow of nitrogen and dispersed in de-ionized (DI) water by sonication to form a 2 mg catalyst per ml suspension.

9.4.4 *Thermal annealing of the carbon supported Pt_3Sn as prepared (Pt_3Sn/C annealed).* The Pt_3Sn NPs supported carbon black (Ketjen EC-300J) was annealed under a gentle flow of Ar + 5% H_2 in a tube furnace at 400˚C for 1 h. The annealed Pt_3Sn/C was dispersed in DI water to form a 2 mg catalyst per ml suspension.

9.4.5 *Commercial Pt catalysts*. TANAKA Pt (50.5% Pt, 5 nm) was dispersed in DI water to form a 0.5 mg catalyst/ml suspension and used for CO oxidation. E-TEK Pt (20% Pt, 2-3 nm) was sonicated with DI water to form a 2 mg catalyst/ml suspension and used for methanol oxidation reaction (MOR).

9.4.6 *Electrochemical measurement*. 20 μl of catalyst in water suspension was deposited on a glassy carbon rotating disk (5 mm in diameter, mirror polished) and dried under vacuum at room temperature. 10 μl of 0.1% wt Nafion water solution was deposited over the catalyst and dried. Ag/AgCl electrode and Pt wire were used as the reference and counter electrodes, respectively.

In the CO experiments, the rotating disk electrode was first immersed in the CO saturated 0.1 M $HClO_4$ at -0.20 V to form a CO adlayer on the NP surface. The CO stripping voltammetry was performed by scanning between -0.20 V and 0.70 V in the Ar purged 0.1 M $HClO_4$ at 50 mV/s sweep rate. The CO bulk oxidation polarization curves

were acquired at 1600 rpm rotating speed and 20 mV/s sweep rate. The upper potential limit for the CO bulk oxidation was 0.30 V for the Pt_3Sn and 0.47 V for the Pt.

In the MOR experiments, the electrodes were first immersed in the nitrogen saturated 0.1 M $HClO_4$ solution, and the potential was scanned from -0.25 to 0.7 V at a scan rate of 50 mV/s. The scan was repeated several times to obtain a stable cyclic voltammograms (CV) curve. CVs were used to estimate the electrochemically active surface area (ECASA) of the catalyst by calculating the H_{upd} area of the catalyst. CVs for MOR were conducted in 0.1 M $HClO_4$ and 0.1 M methanol from 0 to 0.7 V at a scan rate of 50 mV/s. The MOR currents were normalized to ECASAs or to Pt weight. The stability was tested by chronoamperometry at 0.3 V in 0.1 M $HClO_4$ and 0.1 M methanol for 1 h. The currents were also normalized with ECASAs or Pt weight. After the stability test, the electrode was rinsed with DI water then immersed in fresh 0.1 M $HClO_4$. Potential scan from -0.25 to 0.7 V at a scan rate of 50 mV/s was repeated to record a stable CV after stability test.

9.4.7 *Characterization*. Transmission electron microscopy (TEM) and high resolution TEM (HRTEM) images were acquired on a Philips CM20 (200 kV) and a JEOL 2010 (200 kV) transmission electron microscope. X-ray powder diffraction patterns of the samples were recorded on a Bruker AXS D8-Advanced diffractometer with Cu K_α radiation (λ=1.5418 Å). The compositions of the samples were measured by Inductively Coupled Plasma – Atomic Emission Spectroscopy (ICP-AES) and Energy Dispersive X-ray Spectroscopy (EDS) on a LEO 1560 scanning electron microscope. Electrochemical measurements were performed on a Pine Electrochemical Analyzer, Model AFCBP1.

Acknowledgement. Supported in part by ExxonMobil Research and Engineering Co.

9.5 References

1. Chen, A.; Holt-Hindle, P., *Chem. Rev.* **2010,** 110, 3767-3804.

2. Ferrando, R.; Jellinek, J.; Johnston, R. L., *Chem. Rev.* **2008,** 108, 845-910.

3. Liu, Y.; Li, D.; Sun, S., *J. Mater. Chem*. 2011, 21, 12579-12587.

4. Wang, D.; Li, Y., *Adv. Mater*. **2011,** 23(9), 1044-1060.

5. Kua, J.; Goddard, W. A., *J. Am. Chem. Soc.* **1999,** 121, 10928-10941.

6. Stamenkovic, V. R.; Mun, B. S.; Arenz, M.; Mayrhofer, K. J. J.; Lucas, C. A.; Wang, G.; Ross, P. N.; Markovic, N. M., *Nat Mater* **2007,** 6, 241-247.

7. Markovic, N. M.; Ross, P. N., *Surf. Sci. Rep.* **2002,** 45, 117-229.

8. Wang, Y.; Mi, Y.; Redmon, N.; Holiday, J., *J. Phys. Chem. C* **2010,** 114, 317-326.

9. Huidobro, A.; Sepulveda-Escribano, A.; RodrIguez-Reinoso, F., *J. Catal.* **2002,** 212, 94-103.

10. Santori, G. F.; Casella, M. L.; Siri, G. J.; Adúriz, H. R.; Ferrettia, O. A., *React. Kinet. Catal. Lett.* **2002,** 75, 225-230.

11. Merlo, A. B.; Vetere, V.; Ruggera, J. F.; Casella, M. L., *Catal. Commun.* **2009**, (13), 1665-1669.

12. Burch, R.; Garla, L. C., *J. Catal.* **1981,** 71, 360-372.

13. Llorca, J.; Homs, N.; Fierro, J. L. G.; Sales, J.; Piscina, P. R. d. l., *J. Catal.* **1997,** 166, 44-52.

14. Lieske, H.; Volter, J., *J. Catal.* **1984,** 90, 96-105.

15. Stamenkovic, V.; Arenz, M.; Blizanac, B. B.; Mayrhofer, K. J. J.; Ross, P. N.; Markovic, N. M., *Surf. Sci.* **2005,** 576, 145-157.

16. Stamenkovic, V. R.; Arenz, M.; Lucas, C. A.; Gallagher, M. E.; Ross, P. N.; Markovic, N. M., *J. Am. Chem. Soc.* **2003,** 125, 2736-2745.

17. Gasteiger, H. A.; Markovic, N. M.; Ross, P. N., *J. Phys. Chem.* **1995,** 99, 8945-8949.

18. Hayden, B. E.; Rendall, M. E.; South, O., *J. Am. Chem. Soc.* **2003,** 125, 7738-7742.

19. Gasteiger, H. A.; Marković, N. M.; Ross, P. N., *Catal. Lett.* **1996,** 36, 1-8.

20. Crabb, E. M.; Marshall, R.; Thompsett, D., *J. Electrochem. Soc.* **2000,** 147, 4440-4447.

21. Liu, Z.; Reed, D.; Kwon, G.; Shamsuzzoha, M.; Nikles, D. E., *J. Phys. Chem. C* **2007,** 111, 14223-14229.

22. Honma, I.; Toda, T., *J. Electrochem. Soc.* **2003,** 150, A1689-A1692.

23. Neto, A. O.; Dias, R. R.; Tusi, M. M.; Linardi, M.; Spinacé, E. V., *J. Power Sources* **2007,** 166, 87-91.

24. Vigier, F.; Coutanceau, C.; Hahn, F.; Belgsir, E. M.; Lamy, C., *J. Electroanal. Chem.* **2004,** 563, 81-89.

25. Melke, J.; Schoekel, A.; Dixon, D.; Cremers, C.; Ramaker, D. E.; Roth, C., *J. Phys. Chem. C* **2010,** 114, 5914-5925.

26. Jiang, L.; Zhou, Z.; Li, W.; Zhou, W.; Song, S.; Li, H.; Sun, G.; Xin, Q., *Energy Fuels* **2004,** 18, 866-871.

27. Neto, A. O.; Vasconcelos, T. R. R.; Silva, R. W. R. V. D.; Linardi, M.; Spinacé, E. V., *J. Appl. Electrochem.* **2005,** 35, 193-198.

28. Dupont, C.; Jugnet, Y.; Loffreda, D., *J. Am. Chem. Soc.* **2006,** 128, 9129-9136.

29. Boualleg, M.; Baudouin, D.; Basset, J.-M.; Bayard, F.; Candy, J.-P.; Jumas, J.-C.; Veyre, L.; Thieuleux, C., *Chem. Commun.* **2010,** 46, 4722-4724.

30. Beden, B.; Lamy, C.; de Tacconi, N. R.; Arvia, A. J., *Electrochim. Acta* **1990,** 35, 691-704.

31. Lee, S. W.; Chen, S.; Sheng, W.; Yabuuchi, N.; Kim, Y.-T.; Mitani, T.; Vescovo, E.; Shao-Horn, Y., *J. Am. Chem. Soc.* **2009,** 131, 15669-15677.

32. Sharma, S.; Ganguly, A.; Papakonstantinou, P.; Miao, X.; Li, M.; Hutchison, J. L.; Delichatsios, M.; Ukleja, S., *J. Phys. Chem. C* 114, 19459-19466.

9.6 Supporting information

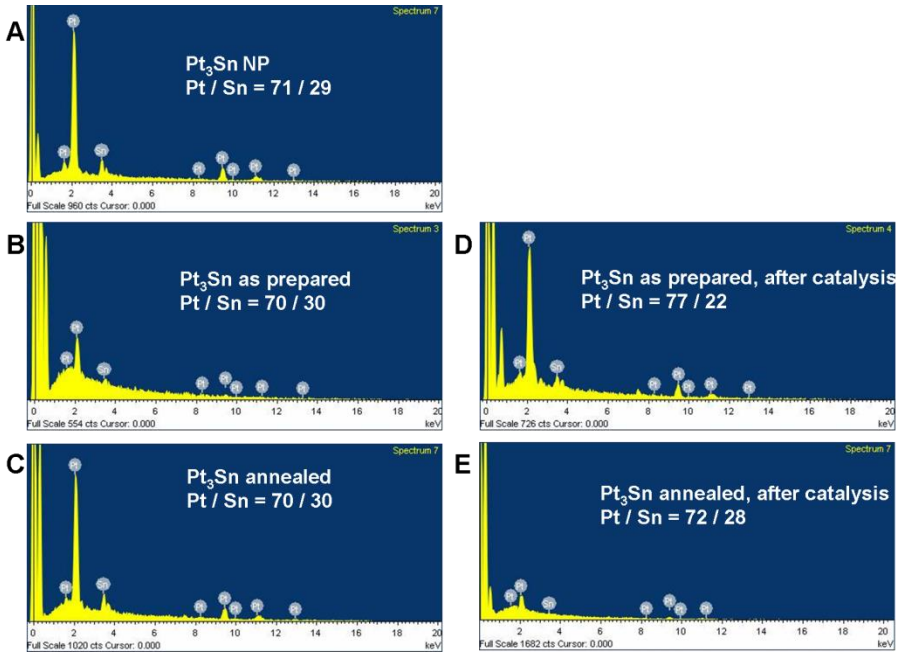

Figure S9-1. EDS analyses of (A) the typical 5.2 nm Pt_3Sn NPs, (B) Pt_3Sn as prepared (Pt_3Sn/C, after acetic acid treatment), (C) Pt_3Sn annealed (Pt_3Sn/C, after acetic acid and annealing treatments), (D) Pt_3Sn as prepared after catalysis, (E) Pt_3Sn annealed after catalysis.

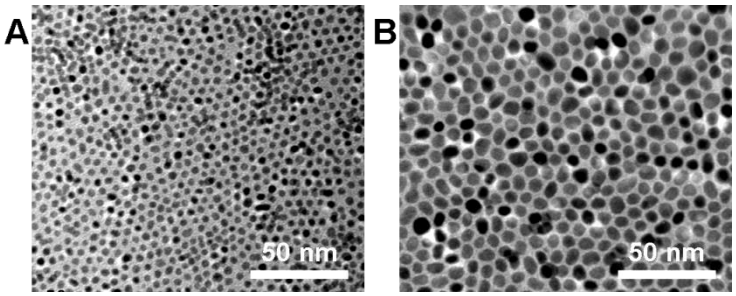

Figure S9-2. TEM images of (A) the 3.6 ± 0.3 nm (B) the 6.6 ± 0.9 nm Pt_3Sn NPs synthesized from precursor injection at 180˚C and 240˚C, respectively.

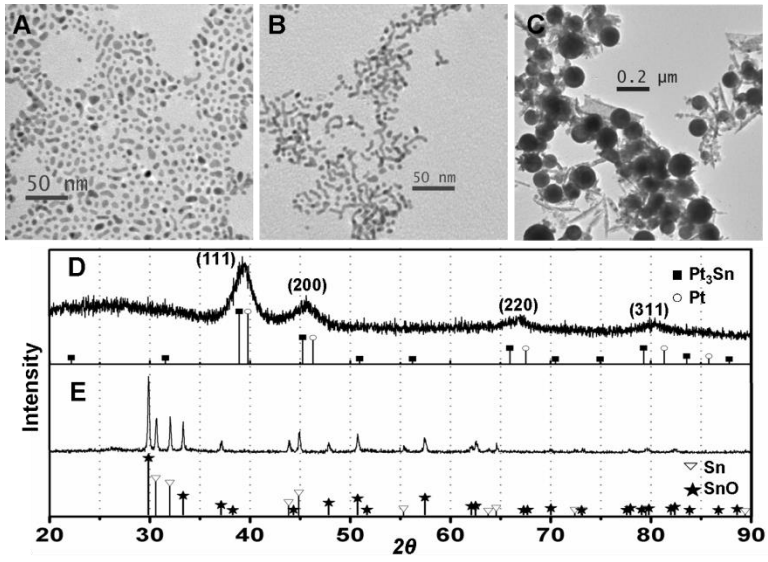

Figure S9-3. TEM images of (A) polydisperse Pt_3Sn NPs from the synthesis with precursors added initially, (B) the Pt and Pt_3Sn mixture synthesized with morpholine borane as a reducing agent, (C) Sn and SnO NPs from the synthesis without $Pt(acac)_2$. (D) XRD of the NPs shown in (B), indicating a mixture of Pt_3Sn (■, PDF 03-065-0958) and Pt (○, PDF 01-084-0646) phases, and (E) XRD of the NPs shown in (C) with Sn (∇, PDF 01-086-2265) and SnO (★, PDF 01-085-0423).

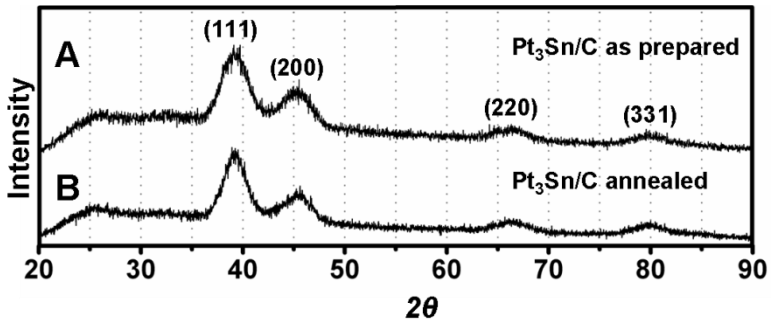

Figure S9-4. XRDs of (A) the Pt_3Sn as prepared and (B) the Pt_3Sn annealed.

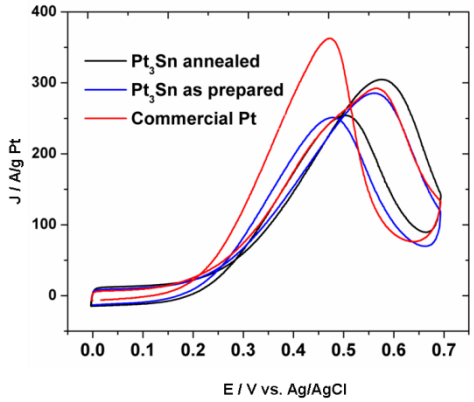

Figure S9-5. J-V curves reflecting MOR catalysis in 0.1 M $HClO_4$ and 0.1 M methanol, at 50 mV/s, Pt_3Sn annealed (black), Pt_3Sn as prepared (blue), and commercial Pt (red), the current density was normalized to weight of Pt.

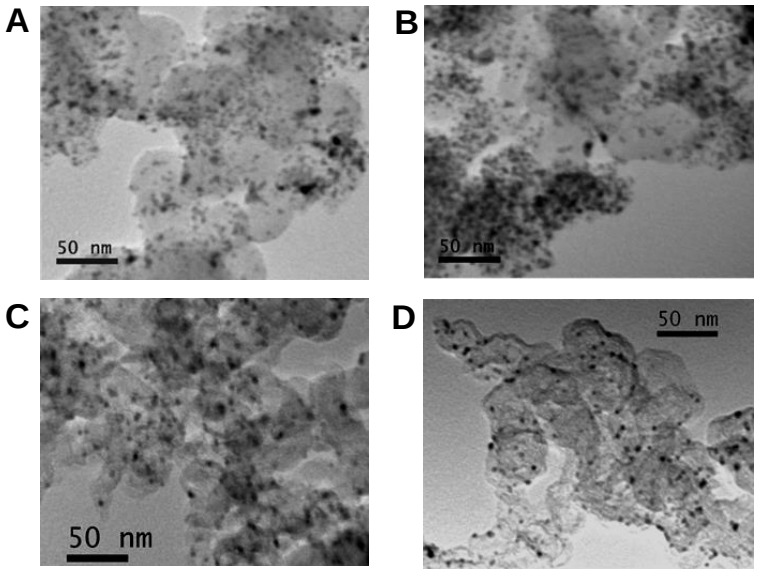

Figure S9-6. TEM images of the commercial Pt/C catalyst before (A) and after (B) stability tests, as well as the Pt_3Sn/C as prepared (C) and Pt_3Sn/C annealed (D) after stability test.